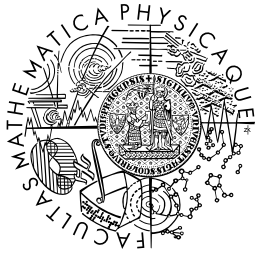

FACULTY
OF MATHEMATICS
AND PHYSICS
Charles University

DOCTORAL THESIS

DAVID EINŠPIGEL

TIME-DOMAIN MODELLING OF GLOBAL BAROTROPIC OCEAN TIDES

Department of geophysics

Supervisor:	prof. RNDr. Zdeněk Martinec, DrSc.
Study programme:	Physics
Study branch:	Geophysics

Prague 2016

I declare that I carried out this doctoral thesis independently, and only with the cited sources, literature and other professional sources.

I understand that my work relates to the rights and obligations under the Act No. 121/20000 Sb., the Copyright Act, as amended, in particular the fact that the Charles University in Prague has the right to conclude a license agreement on the use of this work as a school work pursuant to Section 60 subsection 1 of the Copyright Act.

In Prague 15.12.2016 David Einšpigel

Title: Time-domain modelling of global barotropic ocean tides

Author: David Einšpigel

Department: Department of geophysics

Supervisor: prof. RNDr. Zdeněk Martinec, DrSc., Department of geophysics

Abstract: Traditionally, ocean tides have been modelled in frequency domain with forcing of selected tidal constituents. It is a natural approach, however, non-linearities of ocean dynamics are implicitly neglected. An alternative approach is time-domain modelling with forcing given by the full lunisolar potential, i.e., all tidal constituents are included. This approach has been applied in several ocean tide models, however, a few challenging tasks still remain to solve, for example, the assimilation of satellite altimetry data. In this thesis, we present DEBOT, a global and time-domain barotropic ocean tide model with the full lunisolar forcing. DEBOT has been developed "from scratch". The model is based on the shallow water equations which are newly derived in geographical (spherical) coordinates. The derivation includes the boundary conditions and the Reynolds tensor in a physically consistent form. The numerical model employs finite differences in space and a generalized forward-backward scheme in time. The validity of the code is demonstrated by the tests based on integral invariants. DEBOT has two modes for ocean tide modelling: DEBOT-h, a purely hydrodynamical mode, and DEBOT-a, an assimilative mode. We introduce the assimilative scheme applicable in a time-domain model, which is an alternative to existing frequency-domain techniques used in other assimilative ocean tide models. The accuracy of DEBOT in both modes is assessed against tide gauge data through a series of tests. The tests demonstrate that DEBOT is comparable to state-of-the-art global ocean tide models for major tidal constituents. Furthermore, as the signals of all tidal constituents are included in DEBOT, modelling of minor tidal constituents and non-linear compound tides, which are often overlooked in other studies, are also discussed. Our modelling approach can be useful for those applications where the frequency domain approach is not suitable.

Keywords: Global ocean tides; Shallow water equations; Tidal potential; Time-domain modelling; Data assimilation

Název práce: Modelování globálních barotropních oceánských slapů v časové oblasti

Autor: David Einšpigel

Katedra: Katedra geofyziky

Vedoucí disertační práce: prof. RNDr. Zdeněk Martinec, DrSc., Katedra geofyziky

Abstrakt: Oceánské slapy se tradičně modelují ve frekvenční oblasti s buzením na vybraných slapových frekvencí. Je to přírozený přístup, nicméně nelinearity oceánské dynamiky nejsou přímo zahrnuty. Alternativou je modelování v časové oblasti s buzením, které je dáno kompletním lunisolárním slapovým potenciálem, tj. všechny slapové frekvence jsou zahrnuty. Tento přístup byl uplatněn v několika oceánských slapových modelech, nicméně stále zůstává pár problémů k vyřešení, například asimilace satelitních altimetrických dat. V této práci představujeme DEBOT, globální a časový barotropní oceánský slapový model s úplným lunisolárním buzením. DEBOT byl vyvinut „od píky". Základem modelu jsou rovnice mělké vody, které jsou nově odvozeny v geografických (sférických) souřadnicích. Odvození zahrnuje okrajové podmínky a Reynoldsův tenzor ve fyzikálně konzistentním tvaru. Numerický model je řešen v prostoru metodou konečných diferencí a v čase zobecněným forward-backward schématem. Funkčnost kódu je demonstrována testy na zachování integrálních invariantů. DEBOT má dva módy pro modelování oceánských slapů: DEBOT-h, čistě hydrodynamický mód, a DEBOT-a, asimilační mód. Navrhli jsme asimilační schéma vhodné pro časový model, které představuje alternativu k existujícím frekvenčním technikám, jež jsou používány v ostatních asimilačních modelech oceánských slapů. Přesnost obou módů DEBOTu je vyhodnocena pomocí srovnání s daty z měření mořské hladiny. Testy dokazují, že DEBOT je srovnatelný s moderními globálními modely oceánských slapů pro hlavní slapové frekvence. Navíc, protože DEBOT obsahuje signál všech slapových frekvencí, diskutujeme modelování vedlejších slapů a nelineárních složených slapů, které jsou často opomenuty v ostatních studiích. Náš přístup k modelování může být užitečný v případech, kdy frekvenční přístup není vhodný.

Klíčová slova: Globální oceánské slapy; Rovnice mělké vody; Slapový potenciál; Modelování v časové oblasti; Asimilace dat

The research during years 2014 – 2016 was conducted in

Geophysics Section
School of Cosmic Physics
Dublin Institute for Advanced Studies

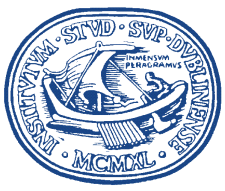

DIAS
Institiúid Ard-Léinn Bhaile Átha Cliath
Dublin Institute for Advanced Studies

Děkuji všem, kdo mi jakkoliv pomohli během mých doktorandských studií. Děkuji svému školiteli profesorovi Zdeňkovi Martincovi za jeho vedení, rady, svobodu, kterou mi poskytl ve vědecké činnosti, a možnost strávit téměř tři roky v Dublinu. Děkuji kolegům z Katedry geofyziky, speciálně Liborovi Šachlovi, Jakubovi Velímskému a Láďovi Hanykovi za diskuze i technickou pomoc. Děkuji osazenstvu Geodynamického semináře za palbu kritiky a připomínek během mých prezentací. V neposlední řadě děkuji svým rodičům za podporu během všech těch let, co jsem studentem.

* * *

I thank everybody who helped me in any way during my PhD studies. I thank Michael Schindelegger for valuable discussions, Detlef Stammer and Richard Ray for providing the shelf seas and coastal tide gauge data, unknown reviewers of my articles for valuable comments and questions and last but not least people of DIAS for the friendly and cheerful environment.

* * *

This research was supported by the grants SVV-2014-260096 and SVV260327/2016, by the European Space Agency Contract No. 4000109562/14/NL/CBi "Swarm+Oceans" under the STSE Programme as well as by The Ministry of Education, Youth and Sports from the Large Infrastructures for Research, Experimental Development and Innovations project "IT4Innovations National Supercomputing Center – LM2015070". The author acknowledges the support.

CONTENTS

INTRODUCTION

Time and tide wait for no man.
— Old English proverb

Ocean tides are an important phenomenon which has a significant impact on the entire Earth system. Therefore, precise ocean tide modelling is needed for many geophysical and geodetic applications. One of the most important application of ocean tide models is removing tidal signals from various measurements, for example satellite altimetry or gravimetry, so any non-tidal signal can be studied (e.g., Fu and Cazenave, 2001; Seeber, 2003; Visser et al., 2010). Among other applications of ocean tide models, we can mention dissipation of tidal energy, generation of internal tides and mixing of the oceans (e.g., Vlasenko et al., 2005; Arbic et al., 2010; Müller et al., 2012; Taguchi et al., 2014), variations of the Earth's rotation due to tides (e.g., Weis, 2006; Schindelegger et al., 2016) or the induced magnetic field generated by motions of conductive seawater in the main geomagnetic field (e.g., Tyler et al., 2003; Kuvshinov and Olsen, 2005; Sabaka et al., 2015; Velímský et al., 2016).

Great progress has been made in ocean tide modelling since the pioneering works of Pekeris and Accad (1969); Accad and Pekeris (1978); Schwiderski (1979, 1980); Parke and Hendershott (1980); Parke (1982). Much of the progress is owing to satellite altimetry. Data from Topex/Poseidon (T/P), a joint satellite mission of NASA and CNES which was launched in 1992, enabled the development of ocean tide models of unprecedented accuracy (Shum et al., 1997). In the next years, more data from T/P, its ancestors Jason-1 and OSTM/Jason-2 and other missions have led not only to improved tidal atlases but also to a better understanding of ocean dynamics and energy budget (Stammer et al., 2014). Satellite altimetry confirmed suggestions of tidal energy dissipation through a conversion of barotropic tides into baroclinic internal waves (Egbert and Ray, 2000). This discovery led to the improvements of purely hydrodynamical models, i.e. those which are governed by physical laws but not con-

strained by any data (Jayne and St. Laurent, 2001; Green and Nycander, 2013; Stammer et al., 2014).

Traditionally, ocean tides have been modelled in frequency domain with forcing of selected tidal constituents, e.g., M_2, S_2, O_1, K_1, etc. This is the case of the historical models from 70s and 80s but also some modern hydrodynamical models, e.g., STM-1B (Hill et al., 2011) and assimilative models, e.g., FES (Lyard et al., 2006; Carrère et al., 2012), HAMTIDE (Zahel, 1995; Taguchi et al., 2014) and TPXO (Egbert et al., 1994; Egbert and Erofeeva, 2002). Such an approach is natural since ocean tides are primarily composed of handful of periodical or quasi-periodical signals, however, it neglects non-linearities of ocean dynamics. It means that compound tides, e.g., M_4, MS_4, MN_4, etc., which are generated mainly on continental shelves by non-linear interactions of astronomical tidal components, can not be predicted by frequency-domain models. Although, we should note that the compound tides are still modelled in FES by an iterative approach, however at the price of expensive computational costs (Carrère et al., 2012). Apart from the compound tides, another non-linearity is caused by the energy dissipation due to the friction at the sea bottom which is usually parameterized in a quadratic form. Therefore, an alternative parameterization has to be implemented in frequency-domain models. STM-1B uses an iterative scheme while the assimilative models include linearised bottom drag terms.

In this thesis, we apply an alternative approach. We deal with ocean tide modelling in time domain with the full lunisolar forcing. This means that all tidal components, including the compound tides, are modelled simultaneously. Of course, this is not a completely novel approach. Several high-quality time-domain models have been developed, e.g., OTIS (Egbert et al., 2004) which is, however, forced by selected tidal components only; TiME (Weis et al., 2008) with the full astronomical forcing but without a parameterization of the important internal tide drag; or baroclinic models STORMTIDE (Müller et al., 2012) and HYCOM (Arbic et al., 2010) which combine ocean circulation and tides.

The model presented in this thesis is called "DEBOT" (David Einšpigel Barotropic Ocean Tides) and incorporates the full lunisolar forcing given by the astronomical tidal potential of the second and third order which is computed from ephemerides, i.e., actual positions of the Moon and Sun. DEBOT has been built up "from scratch" and has been developed since the author's master studies, see the author's master thesis Einšpigel (2012). The model has substantially changed since Einšpigel (2012) from a rather general shallow-water model to a realistic ocean tide model. The derivation of the shallow-water equations, which are a base of the model, has been revised and an original semi-implicit time-stepping scheme has been replaced by a generalized forward-backward scheme. And most importantly, a data assimilation scheme has been developed and implemented in the time-domain model. As a consequence, DEBOT has two modes: the purely hydrodynamical mode, denoted as "DEBOT-h", and the assimilative mode, denoted as "DEBOT-a". These

changes has been documented in two peer-reviewed papers Einšpigel and Martinec (2015, 2016), hereinafter EM15 and EM16. The source code of DEBOT is freely available at `http://geo.mff.cuni.cz/~einspigel/debot.html`.

The structure of the thesis is as follows: In Chapter 1, the shallow-water equations in the geographical coordinates are derived from the fundamental balance laws. Numerical methods employed to solve the shallow-water equations and used in DEBOT are described in Chapter 2. Chapter 3 is a general treatise on ocean tides. Chapter 4 describes DEBOT-h and its results. A parameter study is discussed and DEBOT-h is compared to other purely hydrodynamical models. Chapter 5 introduces the time-domain assimilation scheme, shows results of DEBOT-a and compares DEBOT-a with state-of-the-art empirical and assimilative models. A special attention is paid to minor tidal constituents and compound tides which are often overlooked in global tidal studies. They are discussed in Chapter 6.

CHAPTER

1

DERIVATION OF THE SHALLOW WATER EQUATIONS IN THE GEOGRAPHICAL COORDINATES

Ocean circulation represents a complex free boundary-value problem that is mathematically described by the Navier–Stokes equations supplemented by appropriate boundary conditions. However, as commonly known, there has not been proven yet that there exists a smooth and globally defined solution in three dimensional space and time. This problem has been denoted by the Clay Mathematics Institute as one of the seven most important open problems in mathematics (Fefferman, 2000). Moreover, the complicated nature of the equations restricts possibilities of their numerical solution.

In modelling ocean circulation, the moving free surface represents a crucial problem. An approximate way to overcome this problem is by the so-called *shallow water approximation*. This approximation can be applied when the vertical dimension of the solution domain is significantly smaller in comparison with the horizontal dimension. Under this assumption, the Navier–Stokes equations are reduced to the shallow water equations for the free-surface elevation and the horizontal components of flow velocity. The shallow water equations, which were first derived by Adhémar Jean Claude Barré de Saint–Venant, a french mechanician and mathematician, in 1871 (Barré de Saint-Venant, 1871), are used in the modelling of many geophysical phenomena, such as the oceans, atmosphere, shelf and coastal seas, rivers, and even avalanches. The derivation of the shallow water equations, either in Cartesian or spherical coordinates, can be found in many books and papers (e.g., Pedlosky, 1987; Vallis, 2006; Kolar et al., 1994; Randall, 2013; Gerbeau and Perthame,

2000; Ferrari and Saleri, 2004; Marche, 2006), however, most of them do not consider the turbulent viscosity (Pedlosky, 1987; Vallis, 2006; Randall, 2013), or use stress tensors that are not suitable for large-scale ocean modelling (Gerbeau and Perthame, 2000; Marche, 2006). Furthermore, the derivations are often vague with respect to the assumptions used. Hence, we decided to provide a new derivation in geographical coordinates, which is as detailed and systematic as possible and includes a complete, physically consistent stress tensor, boundary conditions and transparently introduced assumptions. This is the topic of this chapter. The chapter is divided into five sections, each describes one step in the derivation.

(1) We start the derivation with the fundamental balance laws and the assumption of an incompressible fluid which leads to a formulation of the incompressible Navier–Stokes system. The system is supplemented with boundary conditions. In this paper, we assume a friction vector at the bottom and that no fluid crosses the boundaries, see Section 1.1.
(2) The Reynolds tensor which describes energy losses in large-scale ocean motions due to turbulences on very short scales is discussed in Section 1.2.
(3) The so-called spherical approximation is applied. The radial distance of a material point in oceans is approximated by the mean Earth radius a, see Section 1.3
(4) The equations are expressed in a dimensionless form and terms of small magnitudes are neglected (the hydrostatic approximation), see Section 1.4.
(5) The non-dimensionalized equations are integrated in the radial direction from the bottom to the surface, using the Leibniz integral rule and the appropriate boundary conditions are applied. Next, we assume the horizontal flow being only weakly dependent on depth such that the derivatives of velocities with respect to the radial direction are negligible. Section 1.5.
(6) Finally, we check whether the viscous term is physically consistent, see Section 1.6.

1.1 The Navier–Stokes system and the boundary conditions

As a starting point for the derivation, the fundamental balance laws are used, namely the continuity equation and the equation of motion (see, e.g., Hutter and Jöhnk, 2004)

$$\frac{\partial \rho}{\partial t} + \nabla \cdot (\rho \vec{v}) = 0, \tag{1.1}$$

$$\rho \frac{\mathrm{D}\vec{v}}{\mathrm{D}t} = \nabla \cdot \mathbf{t} + \vec{f}, \tag{1.2}$$

where ρ is the applied density, $\vec{v}$ the velocity, $\mathbf{t}$ the stress tensor and $\vec{f}$ the external body forces. Note that the material time derivative $\frac{\mathrm{D}}{\mathrm{D}t}$ in the Eulerian representation is $\frac{\mathrm{D}}{\mathrm{D}t} = \frac{\partial}{\partial t} + \vec{v} \cdot \nabla$.

We consider an incompressible fluid for which the continuity equation (1.1) reduces to

$$\nabla \cdot \vec{v} = 0. \tag{1.3}$$

The external forces include the Coriolis force and gravitation. The stress tensor takes the usual form consisting of the pressure p and a symmetric, trace-free deviatoric tensor $\boldsymbol{\sigma}$

$$\mathbf{t} = -p\mathbf{I} + \boldsymbol{\sigma}. \tag{1.4}$$

Under these conditions, the Navier–Stokes equation has the form

$$\rho\left(\frac{\partial \vec{v}}{\partial t} + \nabla \cdot (\vec{v} \otimes \vec{v})\right) = -\nabla p + \nabla \cdot \boldsymbol{\sigma} - 2\vec{\Omega} \times \vec{v} + \vec{g}, \tag{1.5}$$

where $\vec{\Omega}$ is the vector of the mean angular velocity of the Earth and $\vec{g}$ is the vector of the gravitational acceleration.

Let us write the set of the Navier–Stokes equations (1.3) and (1.5) in the geographical coordinates (see Appendix A). In the formulae below, a is the mean radius of the Earth, r the radial coordinate, ϕ the latitude, λ the longitude, u the longitudinal velocity, v the latitudinal velocity, w the radial velocity, $g = |\vec{g}|$ and f the Coriolis parameter, $f = 2\Omega \sin\phi$, where $\Omega = |\vec{\Omega}|$ is the mean angular velocity of the Earth.

The continuity equation (1.3) in the geographical coordinates is given by

$$\frac{1}{r^2}\frac{\partial(r^2 w)}{\partial r} + \frac{1}{r\cos\phi}\left(\frac{\partial(\cos\phi v)}{\partial\phi} + \frac{\partial u}{\partial\lambda}\right) = 0, \tag{1.6}$$

while the momentum equation in the longitudinal direction is

$$\begin{aligned}\frac{\partial u}{\partial t} + \frac{1}{r^2}\frac{\partial(r^2 uw)}{\partial r} + \frac{1}{r\cos\phi}\left(\frac{\partial(\cos\phi\, uv)}{\partial\phi} + \frac{\partial v^2}{\partial\lambda}\right) + \frac{1}{r}\left(uw - \tan\phi\, uv\right) = fv + \\ \frac{1}{\rho}\left[-\frac{1}{r\cos\phi}\frac{\partial p}{\partial\lambda} + \frac{1}{r^2}\frac{\partial(r^2\sigma_{r\lambda})}{\partial r} + \frac{1}{r\cos\phi}\left(\frac{\partial(\cos\phi\,\sigma_{\phi\lambda})}{\partial\phi} + \frac{\partial\sigma_{\lambda\lambda}}{\partial\lambda}\right) + \right. \\ \left. \frac{1}{r}\left(\sigma_{\lambda r} - \tan\phi\,\sigma_{\lambda\phi}\right)\right],\end{aligned} \tag{1.7}$$

the momentum equation in the latitudinal direction is

$$\begin{aligned}\frac{\partial v}{\partial t} + \frac{1}{r^2}\frac{\partial(r^2 vw)}{\partial r} + \frac{1}{r\cos\phi}\left(\frac{\partial(\cos\phi\, v^2)}{\partial\phi} + \frac{\partial(uv)}{\partial\lambda}\right) + \frac{1}{r}\left(vw + \tan\phi\, u^2\right) = \\ -fu + \frac{1}{\rho}\left[-\frac{1}{r}\frac{\partial p}{\partial\phi} + \frac{1}{r^2}\frac{\partial(r^2\sigma_{r\phi})}{\partial r} + \frac{1}{r\cos\phi}\left(\frac{\partial(\cos\phi\,\sigma_{\phi\phi})}{\partial\phi} + \frac{\partial\sigma_{\lambda\phi}}{\partial\lambda}\right) + \right. \\ \left. \frac{1}{r}\left(\sigma_{\phi r} + \tan\phi\,\sigma_{\lambda\lambda}\right)\right],\end{aligned} \tag{1.8}$$

and the momentum equation in the radial direction is

$$\frac{\partial w}{\partial t} + \frac{1}{r^2}\frac{\partial (r^2 w^2)}{\partial r} + \frac{1}{r\cos\phi}\left(\frac{\partial(\cos\phi\, vw)}{\partial\phi} + \frac{\partial(uw)}{\partial\lambda}\right) - \frac{1}{r}\left(v^2+u^2\right) = -g + \frac{1}{\rho}\left[-\frac{\partial p}{\partial r} + \frac{1}{r^2}\frac{\partial(r^2\sigma_{rr})}{\partial r} + \frac{1}{r\cos\phi}\left(\frac{\partial(\cos\phi\,\sigma_{\phi r})}{\partial\phi} + \frac{\partial\sigma_{\lambda r}}{\partial\lambda}\right) - \frac{1}{r}\left(\sigma_{\phi\phi}+\sigma_{\lambda\lambda}\right)\right]. \tag{1.9}$$

The Navier–Stokes equations must be supplemented with boundary conditions. For an ocean domain, we may have three kinds of boundaries, a coast, an ocean bottom and an ocean free surface. The coast is represented by a two-dimensional coast line where the normal flow condition is prescribed, meaning that no fluid crosses the boundary,

$$\vec{v}_h \cdot \vec{n}_c = 0, \tag{1.10}$$

where $\vec{v}_h = (u,v)$ is the velocity in the horizontal plane and $\vec{n}_c$ is the unit outer normal to the coast line. Additionally, we assume that the coast line does not change over time.

At the ocean bottom and free surface, we also assume no fluid crosses the boundaries. We introduce the elevation of the surface $\zeta(\lambda,\phi,t)$, measured from the geoid to the surface, the bathymetry $b(\lambda,\phi)$, measured from the geoid to the bottom, and the height of water column $h(\lambda,\phi,t) = \zeta + b$ (see Figure 1.1). In this study, the geoid is defined by the mean Earth radius, $r = a = \text{const}$.

Since no fluid crosses the free surface, the vertical velocity of the free surface is the material time derivative of the surface elevation

$$w = \frac{\mathrm{D}\zeta}{\mathrm{D}t} = \frac{\partial\zeta}{\partial t} + \vec{v}\cdot\nabla\zeta. \tag{1.11}$$

The second condition constrains the stress tensor. We assume that no wind or atmospheric pressure act on the ocean surface

$$\mathbf{t}\cdot\vec{n}_s = \vec{0}, \tag{1.12}$$

where $\vec{n}_s$ is the unit outward normal to the free surface which is defined by

$$\vec{n}_s = \frac{1}{\sqrt{1+|\nabla\zeta|^2}}\begin{pmatrix} -\frac{1}{r\cos\phi}\frac{\partial\zeta}{\partial\lambda} \\ -\frac{1}{r}\frac{\partial\zeta}{\partial\phi} \\ 1 \end{pmatrix}. \tag{1.13}$$

The situation at the bottom is analogous. The velocity condition is

$$w = -\frac{\mathrm{D}b}{\mathrm{D}t} = -\vec{v}\cdot\nabla b. \tag{1.14}$$

The stress condition slightly differs from that on the free surface. Only the tangential components of the stress vector are taken in account. Moreover,

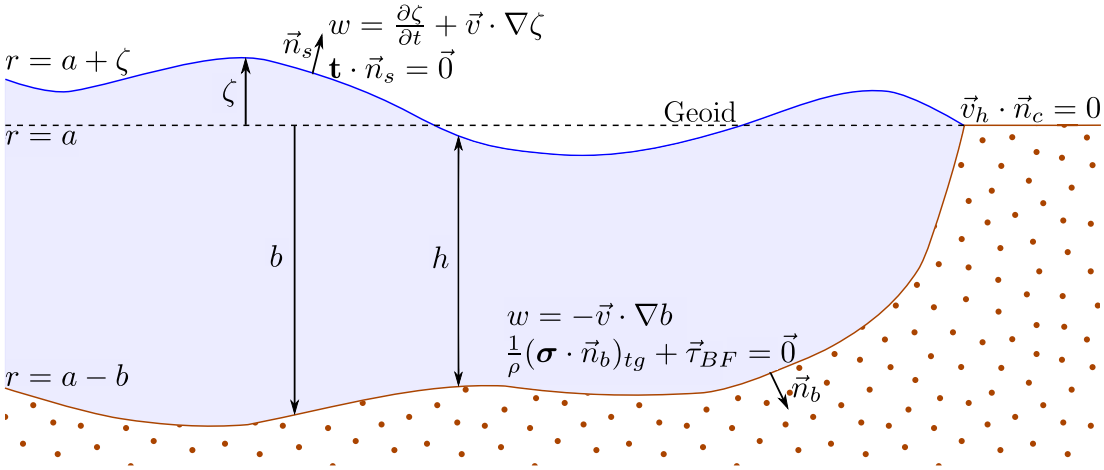

Figure 1.1: Boundary conditions on the free surface, at the ocean bottom and at the coast. The moving elevation of the surface ζ, the varying bathymetry b and the height of a water column $h = \zeta + b$ are shown by arrows.

we shall consider that water moves along the bottom with friction. The shear condition takes the form

$$\frac{1}{\rho}(\boldsymbol{\sigma} \cdot \vec{n}_b)_{tg} + \vec{\tau}_{BF} = \vec{0}, \tag{1.15}$$

where $\vec{n}_b$ is the unit outward normal to the bottom,

$$\vec{n}_b = \frac{1}{\sqrt{1 + |\nabla b|^2}} \begin{pmatrix} -\frac{1}{r\cos\phi}\frac{\partial b}{\partial \lambda} \\ -\frac{1}{r}\frac{\partial b}{\partial \phi} \\ -1 \end{pmatrix}, \tag{1.16}$$

and $\vec{\tau}_{BF}$ is a stress vector due to bottom friction. A form of $\vec{\tau}_{BF}$ is suggested by empirical laws. For example, linear form is used for laminar flow (e.g., Gerbeau and Perthame, 2000), a quadratic form is often used for turbulent flow, while some authors use both models (e.g., Bresch and Desjardins, 2003; Marche, 2006). We consider turbulent flow (see Section 1.2) and assume that the bottom friction vector is quadratic, $\vec{\tau}_{BF} = c_{BF}\vec{v}|\vec{v}|$ with a dimensionless coefficient c_{BF}. This is a standard parameterization of the bottom friction in ocean tide models (e.g., Egbert et al., 2004; Weis et al., 2008; Hill et al., 2011; Green and Nycander, 2013).

1.2 The Reynolds tensor

In oceanography, we are forced to deal with the turbulent character of ocean flow. The Reynolds number, which controls whether the flow is laminar or turbulent, is approximately 10^{11} for an ocean (Pond and Pickard, 1983) which means that the flow is strongly turbulent. The turbulences on very short scales cause energy losses in the large-scale motions, and thus we need to introduce

a new stress tensor $\boldsymbol{\sigma}$, the so-called *Reynolds tensor*. The Reynolds tensor is based on the ideas of Joseph Valentin Boussinesq and Osborne Reynolds from the late nineteenth century who presented a way of how turbulences can mathematically be modelled (see Boussinesq, 1877 and Reynolds, 1895, or Schmitt, 2007). This way assumes that the friction due to short-scale turbulences can be described as linear combinations of the spatial derivatives of the large-scale velocities.

Although the idea of the Reynolds tensor is widely spread and common in oceanography, the form of the tensor differs in various ocean models. Historically, the friction terms in shallow water ocean models were formulated by somewhat ad hoc manner. Several formulations of the friction term were proposed and used in ocean models, for example, $Ah\nabla^2\vec{v}$, $\nabla(Ah\nabla\vec{v})$, $A\nabla^2(h\vec{v})$, where A is a viscous parameter (Shchepetkin and O'Brien, 1996), however, it was shown that these parameterizations can violate the conservation laws of energy, momentum and angular momentum (Gent, 1993; Shchepetkin and O'Brien, 1996; Ochoa et al., 2011). Gent (1993) proposes a form of the friction term which is energetically consistent while Schär and Smith (1993) deduce a form which is consistent with all three laws. Ochoa et al. (2011) summarize various parameterization of the friction and discuss their consistency with the conservation principles. A physically consistent formulation in the shallow water equations must have the following properties which were postulated by Shchepetkin and O'Brien (1996):

(1) The linear momentum conservation principle requires that the viscous term in the momentum equations have the form of the divergence of a tensor.
(2) The angular momentum conservation principle requires that this tensor must be symmetric.
(3) The friction must be dissipative. This implies that the dissipation in the right-hand side of the kinetic energy equation consists of two parts: a term that has a form of the divergence of a vector and a negatively defined source term.
(4) The friction depends on the symmetric part of the local deformation tensor due to invariance of coordinate transformations.

These postulates must be borne in mind when deriving the viscous shallow water equation from the Navier–Stokes equations since vertical integration of a physically consistent three-dimensional stress tensor can lead to an inconsistent two-dimensional friction term. Gent (1993) shows that the vertical integration of the three-dimensional primitive equations with a Laplacian form of the stress tensor results in the friction term which is energetically inconsistent. Hence, one should be very careful in the derivation which includes the Reynolds tensor and check whether the final shallow water equations satisfy the postulates above. This will be done in Section 1.6.

In classical books, such as Pedlosky (1987) and Pond and Pickard (1983),

the Reynolds tensor in Cartesian coordinates is defined as

$$\frac{\boldsymbol{\sigma}}{\rho} = \begin{pmatrix} 2A_H\dfrac{\partial u}{\partial x} & A_H\left(\dfrac{\partial u}{\partial y}+\dfrac{\partial v}{\partial x}\right) & A_V\dfrac{\partial u}{\partial z}+A_H\dfrac{\partial w}{\partial x} \\ A_H\left(\dfrac{\partial u}{\partial y}+\dfrac{\partial v}{\partial x}\right) & 2A_H\dfrac{\partial v}{\partial y} & A_V\dfrac{\partial v}{\partial z}+A_H\dfrac{\partial w}{\partial x} \\ A_V\dfrac{\partial u}{\partial z}+A_H\dfrac{\partial w}{\partial x} & A_V\dfrac{\partial v}{\partial z}+A_H\dfrac{\partial w}{\partial x} & 2A_V\dfrac{\partial w}{\partial z} \end{pmatrix}, \tag{1.17}$$

where A_V and A_H are the vertical and horizontal eddy viscosities, respectively. The estimates of A_V for ocean flow range from 10^{-5} to 10^{-1} m^2/s and from 10 to 10^5 m^2/s for A_H (Pond and Pickard, 1983; Pedlosky, 1987). However, form (1.17) is also an ad hoc definition and such a tensor is physically inconsistent. Two different coefficients, A_H and A_V, suggest an anisotropic fluid, however, in the case of the simplest anisotropic medium, the transverse isotropy, there are five independent coefficients (Hutter and Jöhnk, 2004). This number is reduced to three by the incompressibility condition (1.3) and the zero trace of the Reynolds tensor, as expressed in (1.4). However the trace of the tensor (1.17) is not zero, hence the tensor is inconsistent with the assumption of the transverse isotropy. It can be also shown that vertical integration of this tensor would lead to the friction term in the shallow water equation which would not satisfy the postulates above. Therefore, we need to use a different formulation of the stress tensor. A generally consistent formulation of the Reynolds tensor can be found in Wajsowicz (1993)

$$\frac{\boldsymbol{\sigma}}{\rho} = \boldsymbol{A} : \boldsymbol{E}, \tag{1.18}$$

where $\boldsymbol{A}$ is a fourth-order tensor, whose elements depend on the local state of the fluid, but not directly on the velocity distribution (Batchelor, 1967), and $\boldsymbol{E}$ is the strain rate tensor,

$$\boldsymbol{E} = \frac{1}{2}\left(\nabla\vec{v} + (\nabla\vec{v})^{\mathrm{T}}\right). \tag{1.19}$$

The fourth-order tensor $\boldsymbol{A}$ has 21 independent elements at most. Considering that the fluid is transversal isotropic, there is an axis of symmetry about which the fluid is isotropic and the number of independent elements of $\boldsymbol{A}$ is reduced to 5. For ocean circulation, it is natural to assume that the fluid is symmetric with respect to the radial axis r. Hence, assuming the radial axis is the axis of rotational symmetry, the incompressible fluid and that the trace of $\boldsymbol{\sigma}$ is zero, the Reynolds tensor in geographical coordinates can be expressed as (Wajsow-

icz, 1993)

$$\begin{aligned}\frac{\boldsymbol{\sigma}}{\rho} =& 2A_\delta E_{rr}\vec{e}_r \otimes \vec{e}_r + \\ & \left((A_H + A_\delta)E_{\lambda\lambda} + (A_\delta - A_H)E_{\phi\phi}\right)\vec{e}_\lambda \otimes \vec{e}_\lambda + \\ & \left((A_\delta - A_H)E_{\lambda\lambda} + (A_H + A_\delta)E_{\phi\phi}\right)\vec{e}_\phi \otimes \vec{e}_\phi + \\ & 2A_V E_{r\lambda}(\vec{e}_r \otimes \vec{e}_\lambda + \vec{e}_\lambda \otimes \vec{e}_r) + \\ & 2A_V E_{r\phi}(\vec{e}_r \otimes \vec{e}_\phi + \vec{e}_\phi \otimes \vec{e}_r) + \\ & 2A_H E_{\lambda\phi}(\vec{e}_\lambda \otimes \vec{e}_\phi + \vec{e}_\phi \otimes \vec{e}_\lambda),\end{aligned} \tag{1.20}$$

with three independent coefficients A_H, A_V and A_δ, which can be generally time and spatially varying, however, for the sake of simplicity, we will assume they are constant. A_H and A_V may be identified with the usual horizontal and vertical eddy viscosities, respectively, strictly speaking, horizontal and vertical along the coordinate system. It is assumed that A_V is approximately 10^6 smaller than A_H in the Earth's oceans.

The coefficient A_δ is related to $\overline{w'^2}$, where w' are the small-scale vertical velocities and the overbar denotes the large-scale averaging (Williams, 1972), therefore, the magnitude of A_δ is determined by the degree of vertical turbulences. The magnitude lies between 0 and A_H, depending on the type of motion. For a highly convective flow in the vertical (such as the Jupiter's atmosphere), it can be expected that $A_\delta \approx A_H$. However, for a less convective, or fairly stable flow, such as in the Earth's oceans, it can be assumed that vertical turbulence are negligible compared to horizontal turbulences and $A_\delta \to 0$.

1.3 Spherical approximation

First, let us introduce the so-called *spherical approximation*. The radial coordinate r can be expressed as

$$r = a + z = a\left(1 + \frac{z}{a}\right), \tag{1.21}$$

where z is the new radial coordinate, $z \in (-b,\zeta)$. For oceans, the absolute values of z are taken to be between 10^0 and 10^3 m while $a \approx 6 \times 10^6$ m. Therefore, the term $\frac{z}{a}$ is of the order $O(10^{-3})$ at most and can be neglected if compared with terms $O(1)$. Hence, we shall use the spherical approximation and approximate the radial distance of a material point in the oceans by a,

$$r \approx a \tag{1.22}$$

Equation (1.21) also implies that

$$\frac{\partial}{\partial r} = \frac{\partial}{\partial z}. \tag{1.23}$$

After adopting the spherical approximation, the Navier–Stokes equations slightly change. The continuity equation (1.6) is now

$$0 = \frac{\partial w}{\partial z} + \frac{1}{a\cos\phi}\left(\frac{\partial(\cos\phi v)}{\partial\phi} + \frac{\partial u}{\partial\lambda}\right), \tag{1.24}$$

while the momentum equation in the longitudinal direction (1.7) is

$$\begin{aligned}\frac{\partial u}{\partial t} + \frac{\partial(uw)}{\partial z} + \frac{1}{a\cos\phi}\left(\frac{\partial(\cos\phi\, uv)}{\partial\phi} + \frac{\partial v^2}{\partial\lambda}\right) + \frac{1}{a}\left(uw - \tan\phi\, uv\right) = fv + \\ \frac{1}{\rho}\left[-\frac{1}{a\cos\phi}\frac{\partial p}{\partial\lambda} + \frac{\partial\sigma_{z\lambda}}{\partial z} + \frac{1}{a\cos\phi}\left(\frac{\partial(\cos\phi\,\sigma_{\phi\lambda})}{\partial\phi} + \frac{\partial\sigma_{\lambda\lambda}}{\partial\lambda}\right) + \right. \\ \left. \frac{1}{a}\left(\sigma_{\lambda z} - \tan\phi\,\sigma_{\lambda\phi}\right)\right],\end{aligned} \tag{1.25}$$

the momentum equation in the latitudinal direction (1.8) is

$$\begin{aligned}\frac{\partial v}{\partial t} + \frac{\partial(vw)}{\partial z} + \frac{1}{a\cos\phi}\left(\frac{\partial(\cos\phi\, v^2)}{\partial\phi} + \frac{\partial(uv)}{\partial\lambda}\right) + \frac{1}{a}\left(vw + \tan\phi\, u^2\right) = -fu + \\ \frac{1}{\rho}\left[-\frac{1}{a}\frac{\partial p}{\partial\phi} + \frac{\partial\sigma_{z\phi}}{\partial z} + \frac{1}{a\cos\phi}\left(\frac{\partial(\cos\phi\,\sigma_{\phi\phi})}{\partial\phi} + \frac{\partial\sigma_{\lambda\phi}}{\partial\lambda}\right) + \frac{1}{a}\left(\sigma_{\phi z} + \tan\phi\,\sigma_{\lambda\lambda}\right)\right]\end{aligned} \tag{1.26}$$

the momentum equation in the radial direction (1.9) is

$$\begin{aligned}\frac{\partial w}{\partial t} + \frac{\partial w^2}{\partial z} + \frac{1}{a\cos\phi}\left(\frac{\partial(\cos\phi\, vw)}{\partial\phi} + \frac{\partial(uw)}{\partial\lambda}\right) - \frac{1}{a}\left(v^2 + u^2\right) = -g + \\ \frac{1}{\rho}\left[-\frac{\partial p}{\partial z} + \frac{\partial\sigma_{zz}}{\partial z} + \frac{1}{a\cos\phi}\left(\frac{\partial(\cos\phi\,\sigma_{\phi z})}{\partial\phi} + \frac{\partial\sigma_{\lambda z}}{\partial\lambda}\right) - \frac{1}{a}\left(\sigma_{\phi\phi} + \sigma_{\lambda\lambda}\right)\right],\end{aligned} \tag{1.27}$$

and, finally, the Reynolds tensor (1.20) is

$$\begin{aligned}\frac{\boldsymbol{\sigma}}{\rho} =& 2A_\delta E_{zz}\vec{e}_z\otimes\vec{e}_z + \\ & \left((A_H + A_\delta)E_{\lambda\lambda} + (A_\delta - A_H)E_{\phi\phi}\right)\vec{e}_\lambda\otimes\vec{e}_\lambda + \\ & \left((A_\delta - A_H)E_{\lambda\lambda} + (A_H + A_\delta)E_{\phi\phi}\right)\vec{e}_\phi\otimes\vec{e}_\phi + \\ & 2A_V E_{z\lambda}(\vec{e}_z\otimes\vec{e}_\lambda + \vec{e}_\lambda\otimes\vec{e}_z) + \\ & 2A_V E_{z\phi}(\vec{e}_z\otimes\vec{e}_\phi + \vec{e}_\phi\otimes\vec{e}_z) + \\ & 2A_H E_{\lambda\phi}(\vec{e}_\lambda\otimes\vec{e}_\phi + \vec{e}_\phi\otimes\vec{e}_\lambda),\end{aligned} \tag{1.28}$$

where

$$
\begin{aligned}
E_{zz} &= \frac{\partial w}{\partial z}, \\
E_{\lambda\lambda} &= \frac{1}{a}\left(\frac{1}{\cos\phi}\frac{\partial u}{\partial \lambda} + w - \tan\phi\, v\right), \\
E_{\phi\phi} &= \frac{1}{a}\left(\frac{\partial v}{\partial \phi} + w\right), \\
E_{z\lambda} &= \frac{1}{2}\left[\frac{\partial u}{\partial z} + \frac{1}{a}\left(\frac{1}{\cos\phi}\frac{\partial w}{\partial \lambda} - u\right)\right], \\
E_{z\phi} &= \frac{1}{2}\left[\frac{\partial v}{\partial z} + \frac{1}{a}\left(\frac{\partial w}{\partial \phi} - v\right)\right], \\
E_{\lambda\phi} &= \frac{1}{2a}\left(\frac{\partial u}{\partial \phi} + \frac{1}{\cos\phi}\frac{\partial v}{\partial \lambda} + \tan\phi\, u\right).
\end{aligned} \tag{1.29}
$$

1.4 The non-dimensionalized system

Now we introduce dimensionless quantities to express the above equations in a dimensionless form. This allows us to neglect the terms of small magnitudes.

Let H and L be the characteristic scales of the oceans in the vertical and horizontal directions, respectively, and $\epsilon = H/L$. In the case of global ocean circulation, $H \approx 10^3$ m, $L \approx 10^6$ m, $\epsilon = 10^{-3}$ and ϵ can be considered as a small parameter. Let U be the characteristic scale of the horizontal velocities and let $W = \epsilon U$, $P = U^2$ and $T = L/U$ be the characteristic scales of the vertical velocities and the pressure over density and time, respectively.

We can now define the following dimensionless quantities (denoted by the tilde)

$$
\begin{aligned}
\tilde{x} &= \frac{a\lambda}{L}, \qquad \tilde{y} = \frac{a\phi}{L}, \qquad \tilde{z} = \frac{z}{H}, \\
\tilde{\zeta} &= \frac{\zeta}{H}, \qquad \tilde{b} = \frac{b}{H}, \qquad \tilde{h} = \frac{h}{H}, \\
\tilde{u} &= \frac{u}{U}, \qquad \tilde{v} = \frac{v}{U}, \qquad \tilde{w} = \frac{w}{\epsilon U}, \\
\tilde{t} &= \frac{tU}{L}, \qquad \tilde{p} = \frac{p}{\rho U^2}.
\end{aligned}
$$

Similarly, the dimensionless elements of the tensor $\boldsymbol{E}$ (1.29) can be defined as

$$
\begin{aligned}
\tilde{E}_{zz} &= \frac{E_{zz}H}{\epsilon U}, \qquad \tilde{E}_{\lambda\lambda} = \frac{E_{\lambda\lambda}L}{U}, \qquad \tilde{E}_{\phi\phi} = \frac{E_{\phi\phi}L}{U}, \\
\tilde{E}_{z\lambda} &= \frac{E_{z\lambda}H}{U}, \qquad \tilde{E}_{z\phi} = \frac{E_{z\phi}H}{U}, \qquad \tilde{E}_{\lambda\phi} = \frac{E_{\lambda\phi}L}{U}.
\end{aligned}
$$

Furthermore, we define the modified friction coefficient $c_{BF}^0 = c_{BF}/\epsilon$, the spherical parameter $\gamma = L/a$ and five dimensionless numbers, the inverse

Reynolds numbers ν_H, ν_V and ν_δ, the Froude number F_r and the Rossby number R_o, as

$$\nu_H = \frac{A_H}{UL}, \qquad \nu_V = \frac{A_V}{UL}, \qquad \nu_\delta = \frac{A_\delta}{UL}$$
$$F_r = \frac{U}{\sqrt{gH}}, \qquad R_o = \frac{U}{fL}.$$

For the sake of simplicity, we will drop the tilde in the following equations. In the next step, *the hydrostatic approximation* is applied. The equations will be written in the dimensionless forms and the terms of the order $O(\epsilon)$ will be neglected. The terms proportional to the horizontal inverse Reynolds number ν_H cannot be neglected since the horizontal eddy viscosity A_H should have the magnitude such that ν_H is of the order $O(1)$. On the other hand, the terms proportional to the Reynolds numbers ν_V and ν_δ will be neglected since A_V can be roughly estimated as $\epsilon^2 A_H$ and A_δ is approximately zero in the oceans as discussed in Section 1.2. The spherical parameter γ is of the order $O(1)$ since a and L are both of the order $O(10^6)$. The Froude and Rossby numbers will appear in the following equations as $1/F_r^2$ and $1/R_o$ and these inversion values are obviously of the higher order than $O(1)$. The continuity equation (1.24) remains formally unchained in the dimensionless form

$$\frac{\partial w}{\partial z} + \frac{1}{\cos\phi}\left(\frac{\partial(\cos\phi\, v)}{\partial y} + \frac{\partial u}{\partial x}\right) = 0. \tag{1.30}$$

The longitudinal momentum equation (1.25) in the dimensionless form is then

$$\frac{\partial u}{\partial t} + \frac{\partial(uw)}{\partial z} + \frac{1}{\cos\phi}\left(\frac{\partial(\cos\phi\, uv)}{\partial y} + \frac{\partial u^2}{\partial x}\right) + \gamma u\,(\epsilon w - \tan\phi\, v) = -\frac{1}{\cos\phi}\frac{\partial p}{\partial x} +$$
$$\frac{v}{R_o} + \frac{2\nu_V}{\epsilon^2}\frac{\partial E_{z\lambda}}{\partial z} + 2\nu_H\frac{\partial E_{\lambda\phi}}{\partial y} + \frac{1}{\cos\phi}\frac{\partial}{\partial x}\left(\nu_H(E_{\lambda\lambda} - E_{\phi\phi}) + \nu_\delta(E_{\lambda\lambda} + E_{\phi\phi})\right) +$$
$$2\gamma\left(\frac{\nu_V}{\epsilon}E_{z\lambda} - 2\nu_H\tan\phi\, E_{\lambda\phi}\right). \tag{1.31}$$

After neglecting the terms of the order $O(\epsilon)$, we have

$$\frac{\partial u}{\partial t} + \frac{\partial(uw)}{\partial z} + \frac{1}{\cos\phi}\left(\frac{\partial(\cos\phi\, uv)}{\partial y} + \frac{\partial u^2}{\partial x}\right) - \gamma\tan\phi\, uv = -\frac{1}{\cos\phi}\frac{\partial p}{\partial x} + \frac{v}{R_o} +$$
$$\frac{2\nu_V}{\epsilon^2}\frac{\partial E_{z\lambda}}{\partial z} + \nu_H\left(2\frac{\partial E_{\lambda\phi}}{\partial y} + \frac{1}{\cos\phi}\frac{\partial}{\partial x}(E_{\lambda\lambda} - E_{\phi\phi})\right) - 4\gamma\nu_H\tan\phi\, E_{\lambda\phi}. \tag{1.32}$$

The latitudinal momentum equation (1.26) in the dimensionless form is

$$\frac{\partial v}{\partial t} + \frac{\partial(vw)}{\partial z} + \frac{1}{\cos\phi}\left(\frac{\partial(\cos\phi\, v^2)}{\partial y} + \frac{\partial(uv)}{\partial x}\right) + \gamma(\epsilon vw + \tan\phi\, u^2) = -\frac{\partial p}{\partial y} -$$
$$\frac{u}{R_o} + \frac{2\nu_v}{\epsilon^2}\frac{\partial E_{z\phi}}{\partial z} + \frac{\partial}{\partial y}\left(\nu_H(E_{\phi\phi} - E_{\lambda\lambda}) + \nu_\delta(E_{\phi\phi} + E_{\lambda\lambda})\right) + \frac{2\nu_H}{\cos\phi}\frac{\partial E_{\lambda\phi}}{\partial x} +$$
$$2\gamma\left(\frac{\nu_V}{\epsilon}E_{z\phi} + \tan\phi(E_{\lambda\lambda} - E_{\phi\phi})\right). \tag{1.33}$$

After neglecting the terms of the order $O(\epsilon)$, we have

$$\frac{\partial v}{\partial t}+\frac{\partial (vw)}{\partial z}+\frac{1}{\cos\phi}\left(\frac{\partial(\cos\phi\, v^2)}{\partial y}+\frac{\partial(uv)}{\partial x}\right)+\gamma\tan\phi\, u^2=-\frac{\partial p}{\partial y}-\frac{u}{R_o}+$$
$$\frac{2\nu_v}{\epsilon^2}\frac{\partial E_{z\phi}}{\partial z}+\nu_H\left(\frac{\partial}{\partial y}(E_{\phi\phi}-E_{\lambda\lambda})+\frac{2}{\cos\phi}\frac{\partial E_{\lambda\phi}}{\partial x}\right)+2\gamma\tan\phi(E_{\lambda\lambda}-E_{\phi\phi}). \quad (1.34)$$

Finally, the radial momentum equation (1.27) in the dimensionless form is

$$\epsilon^2\left(\frac{\partial w}{\partial t}+\frac{\partial w^2}{\partial z}+\frac{1}{\cos\phi}\left(\frac{\partial(\cos\phi\, vw)}{\partial y}+\frac{\partial(uw)}{\partial x}\right)\right)-\epsilon\gamma(v^2+u^2)=-\frac{\partial p}{\partial z}-$$
$$\frac{1}{F_r^2}+2\nu_\delta\frac{\partial E_{zz}}{\partial z}+\frac{2\nu_V}{\cos\phi}\left(\frac{\partial}{\partial y}(\cos\phi\, E_{z\phi})+\frac{\partial E_{z\lambda}}{\partial x}\right)-2\nu_\delta\epsilon\gamma(E_{\lambda\lambda}+E_{\phi\phi}), \quad (1.35)$$

and, after neglecting the terms of the order $O(\epsilon)$, we obtain the equation of hydrostatic balance

$$\frac{\partial p}{\partial z}=-\frac{1}{F_r^2}. \quad (1.36)$$

We will now express the dimensionless form of the boundary conditions. The dimensionless velocity boundary conditions (1.11) and (1.14) read as

$$w|_{z=\zeta}=\frac{\partial\zeta}{\partial t}+\frac{u}{\cos\phi}\frac{\partial\zeta}{\partial x}+v\frac{\partial\zeta}{\partial y}, \quad (1.37)$$

$$w|_{z=-b}=-\frac{u}{\cos\phi}\frac{\partial b}{\partial x}-v\frac{\partial b}{\partial y}. \quad (1.38)$$

The longitudinal component of the surface stress condition (1.12) is

$$\frac{2\nu_V}{\epsilon^2}E_{z\lambda}-2\nu_H\frac{\partial\zeta}{\partial y}E_{\lambda\phi}-\frac{1}{\cos\phi}\frac{\partial\zeta}{\partial x}\left(-p+\nu_H(E_{\lambda\lambda}-E_{\phi\phi})+\nu_\delta(E_{\lambda\lambda}+E_{\phi\phi})\right)=0, \quad (1.39)$$

and, after neglecting the terms of the order $O(\epsilon)$, we have

$$\frac{2\nu_V}{\epsilon^2}E_{z\lambda}-2\nu_H\frac{\partial\zeta}{\partial y}E_{\lambda\phi}-\frac{1}{\cos\phi}\frac{\partial\zeta}{\partial x}\left(-p+\nu_H(E_{\lambda\lambda}-E_{\phi\phi})\right)=0 \quad (1.40)$$

The latitudinal component of the surface stress condition is

$$\frac{2\nu_V}{\epsilon^2}E_{z\phi}-\frac{\partial\zeta}{\partial y}\left(-p+\nu_H(E_{\phi\phi}-E_{\lambda\lambda})+\nu_\delta(E_{\phi\phi}+E_{\lambda\lambda})\right)-\frac{2\nu_H}{\cos\phi}\frac{\partial\zeta}{\partial x}E_{\lambda\phi}=0, \quad (1.41)$$

and, after neglecting the terms of the order $O(\epsilon)$, we have

$$\frac{2\nu_V}{\epsilon^2}E_{z\phi}-\frac{\partial\zeta}{\partial y}\left(-p+\nu_H(E_{\phi\phi}-E_{\lambda\lambda})\right)-\frac{2\nu_H}{\cos\phi}\frac{\partial\zeta}{\partial x}E_{\lambda\phi}=0. \quad (1.42)$$

Finally, the radial component of the surface stress condition is

$$-p+2\nu_\delta E_{zz}-2\nu_V\frac{\partial\zeta}{\partial y}E_{z\phi}-\frac{2\nu_V}{\cos\phi}\frac{\partial\zeta}{\partial x}E_{z\lambda}=0, \quad (1.43)$$

and, after neglecting the terms of the order $O(\epsilon)$, we have

$$-p = 0. \tag{1.44}$$

The treatment of the boundary conditions at the bottom is analogous. The longitudinal component of the bottom stress condition (1.15) is

$$\frac{2\nu_V}{\epsilon^2}E_{z\lambda} + 2\nu_H\frac{\partial b}{\partial y}E_{\lambda\phi} + \frac{1}{\cos\phi}\frac{\partial b}{\partial x}\left(\nu_H(E_{\lambda\lambda} - E_{\phi\phi}) + \nu_\delta(E_{\lambda\lambda} + E_{\phi\phi})\right) = Nc_{BF}^0 u\sqrt{u^2+v^2+\epsilon^2w^2}, \tag{1.45}$$

where N is the norm of the outward normal $N = \sqrt{1+\epsilon^2|\nabla b|^2}$. After neglecting the terms of the order $O(\epsilon)$, the equation reads as

$$\frac{2\nu_V}{\epsilon^2}E_{z\lambda} + 2\nu_H\frac{\partial b}{\partial y}E_{\lambda\phi} + \frac{\nu_H}{\cos\phi}\frac{\partial b}{\partial x}(E_{\lambda\lambda} - E_{\phi\phi}) = c_{BF}^0 u\sqrt{u^2+v^2}, \tag{1.46}$$

The latitudinal component of the bottom stress condition is

$$\frac{2\nu_V}{\epsilon^2}E_{z\phi} + \frac{\partial b}{\partial y}\left(\nu_H(E_{\phi\phi} - E_{\lambda\lambda}) + \nu_\delta(E_{\phi\phi} + E_{\lambda\lambda})\right) + \frac{2\nu_H}{\cos\phi}\frac{\partial b}{\partial x}E_{\lambda\phi} = Nc_{BF}^0 v\sqrt{u^2+v^2+\epsilon^2w^2}, \tag{1.47}$$

and, after neglecting the terms of the order $O(\epsilon)$, we have

$$\frac{2\nu_V}{\epsilon^2}E_{z\phi} + \nu_H\frac{\partial b}{\partial y}(E_{\phi\phi} - E_{\lambda\lambda}) + \frac{2\nu_H}{\cos\phi}\frac{\partial b}{\partial x}E_{\lambda\phi} = c_{BF}^0 v\sqrt{u^2+v^2} \tag{1.48}$$

1.5 Vertical averaging

The next step aims to eliminate the dependency on the vertical dimension in the above equations and to simplify the 3D system to a 2D problem.

To do this, let us define the vertically averaged quantity of function $f(t,x,y,z)$ as

$$\bar{f}(t,x,y) = \frac{1}{h(t,x,y)}\int_{-b}^{\zeta} f(t,x,y,z)\,\mathrm{d}z. \tag{1.49}$$

Our strategy is to integrate the non-dimensionalized Navier–Stokes equations in the radial direction from the bottom $z = -b$ to the surface $z = \zeta$, using the Leibniz integral rule and applying the appropriate boundary conditions. Let us start with the integration of the continuity equation (1.30)

$$\begin{aligned}
0 &= \int_{-b}^{\zeta}\frac{\partial w}{\partial z} + \frac{1}{\cos\phi}\left(\frac{\partial(\cos\phi\, v)}{\partial y} + \frac{\partial u}{\partial x}\right)\mathrm{d}z = \\
&= \int_{-b}^{\zeta}\frac{1}{\cos\phi}\left(\frac{\partial(\cos\phi\, v)}{\partial y} + \frac{\partial u}{\partial x}\right)\mathrm{d}z + w|_{z=\zeta} - w|_{z=-b} = \\
&= \frac{1}{\cos\phi}\left(\frac{\partial}{\partial x}\int_{-b}^{\zeta} u\,\mathrm{d}z + \frac{\partial}{\partial y}\int_{-b}^{\zeta}\cos\phi\, v\,\mathrm{d}z\right) - \frac{u|_{z=\zeta}}{\cos\phi}\frac{\partial\zeta}{\partial x} - \frac{u|_{z=-b}}{\cos\phi}\frac{\partial b}{\partial x} - \\
&\quad v|_{z=\zeta}\frac{\partial\zeta}{\partial y} - v|_{z=-b}\frac{\partial b}{\partial y} + w|_{z=\zeta} - w|_{z=-b}.
\end{aligned} \tag{1.50}$$

After applying the boundary conditions (1.37) and (1.38), we obtain the equation for the surface elevation

$$\frac{\partial \zeta}{\partial t} + \frac{1}{\cos\phi}\left(\frac{\partial(h\bar{u})}{\partial x} + \frac{\partial(h\bar{v})}{\partial y}\right) = 0. \tag{1.51}$$

The horizontal components of the equation of motion (1.32) and (1.34) are averaged in a similar way. We integrate these equations in the radial direction and apply the velocity boundary conditions (1.37) and (1.38) and the stress boundary conditions (1.40), (1.42), (1.44), (1.46) and (1.48), which yields

$$\begin{aligned}
&\frac{\partial(h\bar{u})}{\partial t} + \frac{1}{\cos\phi}\left(\frac{\partial(\cos\phi\, h\overline{uv})}{\partial y} + \frac{\partial h\overline{u^2}}{\partial x}\right) - \gamma\tan\phi\, h\overline{uv} = \\
&-\frac{1}{\cos\phi}\left(\frac{\partial(h\bar{p})}{\partial x} - \frac{\partial b}{\partial x}p|_{z=-b}\right) + \frac{h\bar{v}}{R_o} - c^0_{BF}u\sqrt{u^2+v^2}|_{z=-b} + \\
&\nu_H\left[2\frac{\partial}{\partial y}(h\bar{E}_{\lambda\phi}) + \frac{1}{\cos\phi}\frac{\partial}{\partial x}\left(h(\bar{E}_{\lambda\lambda} - \bar{E}_{\phi\phi})\right) - 4\gamma\tan\phi\, h\bar{E}_{\lambda\phi}\right],
\end{aligned} \tag{1.52}$$

and

$$\begin{aligned}
&\frac{\partial(h\bar{v})}{\partial t} + \frac{1}{\cos\phi}\left(\frac{\partial(\cos\phi\, h\overline{v^2})}{\partial y} + \frac{\partial(h\overline{uv})}{\partial x}\right) + \gamma\tan\phi\, h\overline{u^2} = \\
&-\frac{\partial(h\bar{p})}{\partial y} + \frac{\partial b}{\partial y}p|_{z=-b} - \frac{h\bar{u}}{R_o} - c^0_{BF}v\sqrt{u^2+v^2}|_{z=-b} + \\
&\nu_H\left[\frac{\partial}{\partial y}\left(h(\bar{E}_{\phi\phi} - \bar{E}_{\lambda\lambda})\right) + \frac{2}{\cos\phi}\frac{\partial}{\partial x}(h\bar{E}_{\lambda\phi}) + 2\gamma\tan\phi\, h(\bar{E}_{\lambda\lambda} - \bar{E}_{\phi\phi})\right].
\end{aligned} \tag{1.53}$$

The pressure in these equations is given by the equation of hydrostatic balance (1.36),

$$p(t,x,y,z) = -\frac{1}{F_r^2}(z - \zeta(t,x,y,)). \tag{1.54}$$

Hence, integrating over z from $-b$ to ζ, and dividing by h, we obtain the vertically averaged pressure

$$\bar{p}(t,x,y) = \frac{h^2}{2F_r^2}. \tag{1.55}$$

Additionally, the pressure on the bottom is

$$p(t,x,y,z=-b) = \frac{h}{F_r^2}. \tag{1.56}$$

Therefore, it holds that

$$-\frac{1}{\cos\phi}\left(\frac{\partial(h\bar{p})}{\partial x} - \frac{\partial b}{\partial x}p|_{z=-b}\right) = -\frac{h}{F_r^2\cos\phi}\frac{\partial\zeta}{\partial x}, \tag{1.57}$$

$$-\frac{\partial(h\bar{p})}{\partial y} + \frac{\partial b}{\partial y}p|_{z=-b} = -\frac{h}{F_r^2}\frac{\partial\zeta}{\partial y}. \tag{1.58}$$

In the next step, we will assume that the horizontal flow is only weakly dependent on the depth such that the derivatives of the velocities with respect to z are small quantities of the order $O(\epsilon)$:

$$\frac{\partial u}{\partial z}(t,x,y,z) = O(\epsilon), \qquad \frac{\partial v}{\partial z}(t,x,y,z) = O(\epsilon). \tag{1.59}$$

Besides the hydrostatic approximation, this is the second assumption of the shallow water approximation. Therefore, we can write

$$u(t,x,y,z) = \bar{u}(t,x,y) + O(\epsilon), \qquad v(t,x,y,z) = \bar{v}(t,x,y) + O(\epsilon), \tag{1.60}$$

which implies that

$$\overline{u^2} = \bar{u}^2 + O(\epsilon), \qquad \overline{v^2} = \bar{v}^2 + O(\epsilon), \qquad \overline{u v} = \bar{u}\bar{v} + O(\epsilon) \tag{1.61}$$

and

$$\bar{E}_{\lambda\lambda} - \bar{E}_{\phi\phi} = \frac{1}{\cos\phi}\frac{\partial \bar{u}}{\partial x} - \frac{\partial \bar{v}}{\partial y} - \gamma \tan\phi\, \bar{v} + O(\epsilon), \tag{1.62}$$

$$\bar{E}_{\lambda\phi} = \frac{1}{2}\left(\frac{\partial \bar{u}}{\partial y} + \frac{1}{\cos\phi}\frac{\partial \bar{v}}{\partial x} + \gamma \tan\phi\, \bar{u}\right) + O(\epsilon). \tag{1.63}$$

Substituting equations (1.57) and (1.58) and the approximations (1.60)–(1.63) into the horizontal components of the equations of motion (1.52) and (1.53), we obtain the nondimensionalized system of the shallow water equation with the precision of $O(\epsilon)$

$$\frac{\partial \zeta}{\partial t} + \frac{1}{\cos\phi}\left(\frac{\partial (h\bar{u})}{\partial x} + \frac{\partial (h\bar{v})}{\partial y}\right) = 0, \tag{1.64}$$

$$\frac{\partial (h\bar{u})}{\partial t} + \frac{1}{\cos\phi}\left(\frac{\partial (\cos\phi\, h\bar{u}\bar{v})}{\partial y} + \frac{\partial h\bar{u}^2}{\partial x}\right) - \gamma \tan\phi\, h\bar{u}\bar{v} = -\frac{h}{F_r^2 \cos\phi}\frac{\partial \zeta}{\partial x} + \frac{h\bar{v}}{R_o} - c_{BF}^0 \bar{u}\sqrt{\bar{u}^2 + \bar{v}^2} + \nu_H \left[2\frac{\partial}{\partial y}(h\bar{E}_{\lambda\phi}) + \frac{1}{\cos\phi}\frac{\partial}{\partial x}\left(h(\bar{E}_{\lambda\lambda} - \bar{E}_{\phi\phi})\right) - 4\gamma \tan\phi\, h\bar{E}_{\lambda\phi}\right], \tag{1.65}$$

$$\frac{\partial (h\bar{v})}{\partial t} + \frac{1}{\cos\phi}\left(\frac{\partial (\cos\phi\, h\bar{v}^2)}{\partial y} + \frac{\partial (h\bar{u}\bar{v})}{\partial x}\right) + \gamma \tan\phi\, h\bar{u}^2 = -\frac{h}{F_r^2}\frac{\partial \zeta}{\partial y} - \frac{h\bar{u}}{R_o} - c_{BF}^0 \bar{v}\sqrt{\bar{u}^2 + \bar{v}^2} + \nu_H \left[\frac{\partial}{\partial y}\left(h(\bar{E}_{\phi\phi} - \bar{E}_{\lambda\lambda})\right) + \frac{2}{\cos\phi}\frac{\partial}{\partial x}(h\bar{E}_{\lambda\phi}) + 2\gamma \tan\phi\, h(\bar{E}_{\lambda\lambda} - \bar{E}_{\phi\phi})\right]. \tag{1.66}$$

1.6 The final form of the shallow water equations

The shallow water equations are now written in the dimensionless form. However, it is more practical to use physical quantities rather than the dimensionless quantities. Hence, we shall use the relations from the beginning of Section 1.4 and apply them to the dimensionless shallow water equations (note that the dimensionless quantities were denoted by the tilde, however, we dropped it from the equations for the sake of simplicity). Then, the shallow water equations in the geographical coordinates have the final form

$$\frac{\partial \zeta}{\partial t} + \frac{1}{a\cos\phi}\left(\frac{\partial (h\bar{u})}{\partial \lambda} + \frac{\partial (\cos\phi\, h\bar{v})}{\partial \phi}\right) = 0, \tag{1.67}$$

$$\frac{\partial (h\bar{u})}{\partial t} + \frac{1}{a}\frac{\partial (h\bar{u}\bar{v})}{\partial \phi} + \frac{1}{a\cos\phi}\frac{\partial (h\bar{u}\bar{u})}{\partial \lambda} - 2\frac{\tan\phi}{a}h\bar{u}\bar{v} = -\frac{gh}{a\cos\phi}\frac{\partial \zeta}{\partial \lambda} + fh\bar{v} - c_{BF}\bar{u}\sqrt{\bar{u}^2+\bar{v}^2} + \frac{A_H}{a}\left[2\frac{\partial}{\partial \phi}(h\bar{E}_{\lambda\phi}) + \frac{1}{\cos\phi}\frac{\partial}{\partial \lambda}\left(h(\bar{E}_{\lambda\lambda} - \bar{E}_{\phi\phi})\right) - 4\tan\phi\, h\bar{E}_{\lambda\phi}\right], \tag{1.68}$$

$$\frac{\partial (h\bar{v})}{\partial t} + \frac{1}{a}\frac{\partial (h\bar{v}\bar{v})}{\partial \phi} + \frac{1}{a\cos\phi}\frac{\partial (h\bar{v}\bar{u})}{\partial \lambda} + \frac{\tan\phi}{a}(h\bar{u}\bar{u} - h\bar{v}\bar{v}) = -\frac{gh}{a}\frac{\partial \zeta}{\partial \phi} - fh\bar{u} - c_{BF}\bar{v}\sqrt{\bar{u}^2+\bar{v}^2} + \frac{A_H}{a}\left[\frac{\partial}{\partial \phi}\left(h(\bar{E}_{\phi\phi} - \bar{E}_{\lambda\lambda})\right) + \frac{2}{\cos\phi}\frac{\partial}{\partial \lambda}(h\bar{E}_{\lambda\phi}) + 2\tan\phi\, h(\bar{E}_{\lambda\lambda} - \bar{E}_{\phi\phi})\right], \tag{1.69}$$

where

$$\bar{E}_{\lambda\lambda} - \bar{E}_{\phi\phi} = \frac{1}{a}\left(\frac{1}{\cos\phi}\frac{\partial \bar{u}}{\partial \lambda} - \frac{\partial \bar{v}}{\partial \phi} - \tan\phi\,\bar{v}\right), \tag{1.70}$$

$$\bar{E}_{\lambda\phi} = \frac{1}{2a}\left(\frac{\partial \bar{u}}{\partial \phi} + \frac{1}{\cos\phi}\frac{\partial \bar{v}}{\partial \lambda} + \tan\phi\,\bar{u}\right). \tag{1.71}$$

These equations can be rewritten to a more compact form as

$$\frac{\partial \zeta}{\partial t} + \nabla_\Omega \cdot (h\vec{v}) = 0, \tag{1.72}$$

$$\frac{\partial (h\vec{v})}{\partial t} + \nabla_\Omega \cdot (h\vec{v}\otimes\vec{v}) = -gh\nabla_\Omega\zeta + fh\vec{v}\times\vec{e}_z - \vec{\tau}_{BF} + A_H\nabla_\Omega\cdot\boldsymbol{\sigma}, \tag{1.73}$$

where

$$\vec{v} = (\bar{u},\bar{v}), \qquad \vec{\tau}_{BF} = c_{BF}\vec{v}|\vec{v}|, \qquad \boldsymbol{\sigma} = \begin{pmatrix} h(\bar{E}_{\lambda\lambda} - \bar{E}_{\phi\phi}) & 2h\bar{E}_{\lambda\phi} \\ 2h\bar{E}_{\lambda\phi} & h(\bar{E}_{\phi\phi} - \bar{E}_{\lambda\lambda}) \end{pmatrix}, \tag{1.74}$$

and ∇_Ω is the spherical nabla operator. Let us check whether the viscous term $A_H \nabla_\Omega \cdot \boldsymbol{\sigma}$ is consistent with the postulates (1)–(4) from Section 1.2. Obviously, the first, second and fourth postulates are satisfied. Regarding the third postulate, the kinetic energy equation is (with neglected bottom friction term)

$$\frac{\mathrm{d}}{\mathrm{d}t}\mathrm{KE} = A_H \langle \vec{v} \cdot (\nabla_\Omega \cdot \boldsymbol{\sigma}) \rangle, \tag{1.75}$$

where angle brackets denote a surface integral. The right-hand side can be decomposed

$$A_H \langle \vec{v} \cdot (\nabla_\Omega \cdot \boldsymbol{\sigma}) \rangle = A_H \langle \nabla_\Omega \cdot (\vec{v} \cdot \boldsymbol{\sigma}) \rangle - A_H \langle \nabla_\Omega \vec{v} : \boldsymbol{\sigma} \rangle. \tag{1.76}$$

The left term has the form of the divergence of a vector and the right term is always negative since it can be easily shown that $\nabla_\Omega \vec{v} : \boldsymbol{\sigma} = h(\bar{E}_{\lambda\lambda} - \bar{E}_{\phi\phi})^2 + h(2\bar{E}_{\lambda\phi})^2$. In summary, the viscous term in the shallow water equation is physically consistent.

CHAPTER

2

NUMERICAL METHODS AND TESTS

This chapter is focused on numerical methods which are employed to solve the shallow water equations in the geographical coordinates and are used in the DEBOT model. The equations are spatially discretized by finite differences (Section 2.1) and with respect to time by a generalized forward-backward scheme (Section 2.2). Validity of the numerical methods are tested by the conservation of integral invariants (Section 2.3).

2.1 Spatial finite differences

The shallow water equations are approximated in space by finite differences on a staggered grid using the Arakawa C-grid (Arakawa and Lamb, 1977). This lattice is very common in shallow water modelling. As you can see in Figure 2.1, the ocean domain is divided into cells. In the centres of the cells, there are ζ-points where the surface elevation ζ, height of water column h and diagonal parts of the advection tensor $\mathbf{P} = h\vec{v} \otimes \vec{v}$ and viscous tensor $\boldsymbol{\sigma}$ are evaluated. The zonal velocities u are evaluated at the east/west edges of the cells (u-points) while the meridional velocities v at the north/south edges (v-points). The non-diagonal parts of the advection and viscous tensors are evaluated at the corners of the cells (q-points). The grid intervals $\Delta\lambda$ and $\Delta\phi$ are distances between alike points in the zonal and meridional direction, respectively. Land areas can be implemented in the lattice by defining "dry cells", where the elevation is set to be zero. To satisfy the boundary condition (1.10), the velocities on the edges of the dry cells are set to be zero too.

Following the ideas of Lilly (1965); Arakawa and Lamb (1977); Shchepetkin

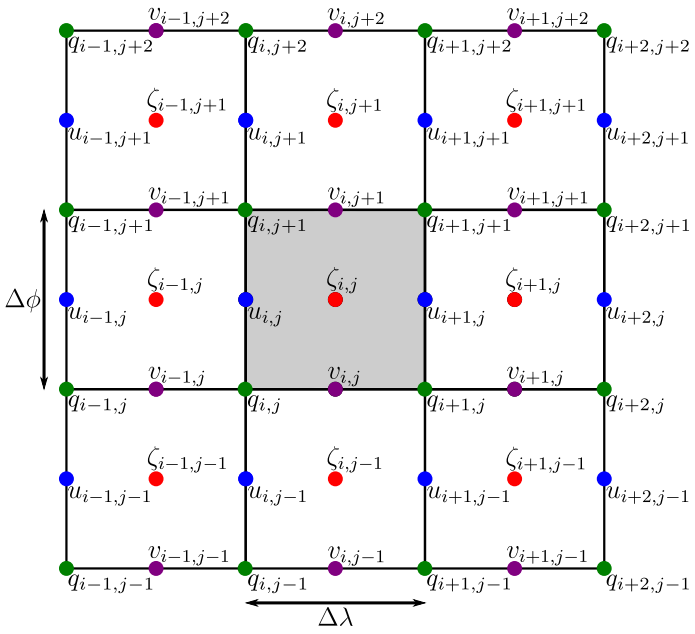

Figure 2.1: The Arakawa C-grid. ζ-points are marked by red dots, u-points by blue dots, v-points by purple dots and q-points by green dots. If grey color denotes the "dry cell", then the velocity points $u_{i,j}$, $u_{i+1,j}$, $v_{i,j}$ and $v_{i,j+1}$ are kept at zero in every time step.

and O'Brien (1996), let us introduce the average and finite-difference operators

$$\overline{x}^{\lambda}(\lambda,\phi) = \frac{x(\lambda+\frac{\Delta\lambda}{2},\phi)+x(\lambda-\frac{\Delta\lambda}{2},\phi)}{2}, \tag{2.1}$$

$$\overline{x}^{\phi}(\lambda,\phi) = \frac{x(\lambda,\phi+\frac{\Delta\phi}{2})+x(\lambda,\phi-\frac{\Delta\phi}{2})}{2}, \tag{2.2}$$

$$\delta_{\lambda}x(\lambda,\phi) = \frac{x(\lambda+\frac{\Delta\lambda}{2},\phi)-x(\lambda-\frac{\Delta\lambda}{2},\phi)}{a\cos\phi\Delta\lambda}, \tag{2.3}$$

$$\delta_{\phi}x(\lambda,\phi) = \frac{x(\lambda,\phi+\frac{\Delta\phi}{2})-x(\lambda,\phi-\frac{\Delta\phi}{2})}{a\Delta\phi}, \tag{2.4}$$

the mass fluxes U and V

$$U = \overline{h}^{\lambda}u, \tag{2.5}$$

$$V = \overline{h}^{\phi}v, \tag{2.6}$$

and denote

$$\Gamma = \frac{\tan\phi}{a}. \tag{2.7}$$

The spatial discretization of equations (1.67)–(1.69) is as follows

$$\frac{\partial \zeta}{\partial t} + \delta_\lambda U + \frac{1}{\cos\phi}\delta_\phi(\cos\phi V) = 0, \tag{2.8}$$

$$\frac{\partial U}{\partial t} + \delta_\lambda(P_{\lambda\lambda}) + \delta_\phi(P_{\lambda\phi}) = -g\overline{h}^{\lambda}\delta_\lambda\zeta + \overline{C_\lambda}^{\lambda} - c_{BF}u\sqrt{u^2 + (\overline{v}^{\lambda\phi})^2} + A_H\left[\delta_\phi(\sigma_{\lambda\phi}) + \delta_\lambda(\sigma_{\lambda\lambda}) - 2\Gamma\overline{\sigma_{\lambda\phi}}^{\phi}\right], \tag{2.9}$$

$$\frac{\partial V}{\partial t} + \delta_\lambda(P_{\lambda\phi}) + \delta_\phi(P_{\phi\phi}) = -g\overline{h}^{\phi}\delta_\phi\zeta + \overline{C_\phi}^{\phi} - c_{BF}v\sqrt{(\overline{u}^{\lambda\phi})^2 + v^2} + A_H\left[\delta_\phi(\sigma_{\phi\phi}) + \delta_\lambda(\sigma_{\lambda\phi}) + 2\Gamma\overline{\sigma_{\lambda\lambda}}^{\phi}\right], \tag{2.10}$$

where the components of the advection tensor **P** are

$$P_{\lambda\lambda} = \overline{U}^{\lambda}\overline{u}^{\lambda}, \tag{2.11}$$

$$P_{\phi\phi} = \overline{V}^{\phi}\overline{v}^{\phi}, \tag{2.12}$$

$$P_{\lambda\phi} = \frac{1}{2}(\overline{U}^{\phi}\overline{v}^{\lambda} + \overline{V}^{\lambda}\overline{u}^{\phi}), \tag{2.13}$$

$P_{\lambda\lambda}$ and $P_{\phi\phi}$ are evaluated at the ζ-points, $P_{\lambda\phi}$ at the q-points. Note that in general $\overline{U}^{\phi}\overline{v}^{\lambda} \neq \overline{V}^{\lambda}\overline{u}^{\phi}$ due to the staggered grid. The Coriolis force and the curvilinear metric terms arisen from the divergence of P are packed together into C_λ and C_ϕ terms to ensure the conservation of the kinetic energy (Arakawa and Lamb, 1977)

$$C_\lambda = h\overline{v}^{\phi}(2\Gamma\overline{u}^{\lambda} + f), \tag{2.14}$$

$$C_\phi = -h(\overline{u}^{\lambda}(\Gamma\overline{u}^{\lambda} + f) - \Gamma\overline{v}^{\phi}\overline{v}^{\phi}), \tag{2.15}$$

C_λ and C_ϕ are evaluated at the ζ-points. The components of the viscous tensor $\boldsymbol{\sigma}$ are

$$\sigma_{\lambda\lambda} = h(\delta_\lambda u - \delta_\phi v - \Gamma\overline{v}^{\lambda}), \tag{2.16}$$

$$\sigma_{\phi\phi} = -\sigma_{\lambda\lambda}, \tag{2.17}$$

$$\sigma_{\lambda\phi} = \overline{h}^{\lambda\phi}(\delta_\phi u + \delta_\lambda v + \Gamma\overline{u}^{\phi}), \tag{2.18}$$

$\sigma_{\lambda\lambda}$ and $\sigma_{\phi\phi}$ are evaluated at the ζ-points, $\sigma_{\lambda\phi}$ at the q-points.

2.2 Time-stepping scheme

The time-stepping scheme used in the DEBOT model is a generalized forward-backward (FB) scheme using a combination of a third-order Adams–Bashforth (AB3) step with a fourth-order Adams–Moulton (AM4) step (Shchepetkin and McWilliams, 2005, 2008), abbreviated as "AB3-AM4 FB scheme". However, there is a slight modification of this scheme in the DEBOT model. The friction at the bottom is approximated by the dimensionless bottom friction function proposed by Backhaus (1983).

The AB3-AM4 FB scheme consists of four parts:

(1) AB3-extrapolation of the elevation and the velocities

$$\begin{pmatrix}\zeta\\ \bar{u}\\ \bar{v}\end{pmatrix}^{n+\frac{1}{2}} = \left(\frac{3}{2}+\delta\right)\begin{pmatrix}\zeta\\ \bar{u}\\ \bar{v}\end{pmatrix}^{n} - \left(\frac{1}{2}+2\delta\right)\begin{pmatrix}\zeta\\ \bar{u}\\ \bar{v}\end{pmatrix}^{n-1} + \delta\begin{pmatrix}\zeta\\ \bar{u}\\ \bar{v}\end{pmatrix}^{n-2}, \quad (2.19)$$

and computation of the height and mass fluxes U and V from the extrapolated values

$$h^{n+\frac{1}{2}} = b + \zeta^{n+\frac{1}{2}}, \qquad U^{n+\frac{1}{2}} = h^{n+\frac{1}{2}}\bar{u}^{n+\frac{1}{2}}, \qquad V^{n+\frac{1}{2}} = h^{n+\frac{1}{2}}\bar{v}^{n+\frac{1}{2}}. \quad (2.20)$$

(2) Updating ζ and h by the continuity equation (1.67)

$$\zeta^{n+1} = \zeta^{n} - \Delta t \nabla_h \mathbf{U}^{n+\frac{1}{2}}, \qquad h^{n+1} = b + \zeta^{n+1} \quad (2.21)$$

where $\nabla_h \mathbf{U}$ is the finite difference approximation of the spatial derivatives in (1.67).

(3) Computation of provisional ζ' for the equation of motion

$$\zeta' = \left(\frac{1}{2}+\gamma+2\epsilon\right)\zeta^{n+1} + \left(\frac{1}{2}-2\gamma-3\epsilon\right)\zeta^{n} + \gamma\zeta^{n+1} + \epsilon\zeta^{n-2}. \quad (2.22)$$

(4) Updating $\bar{u}$ and $\bar{v}$ by the equations of motion (1.68) and (1.69)

$$\begin{pmatrix}\bar{u}\\ \bar{v}\end{pmatrix}^{n+1} = F\left[\begin{pmatrix}h\bar{u}\\ h\bar{v}\end{pmatrix}^{n} + \Delta t\left(\mathcal{P}(\zeta') + \begin{pmatrix}X\\ Y\end{pmatrix}^{n+\frac{1}{2}}\right)\right], \quad (2.23)$$

where F is the discrete bottom friction function (see below), $\mathcal{P}(\zeta')$ represents the gradients of the pressure and X and Y denote additional terms at the u-points and v-points, respectively. The additional terms are the Coriolis, advective and viscous terms, all are determined by the AB3-extrapolated values.

Backhaus (1983) discussed two ways of how the bottom friction can be approximated. An explicit formulation can produce a numerical instability in the case of shallow areas and strong currents. Hence, we use a semi-implicit formulation, which is numerically stable. Let the u-component of the equation of motion have a simple form

$$(hu)^{n+1} = (hu)^{n} + \Delta t(X^{n} - \tau_{BF_u}), \quad (2.24)$$

where X^n again denotes additional terms and τ_{BF_u} is the bottom friction at the u-points, which is formulated semi-implicitly,

$$\tau_{BF_u} = c_{BF}u^{n+1}\left(\sqrt{\bar{u}^2+\bar{v}^2}\right)^{n}. \quad (2.25)$$

By this, equation (2.24) takes the form

$$u^{n+1}\left[h^{n+1} + c_{BF}\Delta t\left(\sqrt{\bar{u}^2+\bar{v}^2}\right)^{n}\right] = (hu)^{n} + \Delta t X^{n}, \quad (2.26)$$

which leads to the expression for the discrete bottom friction function at the u-points

$$F_u = \frac{1}{h^{n+1} + c_{BF}\Delta t \left(\sqrt{\bar{u}^2 + \bar{v}^2}\right)^n}. \tag{2.27}$$

The bottom friction is routinely implemented in all kinds of ocean models, however tidal models should also incorporate another dissipative term which is called the internal tide drag and will be described in Chapter 4. The internal tide drag $\boldsymbol{\tau}_{ITD}$ is linearly dependent on the velocity

$$\boldsymbol{\tau}_{ITD} = \boldsymbol{C}_{ITD} \cdot \vec{v}, \tag{2.28}$$

where $\boldsymbol{C}_{ITD}$ is an internal tide drag tensor. In DEBOT, $\boldsymbol{C}_{ITD}$ has a scalar form C_{ITD} and the internal tide drag is formulated implicitly in a similar way like the bottom friction. As the result, the discrete friction function F_u is modified as

$$F_u = \frac{1}{h^{n+1} + c_{BF}\Delta t \left(\sqrt{\bar{u}^2 + \bar{v}^2}\right)^n + C_{ITD}\Delta t}. \tag{2.29}$$

F_v is obtained in an analogous way.

The AB3-AM4 FB scheme shows second-order accuracy for any values of δ, γ and ϵ, is third-order accurate for $\delta = \frac{5}{12}$ and even up to a fifth-order accuracy can be achieved. However, the scheme can easily become unstable. For a barotropic model, like the DEBOT model, it is practical to choose $\delta = 0.281105$, $\gamma = 0.088$ and $\epsilon = 0.013$ (Shchepetkin and McWilliams, 2008) to obtain the scheme with a large stability range for the combination of waves, advection and the Coriolis rotation. However, the scheme is still limited by the Courant condition of the form

$$\left.\frac{\sqrt{2gh}\Delta t}{\Delta x}\right|_{\max} \leq \frac{\omega_{\max}}{2}, \tag{2.30}$$

where $\omega_{\max} = 1.7802$ for the setting above. For more detailed information about the AB3-AM4 FB scheme, see Shchepetkin and McWilliams (2005, 2008).

The code of the DEBOT model is written in the free-form Fortran language with implemented OpenMP parallelization. Computational times required per a 30-day simulation of ocean tidal circulation for various spatial resolutions are given in Table 2.1. It shows that simulations of duration of a couple of months or even years with the resolution of $15' \times 15'$, or coarser, can be performed by a four or six core computer within a reasonable time. However, for a resolution finer than $15' \times 15'$, the computational time is excessive and the implementation of MPI parallelization and performing computations on a cluster of computers or a supercomputer would be necessary.

Table 2.1: Computational times of a 30-day simulation of global ocean tidal circulation with the North boundary at 85° latitude. Technical parameters: OpenMP parallelization, Intel Fortran compiler, maximal optimization, hardware Intel Six-core i7-3930K, 3.2 GHz.

Resolution	$\Delta t_{\max}$ [s]	Δt [s]	Computational time
$60' \times 60'$	32.999	32	1 m 58 s
$30' \times 30'$	15.693	15	22 m 51 s
$20' \times 20'$	10.233	10	1 h 15 m
$15' \times 15'$	7.574	7	3 h 12 m

2.3 Integral invariants tests

In this section we present results of numerical experiments based on the conservation of integral invariants. As derived by Pedlosky (1987) and McWilliams (2006), they are that the total mass in the shallow water system is preserved, meaning

$$\frac{\mathrm{d}M}{\mathrm{d}t} = 0, \tag{2.31}$$

where

$$M = \int \zeta \, \mathrm{d}S, \tag{2.32}$$

and that the time rate of the total energy is equal to the total power of external forces

$$\frac{\mathrm{d}E}{\mathrm{d}t} = \mathcal{F}, \tag{2.33}$$

where

$$E = \int \frac{1}{2} \left(h(u^2 + v^2) + g\zeta^2 \right) \, \mathrm{d}S, \tag{2.34}$$

and $\mathcal{F}$ is the total power of external forces.

A set of tsunami experiments are performed on a globe with continents at the poles and an island at the equator. The continents are placed at the poles for the sake of simplicity since the shallow water equations in the geographical coordinates (1.67)–(1.69) are divergent at the poles. Moreover, the discretization step in the latitudinal direction decreases towards the poles. The decrease of the discretization step in space results in a restriction of the time step. The continents are confined by the latitudes 85° North and 85° South. The bathymetry and the initial setting of the surface elevation are shown in Figure 2.2. The bathymetry has a shape of a Gaussian hill which leads to the formation of a circle island at the equator. The initial elevation of the free surface is given by a Gaussian depression with the amplitude of 100 m. The initial velocities are set equal to zero and the bottom friction is omitted. Figure 2.3 shows the time evolution of the surface elevation.

We investigate the evolution of the total mass and total energy during the 10-day simulation for several settings of the turbulent viscosity coefficient A_H

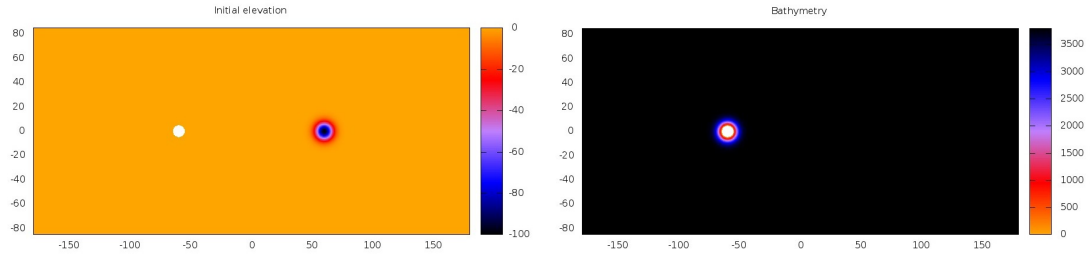

Figure 2.2: The initial surface elevation (left) and bathymetry (right) on the globe with the continents at the poles bounded by the 85° latitudes. The white circle centred at $\lambda = -60°$ and $\phi = 0°$ in both panels is an island of radius $\sim 5°$. The latitude and longitude are in degrees, the bathymetry and surface elevation are in meters.

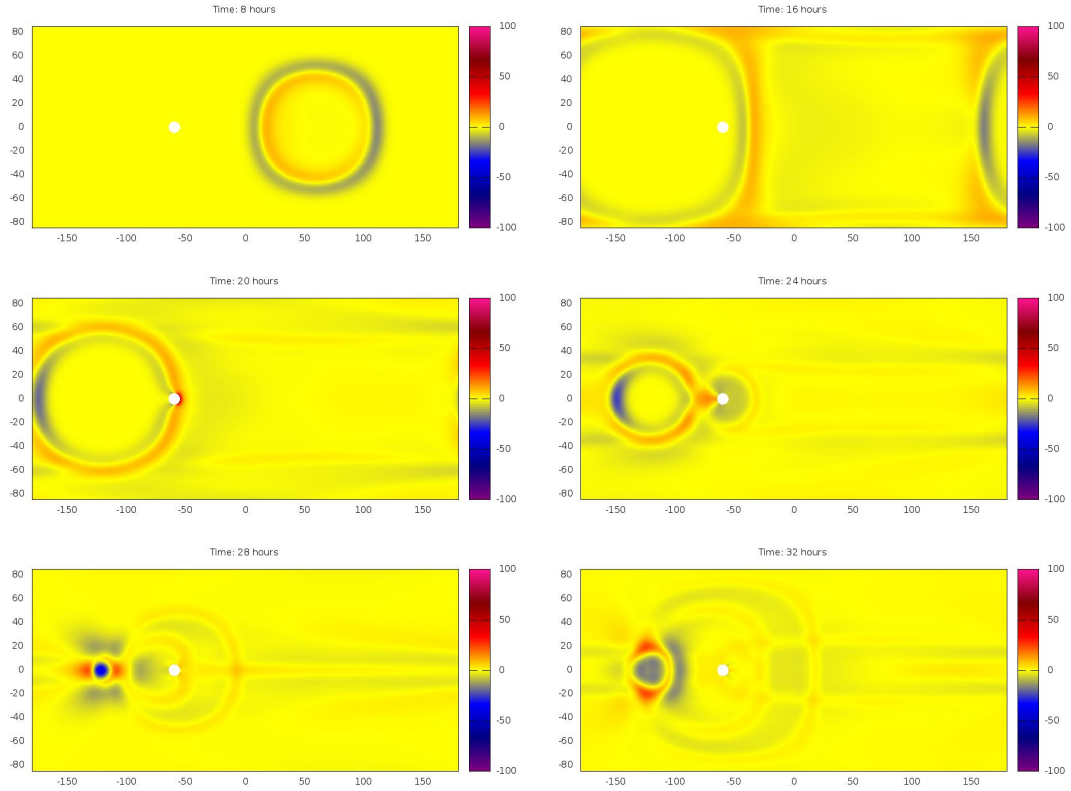

Figure 2.3: The time evolution of the surface elevation (in meters) of the tsunami experiment (Fig. 2.2) for the first 32 hours (spatial resolution $20' \times 20'$, time step 10 s, zero eddy viscosity).

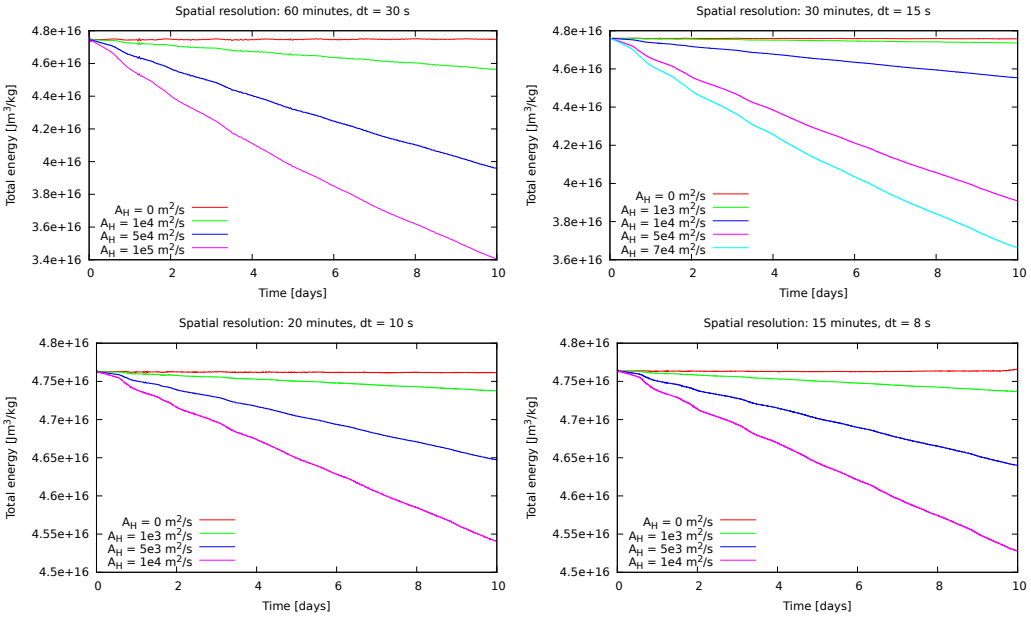

Figure 2.4: Evolution of the total energy from the tsunami experiment (Fig. 2.2) for spatial discretization of $60' \times 60'$, $30' \times 30'$, $20' \times 20'$ and $15' \times 15'$ and several values of the turbulent viscosity coefficient A_H.

with the spatial resolutions $60' \times 60'$, $30' \times 30'$, $20' \times 20'$ and $15' \times 15'$. In all experiments (not shown here), the total volume retains a constant value of -1.939×10^{14} m^3 with random deviations of the order m^3 which is of the order of the numerical errors. Hence, we focus only on the conservation of the energy. The evolution of the total energy is plotted in Figure 2.4. The testing of the energy demonstrates the validity of the numerical code since the energy is preserved in the case of zero eddy viscosity and decreases with non-zero viscosity. The decline of the energy is only slightly affected by the size of the spatial discretization step. For $A_H = 1 \times 10^4$ m^2/s, the final values of the total energy after 10 days are 4.564×10^{16} Jm^3/kg, 4.553×10^{16} Jm^3/kg, 4.541×10^{16} Jm^3/kg and 4.528×10^{16} Jm^3/kg for resolutions $60' \times 60'$, $30' \times 30'$, $20' \times 20'$ and $15' \times 15'$, respectively. The decline of the energy is greater with increasing eddy viscosity, however, the simulation becomes numerically unstable if the eddy viscosity is too large. For example, the simulation with a spatial resolution $30' \times 30'$, time step 15 s and $A_H = 8 \times 10^4$ m^2/s results in an unexpected and obviously unnatural increase of the energy up to 6.5×10^{16} Jm^3/kg at the end of the 10-day simulation (not shown here). We checked whether this energy growth is due to the violation of the Courant condition of the viscous term. However, the same effect is observed if the time step is 5 s, with an even larger increase in magnitude of the energy, with 8×10^{17} Jm^3/kg at the end of the simulation. Hence, this undesirable effect is probably an attribute of the time-stepping scheme in the case of too large A_H. However, a threshold value of A_H above which computations become unstable must be found experimentally for every setting.

CHAPTER

3

OCEAN TIDES

People have observed ocean tides since time immemorial. An understanding of this phenomenon was a matter of intuition, common sense and rules of thumb for centuries. Philosophers and scholars in ancient Greek, Rome and also in China noticed and described the relationships between the tides and lunar cycles (Cartwright, 1999), however, the physical explanation was not known until the 17th century when the foundations of modern physics were laid. Several theories were formulated (see Cartwright, 1999). Johannes Kepler in 1609 suggested that the tides were caused by the Moon's gravitation but was not able to explain why the tides occurred twice a day and not just once. Galileo Galilei in his *Dialogue Concerning the Two Chief World Systems* (1632)[1] proposed that the tides are generated by the rotations of the Earth, around its axis and around the Sun. The theory of René Descartes assumed that the entire space was filled by invisible ether and the Moon's motion induced pressure waves in ether which consequently formed the tides. However, Isaac Newton overcame all previous ideas with his theory of universal gravitation which was formulated in *Principia* (1687).[2] He was the first person who comprehensively explained that the tide-generating force is a consequence of the solar and lunar gravitational attraction.

Newton explained the origin of the tide-generating force however he did not pursue ocean dynamic response to the tidal force at all. The first relevant dynamic theory of the ocean tides came with Pierre-Simon Laplace who formulated the Laplace tidal equations in 1775 (Cartwright, 1999; Smith, 1999; Fok, 2012). The Laplace tidal equations are essentially a simplified version of

[1]The original title in Italian is *Dialogo sopra i due massimi sistemi del mondo*.

[2]The original title of the book in Latin is *Philosophiæ Naturalis Principia Mathematica*, in English *Mathematical Principles of Natural Philosophy*.

the shallow water equations (see Chapter 1) and are still in use today. However, ocean dynamics will be discussed in details in the modelling part of this thesis, in Chapters 4, 5 and 6. This chapter is a rather descriptive overview on the ocean tides. The tide-generating potential and the tidal force which acts on the ocean are described in Sections 3.1 and 3.2, respectively. Then, the harmonic development of the tide-generating potential is discussed in Sections 3.3–3.5. Basic information about non-astronomical tides, i.e., the radiational and compound tides, are provided in Section 3.6. Finally, the methods of tidal analysis (the harmonic analysis and response method) are reviewed in Section 3.7.

3.1 Tide-generating potential

The tides on the Earth are a consequence of the gravitational forces of the Moon and Sun. Let V be the potential of these tide-generating forces. Then, at an arbitrary point on the Earth P, V can be defined in terms of the Legendre polynomials as

$$V(P) = \frac{\mathcal{G}M}{d} \sum_{l=2}^{\infty} \left(\frac{a}{d}\right)^l P_l(\cos\theta), \tag{3.1}$$

where $\mathcal{G}$ is the gravitational constant, M the mass of a celestial body, a the mean Earth's radius, d the geocentric distance of the celestial body, θ the zenith distance at the point P (see Figure 3.1) and $P_l(x)$ is the Legendre polynomial of degree l. There are many books and lecture notes with a derivation of (3.1), e.g., Pugh (1987); Novotný (1998) and the interested reader is referred to them for details. Note that the potential (3.1) is defined positively as is conventional in geodesy while the convention in physics involves a negative sign in (3.1). In the geodetic convention, an increase of the potential is associated with a rise of the ocean surface.

The zenith distance θ can be expressed in terms of terrestrial and celestial coordinates as

$$\cos\theta = \sin\phi \sin\delta + \cos\phi \cos\delta \cos H, \tag{3.2}$$

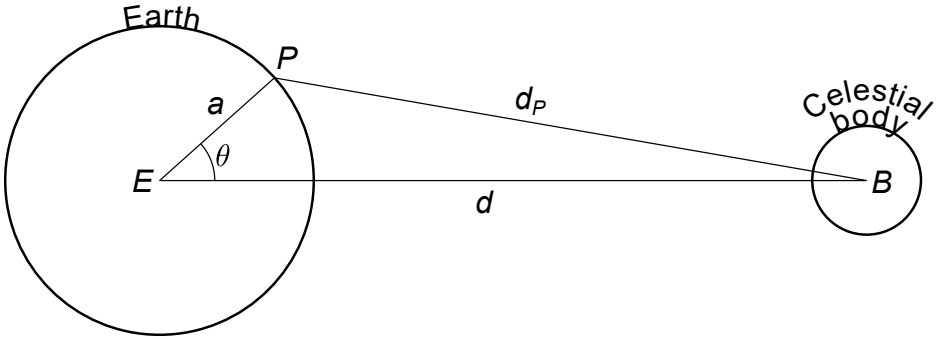

Figure 3.1: Definition of the geocentric distance d and zenith distance θ of a celestial body at an arbitrary point on the Earth P.

where δ is the declination of the celestial body, ϕ the latitude at P and H the local hour angle which is

$$H = \Omega T_{Gr} + \lambda - \alpha, \tag{3.3}$$

where Ω is the angular speed of the Earth's rotation, T_{Gr} the Greenwich sidereal time (which is 00:00 at the moment when the vernal equinox crosses the prime meridian at Greenwich), λ the longitude at P and α the right ascension of the celestial body.

In the equatorial coordinate system, the right ascension and declination are celestial equivalents of the terrestrial longitude and latitude. The declination describes the angle from the celestial equator towards the north celestial pole. The right ascension is measured eastward from the First Point of Aries ♈ which is the point in the sky where the Sun is at the vernal equinox.[3] The celestial poles and celestial equator are defined as projections of the Earth's poles and equator at the vernal equinox onto the celestial sphere, respectively. See also Figures 3.2 and 3.3 for a graphical description of the astronomical nomenclature.

Using equation (3.2) and the addition theorem for the Legendre polynomials, $P_l(\cos\theta)$ can be expanded into (e.g., Hobson, 1965)

$$P_l(\cos\theta) = \sum_{m=0}^{l} (2 - \delta_{0m}) \frac{(l-m)!}{(l+m)!} P_{lm}(\sin\phi) P_{lm}(\sin\delta) \cos(mH), \tag{3.4}$$

where $P_{lm}(x)$ is the associated Legendre function of degree l and order m and δ_{0m} is the Kronecker delta ($\delta_{00} = 1$ and $\delta_{0m} = 0$ if $m \neq 0$). Substitution of equation 3.4 into equation 3.1 results in the following formulation of the tide-generating potential

$$V(P) = \frac{\mathcal{G}M}{d} \sum_{l=2}^{\infty} \left(\frac{a}{d}\right)^l \sum_{m=0}^{l} (2 - \delta_{0m}) \frac{(l-m)!}{(l+m)!} P_{lm}(\sin\phi) P_{lm}(\sin\delta) \cos(mH). \tag{3.5}$$

The potential is proportional to $d^{-(l+1)}$, hence, usually, only the second degree potential is considered and the potential of higher degrees is neglected. However, some signals generated by the third degree potential can also be observed. This is the case of the M_3 tide which has been detected by many tide gauges and its coefficient of the harmonic expansion (see Section 3.3) is comparable to coefficients of some minor tidal constituents generated by the second degree potential, see tables in Doodson (1921); Cartwright and Tayler (1971);

[3] The First Point of Aries was defined by Hipparchus of Nicaea in 130 BC when it was located in the western part of the constellation of Aries near the border with Pisces. It was called the First Point of Aries because at this point, the Sun entered the constellation of Aries during its eastward movement in the sky. However, because of the Earth's axial precession, the points slowly moves westwards, approximately one degree per 72 years, and is now located in the constellation of Pisces, near its border with Aquarius, about 30° away from the time of Hipparchus.

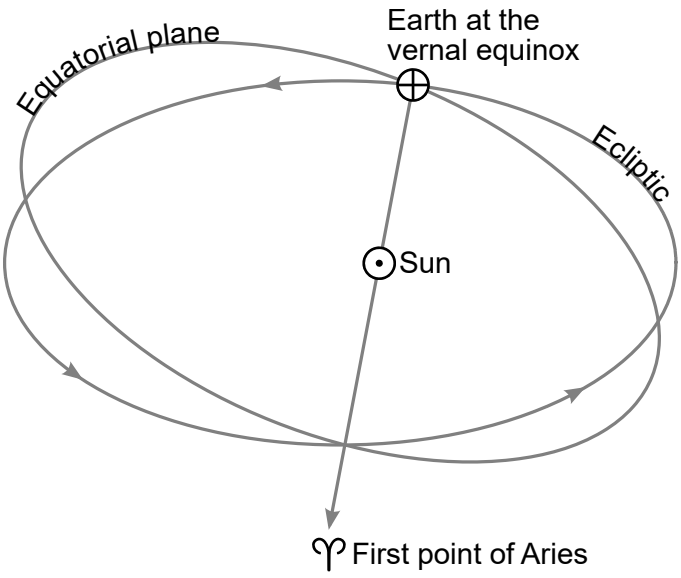

Figure 3.2: The ecliptic is defined by the mean Earth's orbit around the Sun, the equatorial plane by the Earth's equator at the equinoxes. The position of the Sun in the sky at the vernal equinox determines the First Point of Aries ♈ which is the reference point for the right ascension (see Figure 3.3).

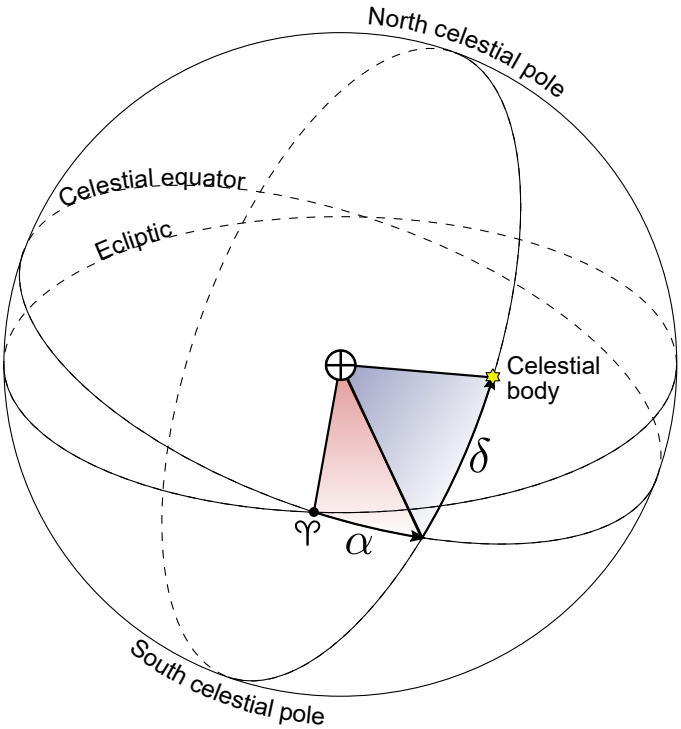

Figure 3.3: The equatorial coordinate system. The celestial poles are projections of the Earth's poles onto the celestial sphere at the vernal equinox, the celestial equator is a projection of the Earth's equator. ♈ denotes the First Point of Aries, α the right ascension and δ the declination of a celestial body.

Cartwright and Edden (1973).[4] Therefore in this thesis, the tide-generating potential of the second and third degree, V_2 and V_3, respectively, is considered, which can be formulated as

$$\begin{aligned} V_2 = \frac{3}{4}\frac{\mathcal{G}Ma^2}{d^3}\Big[&3\left(\sin^2\phi - \frac{1}{3}\right)\left(\sin^2\delta - \frac{1}{3}\right) + \\ &\sin(2\phi)\sin(2\delta)\cos H + \\ &\cos^2\phi\cos^2\delta\cos(2H)\Big], \end{aligned} \tag{3.6}$$

$$\begin{aligned} V_3 = \frac{1}{4}\frac{\mathcal{G}Ma^3}{d^4}\Big[&\left(5\sin^2\phi - 3\right)\left(5\sin^2\delta - 3\right)\sin\phi\sin\delta + \\ &\frac{3}{2}\left(5\sin^2\phi - 1\right)\left(5\sin^2\delta - 1\right)\cos\phi\cos\delta\cos H + \\ &\frac{15}{4}\sin(2\phi)\cos\phi\sin(2\delta)\cos\delta\cos(2H) + \\ &\frac{5}{2}\cos^3\phi\cos^3\delta\cos(3H)\Big]. \end{aligned} \tag{3.7}$$

Note that only the lunar third degree potential is of some importance since for the Moon $a/d_{\leftmoon} \approx 1.7 \times 10^{-2}$ while for the Sun $a/d_{\odot} \approx 4. \times 10^{-5}$. Hence, the solar potential of the third degree is about five orders of magnitude smaller than the second order potential and can be neglected.

As evident from equations (3.6) and (3.7), the tidal potential can be divided into tidal species corresponding to different period bands. The first term in (3.6), V_{20}, is called the zonal term or the long-period species with the fundamental periods of half a month (for the Moon) and half a year (for the Sun) which can be explained by the fact that the term is independent on H and varies with the squared sine of the declination. The term is always negative in polar latitudes and positive in mid-latitudes and the nodal lines are the parallels $35°16'$ North and South. The second term in (3.6), V_{21}, is called the tesseral term or the diurnal species and corresponds to tidal variations once a day as it contains H. The species reaches maximal and minimal values at the latitudes of $45°$ and is always zero at the equator and poles. The third term in (3.6), V_{22}, is called the sectoral term or the semi-diurnal species, containing $2H$, and thus shows variations with periods of approximately 12 hours. Finally, the last term in (3.7), V_{33}, is the ter-diurnal species corresponding to three times per day variations. The semi- and ter-diurnal species have maximal amplitudes at the equator and are zero at the poles. The illustration of the tidal species is shown in Figure 3.4. Note that V_{33} is two orders of magnitude smaller than V_2.

[4] Doodson also included the potential of the fourth degree in his harmonic development, however coefficients of the fourth degree constituents were so small that he ignored them in his final tables. Cartwright, Tayler and Edden did not included the fourth degree potential in their calculations at all.

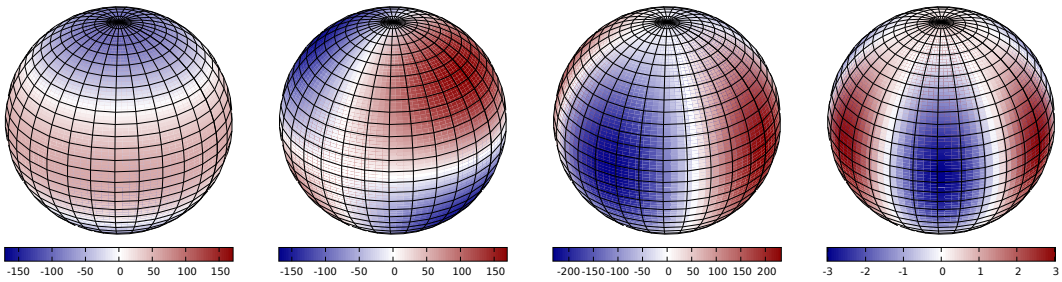

Figure 3.4: The four species of the tide-generating potential: the long-period (left), diurnal (centre left), semi-diurnal (centre right) and ter-diurnal species. The potential is generated by the Moon at an arbitrary time. The color scales are in 10^{-8} Nm.

3.2 Tidal forcing in oceans

The tidal forcing $\vec{T}$ which acts on the ocean in the shallow water approximation (Chapter 1) is defined as the positive spherical gradient of the tide-generating potential

$$\vec{T} = h(\gamma_2 \nabla_\Omega V_2 + \gamma_3 \nabla_\Omega V_3). \tag{3.8}$$

The positive gradient of the tide-generating potential is due to the geodetic convention mentioned at the beginning of Section 3.1. h is the height of the water column which must be added since the momentum equation in the shallow water approximation (equation (1.73)) is formulated in terms of horizontal transports $h\vec{v}$. γ_2 and γ_3 are the diminishing factors which accounts for the effect of the solid Earth tides. They represent an additional gravitational potential and a displacement which are generated as a response of the solid Earth to the tidal force (Novotný, 1998; Agnew, 2007). It holds that $\gamma_l = 1 + k_l - h_l$, where k_l and h_l are the Love numbers of the lth degree which can be computed from standard Earth models (Agnew, 2007). In this thesis, $\gamma_2 = 0.6948$ (Agnew, 2007) and $\gamma_3 = 0.804$ (Melchior, 1972) are used.

If equation (3.8) is developed in terms of degrees and directions, the second degree forcing in the zonal direction is

$$T_{2\lambda} = -h\gamma_2 \frac{3}{2} \frac{\mathcal{G}Ma}{d^3} \Big[\cos\phi \cos^2\delta \sin(2H) + \sin\phi \sin(2\delta) \sin H\Big], \tag{3.9}$$

and in the meridional direction is

$$T_{2\phi} = h\gamma_2 \frac{3}{4} \frac{\mathcal{G}Ma}{d^3} \Big[\sin(2\phi)\left(3\sin^2\delta - 1\right) + 2\cos(2\phi)\sin(2\delta)\cos H - \sin(2\phi)\cos^2\delta\cos(2H)\Big]. \tag{3.10}$$

The third degree forcing in the zonal direction is

$$T_{3\lambda} = -h\gamma_3 \frac{15}{8} \frac{\mathcal{G}Ma^2}{d^4} \left[5 \left(\sin^2\phi - \frac{1}{5} \right) \left(\sin^{\delta} - \frac{1}{5} \right) \cos\delta \sin H + \right. \\ \sin(2\phi) \sin(2\delta) \cos\delta \sin(2H) + \\ \left. \cos^2\phi \cos^3\delta \sin(3H) \right], \tag{3.11}$$

and in the meridional direction is

$$T_{3\phi} = h\gamma_3 \frac{15}{8} \frac{\mathcal{G}Ma^2}{d^4} \left\{ \frac{10}{3} \left[\left(\sin^2\phi - \frac{3}{5} \right) + \sin\phi \sin(2\phi) \right] \sin\delta \left[\sin^2\delta - \frac{3}{5} \right] + \right. \\ 5 \left[\sin(2\phi) \cos\phi - \left(\sin^2\phi - \frac{1}{5} \right) \sin\phi \right] \cos\delta \left[\sin^2\delta - \frac{1}{5} \right] \cos H + \\ \left[\cos(2\phi) - \sin^2\phi \right] \cos\phi \sin(2\delta) \cos\delta \cos(2H) - \\ \left. \cos^2\phi \sin\phi \cos^3\delta \cos(3H) \right\}. \tag{3.12}$$

3.3 Harmonic development of the potential

The tide-generating potential is a function of actual positions of the Moon and Sun. Since the orbital motions of the Earth around the Sun and the Moon around the Earth have a periodic character, it is possible to formulate the tidal potential as a series of harmonic functions. The amplitudes of these harmonic functions are assumed to be constant in time while their arguments are determined by linear combinations of fundamental astronomical angles which vary almost linearly with time. The first development was given by George Howard Darwin (Darwin, 1883) however, his development was quasi-harmonic and included only 39 terms. The first truly harmonic and comprehensive development was provided by Arthur Thomas Doodson (Doodson, 1921) who used modern Brown's lunar theory (Brown, 1905) and his expansion included 386 terms. The harmonic development were then independently recalculated by David Edgar Cartwright using revised astronomical constants and a different method (Cartwright and Tayler, 1971; Cartwright and Edden, 1973; see also Section 3.5). Later, other authors provided more extensive harmonic decompositions of the tidal potential (Tamura, 1987; Xi, 1987; Hartmann and Wenzel, 1995; Roosbeek, 1996; Kudryavtsev, 2004), motivated by very precise astronomical measurements and a need of greater accuracy for analysis of some tidal data, e.g., gravity tides from superconductive gravimeters (Agnew, 2007). The most recent expansion by Kudryavtsev (2004) includes 27 000 harmonics.

Each species of the tide-generating potential can be written as

$$V_{lm} = G_{lm}(\phi) \sum_k |\eta_k| \cos(\Theta_k(t) + \chi_k + m\lambda), \tag{3.13}$$

where $G_{lm}(\phi)$ are the geodetic functions, the summation over k is over all harmonics of the species, η_k are the coefficients of the harmonic development and

Table 3.1: Values of the additive phase corrections χ_k depending on the degree l and order m of the tide-generating potential and the sign of the coefficient of the harmonic development η_k.

degree l	order m	$\eta_k > 0$	$\eta_k < 0$
2	0	0°	180°
2	1	90°	−90°
2	2	0°	180°
3	0	90°	−90°
3	1	0°	180°
3	2	90°	−90°
3	3	0°	180°

Θ_k the astronomical arguments or Doodson arguments at Greenwich. χ_k are the so-called additive phase corrections which are multiplies of 90° and were introduced by Doodson and Warburg (1941) to obtain a series of all positive coefficients $|\eta_k|$ and cosine functions only. This is known as the Doodson–Warburg convention. The rules for applying the additive phase corrections are summarized in Table 3.1.

The geodetic functions are (Doodson, 1921)

$$G_{20} = \frac{1}{2} G(1 - 3\sin^2\phi), \tag{3.14}$$

$$G_{21} = G\sin(2\phi), \tag{3.15}$$

$$G_{22} = G\cos^2\phi, \tag{3.16}$$

$$G_{30} = 1.11803 G\sin\phi(3 - 5\sin^2\phi), \tag{3.17}$$

$$G_{31} = 0.72618 G\cos\phi(1 - 5\sin^2\phi), \tag{3.18}$$

$$G_{32} = 2.59808 G\sin\phi\cos^2\phi, \tag{3.19}$$

$$G_{33} = G\cos^3\phi, \tag{3.20}$$

where the constant G is

$$G = \frac{3\mathcal{G} M_{\leftmoon} a^2}{4\bar{d}_{\leftmoon}^3}, \tag{3.21}$$

and $M_{\leftmoon}$ and $\bar{d}_{\leftmoon}$ are the mass and mean geocentric distance of the Moon. An analogous constant and geodetic functions can be introduced for the solar tides using the Sun's mass $M_\odot$ and mean geocentric distance $\bar{d}_\odot$, however, it is more convenient to normalize all coefficients of the harmonic development η_k with respect to one constant G so the coefficients show relative importance of the harmonics. It means that η_k of the solar harmonics contain the factor $\frac{M_\odot \bar{d}_{\leftmoon}^3}{M_{\leftmoon} \bar{d}_\odot^3}$.

The Doodson arguments at Greenwich Θ_k are linear combinations of the six fundamental astronomical angles

$$\Theta_k(t) = n_1\tau + n_2 s + n_3 h + n_4 p + n_5 N' + n_6 p_s, \tag{3.22}$$

Table 3.2: Fundamental tidal frequencies and periods (from Agnew, 2007).

Symbol	Freq. (cycles/day)	Period	What is it?
τ	0.9661368	24 h 50 m 28.3 s	Lunar day
s	0.0366011	27.3216 d	Tropical month
h	0.0027379	365.2422 d	Solar year
p	0.0003095	8.847 yr	Lunar apsidal precession
N	0.0001471	18.613 yr	Lunar nodal precession
p_s	0.0000001	20941 yr	Solar apsidal precession

where τ is Greenwich mean lunar time (reduced to angle), s the Moon's mean longitude, h the Sun's mean longitude, p the longitude of the Moon's perigee (the point of least distance of the Moon from the Earth), $N' = -N$, where N is the longitude of the Moon's ascending node (the point where the orbit of the Moon crosses the ecliptic from south to north), p_s is the longitude of the Sun's perigee (the point of least distance of the Sun from the Earth) and $n_1, \ldots, n_6$ are integers. These angles, which are six independent variables needed for the expansions of V_2 and V_3, were chosen by Doodson (1921). Their corresponding frequencies and periods are listed in Table 3.2. It should be note that all angles are referred to the ecliptic and not to the equatorial plane like the right ascension and declination defined earlier in this chapter (Section 3.1). Greenwich mean lunar tide is related to Greenwich mean solar time [5] t and the mean longitudes of the Moon and Sun through

$$\tau = 15^\circ t + h - s. \tag{3.23}$$

The relationships between the angles are also illustrated in Figure 3.5.

Numerical values of the angles s, h, p, N', p_s are given by the polynomial expressions (Simon et al., 1994)

$$\begin{aligned} s &= 218^\circ.31665436 + 481267^\circ.881342397T - 0^\circ.001326750T^2 + \\ &\quad 0^\circ.000001856T^3 - 0^\circ.000000015T^4, && (3.24)\\ h &= 280^\circ.46645683 + 36000^\circ.769750953T + 0^\circ.000303217T^2 + \\ &\quad 0^\circ.000000020T^3 - 0^\circ.000000007T^4, && (3.25)\\ p &= 83^\circ.35324299 + 4069^\circ.013711056T - 0^\circ.010323778T^2 - \\ &\quad 0^\circ.000012492T^3 + 0^\circ.000000053T^4, && (3.26)\\ N' &= 234^\circ.95544496 + 1934^\circ.136184889T - 0^\circ.002076167T^2 - \\ &\quad 0^\circ.000002139T^3 + 0^\circ.000000016T^4, && (3.27)\\ p_s &= 282^\circ.93734808 + 1^\circ.719459803T + 0^\circ.000456883T^2 - \\ &\quad 0^\circ.000000018T^3 - 0^\circ.000000003T^4, && (3.28) \end{aligned}$$

[5] By definition, Universal Time (UT1) is mean solar time at Greenwich. Coordinated Universal Time (UTC), used as an international time standard for civil purposes, is equal to UT1 within 0.9 seconds.

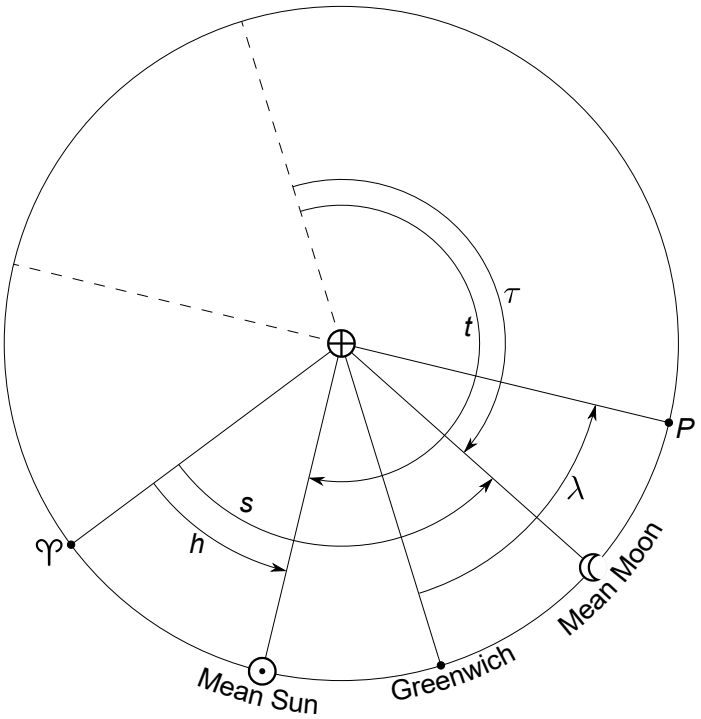

Figure 3.5: The fundamental angles which determine the Doodson arguments. Greenwich mean solar time and Greenwich mean lunar time are denoted by t and τ, respectively. Local mean solar time and local mean lunar time at an arbitrary point on the Earth P are $t + \lambda$ and $\tau + \lambda$, respectively, where λ is the latitude at P. The Moon's mean longitude s and Sun's mean longitude h are measured in the ecliptic, eastward from the First Point of Aries ♈.

where the origin of time T is the epoch J2000.0 which is defined to be equivalent to January 1, 2000, 11:58:55.816 Coordinated Universal Time (UTC), i.e., approximately noon at Greenwich.[6] T is time in Julian centuries,[7] i.e., 36 525 mean solar days.[8] The expressions are referred to the equinox of date, i.e., the effect of the Earth's axial precession is considered. The terms of higher order than T in (3.24)–(3.28) arise mainly from planetary perturbations on the eccentricity of the Moon's orbit and on the eccentricity of the Sun's apparent orbit (Smith, 1999). Obviously, on short-term time scales (years), the motions of the Moon and Sun can be regarded as linear in time.

[6]J2000.0 is a Julian epoch corresponding to January 1, 2000, 12:00:00 Terrestrial Time (TT). TT is a theoretical uniform time scale which is not defined by any measurements. Within miliseconds accuracy, TT is parallel to International Atomic Time (TAI, based on atomic clocks) and ahead of TAI by 32.184 seconds (due to historical reasons). TT is also ahead of UTC, by roughly 68 seconds in 2015 (`http://maia.usno.navy.mil/ser7/tai-utc.dat`) and the gap is increasing in time due to slowing of the Earth's rotation. TT and UTC were approximately equal around 1900.

[7]The expressions in Simon et al. (1994) are formulated in Barycentric Dynamical Time (TDB), a relativistic coordinate time scale, which is equivalent to Terrestrial Time within accuracy of 2 miliseconds.

[8]One mean solar day is 86 400 SI seconds.

The argument Θ_k of each harmonic is determined by a unique combination of the integers $n_1, \ldots, n_6$, for example,

$$\Theta_k = 2\tau + 4s - 3h + p + 2N' - p_s. \tag{3.29}$$

In order to write such an expression in short, Doodson (1921) introduced a systematic notation. Each tidal harmonic is denoted by the 6-digit *argument-number*, also called the *Doodson number*, in the form

$$n_1(n_2+5)(n_3+5).(n_4+5)(n_5+5)(n_6+5). \tag{3.30}$$

For example, the Doodson number for the expression above is

$$292.674. \tag{3.31}$$

The reason why five is added to $n_2, \ldots, n_6$ is to avoid writing negative values as much as possible and these numbers are only occasionally outside the range -4 to 4. On the other hand, n_1 is never negative and hence, no number needs to be added.

The argument-number is divided into two parts. The reason is that many tidal observations are not long enough to distinguish two harmonics with the identical first part but different second one, i.e., if the arguments of the harmonics differ by multiplies of p, N' or p_s. Doodson (1921) defined that the first three digits of the argument-number are the *constituent-number* and all harmonics with an equal constituent-number form a tidal constituent, e.g., all harmonics with the constituent-number 255 form the M_2 constituent. Analogously, the first two digits of the argument-number are called the *group-number* and all harmonics with an equal group-number form a tidal group, e.g., the group-number 25 form the M_2 group. Finally, the first digit of the argument-number is the *species-number* and determines a tidal species, e.g., 2 stands for the semi-diurnal species.

Sometimes, the Doodson number is extended by another digit containing information about the additive phase correction χ_k. This 7-digit number is called the extensive Doodson number (XDO) and the additional seventh number is a multiple of 90° plus five, e.g., 4 represents $\chi_k = -90^\circ$. This formalism is applied in IHO (2006).

The Doodson number is a convenient notation of tidal harmonics, however, in some rare cases, the coefficients $n_2, \ldots, n_6$ are outside the range -4 to 4. Doodson (1921) used $\bar{1}$ for $n_i = -6$, 0 for $n_i = -5$, X for $n_i = 5$ and E for $n_i = 6$ in his tables, however, this system may be insufficient and overflow if one wants to assign the Doodson numbers to the compound tides (also the shallow-water tides) which are generated by non-linearities of ocean dynamics and not by the astronomical tidal potential, see Section 3.6. Therefore, the UK Hydrographic Office replaced the numerical system with an alphabetical system in which Z represents 0, the letters A to N represent 1 to 14 and R to Y represent -8 to -1 (IHO, 2006). For example, the argument-number of the R_2 tide is 274.554 and $\chi_k = 180^\circ$, then its alphabetical XDO is BBYZZYB.

Although the Doodson numbers, whether the numerical or alphabetical ones, provide a systematic notation, there is a convention in the tidal community to use the so-called *Darwin symbols* for selected tidal waves. Unfortunately, this naming system, which was begun by Thomson for few tides and extended by Darwin (and then by other authors for smaller tides), was built in a somewhat ad hoc manner (Agnew, 2007) and thus, the symbols must be memorized. The most important tides and their Darwin symbols are listed in Table 3.3. There is some inconsistency in the usage of the Darwin symbols. They may refer to tides of exact frequencies or to tidal constituents. For example, M_2 may refer to the tide with the Doodson number 255.555 and the period of 12.4206 h (as is in Table 3.3) or to the constituent consisted of all harmonics with the constituent-number 255.

The last column of Table 3.3 shows the origins of the tidal harmonics. The principal tides are tides of a fictitious celestial body which moves in a circular orbit in the equatorial plane. The declinational terms are caused by the lunar and solar declination. The elliptical terms are modulations of the principal tides converting the circular orbits into elliptical ones. The lunar evection and variation are perturbations of the Moon's revolution around the Earth caused by the Sun's gravitational force. The evection is the change in the eccentricity of the Moon's orbit. The variation is a distortion of the Moon's motion during a synodic month.[9] If the hypothetical undisturbed motion of the Moon was circular, the Sun's attraction would change it to the elliptical one with the Earth in the centre of the ellipse, i.e., the variational ellipse is different from the eccentric Keplerian ellipse where the Earth is located in a focus.

The largest term of the long-period species is the permanent Z_0 tide which tends to increase the flattening of the Earth's static figure (Smith, 1999). The solar annual S_a and lunar monthly M_m tides arise from the ellipticity of the orbits and their periods are respectively governed by the mean Sun's longitude relative to the perihelion, $\Theta_{S_a} = h - p_s$, and the mean Moon's longitude relative to the lunar perigee, $\Theta_{M_m} = s - p$. S_a and M_m can be viewed as elliptical modulations of Z_0. The long-period declinational tides are solar semi-annual S_{sa} and lunar monthly M_f. Their periods are respectively 182.622 d, corresponding to the argument $2h$, and 13.661 d, corresponding to the argument $2s$, due to the term $\sin^2\delta$ in the long-period species of the potential V_2 (see equation (3.6) in Section 3.1).

The diurnal tides are all declinational as the diurnal species of V_2 is proportional to $\sin\delta$ (equation (3.6)). As a consequence, these terms tend to occur in pairs balancing each other when the lunar or solar declination is zero. The principal pair of the lunar diurnal tides are O_1 and K_1 which have the arguments $\tau - s$ and $\tau + s$, respectively, and therefore are in phase every 13.661 days. O_1 and K_1 correspond to a circular orbit of a fictitious moon in the mean plane of the real Moon. Two principal solar diurnal tides are P_1 ($\Theta_{P_1} = \tau + s - 2h$) and again K_1 ($\Theta_{K_1} = \tau + s$) which are in phase every 182.622

[9] The synodic month is an average period of the Moon's revolution with respect to the line joining the Sun and Earth which is larger than the tropical month, approximately 29.53 days.

days. They correspond to an apparent circular orbit of a fictitious sun in the ecliptic. Keep in mind that $\tau = t - s + h$, where t is UTC reduced to angle, and so the arguments of P_1 an K_1 may be written as $t - h$ and $t + h$, respectively. It means that P_1 an K_1 are governed by mean solar time and the Sun's longitude, analogously to the lunar O_1 and K_1 tides which are governed by mean lunar time and the Moon's longitude. One can see that K_1 has a contribution from both disturbers, the Moon and Sun. The lunar and solar contributions to the harmonic coefficient η_{K_1} are in ratio of approximately 68:32 (Doodson, 1921). The lunar and solar part of K_1 are inseparable in tidal analyses and hence, K_1 can be called the lunisolar diurnal tide. The principal diurnal tides are accompanied by a series of elliptic tides whose arguments differ by $s - p$ (lunar) or $h - p_s$ (solar). O_1 is modulated mainly by Q_1 ($\Theta_{Q_1} = \tau - s - (s - p)$), which is the largest diurnal elliptical tide, and much smaller tide 155.455 ($\Theta_{155.455} = \tau - s + (s - p)$). The latter is not listed in Table 3.3 however it is usually denoted as M_1 (Doodson, 1921; Pugh, 1987; IHO, 2006) as it is a part of the M_1 constituent and its argument differs from the argument of the M_1 tide (155.655, listed in Table 3.3) by $2p$. A separation of these two harmonics from data would require at least an 8.85-years long time-series (see Section 3.7.1). M_1 (155.655, $\Theta_{M_1} = \tau - s - (s - p)$) and J_1 ($\Theta_{J_1} = \tau + s + (s - p)$) are lunar elliptical modulations of K_1. π_1, S_1 and ϕ_1 modulate solar P_1 and K_1 in an analogous way. The S_1 component consists of two harmonics, 165.554 (not listed in Table 3.3), which is the smaller elliptical modulation of P_1, and 165.556 (listed in Table 3.3), which modulates K_1. Both are very small so their signals in the oceans are barely detectable. However, there exist significant observed signals at this frequency which have a meteorological origin. This is called the radiational S_1 tide and will be explained in Section 3.6.

The principal semi-diurnal tides are lunar M_2, whose period is exactly half a mean lunar day, and solar S_2, whose period is exactly half a mean solar day. M_2 and S_2 correspond to circular orbits of a fictitious moon or sun in the equatorial plane. They are accompanied by a series of elliptical tides. N_2 and smaller L_2 are main elliptical modulations of M_2 with the arguments $2\tau - (s - p)$ and $2\tau + (s - p)$, respectively. Analogously, T_2 ($\Theta_{T_2} = 2\tau + 2s - 2h - (h - p_s)$) and smaller R_2 ($\Theta_{R_2} = \tau + 2s - 2h + (h - p_s)$) modulate S_2. The lunar and solar declinational effects are represented by the K_2 tide. Its argument is obtained by adding $2s$ to the M_2 argument or by adding $2h$ to the S_2 argument. Hence, the lunar part of K_2 is inseparable from its solar part and we may speak of the lunisolar semi-diurnal K_2 tide. K_2 is also accompanied by a series of elliptical tides although almost all are negligibly small. Two largest ones are lunar η_2 and 265.655. The latter is a part of the L_2 component and its argument differ from L_2 (265.455) by $2p$. Hence, it is usually also called L_2 (Pugh, 1987; Smith, 1999).

Table 3.3: The Darwin symbols of the most important tides and their Doodson numbers, harmonic coefficients η_k (Cartwright and Tayler, 1971; Cartwright and Edden, 1973), Doodson arguments Θ_k, additive phase corrections χ_k, frequencies, periods and origin (L stands for lunar, S for solar). Except for M_3, all tides are of the second degree origin.

Darwin symbol	Doodson number	η_k	Θ_k	χ_k [°]	Frequency [°/h]	Period	Origin
			long-period				
Z_0	055.555	0.73806	—	0	0.000000	—	L+S permanent
S_a	056.554	0.01156	$h - p_s$	0	0.041067	365.257 d	S elliptical
S_{sa}	057.555	0.07281	$2h$	0	0.082137	182.622 d	S declinational
M_{Sm}	063.655	0.01579	$s - 2h + p$	0	0.471521	31.812 d	L evectional
M_m	065.455	0.08254	$s - p$	0	0.544375	27.555 d	L elliptical
M_{Sf}	073.555	0.01369	$2s - 2h$	0	1.015896	14.765 d	L variation
M_f	075.555	0.15647	$2s$	0	1.098033	13.661 d	L declinational
M_{tm}	085.455	0.02995	$3s - p$	0	1.642408	9.133 d	L elliptical of M_f
			diurnal				
$2Q_1$	125.755	0.00954	$\tau - 3s + 2p$	−90	12.854286	28.0062 h	L second-order elliptical
σ_1	127.555	0.01151	$\tau - 3s + 2h$	−90	12.927140	27.8484 h	L variation of O_1
Q_1	135.655	0.07214	$\tau - 2s + p$	−90	13.398661	26.8684 h	L larger elliptical of O_1
ρ_1	137.455	0.01370	$\tau - 2s + 2h - p$	−90	13.471515	26.7231 h	L larger evectional
O_1	145.555	0.37690	$\tau - s$	−90	13.943036	25.8193 h	L principal declinational
τ_1	147.555	−0.00492	$\tau - s + 2h$	90	14.025173	25.6681 h	L variation of of K_1
M_1	155.655	−0.02963	$\tau + p$	90	14.496694	24.8332 h	L elliptical of K_1
χ_1	157.455	−0.00567	$\tau + 2h - p$	90	14.569548	24.7091 h	L smaller evectional
π_1	162.556	0.01028	$\tau + s - 3h + p_s$	−90	14.917865	24.1321 h	S larger elliptical of P_1
P_1	163.555	0.17546	$\tau + s - 2h$	−90	14.958931	24.0659 h	S principal declinational
S_1	164.556	−0.00416	$\tau + s - h + p_s$	90	15.000002	24.0000 h	S elliptical of K_1
K_1	165.555	−0.53009	$\tau + s$	90	15.041069	23.9345 h	L+S principal declinational

To be continued on the next page

Table 3.3: (continued)

Darwin symbol	Doodson number	η_k	Θ_k	χ_k [°]	Frequency [°/h]	Period	Origin
ψ_1	166.554	−0.00422	$\tau + s + h - p_s$	90	15.082135	23.8693 h	S elliptical of K_1
ϕ_1	167.555	−0.00755	$\tau + s + 2h$	90	15.123206	23.8045 h	S second-order
θ_1	173.655	−0.00567	$\tau + 2s - 2h + p$	90	15.512590	23.2070 h	L evectional
J_1	175.455	−0.02963	$\tau + 2s - p$	90	15.585443	23.0985 h	L elliptical of K_1
OO_1	185.555	−0.01623	$\tau + 3s$	90	16.139102	22.3061 h	L second-order
			semi-diurnal				
ϵ_2	227.655	0.00669	$2\tau - 3s + 2h + p$	0	27.423834	13.1273 h	L evectional
$2N_2$	235.755	0.02298	$2\tau - 2s + 2p$	0	27.895355	12.9054 h	L second-order elliptical
μ_2	237.555	0.02774	$2\tau - 2s + 2h$	0	27.968208	12.8718 h	L variation
N_2	245.655	0.17380	$2\tau - s + p$	0	28.439730	12.6583 h	L larger elliptical of M_2
ν_2	247.455	0.03301	$2\tau - s + 2h - p$	0	28.512583	12.6260 h	L larger evectional
M_2	255.555	0.90805	2τ	0	28.984104	12.4206 h	L principal
λ_2	263.655	−0.00669	$2\tau + s - 2h + p$	180	29.455625	12.2218 h	L smaller evectional
L_2	265.455	−0.02567	$2\tau + s - p$	180	29.528479	12.1916 h	L smaller elliptical of M_2
T_2	272.556	0.02476	$2\tau + 2s - 3h + p_s$	0	29.958933	12.0164 h	S larger elliptical of S_2
S_2	273.555	0.42248	$2\tau + 2s - 2h$	0	30.000000	12.0000 h	S principal
R_2	274.554	−0.00354	$2\tau + 2s - h - p_s$	180	30.041067	11.9836 h	S smaller elliptical of S_2
K_2	275.555	0.11495	$2\tau + 2s$	0	30.082137	11.9672 h	L+S declinational
η_2	285.455	0.00642	$2\tau + 3s - p$	0	30.626512	11.7545 h	L elliptical of K_2
			ter-diurnal				
M_3	355.555	−0.01188	3τ	180	43.476156	8.2804 h	L parallax

Finally, the M_3 tide is the most important tide of the ter-diurnal species and of the tides generated by the third degree potential V_3. Physically, it represents the fact that the Earth's radius is not negligible compared to the geocentric distance of the Moon. This is called the lunar parallax (Schureman, 1941; Pugh, 1987). It is interesting to mention that the third degree potential generates also a smaller, but not completely negligible, tide which is a part of the M_1 constituent with the frequency of exactly one mean lunar day, Doodson number 155.555 and coefficient $\eta_{155.555} = -0.00660$.

3.4 Nodal parameters

As mentioned in the previous section, Doodson divided the argument-number into two parts. While the first part determines a tidal constituent, the second part determines long-term variations. The reason is that in the harmonic analysis of a time-series (see Section 3.7.1), two harmonic signals are distinguishable only if the length of the time-series is longer than the inverse value of the frequency difference. In other words, if arguments of two harmonics differ by p, an 8.85-years long time-series is needed to separate them unambiguously. If their arguments differ by N' then as 18.6-years long time-series is needed. However, real data often do not span such long intervals which means that extracted tidal constituents are affected by the long-term variations. For example, the M_2 constituent consists of the M_2 tide, 255.555, and the harmonic 255.545 which modulates the amplitude and phase of the M_2 tide through a nodal period of 18.6 years. These long-period modulations can be represented by the so-called *nodal parameters* f_k and μ_k. Then each species of the tide-generating potential can be written as

$$V_{lm} = G_{lm}(\phi) \sum_k |\eta_k| f_k(t) \cos(\Theta_k(t) + \chi_k + m\lambda + \mu_k(t)), \tag{3.32}$$

where the summation over k is now over all constituents of the species and not all harmonics. $f_k(t)$ are called the *nodal factors* and $\mu_k(t)$ the *nodal angles*, both of them are functions of N and sometimes p.[10] Only lunar constituent are affected by the long-period modulations. For solar constituents, it holds that $f_k = 1$ and $\mu_k = 0$. Theoretically, solar constituents are affected by a 20 941-years long cycle of the solar apsidal precession (p_s) however these effects are negligible for all practical purposes.

The computation of the nodal parameters is shown in the following example for M_2. The M_2 tide 255.555 is surrounded by several nearby terms, however the only significant one is 255.545 with the argument $\Theta_{255.545} = 2\tau + N$ and amplitude $\eta_{255.545} = -0.03390$ (Cartwright and Edden, 1973). Let α be the

[10]The name "nodal parameters" might be misleading if f_k and μ_k are also functions of the longitude of the Moon's perigee p. A more precise name could be "long-period parameters" or "nodal and apsidal parameters" however "nodal parameters" is an established concept in the tidal community and the author of this thesis respects this convention.

amplitude ratio, i.e., $\alpha = \eta_{255.545}/\eta \doteq 0.037$ (where $\eta = \eta_{M_2}$). Then the total constituent can be written as (neglecting $m\lambda$ without loss of generality)

$$\begin{aligned}\eta\cos(2\tau) + \alpha\eta\cos(2\tau + N) &= \eta\left[(1 + \alpha\cos N)\cos(2\tau) - \alpha\sin(2\tau)\sin N\right] \\ &= \eta\left[f\cos\mu\cos(2\tau) - f\sin\mu\sin(2\tau)\right] \\ &= \eta f\cos(2\tau + \mu),\end{aligned} \tag{3.33}$$

where

$$f\cos\mu = 1 + \alpha\cos N, \qquad f\sin\mu = \alpha\sin N. \tag{3.34}$$

Then the nodal factor and nodal angle for M_2 are

$$f = \sqrt{1 + 2\alpha\cos N + \alpha^2}, \qquad \mu = \arctan\left(\frac{\alpha\sin N}{1 + \alpha\cos N}\right). \tag{3.35}$$

These formulae can be easily generalized for any lunar constituent which is modulated by J harmonics with the amplitude ratios α_j and argument differences β_j as

$$f_k = \sqrt{\left(1 + \sum_{j=1}^{J}\alpha_j\cos\beta_j\right)^2 + \left(\sum_{j=1}^{J}\alpha_j\sin\beta_j\right)^2}, \tag{3.36}$$

$$\mu_k = \arctan\left(\frac{\sum_{j=1}^{J}\alpha_j\sin\beta_j}{1 + \sum_{j=1}^{J}\alpha_j\cos\beta_j}\right). \tag{3.37}$$

The factors α_j and β_j for the major lunar constituents are given in Table 3.4. α_j are computed from tables in Cartwright and Edden (1973). Only stronger harmonics are listed; those whose coefficient η is larger than 0.00100, other terms are neglected.

The last two columns of Table 3.4 show approximative formulae for f_k and μ_k. These or similar ones can be found in many publications (e.g., Pugh, 1987; IHO, 2006) and are easy to derive by using Taylor series and neglecting small terms, usually those which are $O(\alpha_j^2)$. For example, let us return to the example for M_2 and assume that α^2 is negligible. Then

$$f = \sqrt{1 + 2\alpha\cos N + O(\alpha^2)} = 1 + \alpha\cos N + O(\alpha^2) \approx 1 - 0.037\cos N, \tag{3.38}$$

$$\mu = \frac{\alpha\sin N}{1 + \alpha\cos N} + O(\alpha^3) = \alpha\sin N + O(\alpha^2) \approx -2^\circ\!.1\sin N. \tag{3.39}$$

The formulae for other constituents can be obtained in a similar way. Although these formulae are only an approximation, they are a useful indicator how large the nodal variations may be. It can be seen that the tides representing the changes of the lunar declination (i.e., M_f, all diurnal tides and K_2) have the largest variations of amplitudes (more than 11 %) as well as angles (8°.9 and more). On the other hand, semi-diurnal μ_2, N_2, ν_2 and M_2 are only slightly affected by the nodal cycle with amplitudes varying by 3.7 % and angles by 2°.1.

Table 3.4: Nodal corrections for major tidal constituents. The tidal constituents are denoted by their symbols and Doodson numbers of the main tidal harmonics. Long-period variations are denoted by the last three digits of their Doodson numbers. The factors α_j and β_j are used for the computation of the nodal parameters (equations (3.36) and (3.37)). The approximative formulae for f_k and μ_k are also listed.

					Approximative formulae	
	Tide	Variation	α_j	β_j	f_k	μ_k
M_m	065.455	445	-0.066	N	$1.000 - 0.131 \cos N$	$-3^\circ.1 \sin p$
		465	-0.065	$-N$		
		655	-0.053	p		
		665	-0.002	$p - N$		
M_f	075.555	355	0.043	$-2p$	$1.086 + 0.414 \cos N$	$-23^\circ.7 \sin N$
		565	0.414	$-N$		
		575	0.039	$-2N$		
$2Q_1$	125.755	745	0.188	N	$1.018 + 0.188 \cos N$	$10^\circ.8 \sin N$
σ_1	127.555	545	0.188	N	$1.018 + 0.188 \cos N$	$10^\circ.8 \sin N$
Q_1	135.655	645	0.188	N	$1.018 + 0.188 \cos N$	$10^\circ.8 \sin N$
ρ_1	137.455	445	0.188	N	$1.018 + 0.188 \cos N$	$10^\circ.8 \sin N$
O_1	145.555	535	-0.006	$2N$	$1.018 + 0.189 \cos N$	$10^\circ.8 \sin N$
		545	0.189	N		
		755	-0.006	$2p$		
M_1	155.655	445	0.066	$-2p + N$		
		455	0.360	$-2p$		
		665	0.200	$-N$		
K_1	165.555	545	-0.020	N	$1.009 + 0.116 \cos N$	$-8^\circ.9 \sin N$
		565	0.136	$-N$		
		575	-0.003	$-2N$		
J_1	175.455	465	0.198	$-N$	$1.020 + 0.198 \cos N$	$-11^\circ.3 \sin N$
OO_1	185.555	355	0.150	$-2p$	$1.205 + 0.640 \cos N$	$-36^\circ.7 \sin N$
		565	0.640	$-N$		
		575	0.134	$-2N$		
μ_2	237.555	545	-0.037	N	$1.000 - 0.037 \cos N$	$-2^\circ.1 \sin N$
N_2	245.655	645	-0.037	N	$1.000 - 0.037 \cos N$	$-2^\circ.1 \sin N$
ν_2	247.455	445	-0.037	N	$1.000 - 0.037 \cos N$	$-2^\circ.1 \sin N$
M_2	255.555	545	-0.037	N	$1.000 - 0.037 \cos N$	$-2^\circ.1 \sin N$
L_2	265.455	655	-0.250	$2p$		
		665	-0.110	$2p - N$		
K_2	275.555	545	-0.013	N	$1.044 + 0.285 \cos N$	$-17^\circ.8 \sin N$
		565	0.298	$-N$		
		575	0.032	$-2N$		

The M_1 and L_2 constituents are more complicated and simple approximative formulae can not be obtained. Therefore, the exact formulae for f_k (3.36) and μ_k (3.37) are always used for M_1 and L_2.

It should be noted that equations (3.36) and (3.37) are valid only for the tides of the second degree origin. There are tidal constituents which have also a third degree contribution (e.g., M_1) however there is no way how to include the third degree contribution into the nodal parameters because of the different geodetic functions for degrees 2 and 3 (see equations (3.14)–(3.20)).

3.5 Development of the potential according to CTE

Doodson's harmonic expansion was the most thorough and precise development of the tide-generating potential for many years. The first independent recalculation of the potential after Doodson was provided by Cartwright and Tayler (1971); Cartwright and Edden (1973), hereinafter CTE. CTE were motivated by a new method of analysing tidal data, the so-called response method which was introduced a few years ago (Munk and Cartwright, 1966; see also Section 3.7.2), and used a different approach than Doodson. CTE computed the potential directly from the lunar and solar ephemerides (i.e., the lunar and solar declinations, right-ascensions and geocentric distances) in contrary to Doodson who used a massive algebraic expansion of Brown's series. CTE formulate the tide-generating potential as

$$V = Re\left[g\sum_{l=2}^{\infty}\sum_{m=0}^{l} c_{lm}^{*}(t)W_{lm}(\lambda,\phi)\right], \tag{3.40}$$

where g is the mean gravity acceleration on the Earth's surface, $W_{lm}(\lambda,\phi)$ are complex spherical harmonics

$$W_{lm}(\lambda,\phi) = N_{lm}P_{lm}(\cos\phi)e^{im\lambda} \tag{3.41}$$

with the normalization factor

$$N_{lm} = \sqrt{\frac{2l+1}{4\pi}\frac{(l-m)!}{(l+m)!}}, \tag{3.42}$$

and $c_{lm}^{*}(t)$ denotes the complex conjugated equilibrium tide of degree l and order m. The equilibrium tides represent ocean tides in meters which would occur if the whole Earth was covered by the water only. The nodal parameters are implicitly included in $c_{lm}^{*}(t)$. The equilibrium tides can be expressed in the form of series

$$c_{lm}^{*}(t) = (-1)^{q_{lm}}\sum_{k}|C_k(t)|e^{i(\Theta_k(t)+\chi_k)}, \tag{3.43}$$

where $C_k(t)$ are the equilibrium amplitudes which are tabulated in CTE and the term $(-1)^{q_{lm}}$, $q_{2m} = m + \delta_{0m}$ and $q_{3m} = m + \delta_{0m} + \delta_{1m}$, is introduced to

Table 3.5: Ratios of the equilibrium amplitudes of CTE's expansion $|C_k|$ to those according to Doodson's development $|\eta_k|\frac{G}{g}$ for $l = 2, 3$. The ratios are defined by equation (3.45).

degree l	order m	ratio
2	0	1.58533
2	1	2.58883
2	2	2.58883
3	0	2.99598
3	1	2.24698
3	2	2.54219
3	3	2.39680

obtain series with all positive $|C_k|$ and cosine arguments in order to achieve a consistency with the Doodson's expansion (3.13). The coefficients $C_k(t)$ vary slowly in time since CTE calculated them from highly precise ephemerides. This means that all secular trends were included in the computations in contrary to Doodson who ignored them and his coefficients η_k are therefore constant. The most important effect is a decrease in the obliquity of the ecliptic (the angle between the ecliptic and equatorial plane) due to planetary perturbations which is about $47''$ per century and leads to a trend of about 0.01 % a century in magnitudes of C_k (Smith, 1999).

Apart from the fact that the coefficients of CTE are time variable while those of Doodson are constant, both approaches are equal except for a different normalization of the coefficients. By the comparison of (3.13) and (3.40) we get

$$G_{lm}(\phi)|\eta_k|e^{i(\Theta_k(t)+\chi_k)}e^{im\lambda} = g(-1)^{q_{lm}}|C_k|e^{i(\Theta_k(t)+\chi_k)}N_{lm}P_{lm}(\cos\phi)e^{im\lambda}, \quad (3.44)$$

which leads to

$$\frac{|C_k|}{|\eta_k|\frac{G}{g}} = (-1)^{q_{lm}}\frac{G_{lm}(\phi)}{GN_{lm}P_{lm}(\cos\phi)}. \quad (3.45)$$

The ratios $|C_k| : |\eta_k|\frac{G}{g}$ for degrees $l = 2, 3$ are listed in Table 3.5.

3.6 Radiational and compound tides

In addition to the tidal constituents which are obtained by the development of the tide-generating potential, there are other harmonic signals in the ocean which are classified as tides but are not a direct consequence of the gravitational force of the Moon and Sun. These are the *meteorological* or *radiational* tides, which are due to meteorological effects, and the *compound* or *shallow-water* tides, which are generated by ocean dynamics.

The meteorological tides may be caused by changes in air temperature, barometric pressure or sea breezes. These changes induce fluctuations in the ocean surface elevation which are in general very irregular but there are some

seasonal or daily variations that have a periodical character. These tides are also called radiational (Munk and Cartwright, 1966) as they are related to the cycles in direct solar radiation. The term "radiational tide" seems to be, to the author's best knowledge, more common and established today while "meteorological tide" can be found in older publications (e.g., Schureman, 1941). The solar annual S_a and semi-annual S_{sa} tides are a good example of the radiational tides as they are strongly enhanced by seasonal climate variations while their gravitational forcing is very weak (Pugh, 1987). For this reason, S_a usually refers to the signal with the period of exactly one mean solar year and $-p_s$ in the argument of the gravitational S_a (see Table 3.3) is omitted in tidal analysis. Of course, the frequency difference due to $-p_s$ is negligible however the omission of $-p_s$ is important for a correct definition of the phase shift. Another, very interesting example of the radiational tides is S_1. The ocean tides generated by the solar gravitational potential at the S_1 frequency should be very weak, not exceeding 3 mm (Schindelegger et al., 2016) but the observed tides are higher and may have amplitudes of a few centimeters in extreme causes (Pugh, 1987; Ray and Egbert, 2004; Lyard et al., 2006). This S_1 tide is an ocean response to the atmospheric pressure tides which are generated by the thermal excitation in the upper atmosphere due to solar radiation (Ray and Egbert, 2004; Lyard et al., 2006). Similarly to S_a, S_1 usually refers to the signal with the period of exactly one mean solar day and p_s in the argument of the gravitational S_1 is omitted in tidal analysis. Doodson (1928) and Schureman (1941) employed the phase convention $\chi_{S_1} = 180^\circ$ however there are other phase conventions which are routinely in use (see Ray and Egbert, 2004) so one must be careful when using published S_1 data. The S_2 constituent has also a significant radiational contribution in addition to the astronomical contribution but radiational contributions to other solar constituents (e.g. K_1) are considered to be negligible (Lyard et al., 2006).

The compound tides are generated by non-linear physical processes in the ocean. They are significant mainly in shallow seas, therefore they are also called the shallow-water tides.[11] Tidal waves in the oceans interact with each other which leads to a creation of additional harmonic signals whose frequencies are multiples, sums or differences of the frequencies of the astronomical constituents listed in Table 3.3. For example, let the M_2 wave with the frequency ω_{M_2} interacts with the S_2 wave with the frequency ω_{S_2}. Then, due to non-linearities of ocean dynamics, additional waves are produced and their frequencies are $\omega_{M_2} + \omega_{S_2}$, $\omega_{S_2} - \omega_{M_2}$, $\omega_{M_2} + \omega_{M_2}$, $\omega_{S_2} + \omega_{S_2}$, $\omega_{M_2} + \omega_{M_2} + \omega_{S_2}$, etc. In principle, all combinations of the astronomical tidal constituents are possible, however, only those tides which are composed from the strongest constituents are important for practical purposes. Table 3.6 lists some of the most important compound tides. Their symbols are determined by their origins. A sequence of letters corresponds to a sum of constituents, e.g., $M_2 + S_2 = MS_4$. However, if there is a difference in a combination of constituents,

[11] The author prefers "compound tides" since "shallow-water tides" may suggest that they occur in shallow seas only which is generally not true.

Table 3.6: Selected compound tides. Listed are their symbols, origins, Doodson number, frequencies, periods and global maximal amplitudes from a simulation of the DEBOT-h model (Chapter 4). If there is a tide which has the lunisolar origin (from Table 3.3) and same frequency as one of the compound tides then its symbol is printed in the last column (LS denote lunisolar).

Symbol	Origin	Doodson number	Frequency [°/h]	Period [h]	Amplitude [cm]	LS tide
			long-period			
SM_f	$S_2 - M_2$	073.555	1.015896	354.367	13.73	M_{Sf}
			diurnal			
$2OK_1$	$2 \times O_1 - K_1$	125.755	12.854286	28.0062	5.11	$2Q_1$
MP_1	$M_2 - P_1$	147.555	14.025173	25.6681	12.08	τ_1
$2KP_1$	$2 \times K_1 - P_1$	162.556	14.917865	24.1321	5.06	ϕ_1
SO_1	$S_2 - O_1$	183.555	16.056964	22.4202	10.17	
$2KO_1$	$2 \times K_1 - O_1$	185.555	16.139102	22.3061	14.43	OO_1
			semi-diurnal			
MNS_2	$M_2 + N_2 - S_2$	227.655	27.423834	13.1273	5.34	ϵ_2
$2NM_2$	$2 \times N_2 - M_2$	235.755	27.895355	12.9054	8.31	$2N_2$
$2MS_2$	$2 \times M_2 - S_2$	237.555	27.968208	12.8718	22.71	μ_2
SNM_2	$S_2 + N_2 - M_2$	263.655	29.455625	12.2218	8.96	λ_2
$2MN_2$	$2 \times M_2 - N_2$	265.455	29.528479	12.1916	21.22	L_2
$2SM_2$	$2 \times S_2 - M_2$	291.555	31.015896	11.6070	8.43	
			ter-diurnal			
MO_3	$M_2 + O_1$	345.555	42.927140	8.3863	12.22	
MK_3	$M_2 + K_1$	365.555	44.025173	8.1771	11.94	
			fourth-diurnal			
MN_4	$M_2 + N_4$	445.655	57.423834	6.2692	10.22	
M_4	$2 \times M_2$	455.555	57.968208	6.2103	29.55	
MS_4	$M_2 + S_2$	473.555	58.984104	6.1033	17.29	
MK_4	$M_2 + K_2$	475.555	59.066242	6.0949	6.97	
			sixth-diurnal			
$2MN_6$	$2 \times M_2 + N_2$	645.655	86.407938	4.1663	8.94	
M_6	$3 \times M_2$	655.555	86.952313	4.1402	17.30	
$2MS_6$	$2 \times M_2 + S_2$	673.555	87.968208	4.0924	14.35	
			eighth-diurnal			
M_8	$4 \times M_2$	855.555	115.936417	3.1052	2.21	

then it is indicated by the subscript number and the letter of the tide with negative sign is placed to the right, e.g., $M_2 + N_2 + S_2 = MNS_6$ but $M_2 + N_2 - S_2 = MNS_2$. The nodal parameters of the compound tides are assumed to follow the parameters of the generating constituents. It holds that the nodal factor f_k is always obtained by a multiplication of the nodal factors of the generating constituents while the nodal angle μ_k is obtained by the same combination as the frequency. For example (note that for solar constituents $f = 1$ and $\mu = 0$):

$$\begin{aligned} f_{M_4} &= f_{M_2}^2, & \mu_{M_4} &= 2\mu_{M_2}, \\ f_{MO_3} &= f_{M_2} f_{O_1}, & \mu_{MO_3} &= \mu_{M_2} + \mu_{O_1}, \\ f_{2KO_1} &= f_{K_1}^2 f_{O_1}, & \mu_{2KO_1} &= 2\mu_{K_1} - \mu_{O_1}, \\ f_{MS_4} &= f_{M_2}, & \mu_{MS_4} &= \mu_{M_2}. \end{aligned}$$

Some of the compound tides may reach amplitudes of several decimeters, see the penultimate column of Table 3.6 which shows global maximal amplitudes from a simulation of the DEBOT-h model (Chapter 4). For comparison, the global maximal amplitude of M_2 from the same simulation is 419 cm. Note also that there are compound tides which have the exactly same frequencies as some of the lunisolar tides from Table 3.3. Of course in such case, the nonlinear and gravitational contributions to the tidal wave are indistinguishable.

In some lists of tides or tide gauge data, one can find the terms which are denoted as MA_2 (254.555) and MB_2 (256.555). Their arguments are $2\tau - h$ and $2\tau + h$, respectively, and thus represent an annual modulation of the M_2 tide. Their names suggest they are compound tides however there is no tidal term denoted as A or B. Here, the letter A is intended to signify **a**nnual differences. Theoretically, they may be thought as interactions between M_2 and S_a however their physical origin is more likely due to seasonal changes in the weather and their interaction with the tides (Pugh, 1987). In general, every tide may be accompanied by seasonal variations however in almost all cases, the annual terms are negligible. IHO (2006) lists also NA_2 and NB_2 apart from MA_2 and MB_2.

3.7 Methods of tidal analysis

There are two basic methods how to determine tidal signals from satellite altimetry data or tide gauge measurements, the harmonic analysis and the response method. Both of them are briefly introduced in Sections 3.7.1 and 3.7.2, respectively. The kind reader is referred to the cited literature (Munk and Cartwright, 1966; Pugh, 1987; Emery and Thompson, 1998; Smith, 1999; Parker, 2007; Fok, 2012) for more details. No effort is made to describe methods of processing raw altimetry data since this is beyond the scope of this thesis.

3.7.1 Harmonic analysis

The harmonic analysis is a standard method to determine tides from measurements. It was first formulated by William Thompson (Lord Kelvin) in 1867 and William Ferrel independently in 1874 (Parker, 2007). The harmonic analysis is based on the idea that a time-series of the sea surface elevation ζ at the location (ϕ,λ) can be expressed as a sum of harmonic signals (Emery and Thompson, 1998)

$$\zeta(\phi,\lambda,t) = \sum_k f_k(t) H_k(\phi,\lambda) \cos(\Theta_k(t) + \chi_k + \mu_k(t) - G_k(\phi,\lambda)) + \zeta_r(t), \quad (3.46)$$

where the summation is over tidal constituents, H_k and G_k are the unknown amplitudes and Greenwich phase lags (expressed in interval $\langle 0°,360° \rangle$) of the tidal constituents, respectively. ζ_r is a residual time series containing all non-tidal signals. The Doodson arguments at Greenwich Θ_k and additive phase corrections χ_k were already introduced in Section 3.3. The nodal factors f_k and nodal angles μ_k were discussed in Section 3.4.

Equation (3.46) can be rewritten as

$$\begin{aligned}\zeta(\phi,\lambda,t) = \sum_k [&f_k(t) A_k(\phi,\lambda) \cos(\Theta_k(t) + \chi_k + \mu_k(t)) + \\ &f_k(t) B_k(\phi,\lambda) \sin(\Theta_k(t) + \chi_k + \mu_k(t))] + \zeta_r(t), \end{aligned} \quad (3.47)$$

where A_k and B_k are the in-phase and quadrature amplitudes, respectively. They are related to the amplitudes H_k and Greenwich phase lags G_k through

$$H_k = \sqrt{A_k^2 + B_k^2}, \qquad G_k = \arctan\left(\frac{B_k}{A_k}\right). \quad (3.48)$$

The formulation (3.47) has two advantages over (3.46): its linear form enables a convenient least-square estimate of A_k and B_k and singularities at the points of zero amplitude of any tidal constituents (the so-called "amphidromic points") are avoided. To unambiguously distinguish two tidal constituents of distinct frequencies, ω_1 and ω_2, the Rayleigh criterion must be fulfilled (Pugh, 1987; Emery and Thompson, 1998). It states that

$$T > \frac{1}{|\omega_1 - \omega_2|}, \quad (3.49)$$

where T is the length of the time-series.

3.7.2 Response method

Although the harmonic analysis is simple and convenient, its ability to resolve tidal signals with frequencies very close to each other is limited to a lenght of time-series. Hence, Walter Munk and David Cartwright proposed in 1966 the so-called response method (Munk and Cartwright, 1966). The idea

of the method, which has its origin in electrical engineering, is that the equilibrium tide $c^*_{2m}(t)$ (input) is related to the ocean tidal elevation $\zeta(\lambda,\phi,t)$ (output) through the response weight function $w_{2m}(\lambda,\phi,t)$ (system) under the assumption of the credo of smoothness. The credo of smoothness states that sharp resonance peaks does not occur for the ocean responses to the gravitational forcing. In simple terms, the ocean elevation is "sufficiently smooth". The ocean elevation is expressed as a convolution of the equilibrium tides and the response weight function (here, our attention is restricted on $l = 2$ only)

$$\zeta(\lambda,\phi,t) = Re\left[\sum_{m=0}^{2} c^*_{2m}(t) * w_{2m}(\lambda,\phi,t)\right]. \tag{3.50}$$

This formulation supposes a linear system, therefore it is not suitable for shallow seas where the non-linear compound tides gain importance. However, it can be extended to non-linear equations which also describe also the compound tides (Munk and Cartwright, 1966; Pugh, 1987). This non-linear extension is not discussed here.

The equilibrium tide $c^*_{2m}(t)$ was introduced in Section 3.5. The response weight function $w_{2m}(\lambda,\phi,t)$ is defined for each tidal band m as

$$w_{2m}(\lambda,\phi,t) = \sum_{s=-S}^{S} w_{2ms}(\lambda,\phi)\delta(t - s\Delta T), \tag{3.51}$$

where $\delta(t)$ is the unit impulse function, ΔT the time lag interval, usually equal to two days (Fok, 2012) and $w_{2ms}(\lambda,\phi)$ are the response weights. The number of the response weights (S) is usually 1 or 2 (Fok, 2012). The response weights are obtained from data by a least-square method. They represent the remaining effect at time t of the ocean's response to a unit impulse at time $t - s\Delta T$ (Munk and Cartwright, 1966; Smith, 1999). It means that the ocean tide can be expressed as a weighted sum of past and future values of the equilibrium tides. This can be seen by substituting (3.51) in (3.50) which yields

$$\zeta(\lambda,\phi,t) = Re\left[\sum_{m=0}^{2}\sum_{s=-S}^{S} w_{2ms}(\lambda,\phi)c^*_{2m}(t - s\Delta T)\right]. \tag{3.52}$$

Note that the future values of the equilibrium tide (negative s) are not physically justified and they are just a mathematical concept. Since the nodal parameters are implicitly contained in the equilibrium tide c^*_{2m}, no nodal corrections are applied in the response method.

The Fourier transform of the response weight function is called the tidal admittance $Z_{2m}(\omega_k)$ (Munk and Cartwright, 1966)

$$Z_{2m}(\omega_k) = X_{2m}(\omega_k) + iY_{2m}(\omega_k) = \int_{-\infty}^{\infty} w_{2m}(t)e^{-i\omega_k t}\,\mathrm{d}t. \tag{3.53}$$

Substituting (3.51) in (3.53), the relations for the real and imaginary parts of

the tidal admittance are obtained

$$X_{2m}(\omega_k) = \sum_{s=-S}^{S} \left[u_{2ms} \cos(\omega_k s \Delta T) + v_{2ms} \sin(\omega_k s \Delta T) \right], \tag{3.54}$$

$$Y_{2m}(\omega_k) = \sum_{s=-S}^{S} \left[v_{2ms} \cos(\omega_k s \Delta T) - u_{2ms} \sin(\omega_k s \Delta T) \right], \tag{3.55}$$

where u_{2ms} and v_{2ms} are the real and imaginary parts of the response weight w_{2ms}, i.e., $w_{2ms} = u_{2ms} + iv_{2ms}$. The tidal admittance is related to the harmonic coefficients A_k and B_k through

$$A_k = (-1)^{m+\delta_{0m}} |C_k| X_{2m}(\omega_k), \tag{3.56}$$

$$B_k = (-1)^{m+\delta_{0m}+1} |C_k| Y_{2m}(\omega_k), \tag{3.57}$$

where the equilibrium amplitude $|C_k|$ was already defined in Section 3.5.

CHAPTER

4

DEBOT-H: A PURELY HYDRODYNAMICAL MODEL

By purely hydrodynamical models we consider those tidal models whose solution is not constrained by any measurements of sea level, whether satellite altimetry or tide gauges data. Therefore, the model solution is given by equations of fluid motion, usually the shallow-water equation. DEBOT-h is such a model and this chapter is dedicated to it. Parameters of DEBOT-h are described in Section 4.1. Testing tide gauge data and statistical methods to assess accuracy of DEBOT are described in Section 4.2. Section 4.3 and 4.4 show results of DEBOT-h, their dependency on model parameters and compares DEBOT-h with other purely hydrodynamical models. Finally, Section 4.5 discusses energy and dissipation properties of DEBOT-h.

4.1 Description of DEBOT

DEBOT is based on the shallow water equations (see the derivation in Chapter 1 and numerical methods in Chapter 2)

$$\frac{\partial \zeta}{\partial t} + \nabla_\Omega \cdot (h\vec{v}) = 0, \tag{4.1}$$

$$\frac{\partial (h\vec{v})}{\partial t} + \nabla_\Omega \cdot (h\vec{v} \otimes \vec{v}) = -g_e h \nabla_\Omega \zeta + f h\vec{v} \times \vec{e}_z - \vec{\tau}_{BF} + A_H \nabla_\Omega \cdot \boldsymbol{\sigma} - \vec{\tau}_{ITD} + \vec{T}. \tag{4.2}$$

An attentive reader notices differences between equations (4.2) and (1.73) from the end of Chapter 1. First, the gravitational constant g is replaced by the

"reduced gravity" g_ϵ due to a parametrization of the self-attraction and loading of the water. Second, the internal tide drag $\vec{\tau}_{ITD}$, an additional dissipative term, is added. Third, equation (4.2) contains the tidal forcing $\vec{T}$ which was described in Section 3.2. The bottom friction $\vec{\tau}_{BF}$ and eddy viscosity $A_H \nabla_\Omega \cdot \boldsymbol{\sigma}$ were discussed in Chapter 1.

The self-attraction and loading (SAL) of the water is an essential part of ocean tide modelling since its omission can change computed tidal amplitudes by 10 % or more and phases by 30° or more (Ray, 1998). The effect of SAL can be included as an additional forcing $gh\nabla_\Omega \zeta_{\mathrm{SAL}}$ where ζ_{SAL} is the equilibrium-like tide which is related to the surface elevation ζ through convolution with the SAL Green's function $\mathcal{G}_{\mathrm{SAL}}$ (e.g., Ray, 1998; Egbert et al., 2004)

$$\zeta_{SAL} = \mathcal{G}_{\mathrm{SAL}} * \zeta. \tag{4.3}$$

It is possible to use this convolution formula to compute the full SAL effect, however it would require to solve an integro-differential equation iteratively in every time step which would be computationally impractical. Hence, an alternative approach may be applied. In our model, we adopt a simple scalar approximation of the SAL, proposed by Accad and Pekeris (1978)

$$\zeta_{\mathrm{SAL}} = \epsilon\zeta, \tag{4.4}$$

where ϵ is the scalar factor or SAL coefficient. This eventually leads to a replacement of the gravitational constant g by the "reduced gravity" $g_\epsilon = (1-\epsilon)g$ in equation (4.2). Values of the scaling factor ϵ varies in the literature between 0.08 and 0.12 (Accad and Pekeris, 1978; Parke, 1982; Ray, 1998; Egbert et al., 2004). We are aware that this approximation is crude and none of constant value of ϵ is appropriate for all times and all locations in the ocean (Ray, 1998), however relatively good results can be achieved with the scalar approximation as we will show later. Accad and Pekeris (1978) also proposed an iteration scheme to compute ζ_{SAL} which was implemented in DEBOT and tested, however a combination with a time-stepping scheme used in DEBOT produces unrealistic results. Therefore, the scalar approximation is implemented in DEBOT.

Energy conversion of barotropic tidal currents into baroclinic (internal) waves is accounted for by the internal tide drag (ITD) which is formulated as the vector $\vec{\tau}_{ITD} = \boldsymbol{C}_{ITD} \cdot \vec{v}$, where $\boldsymbol{C}_{ITD}$ is the internal drag tensor (Green and Nycander, 2013). Several formulations of $\boldsymbol{C}_{ITD}$ have been proposed, e.g., Jayne and St. Laurent (2001); Nycander (2005); Zaron and Egbert (2006), see also Green and Nycander (2013) for a comparison. In DEBOT, a scheme by Jayne and St. Laurent (2001) is implemented, mainly because it is independent on the tidal frequency in contrary to the other formulations. The tensor $\boldsymbol{C}_{ITD}$ is then reduced to a scalar coefficient C_{ITD}

$$C_{ITD} = \kappa \frac{\pi}{L} \hat{h}^2 N_b, \tag{4.5}$$

where $\hat{h}$ is the bottom roughness, which is estimated by a standard deviation of bathymetric data, N_b is the observed buoyancy frequency at the seabed and

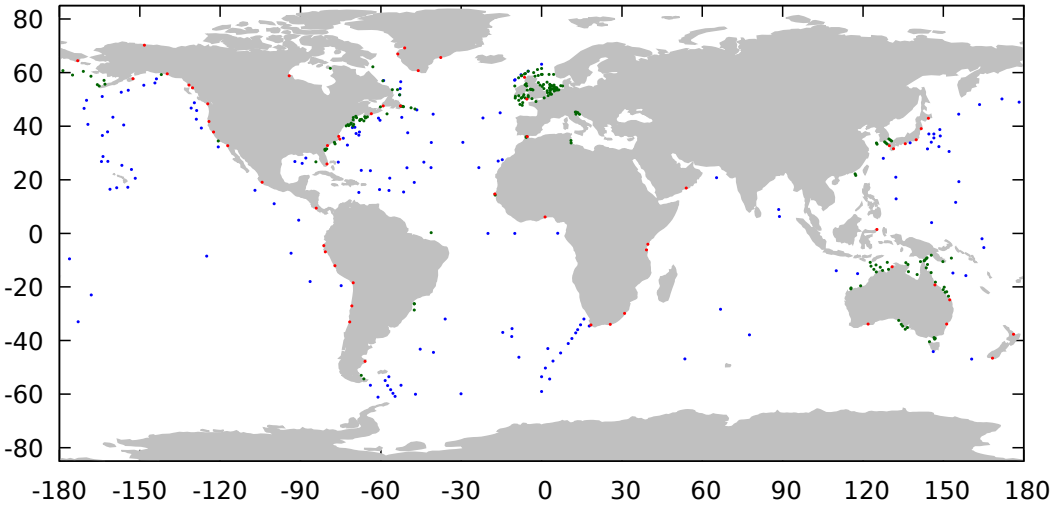

Figure 4.1: Locations of the deep ocean (blue), shelf (green) and coastal (red) tidal station used for the comparisons in this study.

L is a wave or topography length scale which is a tunable parameter. In this study, for practical reasons, we keep $L = 10\,000$ m as suggested by Jayne and St. Laurent (2001); Green and Nycander (2013) and introduce an independent tunable factor κ which is of the order $\mathcal{O}(1)$. The observed buoyancy frequencies were computed from the temperature and salinity datasets of the World Ocean Atlas 2013 (Locarnini et al., 2013; Zweng et al., 2013).

4.2 Testing data and methods of comparison

DEBOT outputs are compared to "ground truth" tidal data. In this paper, we present comparisons with data from deep-ocean bottom pressure recorders, shelf seas tidal stations and tide gauges along coastlines. Locations of all tidal stations are shown in Figure 4.1. The same datasets were used in a recent comparison of state-of-the-art global barotropic ocean tide models by Stammer et al. (2014).

The deep ocean data consists of harmonic constants derived from 151 bottom pressure recorder (BPR) stations. The data were compiled and described in detail by Ray (2013). Bottom pressure data provide the best information for an assessment of barotropic tide models in the deep, open ocean since other type of measurements, like island-tide gauge data are influenced by undesirable effects such as internal tides, or local tide effects.

The test data for shelf seas consist of harmonic constants from 194 stations located in shallow waters (less than 200 m) but not along continental coastlines. The great majority of the stations are BPR on shelves, however, some

tide gauges at small offshore islands are included, especially near Australia. Tide gauges at continental coasts are avoided. A core of the shallow water data is the dataset compiled and used by Ray et al. (2011), however other stations were added: from the Patagonian Shelf off Tierra del Fuego (Richter et al., 2012), the Gulf of Gabes (Sammari et al., 2006), or South China Sea (Beardsley et al., 2004), and also some unpublished data were added, e.g., data from the Savu Sea (Stammer et al., 2014). As evident from Figure 4.1, a substantial portion of the shallow water stations is located on the northwest European Shelf, 76 stations from 194. Hence, to avoid overweighting by one geographical region in global statistics, all statistical evaluations in this study will be made separately for the NW European Shelf and for the remaining stations around the globe, unless otherwise specified.

Finally, the coastal data consist of a set of harmonic constants from 56 tide gauges located along continental coastlines or nearby islands, such as the station at Zanzibar. This is a subset of data published by Ponchaut et al. (2001) after removing tide gauges at open ocean islands. It should be note that 56 tide gauges are not enough for a global assessment and moreover, some of station locations are deemed to be land by DEBOT. Though these stations are excluded from the comparisons, this dataset may still bring some useful information about the model.

The testing data are in a form of harmonic constants of selected tidal constituents, i.e., their amplitudes and Greenwich phase lags, whilst DEBOT is a time-domain model with full lunisolar tidal forcing and thus all tidal constituents are a priori included. Therefore, harmonic constants need to be extracted from real-time simulations by a harmonic analysis (see Section 3.7.1). The DEBOT simulations run for 401 days. Such long time-series enable the amplitudes and phase lags of all relevant tidal constituents to be deduced. 267 tidal constituents are selected from the tables in IHO (2006) so that the Rayleigh criterion (3.49) is satisfied. Their in-phase and quadrature amplitudes are then computed by the least square method. Of the 267 constituents, 23 are used for the comparison in this thesis. They are listed in Table 4.1.

For each testing stations and for every tide from Table 4.1, the tidal signals, the root mean squares (RMS) differences and the relative RMS differences are computed. The signal is defined by

$$\text{Signal}_k = \sqrt{\overline{H_{\text{sta},k}^2}/2}, \tag{4.6}$$

where the overbar denotes an average over all stations and $H_{\text{sta},k}$ is the amplitude of the kth tide at a station. The RMS difference and the relative RMS difference are defined by

$$\text{RMS}_k = \sqrt{\overline{\left(H_{\text{sta},k}\cos(\omega_k t - G_{\text{sta},k}) - H_{\text{mod},k}\cos(\omega_k t - G_{\text{mod},k})\right)^2}}, \tag{4.7}$$

$$\text{Relative RMS}_k = \frac{\text{RMS}_k}{\text{Signal}_k}, \tag{4.8}$$

where the overbar denotes an average over all stations and over one full cycle of the constituent, i.e., $\omega_k t$ varies from 0 to 2π, $G_{\text{sta},k}$ is the Greenwich phase lag

Table 4.1: 23 selected tidal constituents used for the comparison of the DEBOT model with the tide gauge data. Listed are their signals in the deep ocean (DO), on the northwest European Shelf (ES), in shallow waters elsewhere (SE) and along coastlines (C), number of stations where the tide is determined, periods in hours and origins ("M" denotes the Moon, "S" denotes the Sun). The tides in bold are the major tidal constituents used for the comparison in this chapter and Chapter 5. The other tides are the minor tidal constituents which are discussed in Chapter 6.

	Signal [cm]				Number of stations				Period [h]	
Tide	DO	ES	SE	C	DO	ES	SE	C		Origin
$2Q_1$	0.25	0.36	0.44	0.34	121	3	4	56	28.006	M
σ_1	0.29	0.43	0.41	—	119	3	3	—	27.848	M
$\boldsymbol{Q_1}$	**1.79**	**2.14**	**2.69**	**2.21**	**148**	**76**	**74**	**56**	**26.868**	**M**
ρ_1	0.35	0.27	0.51	—	117	1	3	—	26.723	M
$\boldsymbol{O_1}$	**8.75**	**5.59**	**10.91**	**11.30**	**151**	**76**	**118**	**56**	**25.819**	**M**
$\boldsymbol{P_1}$	**3.99**	**1.50**	**5.91**	**5.73**	**146**	**27**	**82**	**56**	**24.066**	**S**
$\boldsymbol{K_1}$	**12.51**	**5.51**	**17.07**	**18.47**	**151**	**76**	**118**	**56**	**23.934**	**M + S**
J_1	0.71	0.92	0.85	1.09	125	51	12	56	23.098	M
OO_1	0.43	0.93	0.50	0.67	124	51	12	56	22.306	M
$2N_2$	0.80	6.02	1.70	1.73	123	2	24	56	12.905	M
μ_2	0.95	4.44	2.44	—	123	27	52	—	12.872	M
$\boldsymbol{N_2}$	**6.36**	**17.02**	**12.54**	**13.57**	**151**	**76**	**113**	**56**	**12.658**	**M**
ν_2	1.13	3.24	2.18	—	121	26	19	—	12.626	M
$\boldsymbol{M_2}$	**30.22**	**87.74**	**53.95**	**65.38**	**151**	**76**	**118**	**56**	**12.421**	**M**
L_2	0.75	4.57	3.13	—	124	59	41	—	12.192	M
T_2	0.63	1.99	1.69	—	118	11	21	—	12.016	S
$\boldsymbol{S_2}$	**11.21**	**29.96**	**21.72**	**23.93**	**151**	**76**	**118**	**56**	**12.000**	**S**
R_2	0.12	0.85	0.59	—	116	3	2	—	11.984	S
$\boldsymbol{K_2}$	**3.12**	**7.30**	**7.09**	**6.68**	**146**	**28**	**81**	**56**	**11.967**	**M + S**
M_3	0.23	0.92	1.18	0.68	130	67	15	56	8.280	M
MN_4	0.09	1.76	1.45	0.77	120	75	14	56	6.269	$M_2 + N_2$
M_4	0.22	4.68	1.82	2.03	130	76	63	56	6.210	$2 \times M_2$
MS_4	0.12	2.91	1.49	1.42	121	75	44	56	6.103	$M_2 + S_2$

of the kth tide at a station and $H_{\mathrm{mod},k}$ and $G_{\mathrm{mod},k}$ are the modelled amplitude and phase lags, respectively. Finally, the overall signal, the root sum squares (RSS) and the relative RSS are computed as

$$\text{Overall signal} = \sqrt{\sum_k \text{Signal}_k^2}, \tag{4.9}$$

$$\text{RSS} = \sqrt{\sum_k \text{RMS}_k^2}, \tag{4.10}$$

$$\text{Relative RSS} = \frac{\text{RSS}}{\text{Overall signal}}, \tag{4.11}$$

where the summation is over 23 tides listed in Table 4.1.

The RMS statistic is not the only way how to evaluate model errors. Another possibility is a median statistic which is less sensitive to outliers than the RMS. Hence, the median absolute differences (MAD) between the in-phase and quadrature amplitudes of DEBOT and the testing data are computed as

$$\text{MAD}_k = \text{med}\left(|A_{\mathrm{sta},k} - A_{\mathrm{mod},k}|, |B_{\mathrm{sta},k} - B_{\mathrm{mod},k}|\right), \tag{4.12}$$

where the median is computed from all stations. We note that, in this study, the MAD are usually in a good agreement with the RMS differences, except for a few cases, and hence, we will focus mainly on the RMS statistic.

The final comparative method, which is not statistical but can be used for an evaluation of model predictions at selected stations or locations, is the absolute vector difference (AVD)

$$\text{AVD}_k = \sqrt{H_{\mathrm{sta},k}^2 + H_{\mathrm{mod},k}^2 - 2H_{\mathrm{sta},k}H_{\mathrm{mod},k}\cos(G_{\mathrm{sta},k} - G_{\mathrm{mod},k})}. \tag{4.13}$$

4.3 Results of simulations: a parameter study

The DEBOT-h solution is dependant on several parameters: the ITD factor κ, SAL coefficient ϵ, eddy viscosity coefficient A_H, bottom friction coefficient c_{BF}, bathymetric dataset and spatial resolution. In this section, we investigate the effects of all these parameters using the testing data and methods described in the previous section. Hundreds of DEBOT-h simulations have been carried out in order to find the best setting in terms of the RMS differences. Here, we present only a portion of all results to describe main characteristics of the model.

First, the combined effect of the bathymetry, spatial resolutions and ITD parameterization is studied. We test two bathymetric datasets, ETOPO1 (Amante and Eakins, 2009) and GEBCO (IOC et al., 2003), both distributed as $1' \times 1'$ models. The bathymetric data are implemented into DEBOT as averages over intervals equivalent to the spatial discretization step in both latitudinal and longitudinal directions. Figure 4.2 shows the RSS differences between DEBOT-h and the tidal stations for ETOPO and GEBCO, the spatial resolutions $30' \times 30'$ and $15' \times 15'$ and various ITD factor κ. Several observations can be made:

(1) As expected, the RSS differences are much larger when the ITD is neglected ($\kappa = 0.0$).
(2) Significantly better results in the cases of the finer resolutions $15' \times 15'$ for both bathymetric datasets.
(3) The ITD is applied in depths greater than 500 m. However, we have also carried out simulations with the ITD cut-off depth of 100 m, that is, the ITD is applied in depths greater than 100 m. The red points in Figure 4.2 stand for the experiments when the ITD cut-off depth is 100 m. The results for both border depths are similar, however, it seems that smaller RSS are achieved with the cut-off depth of 500 m. This is also our general experience from many other experiments (not shown here). Hence, in the rest of the paper, all our results are obtained with the ITD cut-off depth 500 m.
(4) GEBCO seems to be a generally better choice of the bathymetry than ETOPO.
(5) Since the bottom roughness $\hat{h}$ in the formula for the ITD parameterization (4.5) is computed from the bathymetric data, it is not surprising that the smallest RSS differences are given by different values of κ for GEBCO and ETOPO.
(6) Although the ITD is computed from local values of the bottom roughness and observed buoyancy frequency, it seems that the factor κ should be also spatially dependent since the best RSS differences in each testing dataset can be achieved with different values of κ. This also follows from Figure 4.3 which shows the relative RMS differences of eight major tidal constituents, Q_1, O_1, P_1, S_1, K_1, N_2, M_2, S_2 and K_2, for various κ. While the best RMS differences between DEBOT-h and the datasets in the deep ocean, on the northwest European shelf and along coastlines are given by $\kappa \approx 1.5$, the best RMS differences in other shelf areas are given by $\kappa \approx 0.8$.

We have also carried out model simulations with finer spatial resolutions for fixed parameters which is shown in Figure 4.4. The RMS differences are not in general smaller for the resolutions of $6' \times 6'$ and $10' \times 10'$ than for the resolution of $15' \times 15'$. This unexpected behaviour indicates that a different combination of parameters should be chosen for resolutions finer than $15' \times 15'$. Unfortunately, our computational possibilities are limited which prevents us to perform a comprehensive parameter study for a very fine resolution. Therefore, the following parameter study is for the $15' \times 15'$ resolution.

Second, the effect of the self-attraction and loading of the water is investigated. Figure 4.5 shows the relative RMS differences for various values of the SAL coefficient ϵ. The immediate finding is that neglecting the SAL ($\epsilon = 0$) results in large RMS differences which is an expected behaviour. Another finding is that the best RMS differences of each dataset and also each tidal constituent are related to different values of ϵ which points out limitations of the SAL scalar approximation. We pick up $\epsilon = 0.1$ as a global compromise, however in future studies, the SAL should be treated in a more rigorous way.

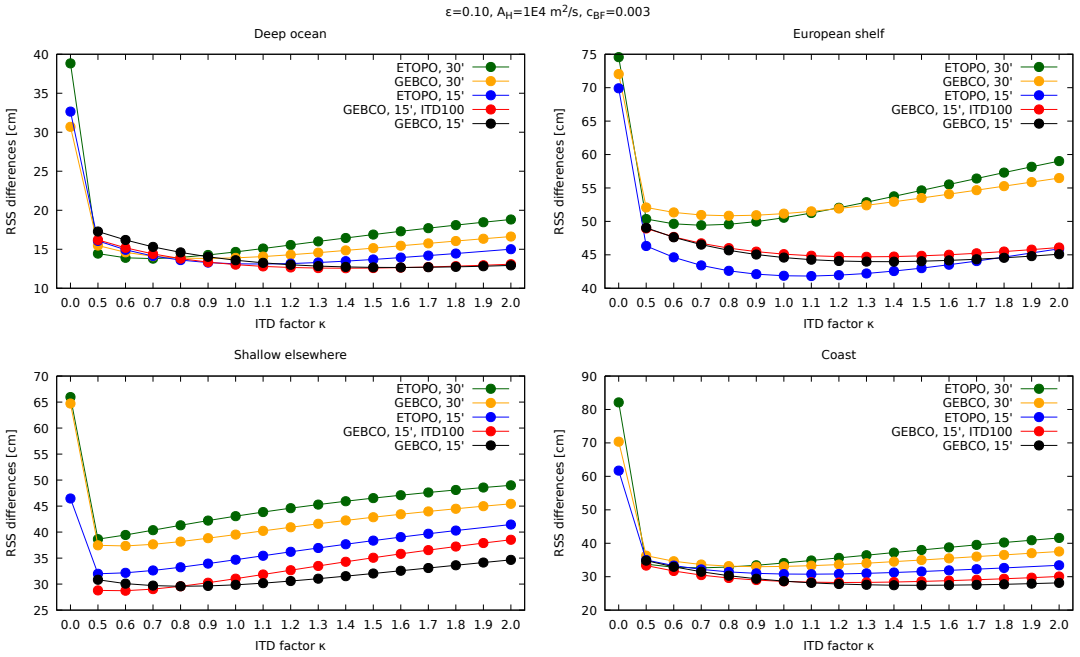

Figure 4.2: The RSS differences between DEBOT-h and the tidal stations in the deep-ocean (topleft), on the northwest European shelf (top right), in shallow waters elsewhere (bottom left) and along continental coastlines (bottom right) for two bathymetric datasets, ETOPO and GEBCO, spatial resolutions 30′ and 15′ and various ITD factors κ. "ITD100" denotes simulations with the ITD applied in depths greater than 100 m, otherwise it is applied in depths greater than 500 m.

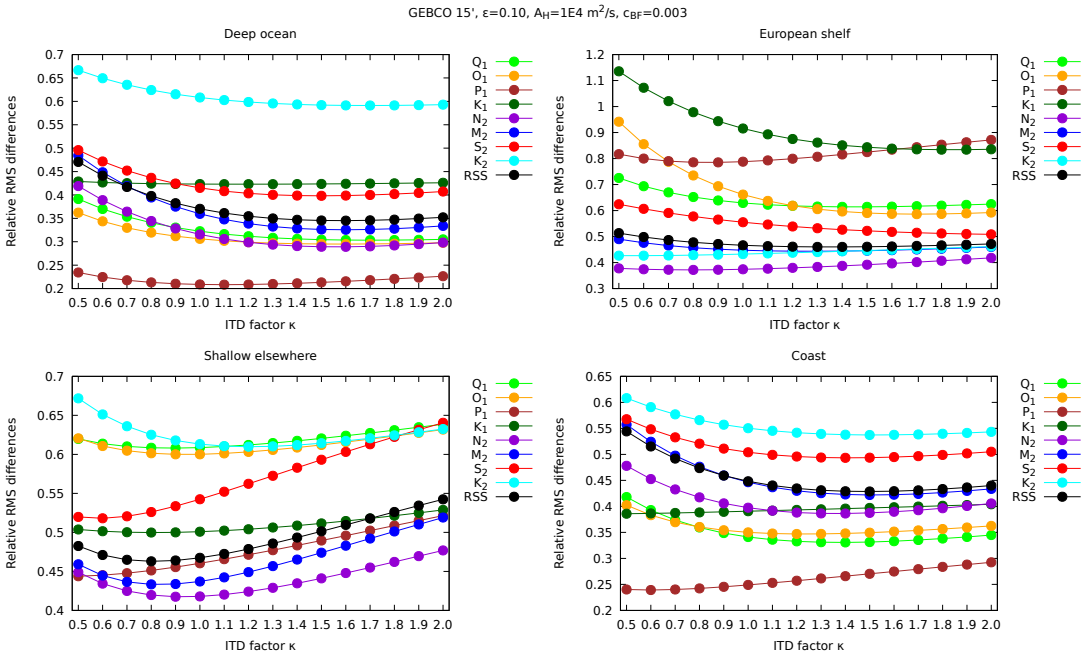

Figure 4.3: The relative RMS differences between DEBOT-h and data from tidal stations for various ITD factors κ.

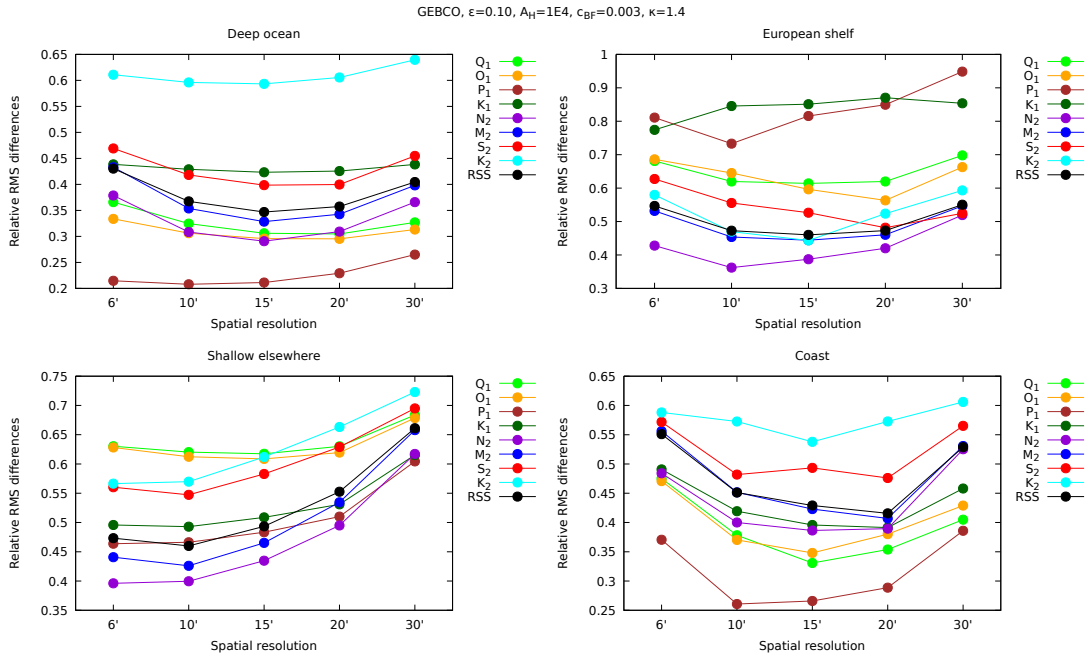

Figure 4.4: The relative RMS differences between DEBOT-h and data from tidal stations for various spatial resolutions.

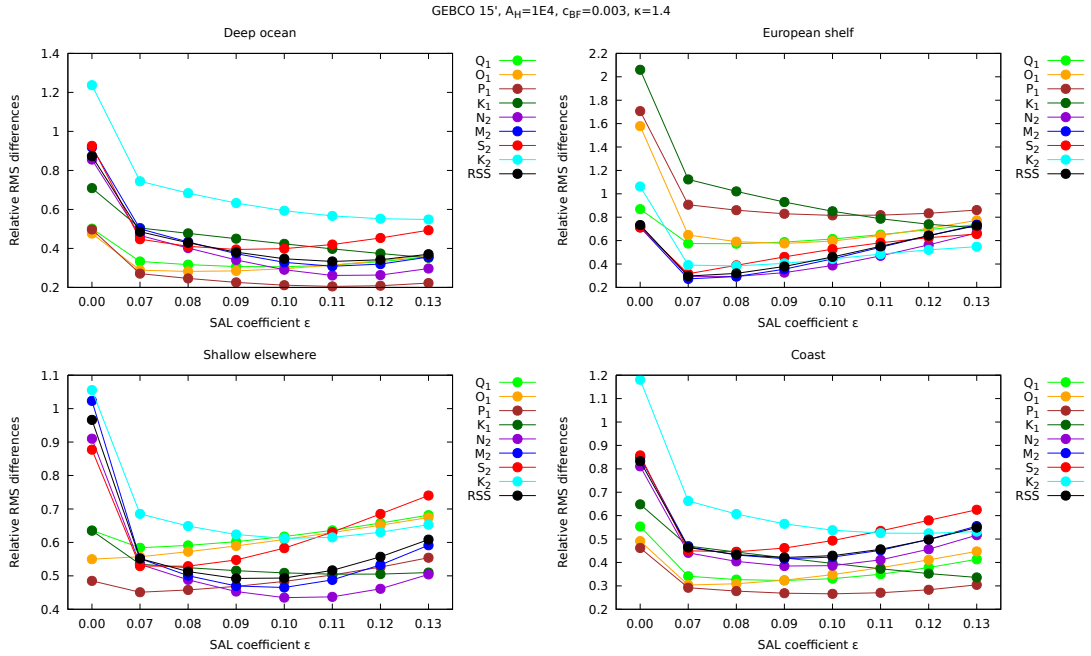

Figure 4.5: The relative RMS differences between DEBOT-h and the tidal stations for various SAL coefficients ϵ.

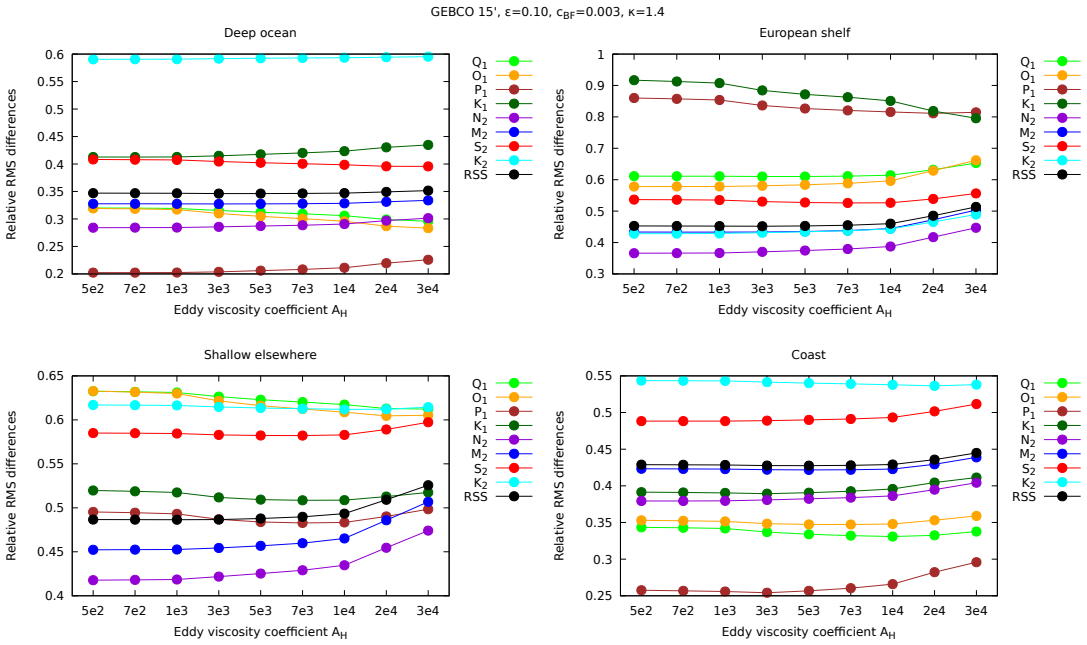

Figure 4.6: The relative RMS differences between DEBOT-h and the tidal stations for various eddy viscosity coefficients A_H.

Third, the effect of the eddy viscosity is shown in Figure 4.6. There is hardly any sensitivity to the eddy viscosity coefficient A_H in the range from 5×10^2 $\frac{\mathrm{m}^2}{\mathrm{s}}$ to 10^4 $\frac{\mathrm{m}^2}{\mathrm{s}}$ and only slightly worse results are for $A_H > 10^4$ $\frac{\mathrm{m}^2}{\mathrm{s}}$. Obviously, the main source of the energy dissipation in DEBOT-h is the ITD while the eddy viscosity plays a secondary role in the energy budget (see Section 4.5). Note that in the older version of DEBOT without the ITD (EM15), the eddy viscosity represents an important frictional term and larger values of A_H are accompanied by better RMS differences. However, the eddy viscosity term is still needed in present DEBOT-h to eschew numerical instabilities which can occur if this term is omitted. Furthermore, in the case of too large A_H, greater than 10^5 $\frac{\mathrm{m}^2}{\mathrm{s}}$, the model produces completely unrealistic results (not shown here) and thus, A_H must be kept in the range circa $10^2 - 10^4$ $\frac{\mathrm{m}^2}{\mathrm{s}}$.

Finally, the effect of the bottom friction is shown in Figure 4.7. In the deep ocean, the results are almost insensitive to the value of c_{BF} while in the shelf seas, the bottom friction has a much greater impact on the resulted RMS differences and $c_{BF} = 0.002$ or $c_{BF} = 0.003$ seems to be an optimal value.

4.4 The best setting

After performing hundreds of simulations, we concluded that the best DEBOT-h setting in terms of the RMS statistic is as follows: the GEBCO bathymetry, $\kappa = 1.4$, $\epsilon = 0.1$, $A_H = 10^4$ $\frac{\mathrm{m}^2}{\mathrm{s}}$ and $c_{BF} = 0.003$. This setting is picked up as a compromise between the deep ocean and shelf seas. Table 4.2 summa-

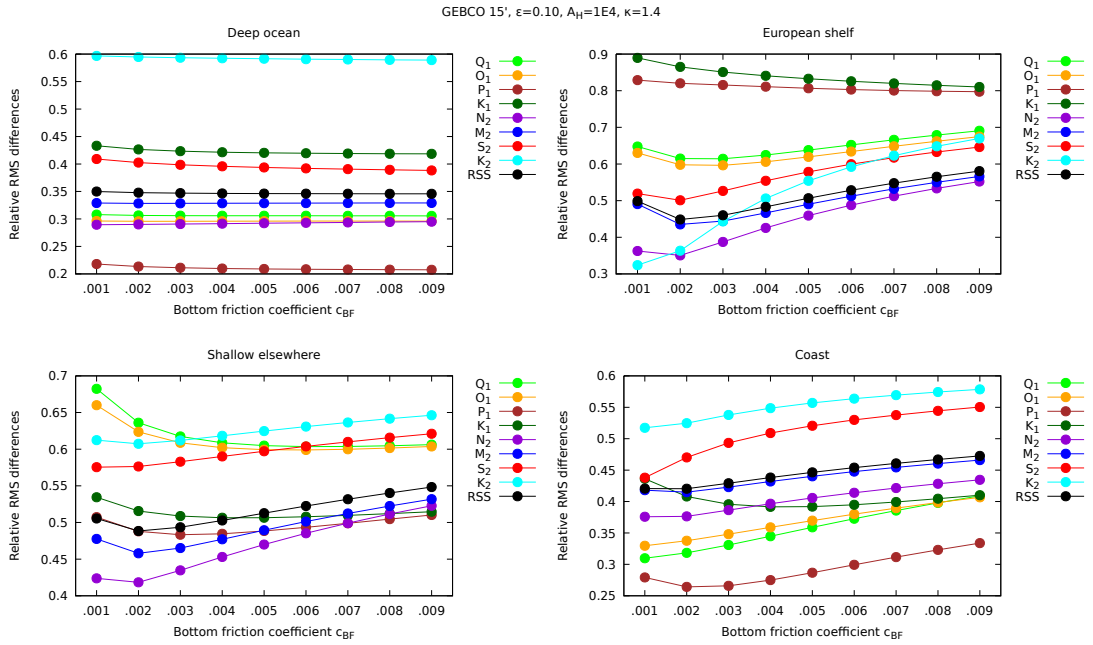

Figure 4.7: The relative RMS differences between DEBOT-h and the tidal stations for various bottom-friction coefficients c_{BF}.

rizes the RMS differences of this model setting against the testing tidal stations (RMS_{TS}) and also against data-assimilative TPXO8 over the entire ocean domain (RMS_{alt}). As will be shown in the next chapter, assimilative models are much more precise than purely hydrodynamical by approximately one order of magnitude and therefore, TPXO8 can be used as another tool to evaluate errors of DEBOT-h. RMS_{alt} in the deep ocean are computed from all gridpoints with depths greater than 1000 m and in the shelf seas from all gridpoints with depths greater than 20 m but shallower than 200 m. In the deep ocean, both RMS statistics are almost identical while on the continental shelves, RMS_{alt} give generally better results than RMS_{TS}. This suggests that RMS_{TS} may be skewed by some outliers which is illustrated by Figure 4.8. The left part shows the histogram of the absolute vector differences between DEBOT-h and the shelf seas tidal stations. The mean value of the AVD is 33.3 cm but the median is 23.5 cm. Hence, while model errors are less than 25 cm at most locations in the shelf seas, there is still a handful of locations with much greater errors. The right part shows locations of the tidal stations on the northwest Europeans shelf and their AVD. In simple words, the closer to land, the worse prediction with the largest errors in the English channel and the Irish sea. Regarding the other shallow water areas, two stations with by far largest AVD are located on the Patagonian shelf. Our conclusion is that the DEBOT-h errors on the continental shelves are generally about 20 cm or less but much larger in some coastal areas, bay, straits, etc.

Table 4.3 compares DEBOT-h with other state-of-the-art purely hydrodynamical models. Only the M_2 tide is considered here. The other models are

Table 4.2: Tidal signals and RMS differences (in cm) between DEBOT-h and the tidal stations (RMS_{TS}) and between DEBOT-h and TPXO8 (RMS_{alt}).

	Q_1	O_1	P_1	K_1	N_2	M_2	S_2	K_2
				Deep ocean				
Signal	1.79	8.75	3.99	12.51	6.36	30.22	11.21	3.12
RMS_{TS}	0.55	2.59	0.84	5.29	1.85	9.92	4.47	1.85
RMS_{alt}	0.57	2.97	0.80	4.10	1.88	10.38	4.87	1.62
				European shelf				
Signal	2.14	5.59	1.50	5.51	17.02	87.74	29.96	7.30
RMS_{TS}	1.32	3.34	1.23	4.69	6.59	38.98	15.78	3.24
				Shelf seas elsewhere				
Signal	2.69	10.91	5.91	17.07	12.54	53.95	21.72	7.09
RMS_{TS}	1.66	6.64	2.85	8.68	5.45	25.10	12.66	4.34
				Shelf seas overall				
Signal	2.49	9.20	4.70	13.75	14.46	69.18	25.27	7.18
RMS_{TS}	1.53	5.58	2.35	7.38	5.93	31.28	13.96	3.94
RMS_{alt}	1.22	6.70	2.09	6.99	4.15	22.49	10.16	2.97
				Coast				
Signal	1.93	9.74	4.93	15.94	11.18	55.54	21.44	6.02
RMS_{TS}	0.64	3.39	1.31	6.31	4.32	23.49	10.58	3.24

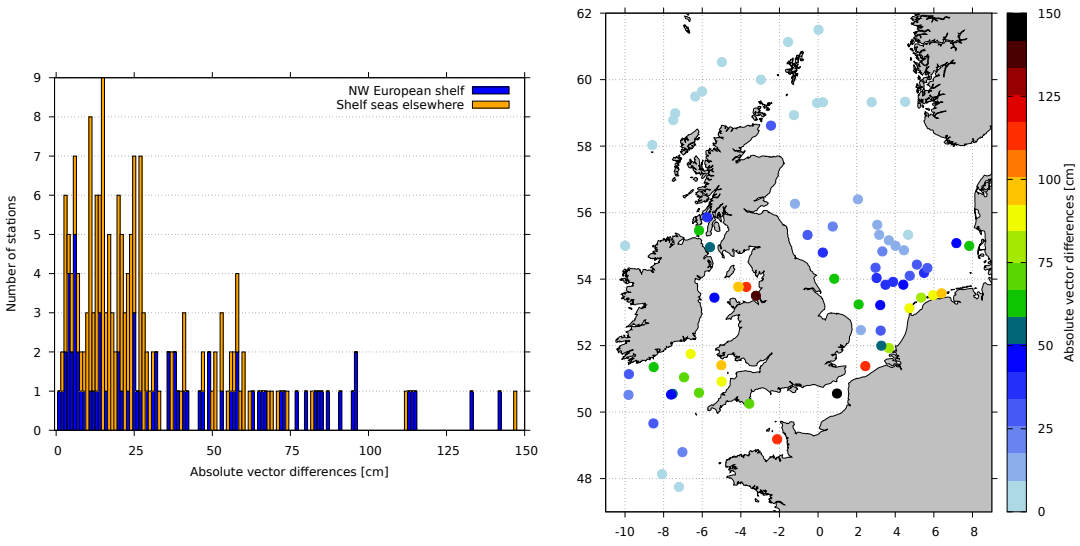

Figure 4.8: Left: Histogram of the absolute vector differences between DEBOT-h and the shallow seas tidal stations (the mean value of all stations is 33.3 cm, the median is 23.5 cm). Right: Map of the tidal stations on the northwest European shelf and their AVD indicated by color.

Table 4.3: The M_2 RMS differences (in cm) of DEBOT-h and other purely hydrodynamical models against the deep ocean and shelf seas tidal stations (RMS_{TS}) and against TPXO8 (RMS_{alt}).

	Deep ocean		Shelf seas	
Model	RMS_{TS}	RMS_{alt}	RMS_{TS}	RMS_{alt}
DEBOT-h	**9.92**	**10.38**	**31.3**	**22.5**
HIM	8.75	5.25	33.7	22.3
OTIS-GN	7.54	6.76	25.3	18.6
STORMTIDE	8.33	7.76	48.2	27.9
OTIS	5.63	4.65	23.6	24.0
STM-1B	12.69	7.74	30.5	25.8
HYCOM	7.82	7.00	49.0	26.2

HIM (Arbic et al., 2008), OTIS-GN (Green and Nycander, 2013), STORMTIDE (Müller et al., 2012), OTIS (Egbert et al., 2004), STM-1B (Hill et al., 2011) and HYCOM (Arbic et al., 2010). The RMS values are taken from Stammer et al. (2014). We can say that DEBOT-h is comparable in accuracy with the other models in the shelf seas, however it is still a little bit worse in the deep ocean. This may be caused by several reasons. First, different bathymetry and resolution of the other models (DEBOT-h has the resolution of $15'$ while the others $7.5'$ or finer). However, since the RMS differences of DEBOT-h on the continental shelves are relatively good, we rather think that the problem may be in the parameterization of the ITD and the scalar approximation of the SAL. Future works should be focused on an implementation of more rigorous parameterization of the ITD and SAL.

Besides statistical methods, model errors might be also evaluated by a visual inspection of global charts. Figure 4.9 shows the M_2 amplitudes and Greenwich phase lags of the surface elevations and zonal and meridional transports ($h\vec{v}$) for DEBOT-h and DEBOT-a (amplitudes and phase lags for other major constituents are shown in Figures B.1–B.8 in Appendix B). Moreover, Figure 4.10 shows the absolute vector differences of all three variables between DEBOT-h and DEBOT-a and also between DEBOT-a and the independent, data-assimilative TPXO model for reference (AVD for other major constituents are shown in Figures B.9–B.16 in Appendix B). As can be seen, general patterns of both DEBOT-h and DEBOT-a are same, however there are some problematic spots. Especially two large areas in the Pacific ocean with the surface elevations AVD up to 40 cm which are probably the main reason of large RMS_{alt} in the deep ocean. Another problematic areas are a belt along the west coast of North America and the Southern Ocean, especially in the Weddel and Ross seas which are mostly covered by ice shelves. The ice-covered area of the Weddel and Ross seas are not included in our solution and obviously, their omission produces large errors. On the other hand, DEBOT-h seems to be generally good in the Atlantic and Indian oceans and the northwest part of the

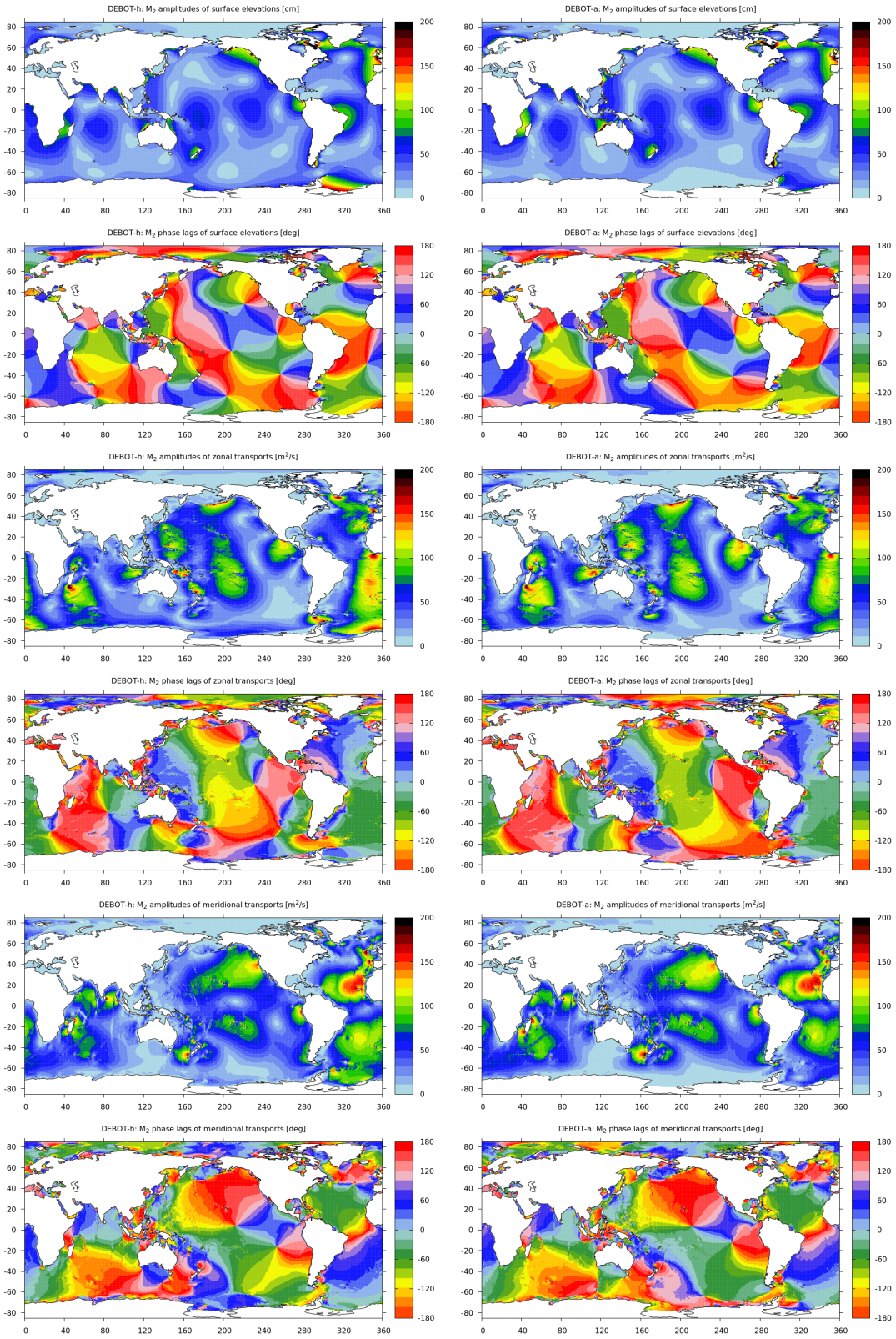

Figure 4.9: Comparison of DEBOT-h (left) and DEBOT-a (right): M_2 amplitudes and Greenwich phase lags of the surface elevations (two top panels), zonal transports (two middle panels) and meridional transports (two bottom panels).

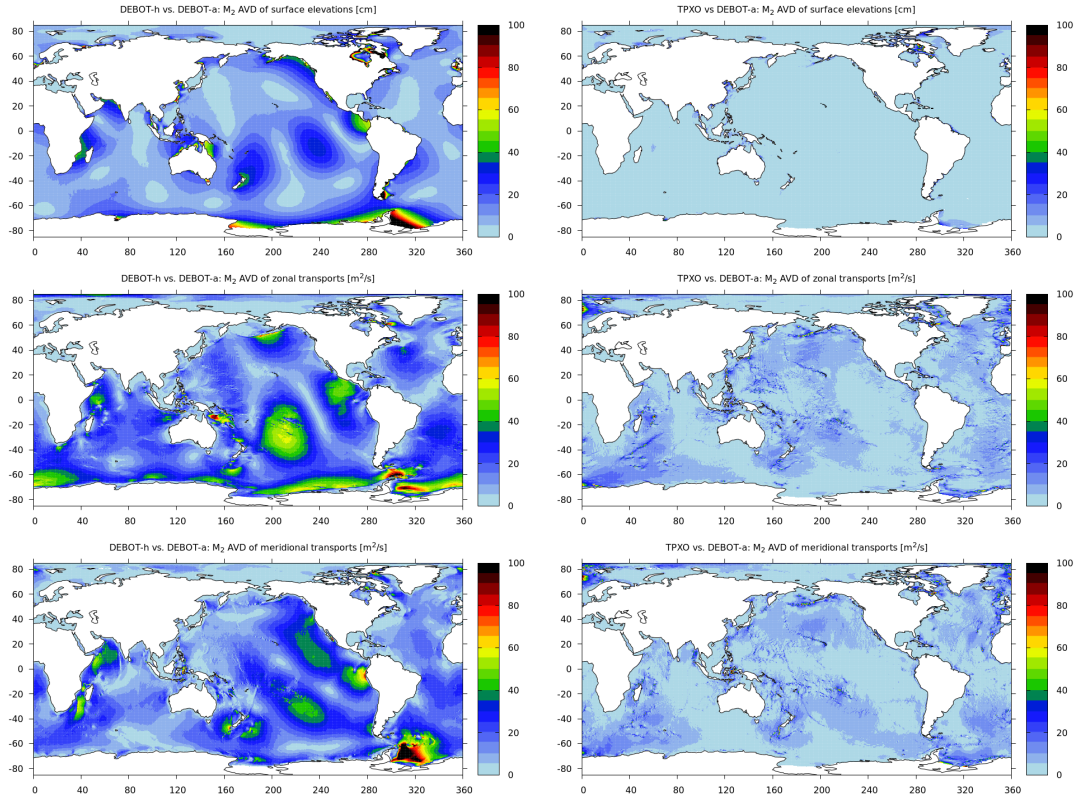

Figure 4.10: Absolute vector differences between DEBOT-h and DEBOT-a (left) and DEBOT-a and TPXO (right) for the M_2 surface elevations (top), zonal transports (middle) and meridional transports (bottom).

Pacific ocean (except some smaller areas, e.g., Hudson bay, the Mozambique channel, the Patagonian shelf, the Irish sea, etc.).

4.5 The energy and dissipation in DEBOT-h

The energy and dissipation properties of DEBOT-h are discussed in this section. First, let us summarize basic formulae for the energy and dissipation of a barotropic ocean model. For details, see classical texts, e.g., Pond and Pickard (1983); Pedlosky (1987). The kinetic energy E_K and potential energy E_P are defined as

$$E_K = \frac{\rho}{2} h(u^2 + v^2), \qquad E_P = \frac{\rho}{2} g\zeta^2, \tag{4.14}$$

where ρ is the density of the ocean water. The dissipation D in DEBOT-h consists of three parts, the dissipation due to the internal tide drag D_{ITD}, due to the bottom friction D_{BF} and due to the eddy viscosity D_{EV},

$$D_{ITD} = \rho C_{ITD} |\vec{v}|^2, \qquad D_{BF} = \rho c_{BF} |\vec{v}|^3, \qquad D_{EV} = -\rho A_H \vec{v} \cdot \nabla_\Omega \cdot \boldsymbol{\sigma}. \tag{4.15}$$

For the best setting in terms of the surface elevation, which was discussed in the previous section, the globally integrated, time-averaged energy is

449.27 PJ and the dissipation is 4.23 TW. The energy is in a relatively good agreement with the value 517.11 PJ computed from the TPXO8 dataset. The dissipation is larger than the observed values 3.51 TW (Egbert and Ray, 2003) and 3.54 TW (Taguchi et al., 2014) by about 21 %, however the tidal dissipation in models which do not assimilate any data is usually larger by 5–30 % than the dissipation based on data-constrained models (Arbic et al., 2004; Egbert et al., 2004; Simmons et al., 2004; Griffiths and Peltier, 2009). Therefore, we consider our value 4.23 TW to be acceptable. 52 % of the dissipation (2.20 TW) occurs in waters deeper than 1000 m, which is larger than 40 % (1.42 TW) quoted by Taguchi et al. (2014). DEBOT-h is thus not completely physically consistent and dissipates too much energy in the deep ocean. Note that Egbert and Ray (2003) quotes even a smaller amount of the dissipation in deep waters, 29 %, however they accounted for a less complete deep ocean area.

Time-averaged energy and dissipation are computed for various model parameters. The results are plotted in Figure 4.11 which shows some interesting features. The total energy and dissipation are decreasing with larger values of the internal tide drag factor κ but they are only slightly affected by the eddy viscosity or bottom-friction coefficient. This is consistent with the tests against the tide gauge data from Section 4.3 where the internal tide drag has the major impact on the resulted surface elevations while the bottom friction is important only in shallow and coastal seas and the eddy viscosity hardly has any influence on the elevations. A proportion of D_{ITD}, D_{BF} and D_{EV} is changing with various values of κ, A_H and r. The larger one of these parameters is the larger the corresponding dissipation is and two other dissipation are attenuated.

The global energy and dissipation increase with the increasing resolution and do not converge to the values deduced from the assimilative models. On the other hand, the amount of the deep ocean dissipation decreases with the increasing resolution. The ratio is 30 % and 42 % for $6' \times 6'$ and $10' \times 10'$, respectively, which is in a better agreement with the values quoted by Egbert and Ray (2003) and Taguchi et al. (2014) than for the $15' \times 15'$ resolution.

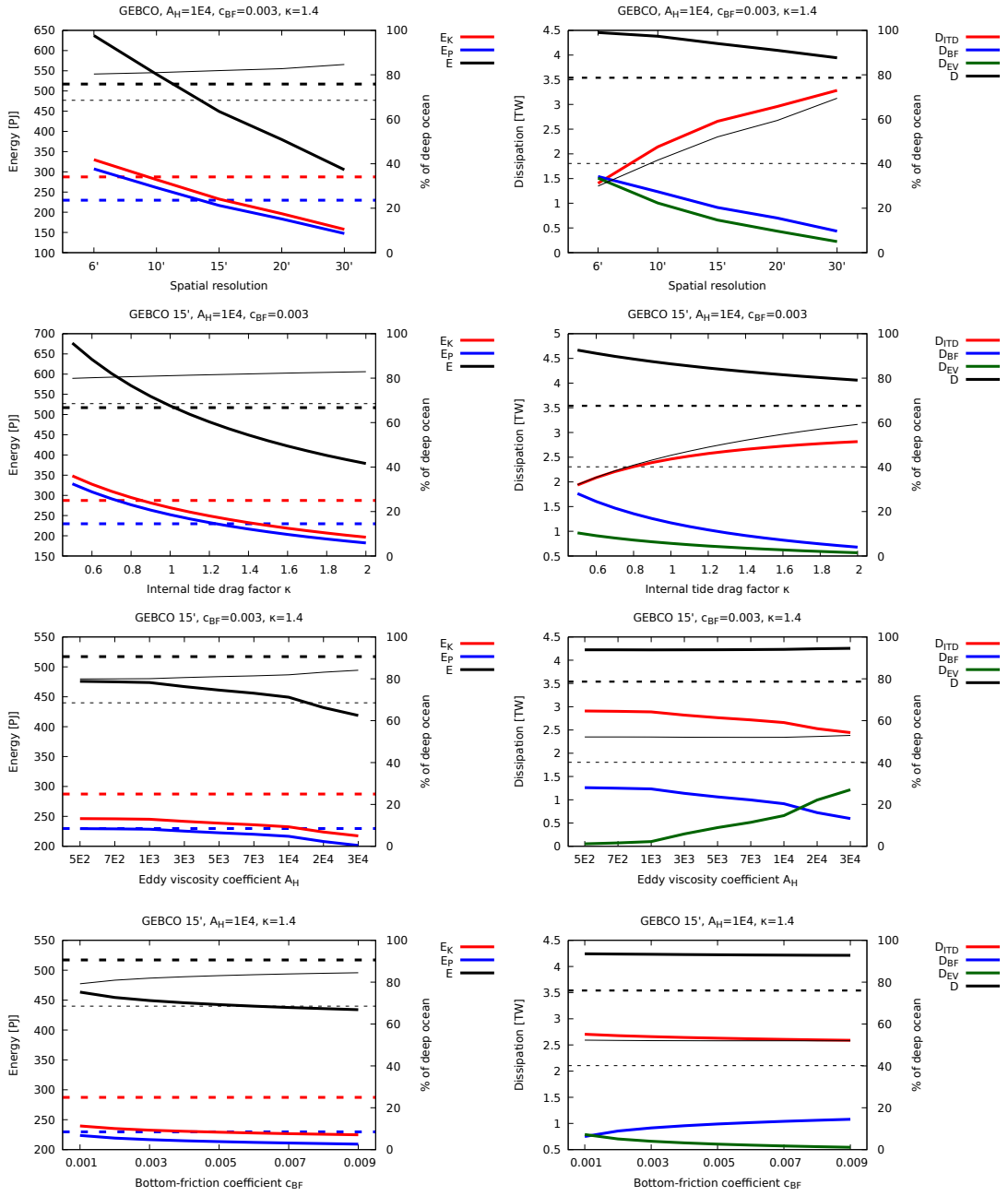

Figure 4.11: Global time-averaged energy (left panel) and dissipation (right panel) for various spatial resolutions (top), internal tide drag factors κ (middle top), eddy viscosity coefficients A_H (middle bottom) and bottom-friction coefficients c_{BF} (bottom). Thin black lines are amounts (in percent, right y-axes) of the energy and dissipation in the deep ocean (depths greater than 1000 m). The dashed lines denote values deduced from assimilative models: the energy is computed from the TPXO8 datasets, the dissipation values are from Taguchi et al. (2014).

CHAPTER

5

DEBOT-A: AN ASSIMILATIVE MODEL

For many years, knowledge of ocean tides was limited due to the fact that most of the tide gauge measurements were located at coasts, islands and ports only and hence there was a lack of information about tides in deep oceans. During 1980s the Naval Surface Weapon Center (NSWC) model by Schwiderski (1980), which assimilated tide gauges to determine global tides, was regarded as the most precise global model, however, it was known that it contained decimal and larger errors (Shum et al., 1997). This has been overcome by satellite altimetry. TOPEX/Poseidon (hereafter T/P), a joint satellite mission between NASA and CNES which was launched in 1992, was specially designed to measure global ocean tides and achieved this goal with a great success. Walter Munk described T/P as "the most successful ocean experiment of all time" (Munk, 2002). During first years of T/P mission, altimetric data significantly helped to develop and improve several global ocean tide models which provided much better accuracy than NSWC. This dramatical progress was described by Shum et al. (1997). T/P stopped to provide scientific data in 2005 after a malfunction, however, its successor Jason-1 was already operating (launched 2001, deactivated 2013). Altimetric observations has continued with the Ocean Surface Topography Mission (OSTM) on the Jason-2 satellite, which has been providing data since 2008, and Jason-3 mission which was launched in January 2016. Data from other satellite missions (e.g., ERS-1,2, GFO, Envisat) are also used. In more than 20 years of satellite altimetry the research on ocean tides has advanced dramatically resulting in improved global tide models and more accurate tide atlases as well as better understanding of tidal dynamics and energy dissipation. This progress was recently described in Stammer et al. (2014).

In this chapter, DEBOT-a, an assimilative model constructed as an exten-

sion of purely hydrodynamical DEBOT-h, is introduced. First, a short review of modern assimilative and empirical models is provided in Section 5.1. The assimilation scheme used in DEBOT-a is introduced and described in Section 5.2 and results of DEBOT-a simulations are shown in Section 5.3.

5.1 A review of modern global ocean tide models

Modern global ocean tide models can be divided into three categories:

(1) Forward (purely) hydrodynamical models which are not constrained by any data (tide gauge and/or altimetry). Purely hydrodynamical modelling was discussed in the previous chapter.
(2) Barotropic hydrodynamical model constrained by tide information through assimilation.
(3) Empirical models which can be either purely empirical models directly derived from satellite data or semi-empirical models which are empirical corrections of reference models.

State-of-the-art global ocean tide models are compared in Stammer et al. (2014) and their accuracy is below 1 cm of root mean square model differences against deep-ocean tidal measurements for major tidal constituents. Here, we briefly describe assimilative and empirical approaches of the modern models.

5.1.1 Assimilative models

The assimilative modelling approach integrates satellite altimetry (and tide gauges) data into barotropic hydrodynamic models. Such models are, for example, TPXO8 (Egbert et al., 1994; Egbert and Erofeeva, 2002), FES2012 (Lyard et al., 2006; Carrère et al., 2012) or HAMTIDE (Zahel, 1995; Taguchi et al., 2014). All models are based on linearised momentum and continuity equation which are solved in spectral domain

$$i\omega\hat{\zeta} + \nabla \cdot \vec{\hat{U}} = 0, \tag{5.1}$$

$$\mathbf{\Omega}\vec{\hat{U}} + gh\nabla\hat{\zeta} = \vec{F}, \tag{5.2}$$

where

$$\mathbf{\Omega} = \begin{pmatrix} i\omega + K & -f \\ f & i\omega + K \end{pmatrix}, \tag{5.3}$$

$$\zeta = \hat{\zeta}e^{-i\omega t}, \tag{5.4}$$

$$h\vec{u} = \vec{U} = \vec{\hat{U}}e^{-i\omega t}, \tag{5.5}$$

where $i = \sqrt{-1}$, ω is the tidal frequency, f the Coriolis coefficient, K the linear drag coefficient and $\vec{F}$ the tidal forcing, self-attraction and loading. Such a linear system can be formally written as

$$\mathbf{S}\vec{u} = \vec{F}. \tag{5.6}$$

A goal of the assimilation is to find such a vector of tidal velocities $\vec{u}$ which is consistent with (5.6) as well as with a vector $\vec{d}$ of tidal data

$$\vec{d} = \mathbf{L}\vec{u}, \tag{5.7}$$

where $\mathbf{L}$ is an observational operator which projects the unknown tidal currents $\vec{u}$ on the observed data $\vec{d}$. A general inversion approach can be applied to satisfy both (5.6) and (5.7) which means to minimize the functional

$$J = \left(\mathbf{S}\vec{u} - \vec{F}\right)^H \mathbf{\Sigma}_m^{-1} \left(\mathbf{S}\vec{u} - \vec{F}\right) + \left(\vec{d} - \mathbf{L}\vec{u}\right)^H \mathbf{\Sigma}_d^{-1} \left(\vec{d} - \mathbf{L}\vec{u}\right), \tag{5.8}$$

where $\mathbf{\Sigma}_m$ and $\mathbf{\Sigma}_d$ are the covariances matrices for the model and data errors and the upper index H denotes the Hermitian transpose. Methods for computing the functional (5.8) and the covariance matrices are not described here and we refer to the aforementioned papers for details.

Model equation (5.6) is linear, hence compound tides, which are generated by non-linear interactions of astronomical tidal constituents, are not included. However, there are two methods of how to include the compound tides into the model's tidal solution. In TPXO8, the prior solution $\vec{u}_0$ is computed for all major tidal constituents simultaneously from the time-domain shallow water equation with the advection, non-linear bottom friction and viscous terms. The prior solution for the compound tides then can be added to the solution of the assimilation process. In FES2012, non-linear forcing functions are added to the spectral-domain shallow water equations (5.1) and (5.2) and the tidal potential forcing at the compound tides frequencies is set to be equal to zero (see Lyard et al. (2006) for details). To be complete, in HAMTIDE, the compound tides are not a part of their solution.

5.1.2 Empirical models

Empirical models are derived by an analysis of satellite altimetry data which means there are no ocean circulation equations to be solved. Such approach lacks deep physical understanding of the tidal dynamics when compared to the assimilative models, however, it can offer more precise estimation of tidal heights without the knowledge of the bathymetry, bottom friction or internal tide drag parametrization. A purely empirical model, which is derived directly from data, is, for instance, OSU12 (Fok, 2012) while semi-empirical models, i.e., those which are empirical corrections to an a priori model, are, for example, DTU10 (Cheng and Andersen, 2012), EOT11a (Savcenko and Bosch, 2012), both use FES2004 (Lyard et al., 2006) as their reference model, or GOT4.8 (Ray, 1999) which uses a collection of both global and regional models as its prior model. Tidal constituents are determined by using the harmonic analysis (GOT4.8, EOT11a) or response method (DTU10, OSU12). Both methods were introduced in Section 3.7.

The empirical models include only the sea surface elevations, however, the tidal currents can still be derived by a least-square method described in Ray

(2001). Let us consider simple linear shallow water equations

$$\nabla \cdot \vec{U} = -i\omega\hat{\zeta}, \tag{5.9}$$

$$\begin{pmatrix} i\omega + K & -f \\ f & i\omega + K \end{pmatrix} \vec{U} = \vec{F} - gh\nabla\hat{\zeta}. \tag{5.10}$$

Then all terms on the right-hand sides are known and the two-dimensional vector $\vec{U}$ is over-determined by the three equation. Hence, the unknown velocities can be found by a least-square method.

5.2 The assimilation scheme in DEBOT-a

DEBOT-a is constructed as an extension of DEBOT-h, which means that it is also a non-linear, time-domain model with the full lunisolar tidal forcing. This is an alternative model compared to the state-of-the-art assimilative models TPXO, FES or HAMTIDE which are all based on linearised, spectral-domain equations and a general inversion scheme is applied for the assimilation of satellite altimetry data as described in Section 5.1.1.

The assimilation scheme used in DEBOT-a is based on a periodical "upgrade" of the surface elevation. It means that the model solution is given by the hydrodynamical model and at regular time intervals ΔT, an assimilation process is applied and the model solution is constrained by data information. A flow diagram of this process is shown in Figure 5.1. The assimilation interval ΔT is generally much larger than the model time step Δt which is only a few seconds ($\Delta t = 7.5$ s for the $15' \times 15'$ resolution).

As data constraints, we use the DTU10 model (Cheng and Andersen, 2012) which is a freely available, state-of-the-art empirical model comparable in accuracy to other empirical or assimilative models mentioned in the previous section. DTU10 is based on an empirical correction to FES2004 and provides the surface elevation amplitudes and Greenwich phase lags of the Q_1, O_1, P_1, S_1, K_1, N_2, M_2, S_2, K_2 and M_4 tidal constituents on a $7.5'$ grid. The data of DTU10 are assimilated into DEBOT in a form of the surface elevation ζ_E which is a superposition of the aforementioned tides excluding the S_1 tide, i.e., $\zeta_E = \sum_i \zeta_{Ei}$, $i = \{Q_1, O_1, P_1, K_1, N_2, M_2, S_2, K_2, M_4\}$. S_1 is a radiational tide

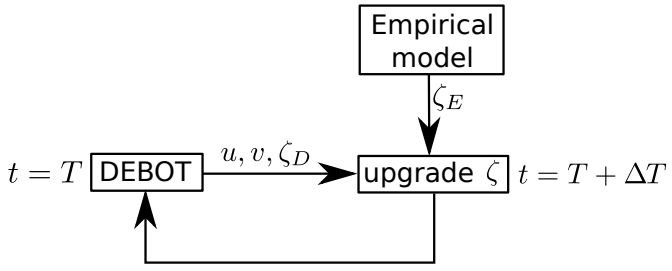

Figure 5.1: Flow diagram of the assimilation process used in DEBOT-a.

generated primarily by diurnal atmospheric pressure loading at the frequency of exactly 1 cycle per solar day whereas the astronomical tidal potential at the same frequency is negligible (Ray and Egbert, 2004). Modelling of the S_1 tide would require a model of atmospheric pressure which, however, is not implemented in DEBOT. This issue should be addressed in future studies, however in this study, we restrict our attention to tidal signals generated by the lunisolar potential only.

The assimilation process is a weighted summation of the surface elevations given by the hydrodynamical model, ζ_D, and the data, ζ_E,

$$\zeta = w\zeta_E + (1-w)\zeta_D, \tag{5.11}$$

where $w \in (0,1)$ is the weight given to the data and ζ the "upgraded" surface elevation. Since the future time level in the DEBOT time-stepping scheme is computed from three previous ones and in order to prevent some "big shocks" to the system, the assimilation process is divided into four time steps with increasing w. Let n denote a time level when the assimilation process is activated. Then $w^n = w/4$, $w^{n+1} = w/2$, $w^{n+2} = 3w/4$ and $w^{n+3} = w$. Let us emphasize that the model time step Δt between the time levels n and $n+1$ is not equal to the assimilation interval ΔT. The assimilation is activated every Nth time step, where $N = \frac{\Delta T}{\Delta t}$. Between the assimilation processes, the model solution is given by the hydrodynamical model only.

There is one obvious critical issue with Equation (5.11). The DEBOT elevations ζ_D are generated by the full tidal potential, i.e., all tidal constituents are included whilst the elevations from DTU10 are composed of 9 tidal constituents only. This means that signals of all other minor tidal constituents which are contained in ζ_D would be destroyed by the assimilation process and the main advantage of ocean tide modelling with the full lunisolar potential would be lost. However, it is possible to overcome this undesirable phenomenon by launching DEBOT-h, computing time series of the elevation for all gridpoints, extracting signals of the minor tidal constituents from the time series and using them as another "data" for DEBOT-a. Then, $\zeta_E = \sum_i \zeta_{Ei} + \sum_j \zeta_{Dj}$, where i stands for the aforementioned tides contained in DTU10 and j stands for other minor tides extracted from DEBOT-h.

5.3 Results of simulations

The assimilation process is dependent on two parameters, the assimilation interval ΔT and the weight w. These parameters are examined through series of tests against the tidal stations (the testing datasets and methods were described in the previous chapter, Section 4.2). A sampling of DEBOT-a, from which the RMS and MAD statistics are computed, is chosen not to be equal to ΔT or multiples of ΔT to avoid picking up only those time steps which explicitly include assimilation. Figures 5.2 and 5.3 show the relative RMS differences between DEBOT-a and the testing data for various values of ΔT and w, respectively. The assimilation process has a great impact on resulted elevations

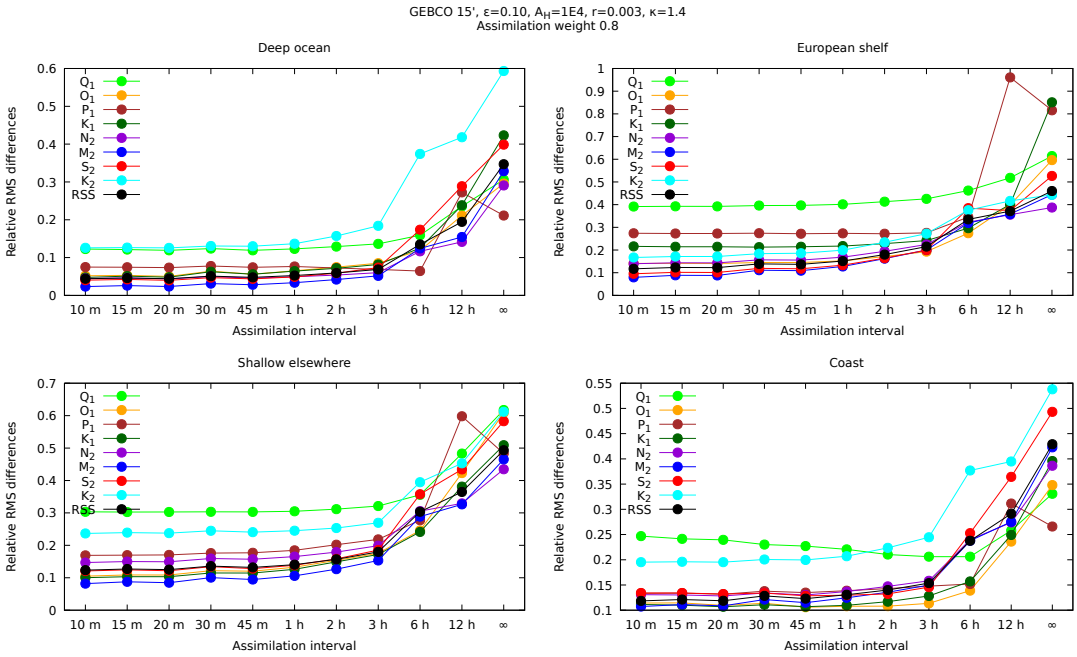

Figure 5.2: The relative RMS differences between DEBOT-a and the tidal stations for various values of the assimilation interval ΔT. Note that ∞ denotes results of non-assimilative DEBOT-h.

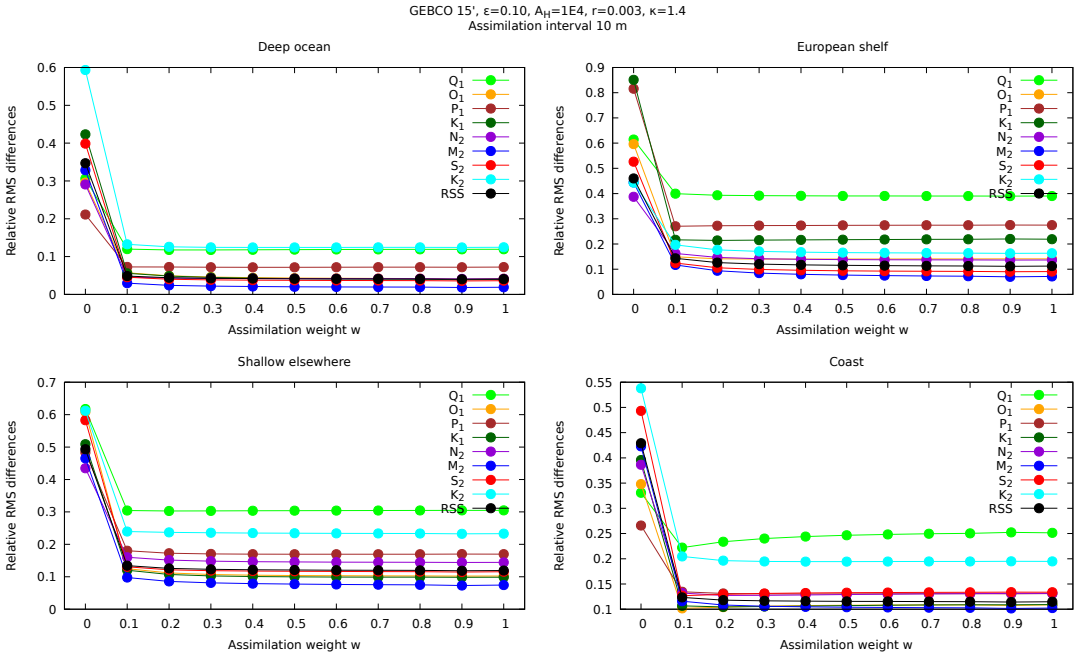

Figure 5.3: The relative RMS differences between DEBOT-a and the tidal stations for various values of the assimilation weight w. Note that 0 denotes results of non-assimilative DEBOT-h.

even for relatively large intervals $\Delta T = 1 - 2$ h and relatively small weights $w < 0.5$. However, better RMS differences are generally achieved with smaller intervals and larger weights, though there are only slight differences among simulations with $\Delta T = 10, 15, 20$ min and $w > 0.5$, up to 1-2 mm in the deep ocean and 1-2 cm in the shelf seas.

We compare our results with other state-of-the-art empirical and assimilative models for the eight major tidal constituents which is summarized in Tables 5.1, 5.2 and 5.3 and Figures 5.4, 5.5 and 5.7. The empirical models are DTU10, GOT4.8, OSU12 and EOT11a. The assimilative models are HAMTIDE, FES2012 and TPXO8. The appropriate values are taken from Stammer et al. (2014). For the comparison we use the results of the simulation with $\Delta T = 10$ min and $w = 1.0$. In these tables, the RSS are computed from the RMS values of the eight major tides only.

In the deep ocean (Table 5.1 and Figure 5.4), DEBOT-a is quite comparable to the other models although some improvements are still required as O_1, K_1 and K_2 are a little bit worse than other models. This may be caused by errors of the prior hydrodynamical model and we believe that better accuracy of DEBOT-a can be achieved by future improvements of hydrodynamical DEBOT-h.

It is interesting that on the northwest European shelf (Table 5.2 and Figure 5.5), DEBOT-a is very good for diurnal constituents, approaching the best numbers, but relatively poor for semi-diurnal constituents, especially for the M_2 tide where DEBOT-a drops behind the other model by about 0.5–3 cm. This suggest that the RMS statistic of the European shelf datasets, which consists of only 76 tidal stations, is affected by some outliers. This can be seen in Figure 5.6 which shows the histogram of the M_2 AVD between DEBOT-a and the shelf seas data and the map of the stations on the NW European shelf with their AVD values. For the NW European shelf, the median of the M_2 AVD is 2.85 cm but the mean value is 5.56 cm. Hence, while the M_2 model errors are less than 3 cm at most locations on the NW European shelf, there are still some problematic spots with much larger errors, namely the station on Jersey island in the English channel and some stations in the Irish sea close to a land. On the other hand, the RMS statistic of the other shelf seas seems to be less affected by outliers and more reliable. As shown in the histogram of Figure 5.6, there are some stations in the "shelf seas elsewhere" with extraordinarily large M_2 AVD, however they are less significant than on the NW European shelf. The median of the M_2 AVD is 2.22 cm in these shelf seas and the mean value is 3.92 cm. The RMS differences of DEBOT-a in the "shelf seas elsewhere" are comparable to other models results without extremal values, as you can see in Table 5.2 and Figure 5.5.

Finally, DEBOT-a is also comparable with the other models along continental coastlines, see Table 5.3 and Figure 5.7. Some tidal station locations are deemed by DEBOT to be land and these stations are not included in the RMS and MAD statistics. This is a little inconsistent with the RMS and median values from other models which were computed from all coastal stations using

Table 5.1: Tidal signals and RMS differences of DEBOT-a and state-of-the-art empirical and assimilative models against the deep ocean BPR stations (in cm).

	Q_1	O_1	P_1	K_1	N_2	M_2	S_2	K_2	RSS
Signal	1.79	8.75	3.99	12.51	6.36	30.22	11.21	3.12	36.62
DEBOT-a	**0.214**	**0.363**	**0.288**	**0.498**	**0.264**	**0.573**	**0.406**	**0.389**	**1.106**
DTU10	0.226	0.277	0.292	0.449	0.274	0.613	0.415	0.383	1.088
GOT4.8	0.165	0.296	0.234	0.423	0.252	0.510	0.369	0.209	0.923
OSU12	0.304	0.369	0.194	0.430	0.441	0.578	0.940	0.287	1.395
EOT11a	0.232	0.317	0.224	0.404	0.335	0.564	0.428	0.365	1.056
HAMTIDE	0.160	0.317	0.199	0.373	0.245	0.513	0.397	0.176	0.904
FES2012	0.216	0.309	0.355	0.471	0.342	0.658	0.407	0.223	1.120
TPXO8	0.153	0.310	0.181	0.442	0.201	0.523	0.338	0.151	0.894

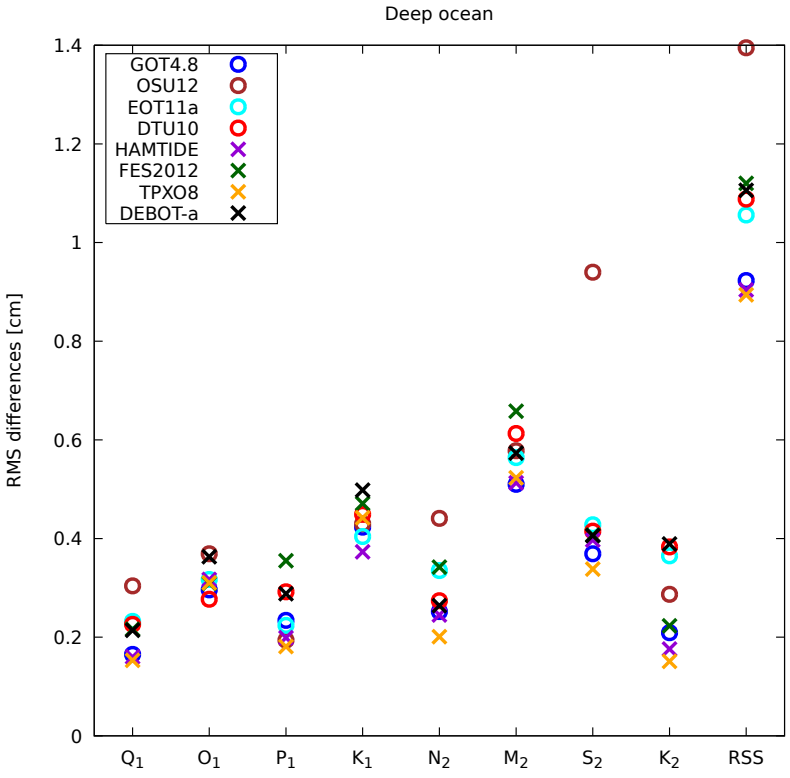

Figure 5.4: The RMS differences of DEBOT-a and state-of-the-art empirical and assimilative models against the deep ocean BPR stations.

Table 5.2: Tidal signals and RMS differences of DEBOT-a and state-of-the-art empirical and assimilative models against the shelf seas tidal stations (in cm).

	Q_1	O_1	P_1	K_1	N_2	M_2	S_2	K_2	RSS
NW European shelf									
Signal	2.1	5.6	1.5	5.5	17.0	87.7	30.0	7.3	94.9
DEBOT-a	**0.84**	**0.79**	**0.41**	**1.21**	**2.32**	**6.25**	**2.72**	**1.19**	**7.50**
DTU10	0.83	0.81	0.51	1.27	2.17	3.50	2.38	0.92	5.17
GOT4.8	0.93	0.92	0.55	1.30	1.97	5.87	2.51	1.09	7.04
OSU12	1.11	1.24	0.69	1.53	1.77	5.04	4.04	1.29	7.22
EOT11a	0.85	0.83	0.50	1.24	2.13	5.53	3.43	1.13	7.17
HAMTIDE	0.92	1.96	0.47	1.14	1.65	3.11	2.64	0.92	5.14
FES2012	0.88	0.82	0.71	1.19	1.39	3.71	1.94	0.63	4.82
TPXO8	0.88	0.72	0.46	1.21	1.58	3.85	1.70	0.74	4.87
Shelf seas elsewhere									
Signal	2.7	10.9	5.9	17.1	12.5	54.0	21.7	7.1	63.6
DEBOT-a	**0.82**	**1.12**	**1.00**	**1.68**	**1.81**	**4.01**	**2.51**	**1.65**	**5.84**
DTU10	0.82	1.11	1.06	1.70	1.80	3.44	2.39	1.57	5.40
GOT4.8	0.69	1.05	0.92	1.68	1.97	4.14	2.93	1.59	6.11
OSU12	1.00	1.17	0.84	1.75	1.87	4.61	3.00	1.15	6.42
EOT11a	0.73	1.07	0.78	1.64	1.86	5.05	3.39	1.31	6.87
HAMTIDE	0.97	1.16	0.80	2.02	2.01	3.89	2.52	1.44	5.88
FES2012	0.80	1.00	0.89	1.51	1.58	3.33	2.30	1.02	4.96
TPXO8	0.82	1.00	0.82	1.47	2.00	3.50	1.93	1.12	5.07

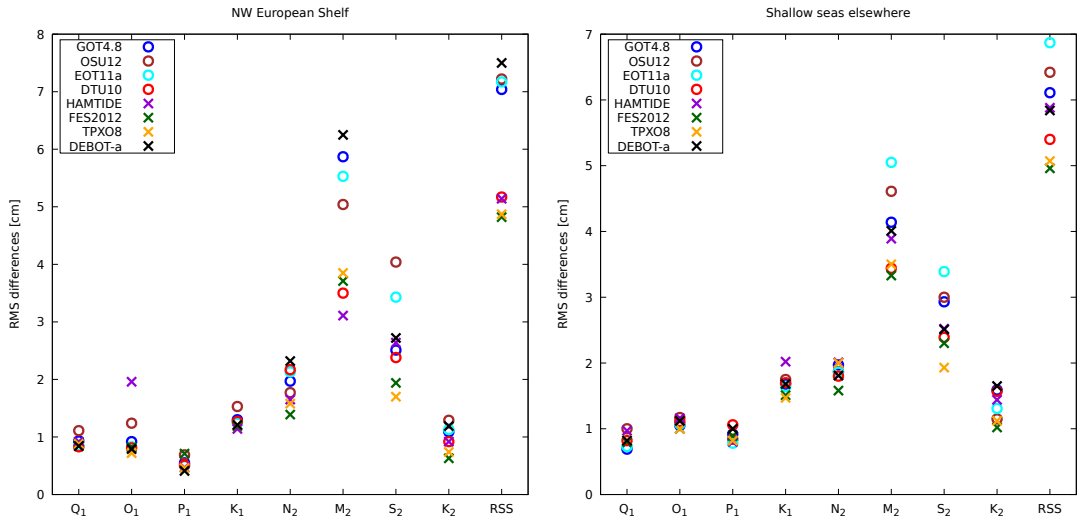

Figure 5.5: The RMS differences of DEBOT-a and state-of-the-art empirical and assimilative models against the tidal stations on the NW European shelf (left) and in shallow seas elsewhere (right).

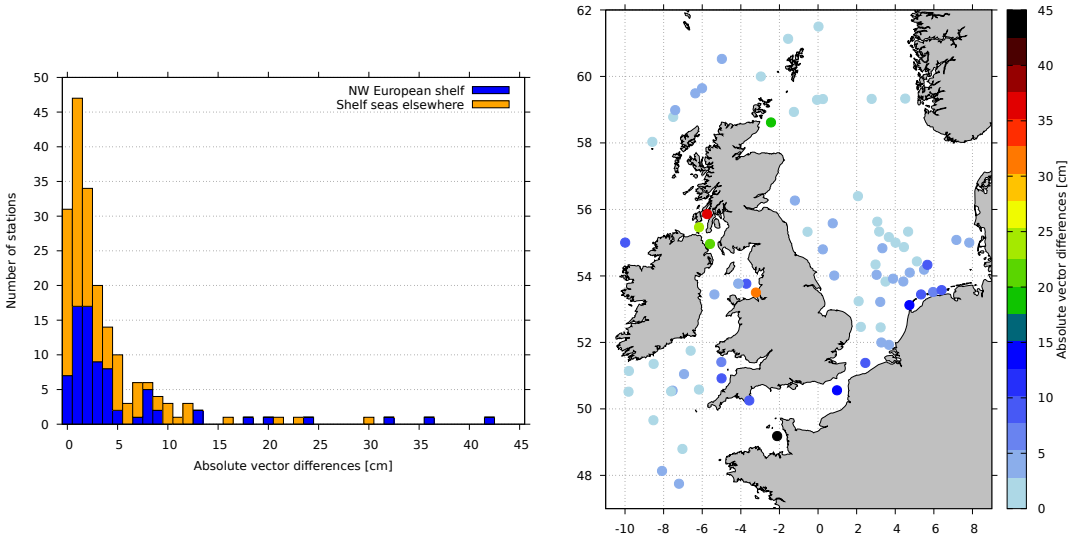

Figure 5.6: Left: Histogram of the absolute vector differences between DEBOT-h and the shallow seas tidal stations (the mean value of all stations is 4.56 cm, the median is 2.52 cm). Right: Map of the tidal stations on the northwest European shelf and their AVD indicated by a color.

some extrapolation where it was necessary (Stammer et al., 2014). Hence, the median statistic is probably more meaningful than the RMS in this case. Nevertheless, the DEBOT-a results are good when compared to the other models, regardless of the used method.

At the end of this section, we present a comparison of tidal currents. There is no global testing dataset of tidal currents, hence we compare DEBOT-h, DEBOT-a, TPXO8 and FES2012 with each other. Table 5.4 shows global signals of the transports $h\vec{v}$ computed for DEBOT-h, DEBOT-a, TPXO8 and FES2012 and the RMS differences of the transports between the models. The RMS differences are also shown in Figure 5.8. The model transports or velocities are not directly constrained by any measurements, therefore the differences might be relatively high. The RMS differences DEBOT-h/TPXO8 and DEBOT-h/FES2012 are higher than DEBOT-a/TPXO8 and DEBOT-a/FES2012, respectively, for all eight major tidal constituents, especially for M_2 and S_2. The RMS differences DEBOT-a/TPXO8, DEBOT-a/FES2012 and TPXO8/FES2012 are approximately the same. This suggests that the assimilative models are better in a prediction of tidal currents than purely hydrodynamical DEBOT-h, however none of the three assimilative models is probably significantly better than the other two. Unfortunately, without a global testing dataset of tidal transports or velocities, it is impossible to say which assimilative model provides the most realistic tidal currents.

Table 5.3: Tidal signals, RMS differences and median absolute differences of DEBOT-a and state-of-the-art empirical and assimilative models against the coastal tide gauges (in cm).

	Q_1	O_1	P_1	K_1	N_2	M_2	S_2	K_2	RSS
Signal	1.9	9.7	4.9	15.9	11.2	55.5	21.4	6.0	63.8
RMS differences									
DEBOT-a	**0.49**	**1.06**	**0.65**	**1.74**	**1.47**	**5.68**	**2.87**	**1.17**	**6.99**
DTU10	0.62	1.29	0.73	2.08	1.72	5.24	2.68	1.40	6.82
GOT4.8	0.46	1.01	0.57	1.80	1.92	7.00	3.53	1.34	8.47
OSU12	1.14	1.68	1.20	3.20	2.15	9.01	5.31	1.41	11.48
EOT11a	0.54	1.32	0.85	2.38	1.78	4.50	2.84	1.49	6.49
HAMTIDE	0.29	1.42	0.71	2.65	2.27	14.63	5.41	1.80	16.17
FES2012	0.32	0.89	0.61	1.65	1.74	6.60	2.27	0.77	7.50
TPXO8	0.43	1.13	0.93	2.01	3.34	15.65	7.79	2.12	18.10
Median absolute differences									
DEBOT-a	**0.16**	**0.34**	**0.28**	**0.56**	**0.37**	**1.20**	**0.64**	**0.40**	**1.64**
DTU10	0.21	0.37	0.37	0.67	0.42	1.28	0.77	0.42	1.83
GOT4.8	0.14	0.42	0.27	0.62	0.60	1.30	0.80	0.37	1.87
OSU12	0.35	0.46	0.26	0.62	0.59	1.19	1.58	0.34	2.27
EOT11a	0.18	0.36	0.30	0.61	0.41	1.06	0.65	0.32	1.56
HAMTIDE	0.12	0.46	0.27	0.68	0.40	1.02	0.66	0.28	1.57
FES2012	0.18	0.43	0.44	0.66	0.47	1.36	0.66	0.24	1.85
TPXO8	0.13	0.26	0.25	0.58	0.28	1.49	0.49	0.21	1.75

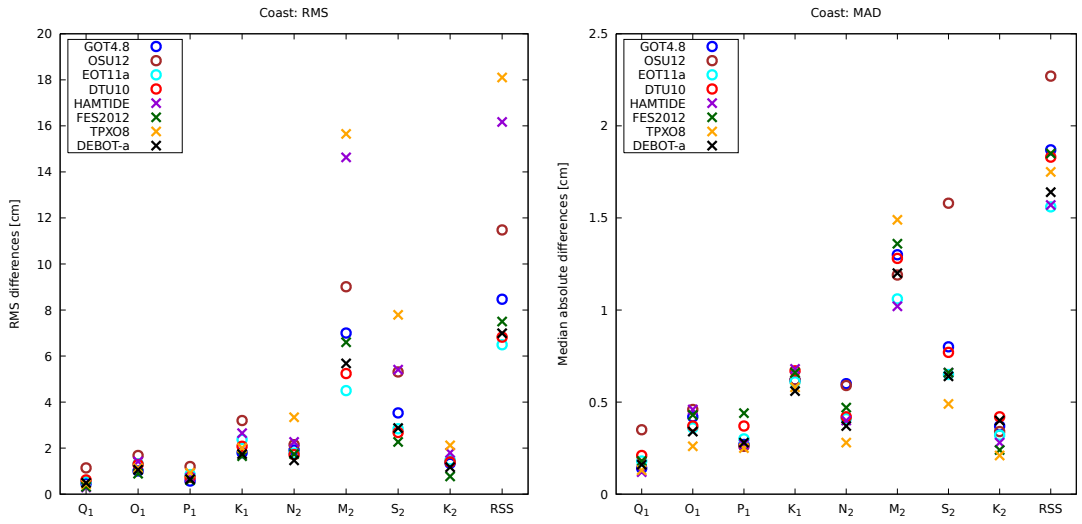

Figure 5.7: The RMS differences (left) and median absolute differences (right) of DEBOT-a and state-of-the-art empirical and assimilative models against the coastal tide gauges.

Table 5.4: Global signals of the transports $h\vec{v}$ computed for DEBOT-h, DEBOT-a, TPXO8 and FES2012 and the RMS differences between the models (in $\frac{m^2}{s}$).

	Q_1	O_1	P_1	K_1	N_2	M_2	S_2	K_2	RSS
					Signal				
DEBOT-h	3.31	15.18	6.06	18.25	10.35	53.58	22.16	5.99	64.16
DEBOT-a	3.11	13.89	6.32	19.49	11.24	53.66	22.24	6.64	64.55
TPXO8	3.08	16.25	7.02	23.22	10.78	51.97	21.37	6.01	64.59
FES2012	5.37	19.10	8.17	25.76	11.46	54.56	22.13	6.32	69.00
					RMS differences				
DEBOT-h/DEBOT-a	1.63	7.29	2.28	8.52	4.09	21.75	10.45	4.00	27.36
DEBOT-h/TPXO8	1.57	10.08	3.82	15.22	4.07	22.35	10.51	3.62	31.46
DEBOT-a/TPXO8	1.46	8.01	3.54	13.20	1.84	7.68	3.75	2.28	18.30
DEBOT-h/FES2012	4.43	14.05	5.60	19.10	5.06	26.28	11.51	3.77	38.42
DEBOT-a/FES2012	4.40	12.57	5.29	17.70	3.33	14.79	5.85	2.53	28.09
TPXO8/FES2012	4.22	13.20	5.92	20.33	3.02	13.85	4.85	1.40	29.44

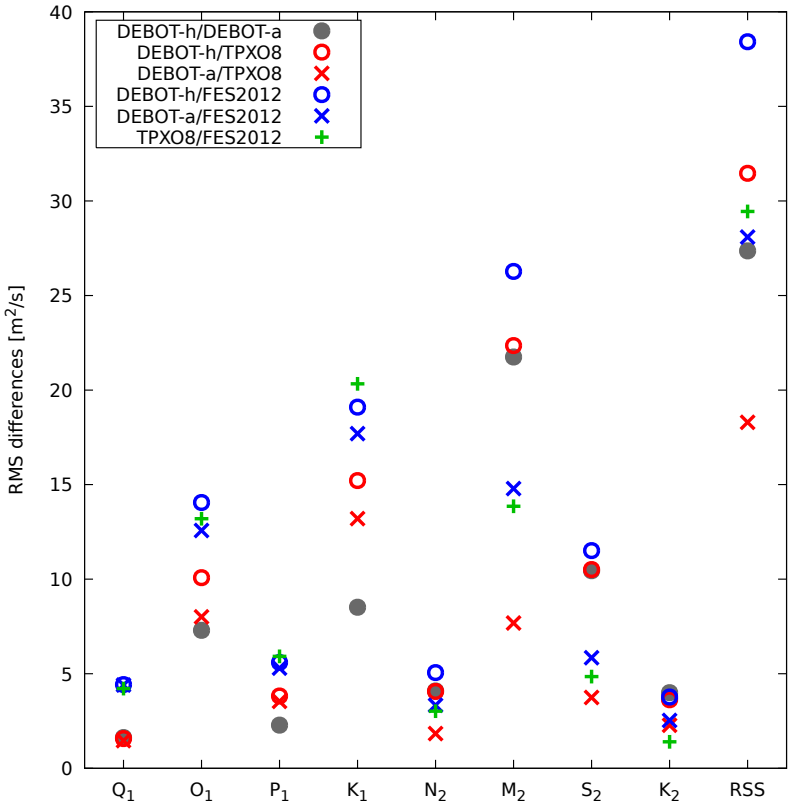

Figure 5.8: Global RMS differences of the transports $h\vec{v}$ between DEBOT-h, DEBOT-a, TPXO8 and FES2012.

CHAPTER

6

MODELLING OF MINOR TIDAL CONSTITUENTS

So far, our attention has been focused on the eight major tides only. However, as DEBOT is a non-linear ocean model forced by the full lunisolar potential of the second and third degree, it allows us to model all tidal constituents simultaneously including non-linear compound tides. Although signals of minor constituents are generally very small compared to the major constituents (especially to M_2), reaching amplitudes usually several millimeters in the deep ocean and several centimeters in the shallow shelf seas, knowledge of them might still be useful in some applications. Hence in this chapter, we deal with DEBOT predictions of selected minor tides. However, we should note that long-term tides of greater periods than diurnal (e.g., fortnightly Mf, monthly Mm, semi-annual Ssa, etc.) are not addressed here due to lack of high-quality testing data. There is a great need for a global test dataset of long-period tides, however it would require very long time-series to distinguish such tidal signals from the background noise (Ray, 2013; Stammer et al., 2014).

Minor tidal constituents are usually not included in global ocean models except for M_4 which is a part of six of the seven modern empirical and assimilative models mentioned in the previous chapter (HAMTIDE is the exception). TPXO8 includes also the non-linear MN_4 and MS_4 tides, however only FES2012 provides global atlases of larger number of tidal constituents, 33 tides in total.

Analogously to the previous chapters, we compute the RMS differences and MAD for selected minor tidal constituents. The constituents was chosen so that DEBOT can be compared to other models. We also excluded those tides which were detected at only a few stations. For example, the R_2 harmonic con-

Table 6.1: Selected minor tidal constituents, their tidal signals and RMS differences between the deep ocean BPR stations and the ocean models (in cm).

		RMS differences			
	Signal	**DEBOT-a**	GOT4.8	FES2012	TPXO8
$2Q_1$	0.25	**0.093**	0.085		
J_1	0.71	**0.344**	0.178	0.131	
OO_1	0.43	**0.376**	0.265		
$2N_2$	0.80	**0.226**	0.271	0.119	
μ_2	0.95	**0.229**	0.409	0.197	
ν_2	1.13	**0.375**	0.075	0.129	
L_2	0.75	**0.393**	0.250	0.235	
T_2	0.63	**0.294**	0.130	0.194	
R_2	0.12	**0.102**		0.101	
M_3	0.23	**0.096**		0.231	
MN_4	0.09	**0.082**		0.073	0.068
M_4	0.22	**0.092**	0.089	0.115	0.075
MS_4	0.12	**0.113**		0.104	0.134

stants are provided by only five shelf seas stations overall and thus, R_2 is excluded from the shelf seas comparison. Final results are summarized in Tables 6.1 (deep ocean) and 6.2 (shelf seas) and graphically in Figure 6.1. DEBOT-a is compared to FES2012, TPXO8 (for three compound tides) and in the deep ocean also to GOT4.8 whose values were inferred from the tidal admittance (Ray, 2013). In Figure 6.1, we also plot values from DEBOT-h to show that the assimilation process, described in Section 5.2, does not affect minor tides. Of course, this is not a case of M_4 which is constrained by the DTU10 dataset.

The values inferred from GOT4.8 in the deep ocean are generally better than the DEBOT-a ones except for $2N_2$ and μ_2. This suggests that it could be beneficial for DEBOT-a—at least in the deep ocean—to be constrained by another data of harmonic constants of minor diurnal and semi-diurnal tides deduced from an empirical model using the tidal admittance. The results of FES2012 are generally better than DEBOT-a for diurnal and semi-diurnal tides but DEBOT-a is obviously better for third-diurnal M_3 owing to the implemented forcing term of the third degree. Regarding non-linear MN_4, M_4 and MS_4, the results of all three models, DEBOT-a, FES2012 and TPXO8, seem to be roughly equal except for the NW European shelf where TPXO8 predictions are significantly better, probably due to a very high resolution of $2'$ for shelf areas. As mentioned, M_4 is included also in DTU10, EOT11a and OSU12. Their RMS differences and MAD against the tidal stations are not shown here but they are roughly the same as in the case of DEBOT-a.

In the deep ocean, the relative RMS differences for minor diurnal and semi-diurnal tides are about 10–30 % of the signal (except for very small R_2) which is the same as for the eight major tides. This suggests that possible future

Table 6.2: Selected minor tidal constituents, their tidal signals, RMS differences and median absolute differences between the shelf seas tidal stations and ocean models (in cm).

		RMS differences			*Median absolute differences*		
	Signal	**DEBOT-a**	FES2012	TPXO8	**DEBOT-a**	FES2012	TPXO8
			NW European shelf				
J_1	0.92	**0.938**	0.872		**0.307**	0.210	
μ_2	4.44	**3.947**	1.104		**0.835**	0.586	
ν_2	3.24	**2.195**	1.034		**0.516**	0.729	
L_2	4.57	**2.686**	1.769		**1.133**	0.897	
T_2	1.99	**1.650**	0.712		**0.733**	0.535	
M_3	0.92	**0.557**	1.000		**0.174**	0.341	
MN_4	1.76	**1.812**	1.141	0.717	**0.625**	0.478	0.274
M_4	4.68	**2.772**	2.270	1.183	**0.707**	0.770	0.420
MS_4	2.91	**3.024**	1.847	1.157	**0.806**	0.716	0.451
			Shelf seas elsewhere				
J_1	0.85	**0.544**	0.423		**0.323**	0.100	
$2N_2$	1.70	**1.100**	0.547		**0.546**	0.244	
μ_2	2.44	**1.998**	1.749		**0.649**	0.461	
ν_2	2.18	**1.272**	0.648		**0.832**	0.313	
L_2	3.13	**2.543**	1.911		**0.872**	0.632	
T_2	1.69	**1.040**	0.558		**0.586**	0.366	
M_3	1.18	**0.544**	1.027		**0.171**	0.508	
MN_4	1.45	**1.067**	0.914	0.597	**0.306**	0.306	0.163
M_4	1.82	**1.254**	0.946	0.928	**0.373**	0.257	0.317
MS_4	1.49	**1.498**	1.331	1.515	**0.345**	0.446	0.562

improvements of DEBOT-h discussed in Section 4.4 (finer resolution, more rigorous treatment of the ITD and SAL) should also lead to more precise determination of minor tidal constituents. In the shelf seas, the relative differences of minor tides are much larger, however, we should emphasize that the RMS differences and MAD for the minor tides in the shelf seas are computed from relatively small number of stations (see Table 4.1 in Section 4.2) and thus they can not provide a general description of a global model and are rather indicative.

In Appendix B, global charts of minor tidal constituents are plotted. Figures B.17–B.36 show the surface elevation amplitudes and Greenwich phase lags from DEBOT-a and FES2012 for reference and also the absolute value differences of the surface elevation between DEBOT-a and FES2012.

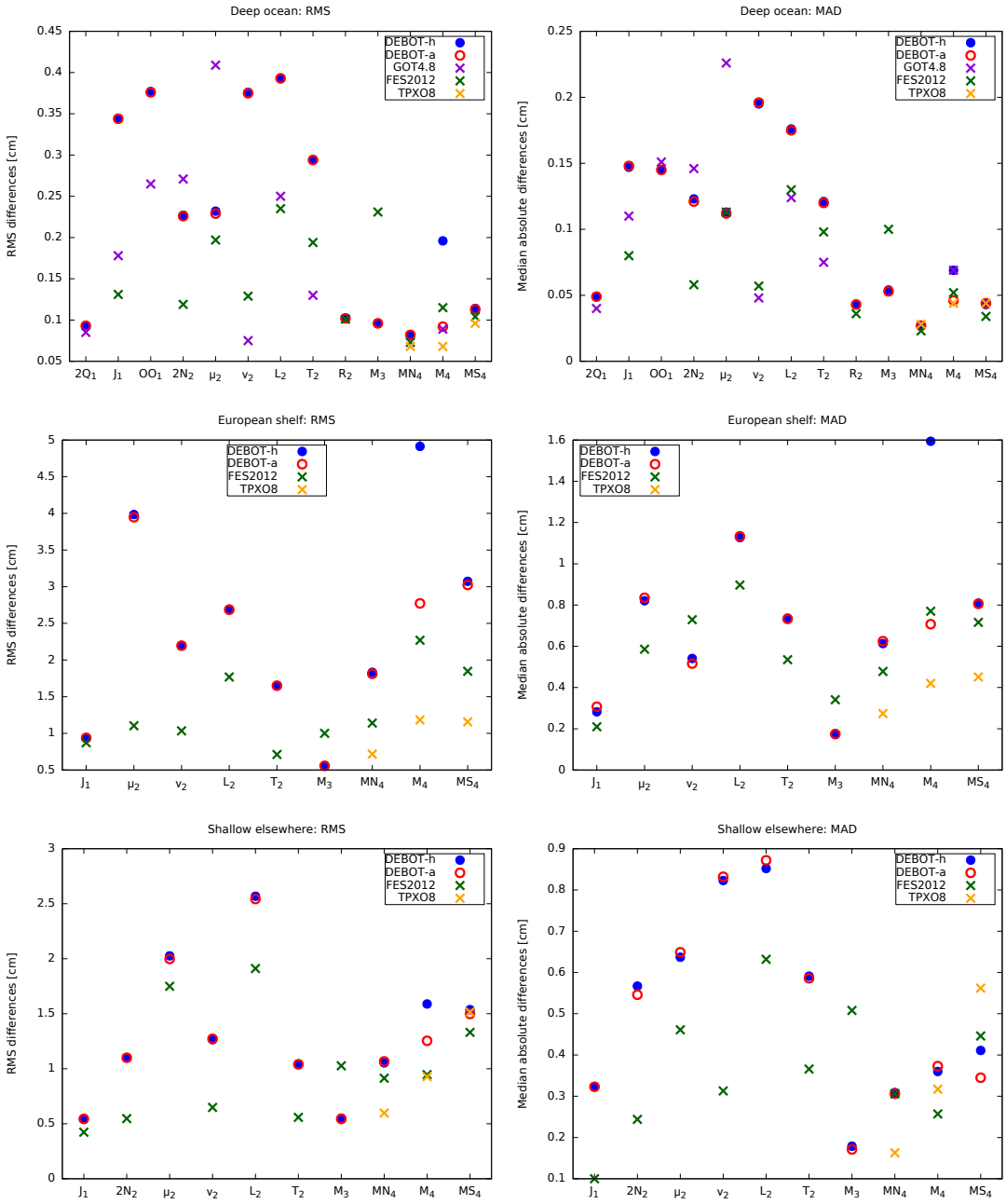

Figure 6.1: The RMS differences (left) and median absolute differences (right) between the ocean models and the deep ocean (top) and shelf seas (middle and bottom) tidal stations for selected minor tidal constituents.

CONCLUSIONS

The DEBOT model, a time-domain global barotropic ocean model has been developed and is presented in this thesis. DEBOT is primarily designed for ocean flow generated by the tidal attraction of the Moon and the Sun, however, it can be used for other ocean applications where the shallow water approximation is convenient, for instance, tsunami wave propagation.

In Chapter 1, the shallow water equations in the geographical coordinates are derived from the complete Navier-Stokes equations, including the full stress tensor with the Reynolds tensor which is usually omitted when performing this derivation and then, a posteriori, added into the final shallow water equations.

The shallow water equations are a base for the numerical model which is described in Chapter 2. The conservation of the total mass and the total energy of the numerical model is tested (Section 2.3). The series of synthetic tests, which comprise a tsunami wave propagating through the global ocean with an artificial island, is presented (Figures 2.2 and 2.3). The results of the tests are satisfactory, meaning that the total mass is preserved in all experiments and the total energy is preserved in the case of zero eddy viscosity and decreases with a non-zero viscosity (Figure 2.4). The eddy viscosity can effectively attenuate the energy, however, a too large eddy viscosity coefficient makes the computations unstable and results in an obviously unnatural increase in the energy.

As mentioned, DEBOT is designed for precise global ocean tides simulations. The model can be launched in two modes: the purely hydrodynamical mode, DEBOT-h, and assimilative mode, DEBOT-a.

Purely hydrodynamical DEBOT-h is presented in Chapter 4. DEBOT-h predictions are tested against the datasets of the deep ocean BPR stations, shelf seas tidal station and tide gauges along continental coastlines. A parametric study at the $15' \times 15'$ spatial resolution has been performed to investigate effects of input parameters and to find the best setting. The parametric study reveals that

(1) GEBCO is a generally better choice of the bathymetric dataset than ETOPO.
(2) The ITD scaling factor κ should be spatially dependent.
(3) The scalar approximation of the SAL is rather crude and should be replaced by some more rigorous formulation. Unfortunately, our attempts with an iterative scheme of the SAL were unsuccessful and hence, it is an open question how the SAL should be treated in our time-domain model.
(4) The eddy viscosity has hardly any effect on resulted ocean tides however it should still be included in the model to avoid numerical instabilities.
(5) The bottom friction is important only in the shelf seas and coastal areas and has almost no effect in the deep ocean which is an expected behaviour.

DEBOT-h is comparable in accuracy with the state-of-the-art purely hydrodynamical models (Table 4.3) in the shelf seas however it is a bit worse in the deep ocean which may be caused by a coarser resolution, the scalar approximation of the SAL or the parameterization of the ITD. A more rigorous treatment of the ITD and SAL and their possible implementation in DEBOT will be addressed in future works in order to reach generally better accuracy.

We also compares DEBOT-h with its data-assimilative version, DEBOT-a to find possible problematic areas of purely hydrodynamical modelling (Figures 4.9 and 4.10). Larger errors are produced in the Southern ocean which is caused by the omission of the ice-covered Weddel and Ross seas from the DEBOT model domain. These seas should be definitively included in future version of DEBOT.

The energy and dissipation properties are also documented. The total dissipation is 4–4.5 TW for various model parameters (Figure 4.11), larger than the observed value of 3.5 TW, however a similar behaviour is common for many other non-assimilative models. DEBOT-h also dissipates too much energy in the deep ocean, about 50 % of the dissipation occurs in waters deeper than 1000 m for the $15' \times 15'$ spatial resolution while the realistic amount is about 40 %. A better ratio of the deep ocean dissipation is achieved at the higher resolutions of $6' \times 6'$ and $10' \times 10'$.

DEBOT-a, the assimilative version of DEBOT, is introduced in Chapter 5. The author proposes a simply yet efficient assimilation scheme which can be used in a time-domain model and it is an alternative to spectral-domain general inversion schemes used in FES, TPXO and HAMTIDE. The surface elevation are periodically constrained by the elevations of the empirical model DTU10. The tests against the "ground truth" tidal data prove that DEBOT-a is comparable in accuracy with the state-of-the-art empirical and assimilative ocean tide models though there are still some locations where DEBOT-a does not reach desired accuracy, e.g., for semi-diurnal tides on the northwest European shelf. We believe that future improvements of prior hydrodynamical model (DEBOT-h) will allow us to achieve better results with DEBOT-a, also in the problematic locations.

Finally, minor tidal constituents and their model predictions are discussed

in Chapter 6. As DEBOT is a non-linear model with the full lunisolar forcing, all tidal constituents can be modelled simultaneously. Selected minor tides modelled by DEBOT-a are tested against the tidal stations and compared with FES2012, TPXO8 and minor tides inferred from GOT4.8. Three conclusions can be drawn:

(1) Good results for M_3 (in comparison with FES2012).
(2) Roughly equal predictions of the non-linear compound MN_4, M_4 and MS_4 tides as FES and TPXO8, except for the NW European shelf where TPXO8 is better.
(3) Generally worse predictions of diurnal and semi-diurnal minor tides than FES and GOT4.8. These tides are not constrained by data and are given by the purely hydrodynamical solution. The future improvements of DEBOT-h, discussed above, should lead to a better estimation of the minor tides too.

DEBOT can be useful for those applications where other ocean tide models are not suitable. The primary goal and original motivation was to use DEBOT for the research conducted in related geophysical disciplines. The model has already been used to study the magnetic field induced by ocean tides (Velímský et al., 2016) and the influence of ocean tides on the Earth's rotation (Schindelegger et al., 2016). The source code of DEBOT is freely available at `http://geo.mff.cuni.cz/~einspigel/debot.html`.

BIBLIOGRAPHY

Y. Accad and C. L. Pekeris. Solution of the tidal equations for the M_2 and S_2 tides in the world oceans from a knowledge of the tidal potential alone. *Phil. Trans. R. Soc. A*, 290(1368):235–266, 1978.

D. C. Agnew. Earth tides. In *Treatise on Geophysics*, pages 163–195. Elsevier, 2007.

C. Amante and B. W. Eakins. ETOPO1 1 arc-minute global relief model: Procedures, data sources and analysis. NOAA Technical Memorandum NESDIS NGDC-24, 19 pp, March 2009.

A. Arakawa and V. L. Lamb. Computational design of the basic dynamical processes of the UCLA general circulation model. In J. Chang, editor, *Methods in Computational Physics, Vol. 17*, pages 174–265. Academic Press, 1977.

B. K. Arbic, S. T. Garner, R. W. Hallberg, and Simmons H. L. The accuracy of surface elevations in forward global barotropic and baroclinic tide models. *Deep-Sea Res. II*, 51:3069–3101, 2004. doi: 10.1016/j.dsr2.2004.09.014.

B. K. Arbic, J. X. Mitrovica, D. R. MacAyeal, and G. A. Milne. On the factors behind large Labrador Sea tides during the last glacial cycle and the potential implications for Heinrich events. *Paleoceanography*, 23:PA3211, 2008. doi: 10.1029/2007PA001573.

B. K. Arbic, A. J. Wallcraft, and E. J. Metzger. Concurrent simulation of the eddying general circulation and tides in a global ocean model. *Ocean Model.*, 32:175–187, 2010.

J. O. Backhaus. A semi-implicit scheme for the shallow water equations for application to shelf sea modeling. *Cont. Sh. Res*, 2(4):243–254, 1983.

A. J. C. Barré de Saint-Venant. Théorie du mouvement non-permanent des eaux, avec application aux crues des rivières et à l'introduction des marées dans leur lit. *C. R. Acad. Sc. Paris*, 73:147–153, 1871.

G. K. Batchelor. *An Introduction to Fluid Dynamics*. Cambridge Univ. Press, Cambridge, UK, 1967.

R. C. Beardsley, T. F. Duda, J. F. Lynch, J. D. Irish, R. S. Ramp, C.-S. Chiu, T. Y. Tang, Y.-J. Yang, and G. Fang. Barotropic tide in the northeast South China Sea. *IEEE J. Oceanic Eng.*, 29:1075–1086, 2004.

J. V. Boussinesq. Essai sur la théorie des eaux courantes, 1877. Mémoires présentés par divers savants à l'Académie des Sciences XXIII.

D. Bresch and B. Desjardins. Existence of weak solutions for 2D viscous shallow water equations and convergence to the quasi-geostrophic model. *Comm. Math. Phys.*, 238(1,2):211–223, 2003.

E. W. Brown. Theory of the motion of the Moon (Part IV). *Mem. R. astr. Soc.*, 57:51–145, 1905.

L. Carrère, F. Lyard, M. Cancet, A. Guillot, and L. Roblou. FES 2012: A new global tidal model taking advantage of nearly 20 years of altimetry. Paper presented at The Symposium 20 Years of Progress in Radar Altimetry, Venice, 2012.

D. E. Cartwright. *Tides: A Scientific History*. Cambridge University Press, 1999.

D. E. Cartwright and A. C. Edden. Corrected tables of tidal harmonics. *Geophys. J. R. astr. Soc.*, 33:253–264, 1973.

D. E. Cartwright and R. J. Tayler. New computations of the tide-generating potential. *Geophys. J. R. astr. Soc.*, 23:45–74, 1971.

Y. Cheng and O. B. Andersen. Multimission empirical ocean tide modeling for shallow waters and polar seas. *J. Geophys. Res.*, 116(C11001):540–552, 2012.

G. H. Darwin. Report of a committee for the harmonic analysis of tidal observations. *Brit. Ass. Rep.*, pages 48–118, 1883.

A. T. Doodson. The harmonic development of the tide-generating potential. *Proc. R. Soc. A*, 100(704):305–329, 1921.

A. T. Doodson. The analysis of tidal observations. *Phil. Trans. R. Soc. A*, 227: 223–279, 1928.

A. T. Doodson and H. D. Warburg. *Admiralty manual of tides*. H.M.S.O. [for] the Hydrographic Department, Admiralty, London, 1941.

G. D. Egbert and S. Y. Erofeeva. Efficient inverse modeling of barotropic ocean tides. *J. Atmos. Oceanic Tech.*, 19:183–204, 2002.

G. D. Egbert and R. D. Ray. Significant dissipation of tidal energy in the deep ocean inferred from satellite altimeter data. *Nature*, 405:775–778, 2000.

G. D. Egbert and R. D. Ray. Semi-diurnal and diurnal tidal dissipation from TOPEX/Poseidon altimetry. *Geophys. Res. Lett.*, 30(17):1907, 2003. doi: 10.1029/2003GL017676.

G. D. Egbert, A. F. Bennett, and M. G. G. Foreman. TOPEX/Poseidon tides estimated using a global inverse model. *J. Geophys. Res.*, 99:24821–24852, 1994.

G. D. Egbert, R. D. Ray, and B. G. Bills. Numerical modeling of the global semidiurnal tide in the present day and in the last glacial maximum. *J. Geophys. Res.*, 109(C03003), 2004. doi: 10.1029/2003JC001973.

D. Einšpigel. Barotropic ocean tide model. Master's thesis, Charles University in Prague, Prague, May 2012.

D. Einšpigel and Z. Martinec. A new derivation of the shallow water equations in geographical coordinates and their application to the global barotropic ocean model (the DEBOT model). *Ocean Modelling*, 92:85–100, 2015.

D. Einšpigel and Z. Martinec. Time-domain modelling of global ocean tides generated by the full lunisolar potential. *submitted to Ocean Dyn.*, 2016.

W. Emery and R. Thompson. *Data analysis methods in physical oceanography*. Pergamon Press, 1998.

C. L. Fefferman. Existence and smoothness of the Navier–Stokes equation, 2000. URL `http://www.claymath.org/millennium/Navier-Stokes_Equations/navierstokes.pdf`. The Clay Mathematics Institute, Cambridge (Massachusetts).

S. Ferrari and F. Saleri. A new two dimensional shallow water model including pressure effects and slow varying bottom topography. *ESAIM: Mathematical Modelling and Numerical Analysing*, 38:211–234, 2004.

H. S. Fok. *Ocean tides modeling using satellite altimetry*. PhD thesis, Ohio State University, Columbus, 2012.

L.-L. Fu and A. Cazenave, editors. *Satellite Altimetry and Earth Sciences: A Handbook of Techniques and Applications*. Academic Press, San Diego, California, 2001.

P. Gent. The energetically consistent shallow water equations. *J. Atmos. Sci.*, 50:1323–1325, 1993.

J.-F. Gerbeau and B. Perthame. Derivation of viscous saint-venant system for laminar shallow water; numerical validation. *Discrete Contin. Dyn. Syst. Ser. B*, 1(1):89–102, 2000.

J. A. M. Green and J. Nycander. A comparison of internal wave-drag parameterizations for tidal model. *J. Phys. Oceanogr.*, 43:104–119, 2013. doi: 10.1175/JPO-D-12-023.1.

S. D. Griffiths and W. R. Peltier. Modeling of polar ocean tides at the last glacial maximum: Amplification, sensitivity, and climatological implications. *J. Climate*, pages 2905–2924, 2009. doi: 10.1175/2008JCLI2540.1.

T. Hartmann and H.-G. Wenzel. The HW95 tidal potential catalogue. *Geophys. Res. Lett.*, 22:3553–3556, 1995.

D. F. Hill, S. D. Griffiths, W. R. Peltier, B. P. Horton, and T. E. Törnqvist. High-resolution numerical modeling of tides in the western atlantic, gulf of mexico, and caribbean sea during the holocene. *J. Geophys. Res.*, 116(C10014), 2011. doi: 10.1029/2010JC006896.

E. W. Hobson. *The Theory of Spherical and Ellipsoidal Harmonics*. Cambridge University Press, 1965.

K. Hutter and K. Jöhnk. *Continuum Methods of Physical Modeling*. Springer-Verlag, Berlin, 2004.

IHO. Harmonic constants product specification, 2006.

IOC, IHO, and BODC. Centenary edition of the GEBCO digital atlas. published on CD-ROM on behalf of the Intergovernmental Oceanographic Commission and the International Hydrographic Organization as part of the General Bathymetric Chart of the Oceans, 2003.

S. R. Jayne and L. C. St. Laurent. Parameterizing tidal dissipation over rough topography. *Geophys. Res. Lett.*, 28(5):811–814, 2001.

R. L. Kolar, W. G. Gray, J. J. Westerink, and Jr. R. A. Luettich. Shallow water modeling in spherical coordinates: equation formulation, numerical implementation, and application. *J. Hydraul. Res.*, 32(1):3–24, 1994.

S. M. Kudryavtsev. Improved harmonic development of the earth tide-generating potential. *J. Geodesy*, 77:829–838, 2004.

A. Kuvshinov and N. Olsen. 3-D modelling of the magnetic fields due to ocean tidal flow. In C. Reigber, H. Lühr, P. Schwintzer, and J. Wickert, editors, *Earth Observation with CHAMP. Results from Three Years in Orbit*, pages 359–366. Springer-Verlag, Berlin, 2005.

D. K. Lilly. On the computational stability of the time-dependent nonlinear geophysical fluid dynamics problem. *Mon. Wea. Rev.*, 93:141–154, 1965.

R. A. Locarnini, A. V. Mishonov, J. I. Antonov, T. P. Boyer, H. E. Garcia, O. K. Baranova, M. M. Zweng, C. R. Paver, J. R. Reagan, D. R. Johnson, M. Hamilton, and D. Seidov. Volume 1: Temperature. In S. Levitus and A. Mishonov, editors, *World Ocean Atlas 2013*. NOAA Atlas NESDIS 73, 2013.

F. Lyard, F. Lefevre, T. Letellier, and O. Francis. Modelling the global ocean tides: Modern insights from FES2004. *Ocean Dyn.*, 56:394–415, 2006.

F. Marche. Derivation of a new two-dimensional viscous shallow water model with varying topography, bottom friction and capillary effects. *European Journal of Mechanics - B/Fluids*, 26(1):49–63, 2006.

Z. Martinec. Continuum mechanics (lecture notes), 2011. URL `http://geo.mff.cuni.cz/vyuka/Martinec-ContinuumMechanics.pdf`. Charles University in Prague.

J. C. McWilliams. *Fundamentals of geophysical fluid dynamics*. Cambridge University Press, 2006.

P. Melchior. Earth tides and polar motions. In A. R. Ritsema, editor, *The Upper Mantle*, chapter 13, pages 361–372. Elsevier, Amsterdam, 1972.

M. Müller, J. Y. Cherniawsky, M. G. G. Foreman, and J.-S. von Storch. Global map of M_2 internal tide and its seasonal variability from high resolution ocean circulation and tide modeling. *Geophys. Res. Lett*, 39(L19607), 2012. doi: 10.1029/2012GL053320.

W. Munk. Testimony before the U.S. Commission on Ocean Policy, 2002. URL `http://govinfo.library.unt.edu/oceancommission/meetings/apr18_19_02/munk_statement.pdf`.

W. H. Munk and D. E. Cartwright. Tidal spectroscopy and prediction. *Phil. Trans. Roy. Soc. A*, 259(1105):553–581, 1966.

O. Novotný. *Motions, gravity field and figure of the Earth*. Universidade Federal de Bahia, Salvador, Bahia, Brazil, 1998. URL `http://geo.mff.cuni.cz/studium/Novotny-Motions-GravityField-FigureOfTheEarth.pdf`. Lecture notes for post-graduate students.

J. Nycander. Generation of internal waves in the deep ocean by tides. *J. Geophys. Res.*, 110(C10028), 2005. doi: 10.1029/2004JC002487.

J. Ochoa, J. Sheinbaum, and A. Jimenez. Lateral friction in reduced-gravity models: Parameterizations consistent with energy dissipation and conservation of angular momentum. *J. Phys. Oceanogr.*, 41:1894–1901, 2011.

M. E. Parke. O_1, P_1, N_2 models of the global ocean tide on an elastic earth plus surface potential and spherical harmonic decompositions for M_2, S_2, and K_1. *Mar. Geod.*, 6(1):35–81, 1982.

M. E. Parke and M. C. Hendershott. M_2, S_2, K_1 models of the global ocean tide on an elastic earth. *Mar. Geod.*, 3:379–408, 1980.

B. B. Parker. *Tidal Analysis and Prediction*. NOAA, Silver Spring, Maryland, 2007. NOAA Special NOS CO-OPS 3.

J. Pedlosky. *Geophysical fluid dynamics*. Springer-Verlag, New York, 2nd edition, 1987.

C. L. Pekeris and Y. Accad. Solution of Laplace's equations for the M_2 tide in the world oceans. *Philos. Trans. R. Soc. A*, A265:413–436, 1969.

F. Ponchaut, F. Lyard, and C. Le Provost. An analysis of the tidal signal in the WOCE sea level dataset. *J. Atmos. Oceanic Technol.*, 18:77–91, 2001.

S. Pond and G. L. Pickard. *Introductory dynamical oceanography*. Butterworh-Heinemann, Oxford, 2nd edition, 1983.

D. T. Pugh. *Tides, Surges and Mean Sea-Level*. John Wiley & Sons, 1987.

D. A. Randall. *An Introduction to Numerical Modeling of the Atmosphere*, chapter 12: Finite Differences on the Sphere. Colorado State University, 2013. URL `http://kiwi.atmos.colostate.edu/group/dave/at604pdf/Chapter_12.pdf`.

R. D. Ray. Ocean self-attraction and loading in numerical tidal model. *Mar. Geod.*, 21(3):181–192, 1998.

R. D. Ray. A global ocean tide model from Topex/Poseidon altimetry: GOT99.2. Technical report, Goddard Space Flight Center, Greenbelt, Maryland, 1999. NASA Tech. Memo. 209478.

R. D. Ray. Inversion of oceanic tidal currents from measured elevations. *J. Mar. Syst.*, 28:1–18, 2001.

R. D. Ray. Precise comparisons of bottom-pressure and altimetric ocean tides. *J. Geophys. Res. Oceans*, 118:4570–4584, 2013. doi: 10.1002/jgrc.20336.

R. D. Ray and G. D. Egbert. The global S_1 tide. *J. Phys. Oceanogr.*, 34:1922–1935, 2004.

R. D. Ray, G. D. Egbert, and S. Y. Erofeeva. Tide predictions in shelf and coastal waters: Status and prospects. In S. Vignudelli, A.G. Kostianoy, P. Cipollini, and J Benveniste, editors, *Coastal Altimetry*, pages 191–216. Springer-Verlag, Berlin, 2011.

O. Reynolds. On the dynamical theory of incompressible viscous fluids and the determination of the criterion. *Phil. Trans. R. Soc. London A*, 186:123–164, 1895.

A. Richter, L. Mendoza, R. Perdomo, J. Hormaechea, R. Savcenko, W. Bosch, and R. Dietrich. Pressure tide gauge records from the Atlantic shelf off Tierra del Fuego, southernmost South America. *Cont. Shelf Res.*, 42:20–29, 2012.

F. Roosbeek. RATGP95: a harmonic development of the tide-generating potential using an analytical method. *Geophys. J. Int.*, 126:197–204, 1996.

T. J. Sabaka, N. Olsen, R. H. Tyler, and A. Kuvshinov. CM5, a pre-Swarm comprehensive geomagnetic field model derived from over 12 yr of CHAMP, Ørsted, SAC-C and observatory data. *Geophys. J. Int.*, 200:1596–1626, 2015. doi: 10.1093/gji/ggu493.

C. Sammari, V. G. Koutitonsky, and M. Moussa. Sea level variability and tidal resonance in the Gulf of Gabes, Tunisia. *Cont. Shelf Res.*, 26:338–350, 2006.

R. Savcenko and W. Bosch. EOT11a — Empirical ocean tide model from multi-mission satellite altimetry. Technical report, Deutsches Geodätisches Forschungsinstitut, München, 2012. DGFI Report No. 89.

C. Schär and R. Smith. Shallow water flow past isolated topography. Part I: Vortex production and wake. *J. Atmos. Sci.*, 50:1373–1400, 1993.

M. Schindelegger, D. Einšpigel, D. Salstein, and J. Böhm. The global S_1 tide in Earth's nutation. *Surv. Geophys.*, 2016. doi: 10.1007/s10712-016-9365-3.

F. G. Schmitt. About Boussinesq's turbulent viscosity hypothesis: historical remarks and a direct evaluation of its validity. *C. R. Mécanique*, 335(9):617–627, 2007.

P. Schureman. *Manual of harmonic analyses and prediction of tides*. U.S. Department of Commerce, Washington, D.C., 1941.

E. W. Schwiderski. Global ocean tides: Part II. The semidiurnal principal lunar tide 884 (M_2). Atlas of tidal charts and maps. Technical report, Naval Surface Weapons Center, Dahlgren, Virginia, 1979.

E. W. Schwiderski. Ocean tides. Part II: A hydrodynamic interpolation. *Mar. Geod.*, 3:219–255, 1980.

G. Seeber. *Satellite Geodesy*. Walter de Gruyter, Berlin, Germany, 2nd edition, 2003.

A. F. Shchepetkin and J. C. McWilliams. The regional oceanic modeling system (ROMS): a split-explicit, free-surface, topography-following-coordinate oceanic model. *Ocean Model.*, 9:347–404, 2005.

A. F. Shchepetkin and J. C. McWilliams. Computational kernel algorithms for fine-scale, multi-process, long-time oceanic simulations. In R. Temam and J. Tribbia, editors, *Handbook of Numerical Analysis: Computational Methods for the Ocean and the Atmosphere*, pages 121–183. Elsevier Science, 2008. ISBN: 978-0-444-51893-4.

A. F. Shchepetkin and J. J. O'Brien. A physically consistent formulation of lateral friction in shallow water equation ocean models. *Monthly Weather Review*, 124:1285–1300, 1996.

C. K. Shum, P. L. Woodworth, O. B. Andersen, G. D. Egbert, O. Francis, C. King, S. M. Klosko, C. Le Provost, X. Li, J.-M. Molines, M. E. Parke, R. D. Ray, M. G. Schlax, D. Stammer, C. C. Tierney, P. Vincent, and C. I. Wunsch. Accuracy assessment of recent ocean tide models. *J. Geophys. Res.*, 102(C11):173–194, 1997.

H. L. Simmons, R. W. Hallberg, and B. K. Arbic. Internal wave generation in a global baroclinic tide model. *Deep-Sea Res. II*, 51:3043–3068, 2004. doi: 10.1016/j.dsr2.2004.09.015.

J. L. Simon, P. Bretagnon, J. Chapront, M. Chaprount-Touzé, G. Francou, and J. Laskar. Numerical expressions for precession formulae and mean elements for the Moon and planets. *Astron. Astrophys.*, 282:663–683, 1994.

A. J. E. Smith. *Application of satellite altimetry for global ocean tide modeling*. PhD thesis, Delft University of Technology, Delft, 1999.

D. Stammer, R. D. Ray, O. B. Andersen, B. K. Arbic, W. Bosch, L. Carrère, Y. Cheng, D. S. Chinn, B. D. Dushaw, G. D. Egbert, S. Y. Erofeeva, H. S. Fok, J. A. M. Green, S. Griffiths, M. A. King, V. Lapin, F. G. Lemoine, S. B. Luthcke, F. Lyard, J. Morison, M. Müller, L. Padman, J. G. Richman, J. F. Shriver, C. K. Shum, E. Taguchi, and Y. Yi. Accuracy assessment of global barotropic ocean tide models. *Rev. Geophys.*, 52, 2014. doi: 10.1002/2014RG000450.

E. Taguchi, W. Zahel, and D. Stammer. Inferring deep ocean tidal energy dissipation from the global high-resolution data-assimilative HAMTIDE model. *J. Geophys. Res. Oceans*, 119:4573–4592, 2014.

Y. Tamura. A harmonic development of the tide-generating potential. *Bull. Info. Marées Terrestres*, 99:6813–6855, 1987.

R. S. Tyler, S. Maus, and H. Lühr. Satellite observations of magnetic fields due to ocean tidal flow. *Science*, 299:239–240, 2003.

G. K. Vallis. *Atmospheric and oceanic fluid dynamics*. Cambridge University Press, Cambridge, 2006.

J. Velímský, Z. Martinec, L. Šachl, D. Einšpigel, and L. Hanyk. Magnetic signatures of barotropic and baroclinic flows in Swarm data. Technical report, Charles University, 2016. ESA Study Contract Report No. 4000109562/14/NL/CBi.

P. N. A. M. Visser, N. Sneeuw, T. Reubelt, M. Losch, and T. van Dam. Space-borne gravimetric satellite constellation and ocean tides: Aliasing effects. *Geophys. J. Int.*, 181:789–805, 2010.

V. Vlasenko, N. Stashchuk, and K. Hutter. *Baroclinic Tides: Theoretical Modeling and Observational Evidence*. Cambridge Univ. Press, Cambridge, U.K., 2005.

R. C. Wajsowicz. A consistent formulation of the anisotropic stress tensor for use in models of the large-scale ocean circulation. *J. Comput. Phys.*, 105:333–338, 1993.

P. Weis. *Ocean tides and the Earth's rotation — results of a high-resolving ocean model force by the lunisolar tidal potential*. PhD thesis, University of Hamburg, 2006.

P. Weis, M. Thomas, and J. Sündermann. Broad frequency tidal dynamics simulated by a high-resolution global ocean tide model forced by ephemerides. *J. Geophys. Res.*, 113(C10), 2008. doi: 10.1029/2007JC004556.

G. P. Williams. Friction term formulation and convective instability in a shallow atmosphere. *J. Atmos. Sci.*, 29:870–876, 1972.

Q. Xi. A new complete development of the tide-generating potential for the epoch J2000.0. *Bull. Info. Marées Terrestres*, 99:6766–6812, 1987.

W. Zahel. Assimilating ocean tide determined data into global tidal models. *J. Mar. Syst.*, 6:3–13, 1995.

E. D. Zaron and G. D. Egbert. Estimating open-ocean barotropic tidal dissipation: The Hawaiian Ridge. *J. Phys. Oceanogr.*, 36:1019–1035, 2006.

M. M. Zweng, J. R. Reagan, J. I. Antonov, R. A. Locarnini, A. V. Mishonov, T. P. Boyer, H. E. Garcia, O. K. Baranova, D. R. Johnson, D. Seidov, and M. M. Biddle. Volume 2: Salinity. In S. Levitus and A. Mishonov, editors, *World Ocean Atlas 2013*. NOAA Atlas NESDIS 74, 2013.

APPENDIX

A

INVARIANT DIFFERENTIAL OPERATORS

Below we briefly introduce curvilinear orthogonal coordinates and summarize important formulae for invariant differential operators in the general right-handed curvilinear orthogonal coordinates and in the geographical coordinates. For more information and the derivation of the formulae, see, e.g., Batchelor (1967); Martinec (2011).

A.1 Basic formulae

Given the Cartesian coordinates of a point P in the 3D space (y_1,y_2,y_3). We can define a system of curvilinear coordinates by specifying three coordinate transformation functions x_k.

$$x_k = x_k(y_1,y_2,y_3) \quad \text{for } k = 1,2,3, \tag{A.1}$$

which are C^1 (continuous first partial derivatives) and the Jacobian of the transformation is nonzero almost everywhere

$$j = \det\left(\frac{\partial x_k}{\partial y_l}\right) \neq 0. \tag{A.2}$$

Then there is a unique inverse of (A.1)

$$y_k = y_k(x_1,x_2,x_3) \quad \text{for } k = 1,2,3. \tag{A.3}$$

The geographical coordinates $r, \phi, \lambda (x_1 \equiv r, x_2 \equiv \phi, x_3 \equiv \lambda)$ are defined by the relations to the rectangular Cartesian coordinates

$$y_1 = r\cos\phi\cos\lambda, \quad y_2 = r\cos\phi\sin\lambda, \quad y_3 = r\sin\phi, \tag{A.4}$$

or inversely

$$r = \sqrt{y_1^2 + y_2^2 + y_3^2}, \quad \phi = \arctan\left(\frac{y_3}{\sqrt{y_1^2 + y_2^2}}\right), \quad \lambda = \arctan\left(\frac{y_2}{y_1}\right). \tag{A.5}$$

The inverse of the Jacobian j is given

$$j^{-1} = r^2 \cos\phi. \tag{A.6}$$

Given the rectangular Cartesian unit base vectors $\vec{i}_1, \vec{i}_2, \vec{i}_3$ and the position vector $\vec{p}$ of the point P, which can be expressed as

$$\vec{p} = p_k \vec{i}_k. \tag{A.7}$$

Then the curvilinear coordinate unit base vectors can be defined by the relations

$$\vec{e}_k = \frac{1}{h_k}\frac{\partial \vec{p}}{\partial x_k}, \quad \text{for } k = 1,2,3, \tag{A.8}$$

where h_k are the scale factors, so-called the Lamé coefficients which are defined by the relation

$$h_k = \sqrt{\frac{\partial \vec{p}}{\partial x_k} \cdot \frac{\partial \vec{p}}{\partial x_k}}. \tag{A.9}$$

We assume that new curvilinear coordinates are orthogonal and the base vectors form a right-hand system, i.e.

$$\vec{e}_k \cdot \vec{e}_l = \delta_{kl}, \quad \vec{e}_k \times \vec{e}_l = \varepsilon_{klm}\vec{e}_m, \tag{A.10}$$

where δ_{kl} is the Kronecker delta and ε_{klm} is the Levi-Civita symbol

$$\delta_{kl} = \begin{cases} 1, & \text{if } k = l, \\ 0, & \text{if } k \neq l, \end{cases} \tag{A.11}$$

$$\varepsilon_{klm} = \begin{cases} +1, & \text{if } (k,l,m) \text{ is } (1,2,3), (3,1,2) \text{ or } (2,3,1), \\ -1, & \text{if } (k,l,m) \text{ is } (1,3,2), (3,2,1) \text{ or } (2,1,3), \\ 0, & \text{if } k = l \text{ or } l = m \text{ or } k = m. \end{cases} \tag{A.12}$$

The Lamé coefficients in the geographical coordinates are

$$h_r = 1, \quad h_\phi = r, \quad h_\lambda = r\cos\phi. \tag{A.13}$$

The unit base vectors $\vec{e}_k$ are functions of position and vary in direction. Therefore spatial derivatives of this base vectors are not zero:

$$\frac{\partial \vec{e}_k}{\partial x_l} = \sum_m \Gamma_{kl}^m \vec{e}_m, \tag{A.14}$$

where Γ_{kl}^{m} are the Christoffel symbols, which can be explicitly expressed by

$$\Gamma_{kl}^{m} = \frac{1}{h_k}\frac{\partial h_l}{\partial x_k}\delta_{lm} - \frac{1}{h_m}\frac{\partial h_k}{\partial x_m}\delta_{kl}. \tag{A.15}$$

Now we can write formulae for the partial derivatives of any vector or tensor. The partial derivative of a vector $\vec{v}$ can be formulated as

$$\frac{\partial \vec{v}}{\partial x_m} = \sum_k v_{k;l}\vec{e}_k, \tag{A.16}$$

where $v_{k;l}$ is the balanced derivative of v_k with respect to x_l

$$v_{k;l} = \frac{\partial v_k}{\partial x_l} + \sum_m \Gamma_{ml}^{k} v_m. \tag{A.17}$$

The partial derivative of a second-order tensor $\mathbf{T}$ can be formulated as

$$\frac{\partial \mathbf{T}}{\partial x_m} = \sum_{kl} T_{kl;m}\vec{e}_k \otimes \vec{e}_l, \tag{A.18}$$

where $T_{kl;m}$ is the balanced derivative of T_{kl} with respect to x_l

$$T_{kl;m} = \frac{\partial T_{kl}}{\partial x_m} + \sum_n \Gamma_{nm}^{k} T_{nl} + \sum_n \Gamma_{nm}^{l} T_{kn}. \tag{A.19}$$

A.2 Invariant differential operators

With use of the previous formulae we can express the invariant differential operators in the curvilinear orthogonal coordinates.

The gradient of a scalar:

$$\nabla f = \frac{1}{h_k}\frac{\partial f}{\partial x_k}\vec{e}_k \tag{A.20}$$

In the geographical coordinates:

$$\nabla f = \frac{\partial f}{\partial r}\vec{e}_r + \frac{1}{r\cos\phi}\frac{\partial f}{\partial \lambda}\vec{e}_\lambda + \frac{1}{r}\frac{\partial f}{\partial \phi}\vec{e}_\phi \tag{A.21}$$

The divergence of a vector:

$$\nabla \cdot \vec{v} = \frac{1}{h_1 h_2 h_3}\left[\frac{\partial}{\partial x_1}(h_2 h_3 v_1) + \frac{\partial}{\partial x_2}(h_1 h_3 v_2) + \frac{\partial}{\partial x_3}(h_2 h_1 v_3)\right] \tag{A.22}$$

In the geographical coordinates:

$$\nabla \cdot \vec{v} = \frac{1}{r^2}\frac{\partial}{\partial r}(r^2 v_r) + \frac{1}{r\cos\phi}\left(\frac{\partial v_\lambda}{\partial \lambda} + \frac{\partial(\cos\phi v_\phi)}{\partial \phi}\right) \tag{A.23}$$

The curl of a vector:

$$\begin{aligned}\nabla \times \vec{v} = &\frac{1}{h_2 h_3}\left[\frac{\partial(h_3 v_3)}{\partial x_2} - \frac{\partial(h_2 v_2)}{\partial x_3}\right]\vec{e}_1 + \\ &\frac{1}{h_1 h_3}\left[\frac{\partial(h_1 v_1)}{\partial x_3} - \frac{\partial(h_3 v_3)}{\partial x_1}\right]\vec{e}_2 + \\ &\frac{1}{h_1 h_2}\left[\frac{\partial(h_2 v_2)}{\partial x_1} - \frac{\partial(h_1 v_1)}{\partial x_2}\right]\vec{e}_3\end{aligned} \tag{A.24}$$

In the geographical coordinates:

$$\begin{aligned}\nabla \times \vec{v} = &\frac{1}{r\cos\phi}\left[\frac{\partial v_\phi}{\partial \lambda} - \frac{\partial(\cos\phi v_\lambda)}{\partial \phi}\right]\vec{e}_r + \\ &\frac{1}{r}\left[\frac{\partial v_r}{\partial \phi} - \frac{\partial(r v_\phi)}{\partial r}\right]\vec{e}_\lambda + \\ &\left[\frac{1}{r}\frac{\partial(r v_\lambda)}{\partial r} - \frac{1}{r\cos\phi}\frac{\partial v_r}{\partial \lambda}\right]\vec{e}_\phi\end{aligned} \tag{A.25}$$

The gradient of a vector:

$$(\nabla \vec{v})_{kl} = \begin{cases} \dfrac{1}{h_k}\left(\dfrac{\partial v_k}{\partial x_k} + \displaystyle\sum_{\substack{m \\ m \neq k}} \frac{1}{h_m}\frac{\partial h_k}{\partial x_m} v_m\right) & \text{if } l = k \\ \dfrac{1}{h_k}\left(\dfrac{\partial v_l}{\partial x_k} - \dfrac{1}{h_l}\dfrac{\partial h_k}{\partial x_l} v_k\right) & \text{if } l \neq k \end{cases} \tag{A.26}$$

In the geographical coordinates:

$$\begin{aligned}\nabla \vec{v} = &\frac{\partial v_r}{\partial r}\vec{e}_r \otimes \vec{e}_r + \frac{\partial v_\lambda}{\partial r}\vec{e}_r \otimes \vec{e}_\lambda + \frac{\partial v_\phi}{\partial r}\vec{e}_r \otimes \vec{e}_\phi + \\ &\frac{1}{r}\left(\frac{1}{\cos\phi}\frac{\partial v_r}{\partial \lambda} - v_\lambda\right)\vec{e}_\lambda \otimes \vec{e}_r + \frac{1}{r}\left(\frac{1}{\cos\phi}\frac{\partial v_\lambda}{\partial \lambda} + v_r - \tan\phi\, v_\phi\right)\vec{e}_\lambda \otimes \vec{e}_\lambda + \\ &\frac{1}{r\cos\phi}\left(\frac{\partial v_\phi}{\partial \lambda} + \sin\phi\, v_\lambda\right)\vec{e}_\lambda \otimes \vec{e}_\phi + \\ &\frac{1}{r}\left(\frac{\partial v_r}{\partial \phi} - v_\phi\right)\vec{e}_\phi \otimes \vec{e}_r + \frac{1}{r}\frac{\partial v_\lambda}{\partial \phi}\vec{e}_\phi \otimes \vec{e}_\lambda + \frac{1}{r}\left(\frac{\partial v_\phi}{\partial \phi} + v_r\right)\vec{e}_\phi \otimes \vec{e}_\phi\end{aligned} \tag{A.27}$$

The divergence of a second-order tensor:

$$\begin{aligned}(\nabla \cdot \mathbf{T})_l = &\frac{1}{h_1 h_2 h_3}\left[\frac{\partial}{\partial x_1}(h_2 h_3 T_{1l}) + \frac{\partial}{\partial x_2}(h_1 h_3 T_{2l}) + \frac{\partial}{\partial x_3}(h_1 h_2 T_{3l})\right] + \\ &\sum_k \frac{1}{h_k h_l}\left(\frac{\partial h_l}{\partial x_k} T_{lk} - \frac{\partial h_k}{\partial x_l} T_{kk}\right)\end{aligned} \tag{A.28}$$

In the geographical coordinates:

$$\nabla \cdot \mathbf{T} = \left[\frac{1}{r^2}\frac{\partial(r^2 T_{rr})}{\partial r} + \frac{1}{r\cos\phi}\left(\frac{\partial T_{\lambda r}}{\partial \lambda} + \frac{\partial(\cos\phi\, T_{\phi r})}{\partial \phi}\right) - \frac{1}{r}\left(T_{\lambda\lambda} + T_{\phi\phi}\right)\right]\vec{e}_r + \left[\frac{1}{r^2}\frac{\partial(r^2 T_{r\lambda})}{\partial r} + \frac{1}{r\cos\phi}\left(\frac{\partial T_{\lambda\lambda}}{\partial \lambda} + \frac{\partial(\cos\phi\, T_{\phi\lambda})}{\partial \phi}\right) + \frac{1}{r}\left(T_{\lambda r} - \tan\phi\, T_{\lambda\phi}\right)\right]\vec{e}_\lambda + \left[\frac{1}{r^2}\frac{\partial(r^2 T_{r\phi})}{\partial r} + \frac{1}{r\cos\phi}\left(\frac{\partial T_{\lambda\phi}}{\partial \lambda} + \frac{\partial(\cos\phi\, T_{\phi\phi})}{\partial \phi}\right) + \frac{1}{r}\left(T_{\phi r} + \tan\phi\, T_{\lambda\lambda}\right)\right]\vec{e}_\phi \tag{A.29}$$

The Laplacian of a scalar:

$$\Delta f = \frac{1}{h_1 h_2 h_3}\left[\frac{\partial}{\partial x_1}\left(\frac{h_2 h_3}{h_1}\frac{\partial f}{\partial x_1}\right) + \frac{\partial}{\partial x_2}\left(\frac{h_1 h_3}{h_2}\frac{\partial f}{\partial x_2}\right) + \frac{\partial}{\partial x_3}\left(\frac{h_1 h_2}{h_3}\frac{\partial f}{\partial x_3}\right)\right] \tag{A.30}$$

In the geographical coordinates:

$$\Delta f = \frac{1}{r^2}\frac{\partial}{\partial r}\left(r^2\frac{\partial f}{\partial r}\right) + \frac{1}{r^2\cos^2\phi}\frac{\partial^2 f}{\partial \lambda^2} + \frac{1}{r^2\cos\phi}\frac{\partial}{\partial \phi}\left(\cos\phi\frac{\partial f}{\partial \phi}\right) \tag{A.31}$$

The Laplacian of a vector can be best obtained by using the vector differential identity

$$\Delta\vec{v} = \nabla \times \nabla \times \vec{v} + \nabla \cdot (\nabla\vec{v}). \tag{A.32}$$

APPENDIX

B

GLOBAL CHARTS OF SELECTED TIDES

Selected tides were extracted from DEBOT simulations and their global charts are plotted and presented in this appendix. Figures B.1–B.8 show the amplitudes and Greenwich phase lags of the surface elevation and zonal and meridional transports for eight major tides, i.e., $Q_1, O1, P_1, K_1, N_2, M_2, S_2, K_2$, and for both DEBOT modes, DEBOT-h (Chapter 4) and DEBOT-a (Chapter 5). Figures B.9–B.16 show the absolute vector differences of all three variables between DEBOT-h and DEBOT-a and also between DEBOT-a and TPXO for reference. Finally, Figures B.17–B.36 show the surface elevation amplitudes and Greenwich phase lags of selected minor tides and compound tides for DEBOT-a and FES2012 for reference and also the absolute value differences of the surface elevation between DEBOT-a and FES2012. The minor and compound tides were chosen so they can be compared to the FES2012 atlas and they are: long-period S_{sa}, M_m, M_f, M_{tm}; diurnal J_1; semi-diurnal $\epsilon_2, 2N_2, \mu_2, \nu_2, \lambda_2, L_2, T_2, R_2$; ter-diurnal M_3; compound $N_4, MN_4, M_4, MS_4, M_6, M_8$. For tidal frequencies and more information about the selected tides, see Tables 3.3 and 3.6 in Chapter 3. All charts in high resolution can be downloaded from `http://geo.mff.cuni.cz/~einspigel/debot.html`.

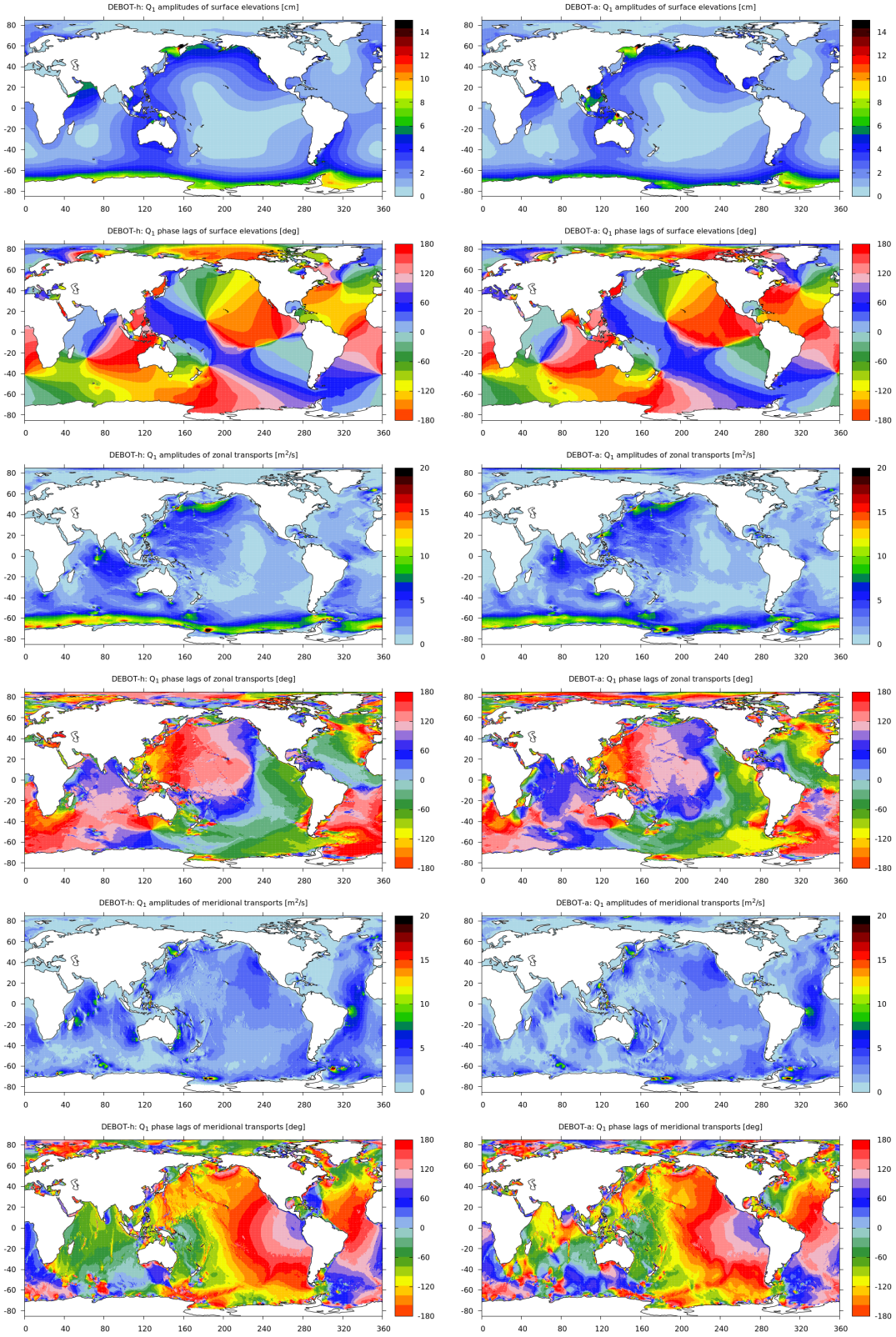

Figure B.1: DEBOT-h (left) and DEBOT-a (right): Q_1 amplitudes and Greenwich phase lags of the surface elevations (two top panels), zonal transports (two middle panels) and meridional transports (two bottom panels).

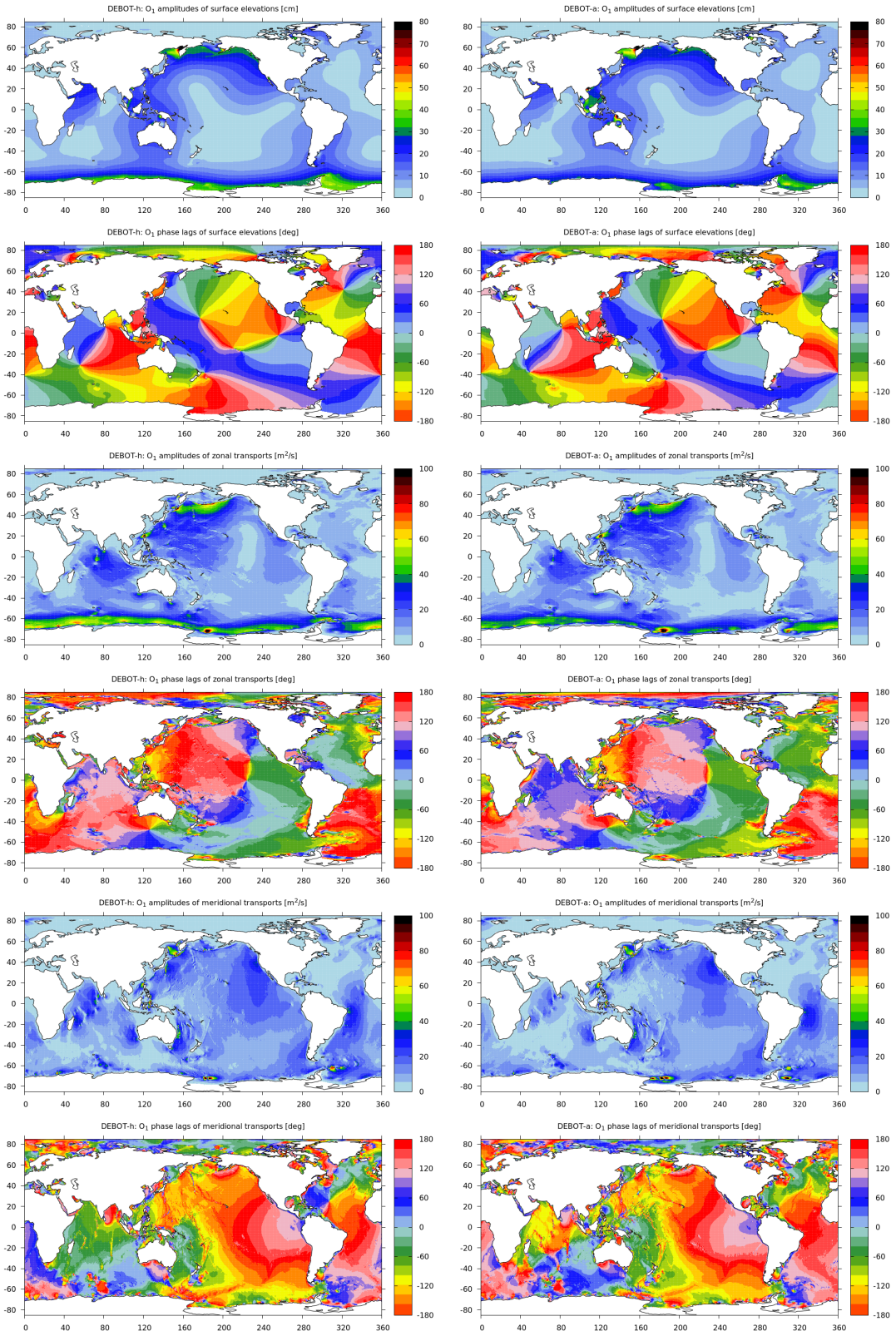

Figure B.2: DEBOT-h (left) and DEBOT-a (right): O_1 amplitudes and Greenwich phase lags of the surface elevations (two top panels), zonal transports (two middle panels) and meridional transports (two bottom panels).

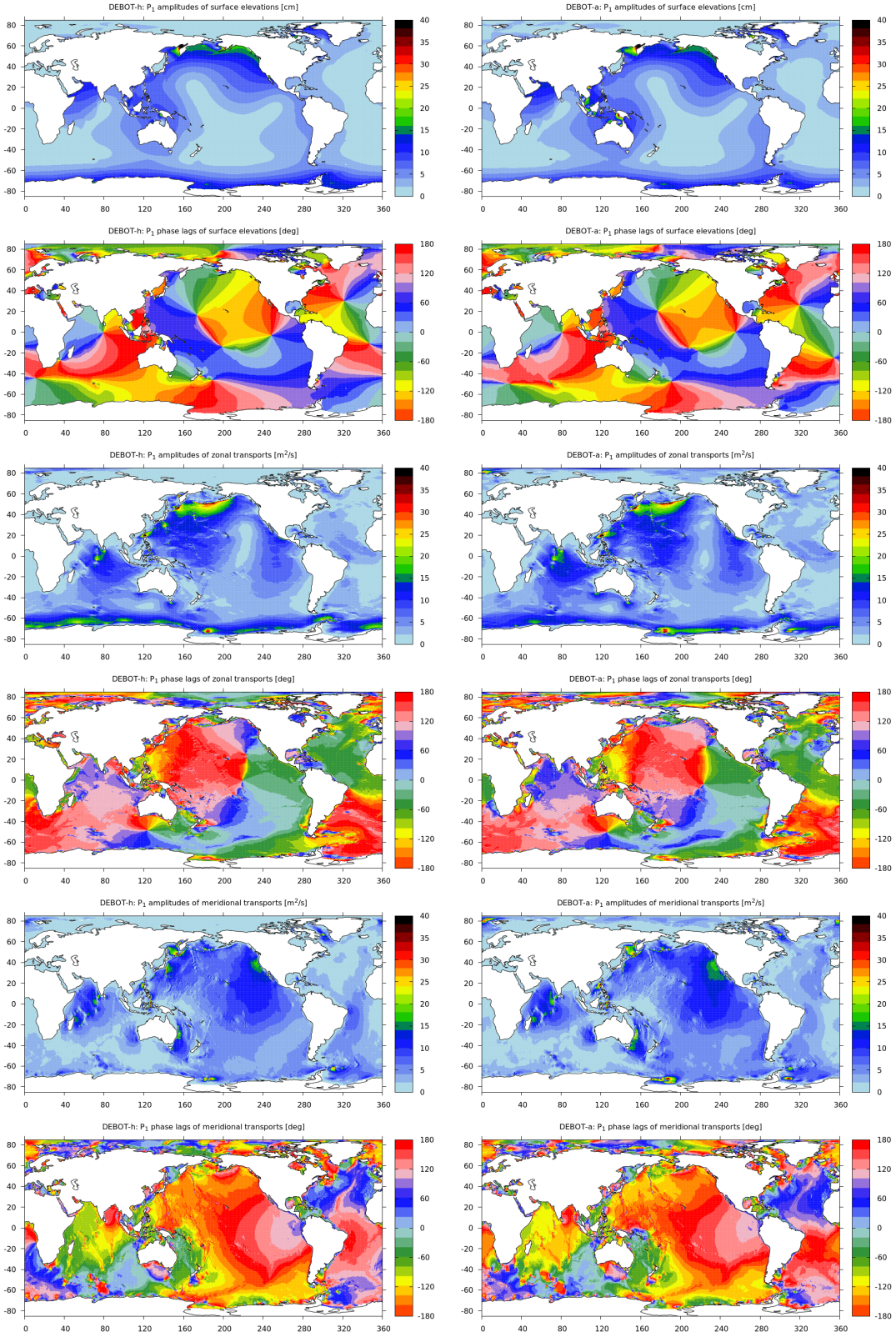

Figure B.3: DEBOT-h (left) and DEBOT-a (right): P_1 amplitudes and Greenwich phase lags of the surface elevations (two top panels), zonal transports (two middle panels) and meridional transports (two bottom panels).

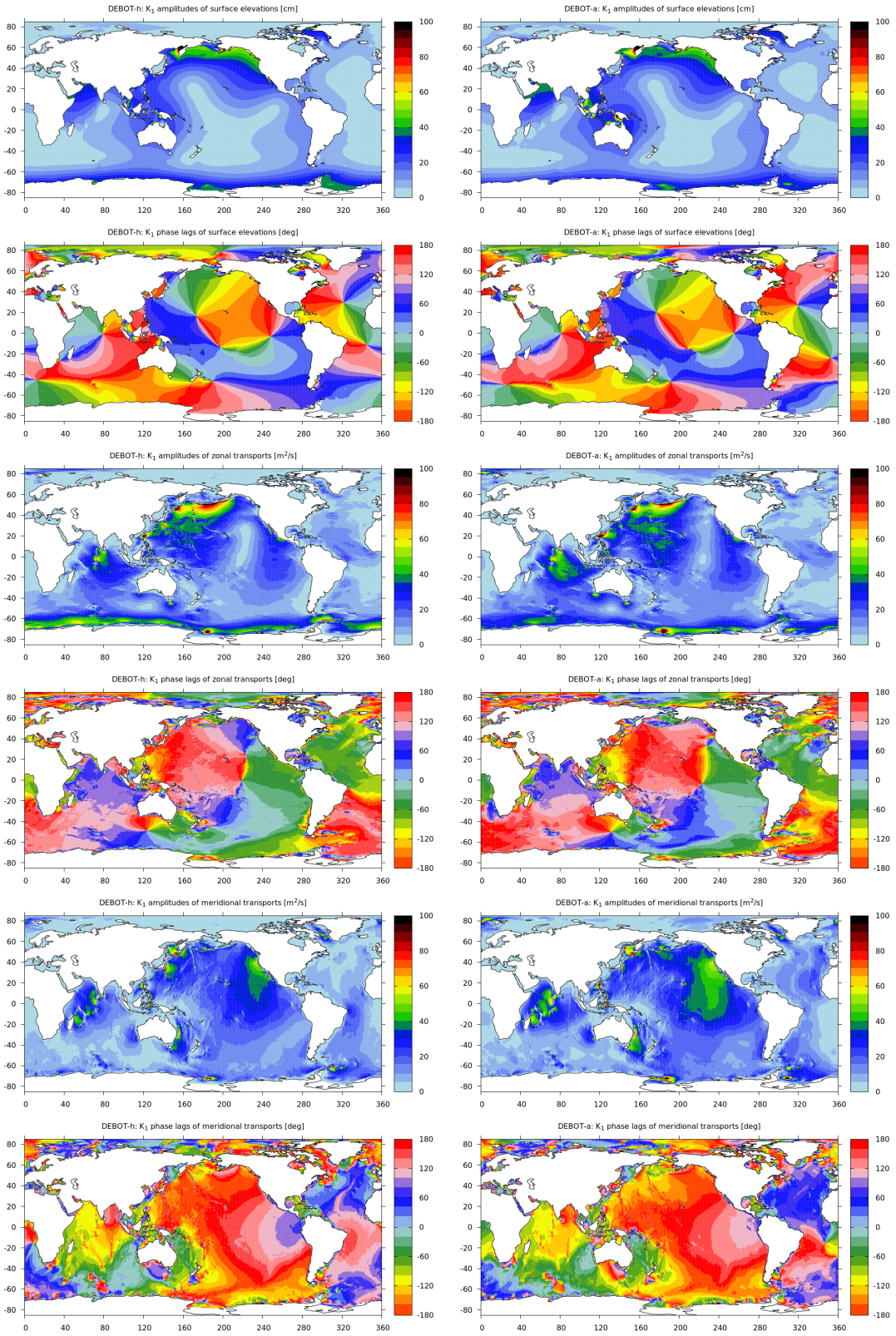

Figure B.4: DEBOT-h (left) and DEBOT-a (right): K_1 amplitudes and Greenwich phase lags of the surface elevations (two top panels), zonal transports (two middle panels) and meridional transports (two bottom panels).

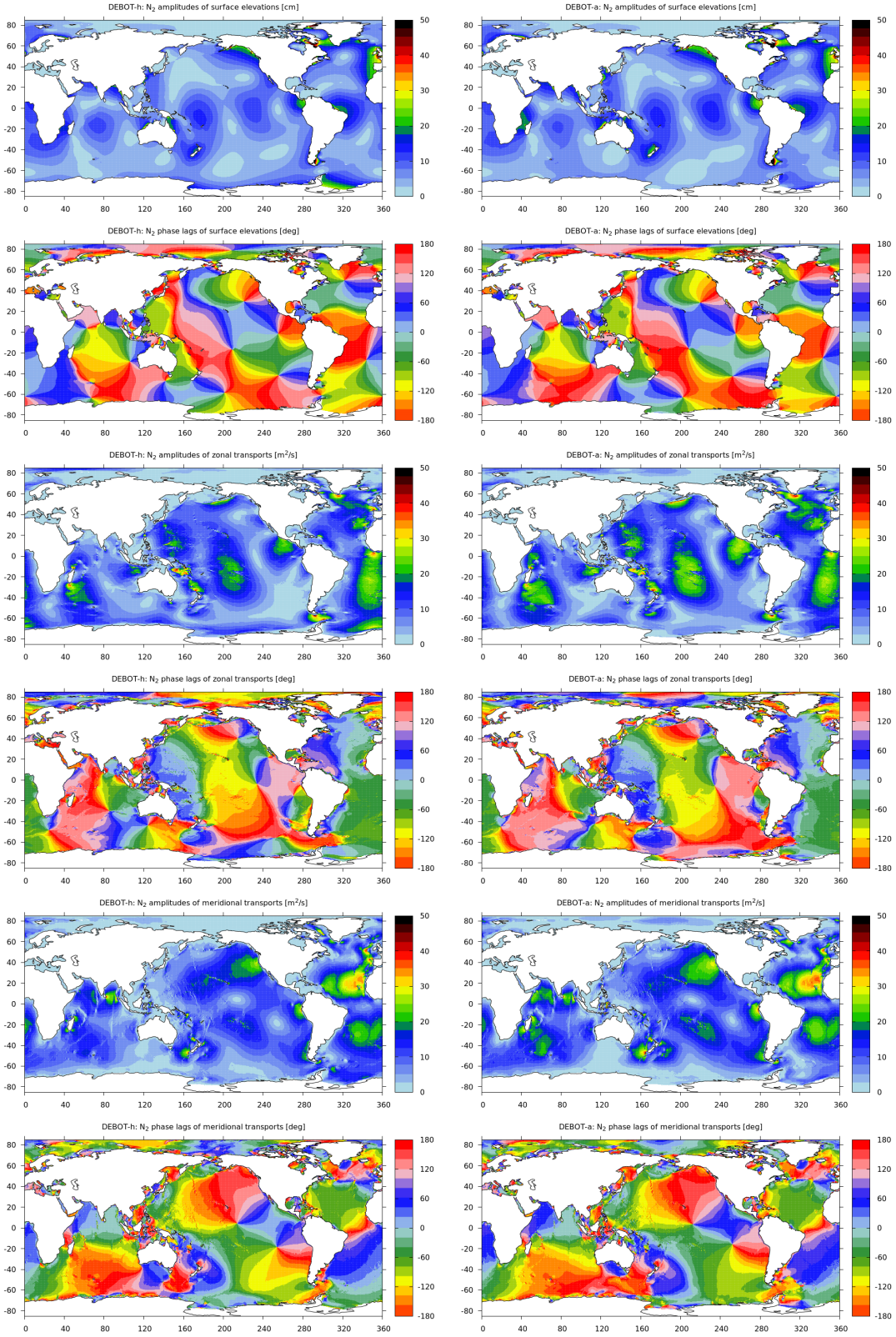

Figure B.5: DEBOT-h (left) and DEBOT-a (right): N_2 amplitudes and Greenwich phase lags of the surface elevations (two top panels), zonal transports (two middle panels) and meridional transports (two bottom panels).

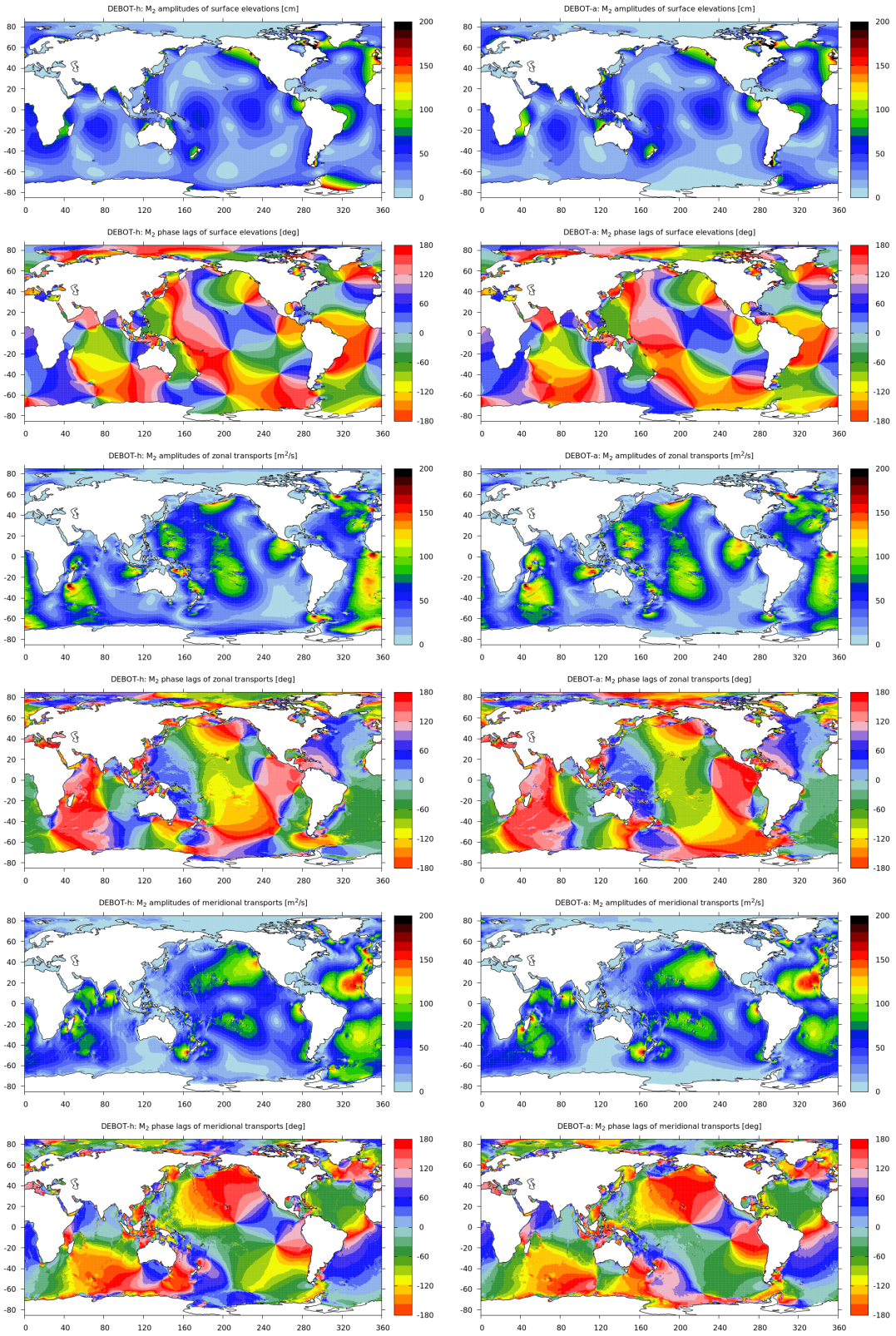

Figure B.6: DEBOT-h (left) and DEBOT-a (right): M_2 amplitudes and Greenwich phase lags of the surface elevations (two top panels), zonal transports (two middle panels) and meridional transports (two bottom panels).

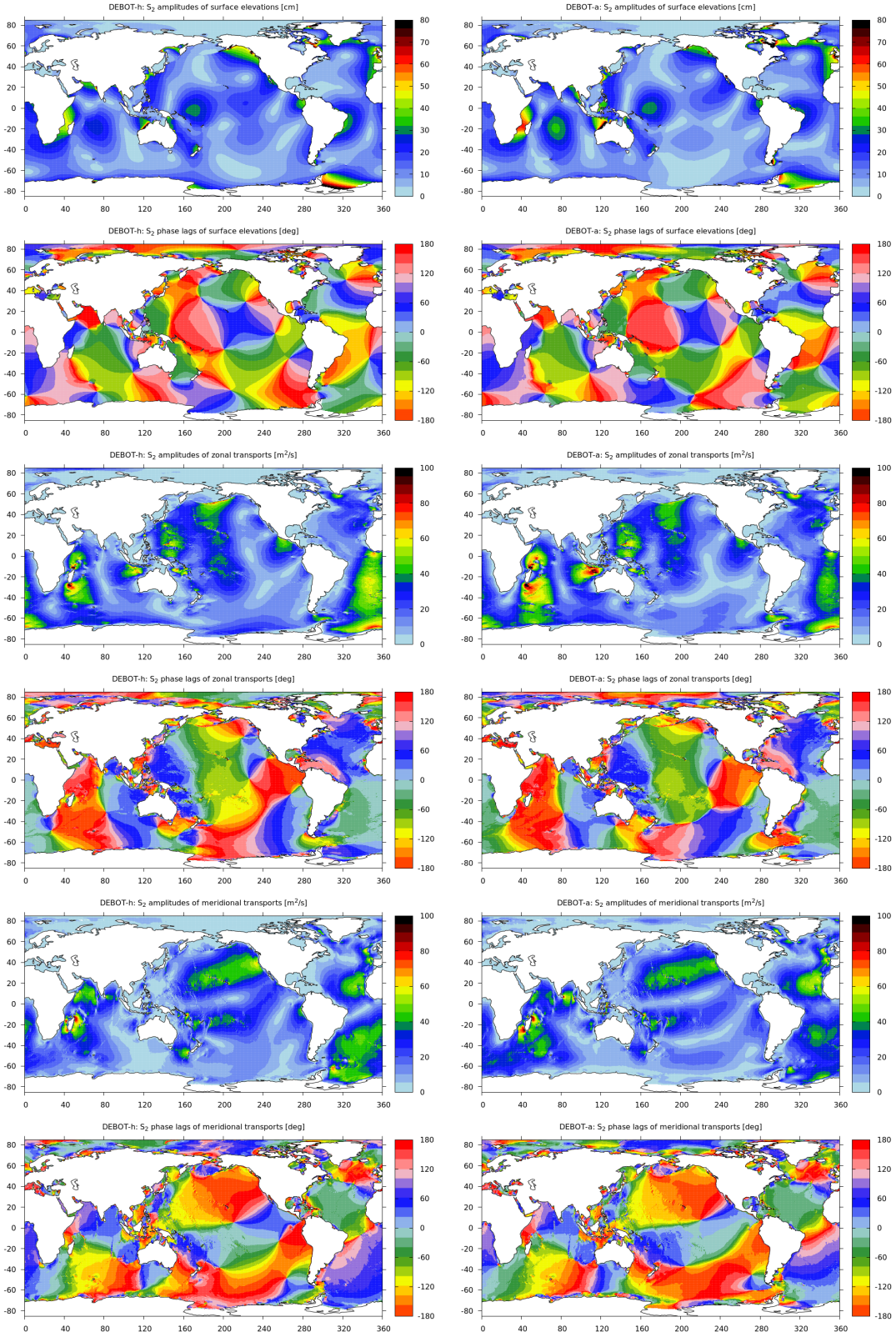

Figure B.7: DEBOT-h (left) and DEBOT-a (right): S_2 amplitudes and Greenwich phase lags of the surface elevations (two top panels), zonal transports (two middle panels) and meridional transports (two bottom panels).

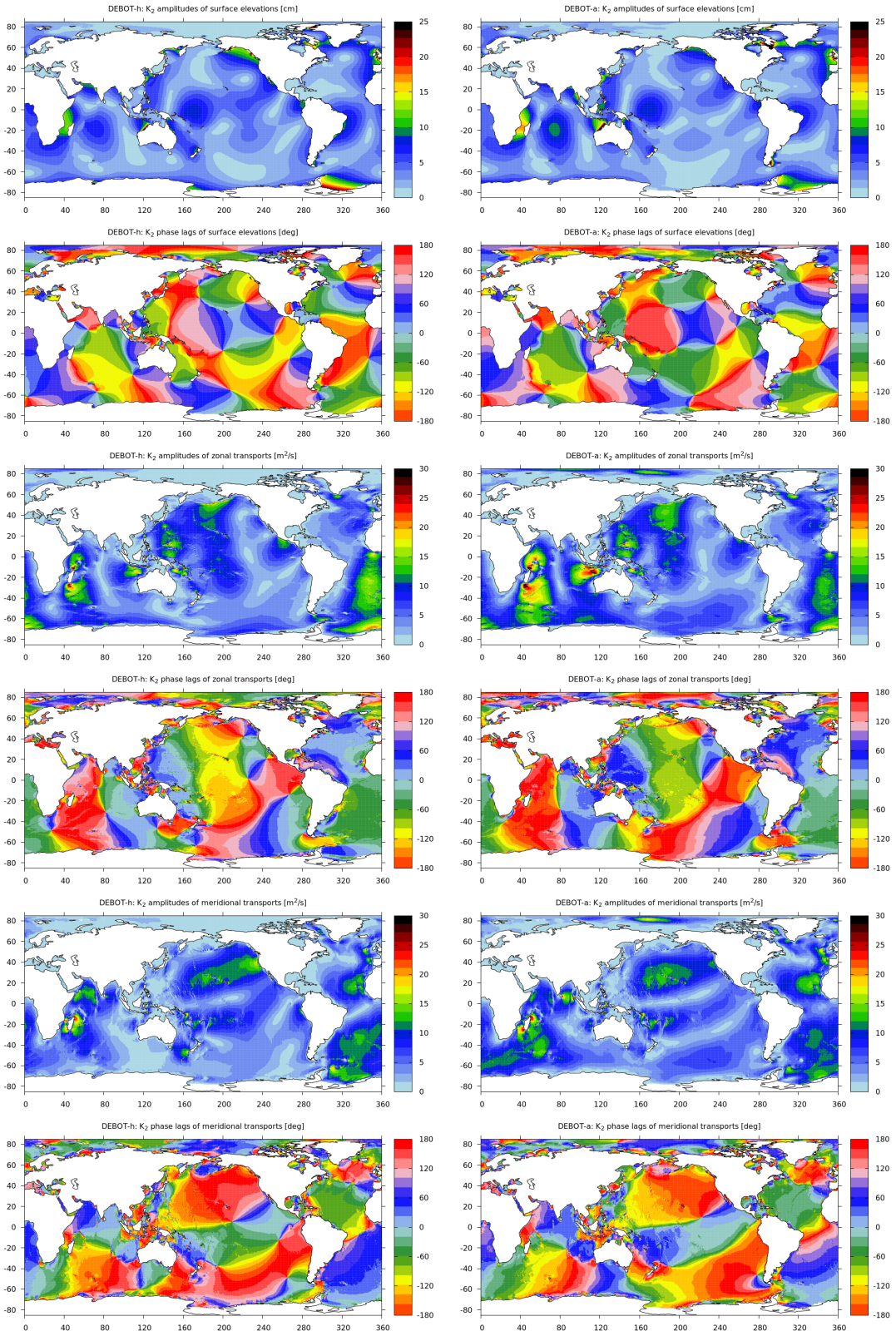

Figure B.8: DEBOT-h (left) and DEBOT-a (right): K_2 amplitudes and Greenwich phase lags of the surface elevations (two top panels), zonal transports (two middle panels) and meridional transports (two bottom panels).

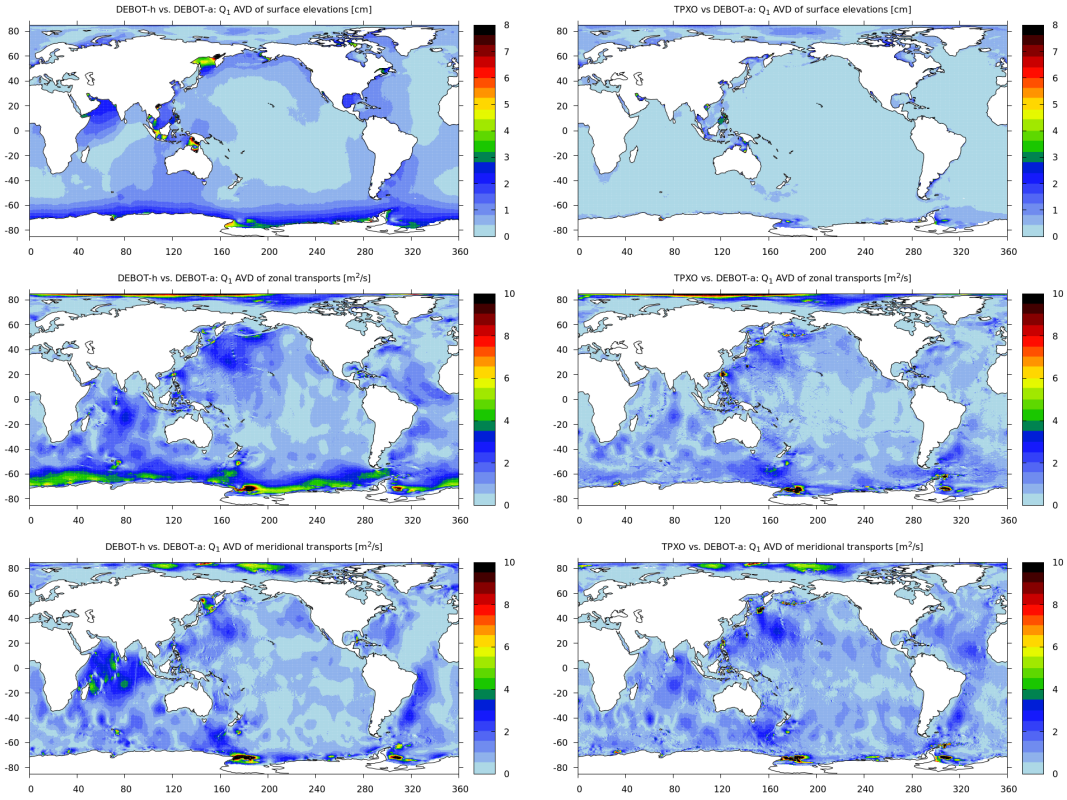

Figure B.9: Absolute vector differences between DEBOT-h and DEBOT-a (left) and DEBOT-a and TPXO (right) for the Q_1 surface elevations (top), zonal transports (middle) and meridional transports (bottom).

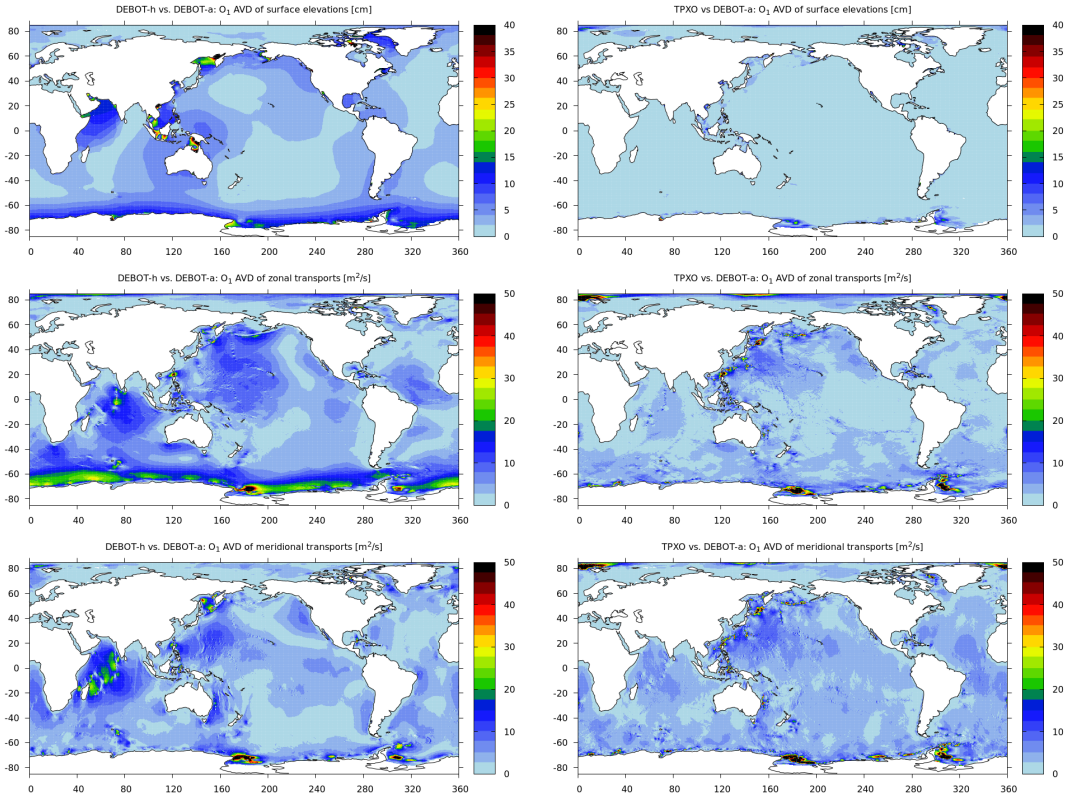

Figure B.10: Absolute vector differences between DEBOT-h and DEBOT-a (left) and DEBOT-a and TPXO (right) for the O_1 surface elevations (top), zonal transports (middle) and meridional transports (bottom).

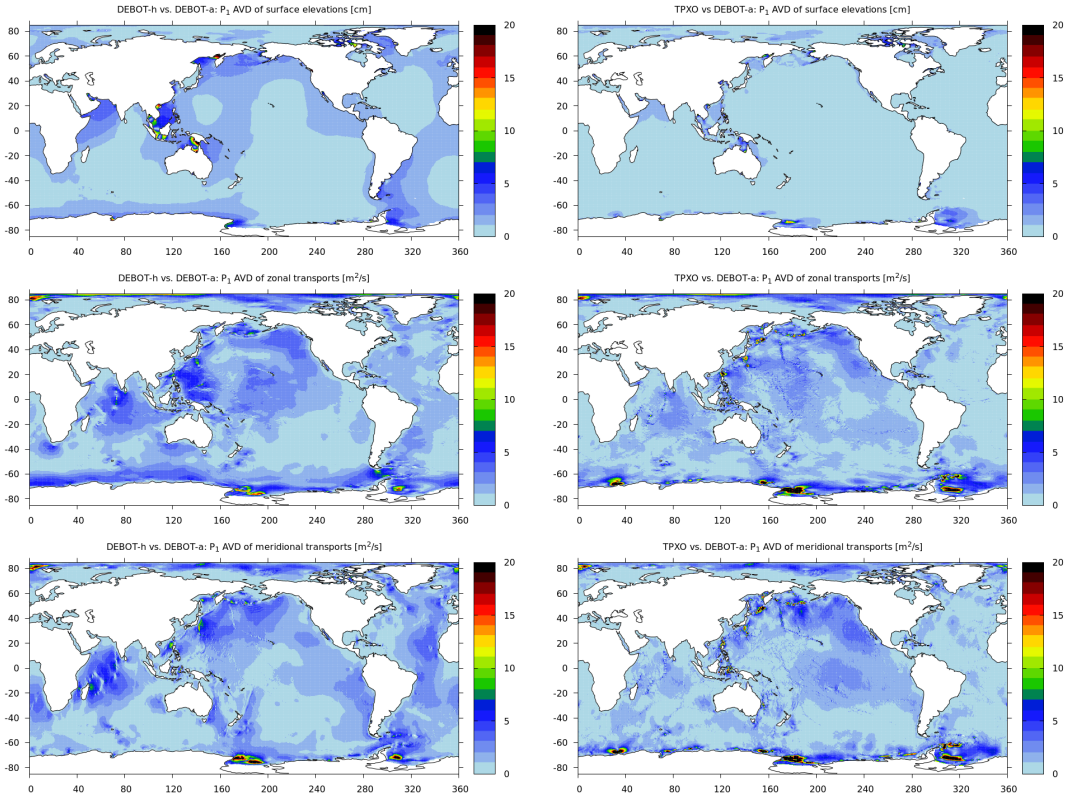

Figure B.11: Absolute vector differences between DEBOT-h and DEBOT-a (left) and DEBOT-a and TPXO (right) for the P_1 surface elevations (top), zonal transports (middle) and meridional transports (bottom).

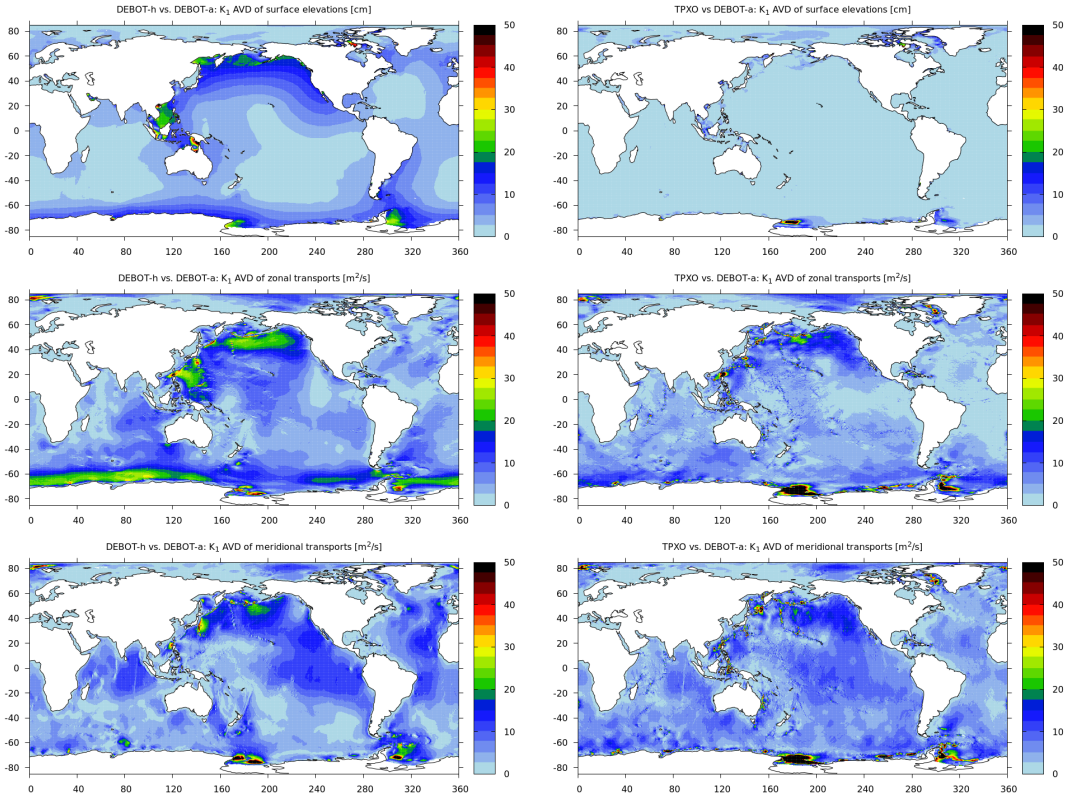

Figure B.12: Absolute vector differences between DEBOT-h and DEBOT-a (left) and DEBOT-a and TPXO (right) for the K_1 surface elevations (top), zonal transports (middle) and meridional transports (bottom).

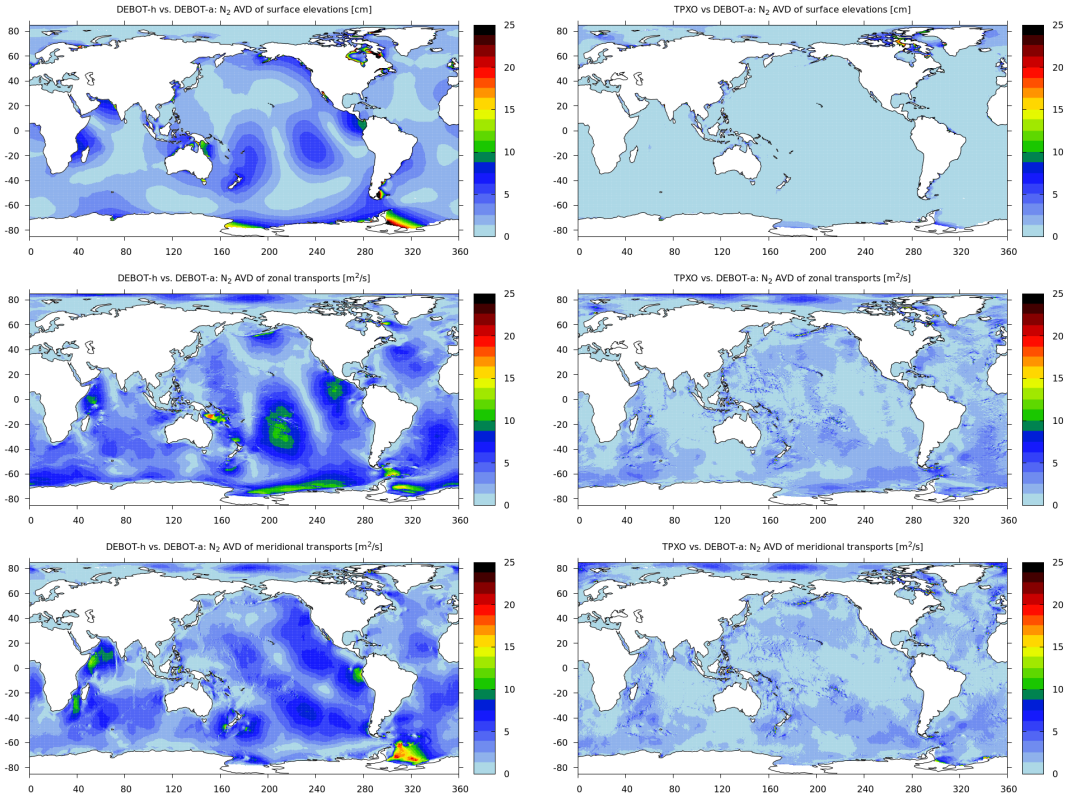

Figure B.13: Absolute vector differences between DEBOT-h and DEBOT-a (left) and DEBOT-a and TPXO (right) for the N_2 surface elevations (top), zonal transports (middle) and meridional transports (bottom).

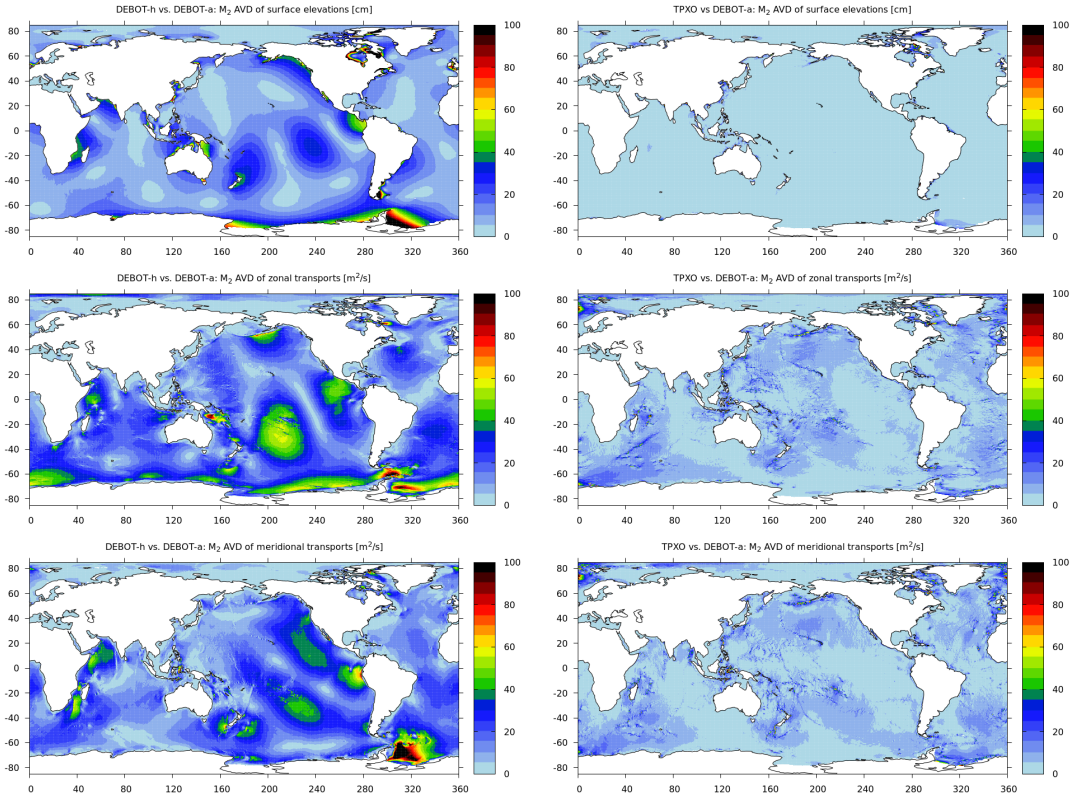

Figure B.14: Absolute vector differences between DEBOT-h and DEBOT-a (left) and DEBOT-a and TPXO (right) for the M_2 surface elevations (top), zonal transports (middle) and meridional transports (bottom).

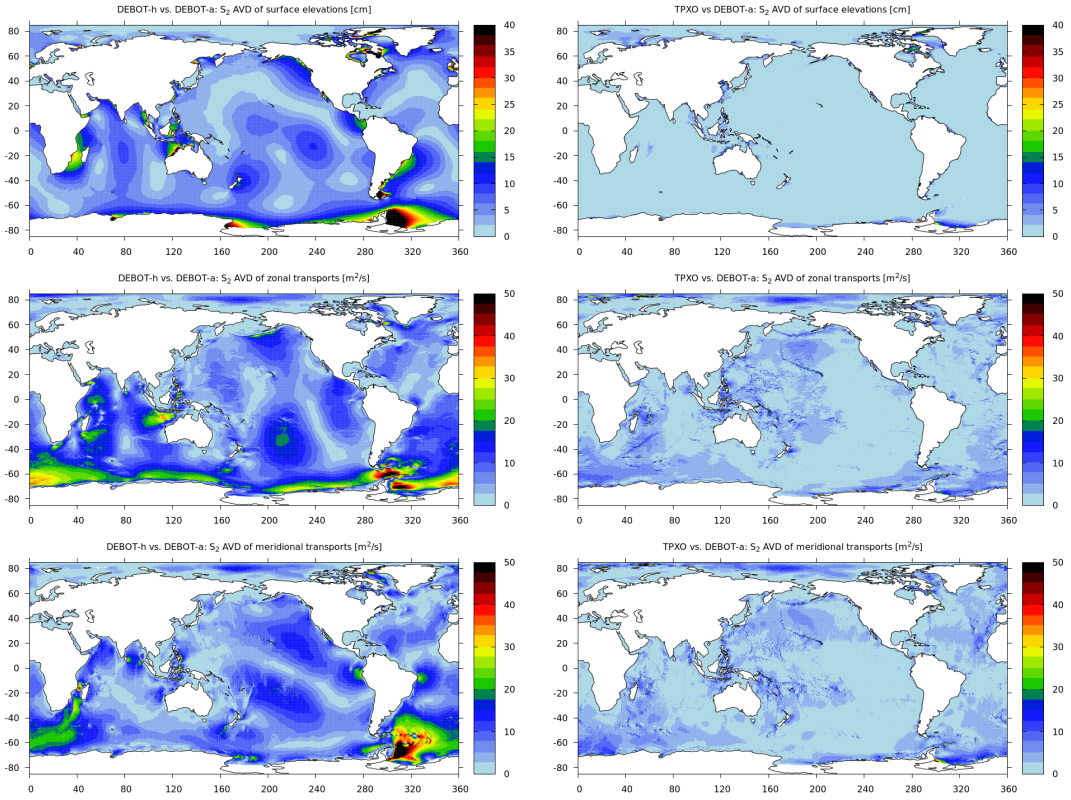

Figure B.15: Absolute vector differences between DEBOT-h and DEBOT-a (left) and DEBOT-a and TPXO (right) for the S_2 surface elevations (top), zonal transports (middle) and meridional transports (bottom).

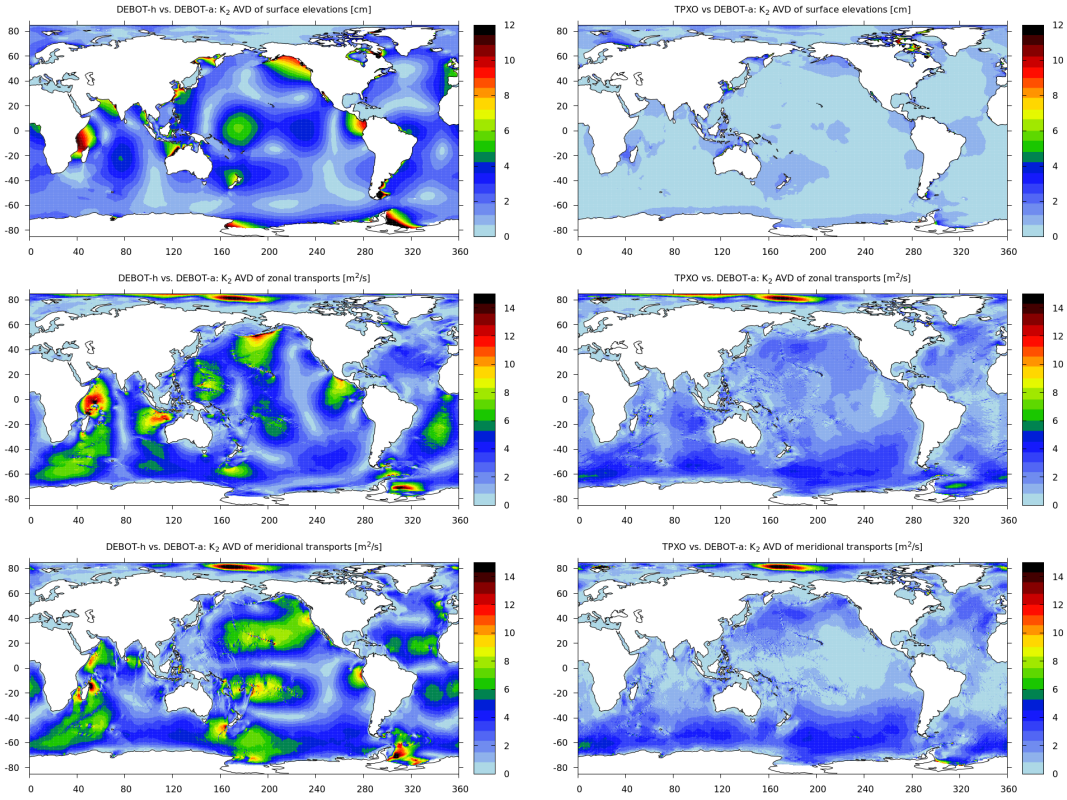

Figure B.16: Absolute vector differences between DEBOT-h and DEBOT-a (left) and DEBOT-a and TPXO (right) for the K_K surface elevations (top), zonal transports (middle) and meridional transports (bottom).

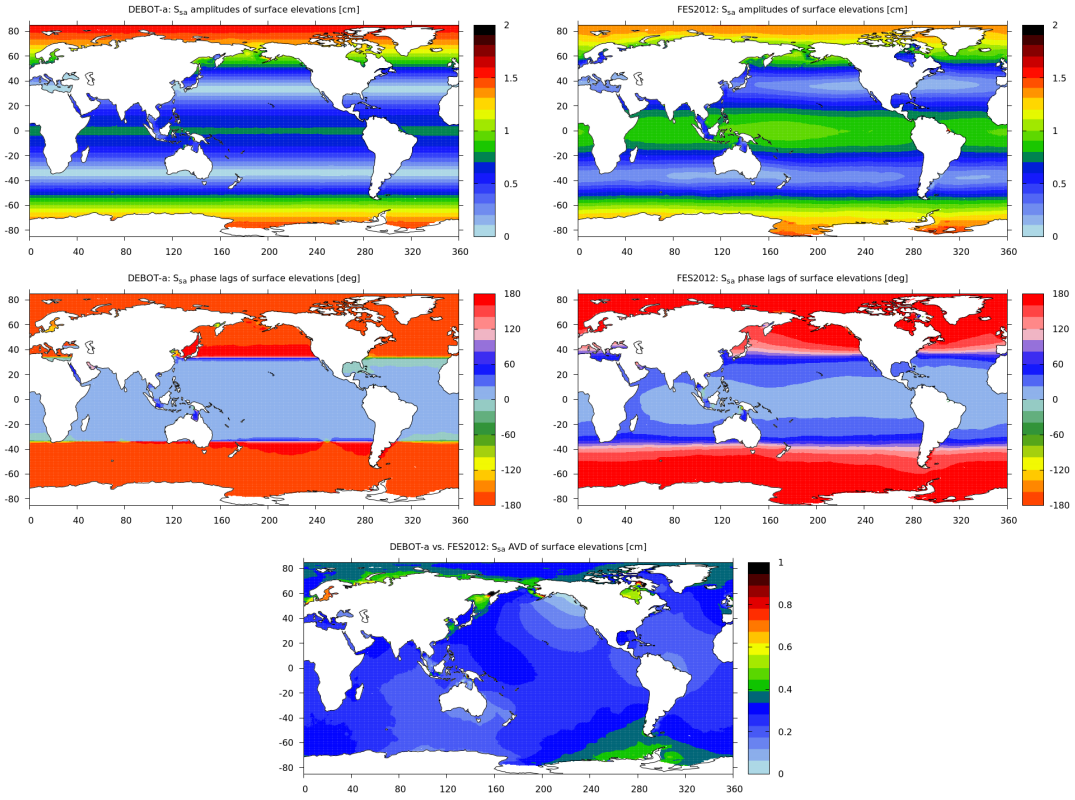

Figure B.17: S_{sa} surface elevation amplitudes (top) and Greenwich phase lags (middle) by DEBOT-a (left) and FES2012 (right) and absolute value differences between the two models (bottom).

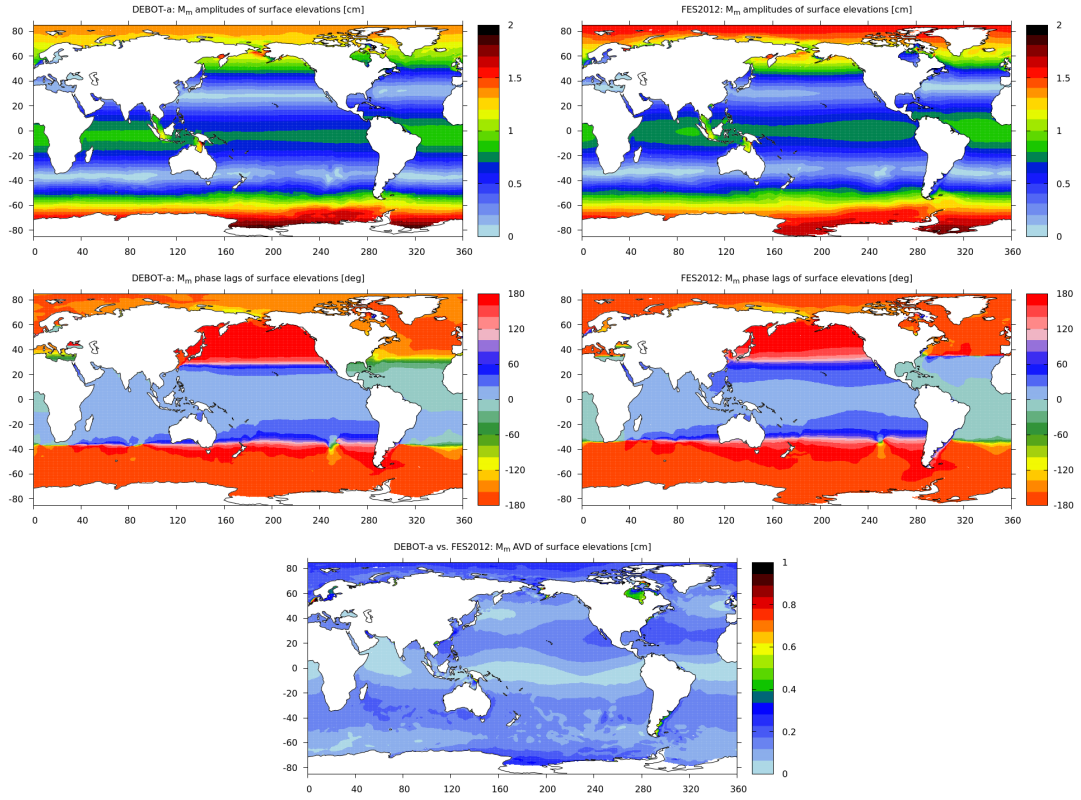

Figure B.18: M_m surface elevation amplitudes (top) and Greenwich phase lags (middle) by DEBOT-a (left) and FES2012 (right) and absolute value differences between the two models (bottom).

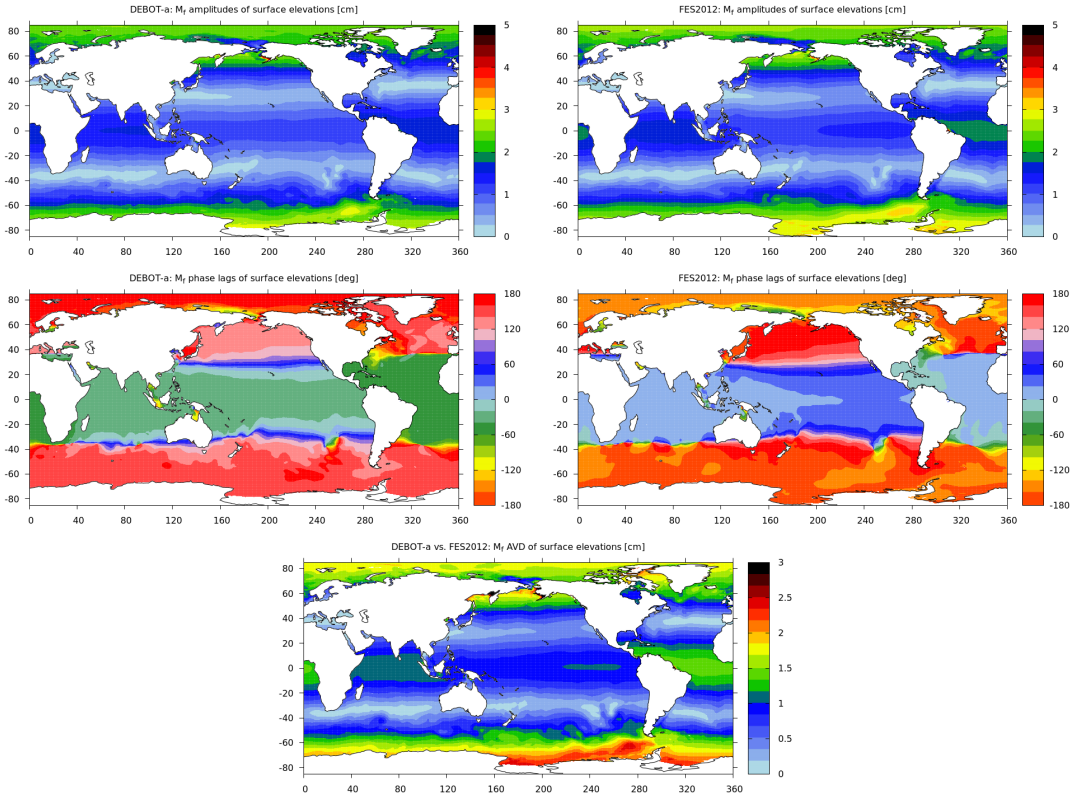

Figure B.19: M_f surface elevation amplitudes (top) and Greenwich phase lags (middle) by DEBOT-a (left) and FES2012 (right) and absolute value differences between the two models (bottom).

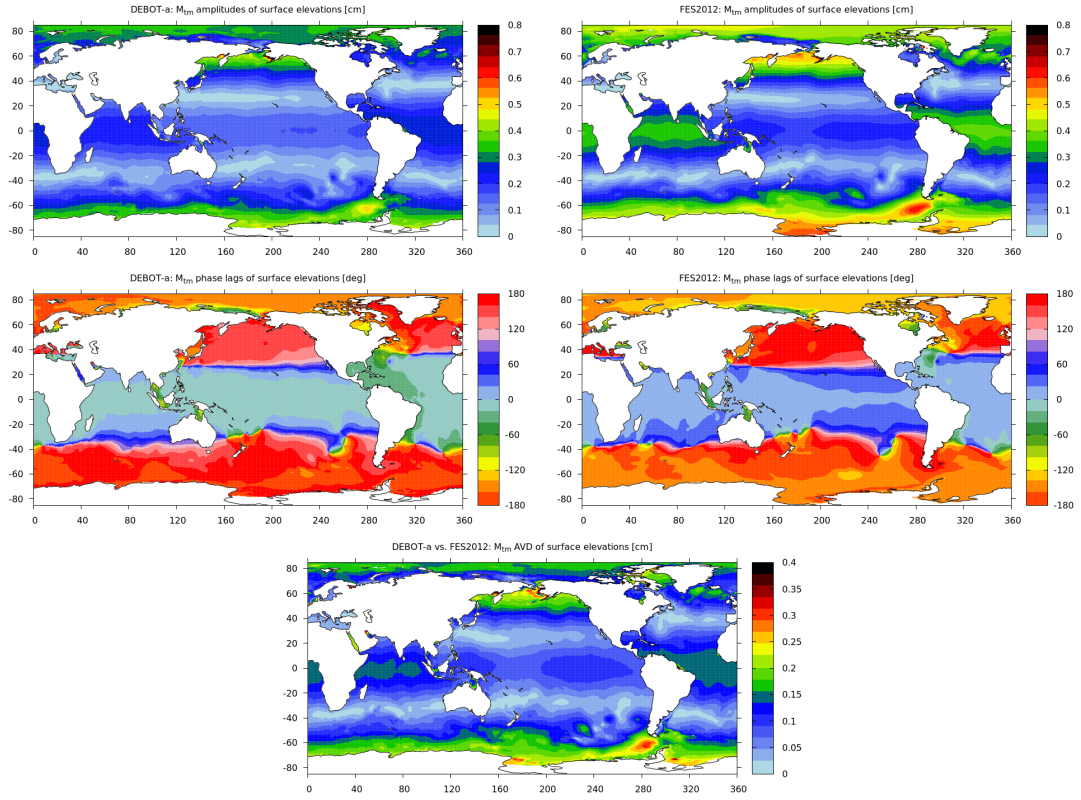

Figure B.20: M_{tm} surface elevation amplitudes (top) and Greenwich phase lags (middle) by DEBOT-a (left) and FES2012 (right) and absolute value differences between the two models (bottom).

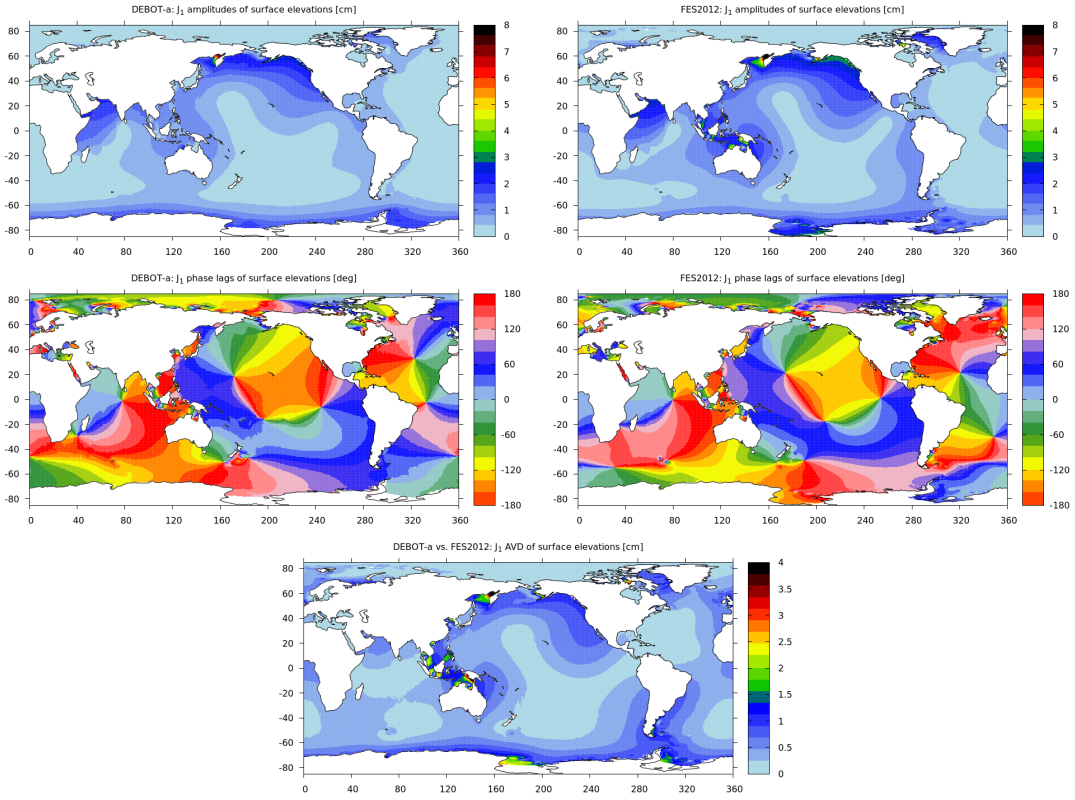

Figure B.21: J_1 surface elevation amplitudes (top) and Greenwich phase lags (middle) by DEBOT-a (left) and FES2012 (right) and absolute value differences between the two models (bottom).

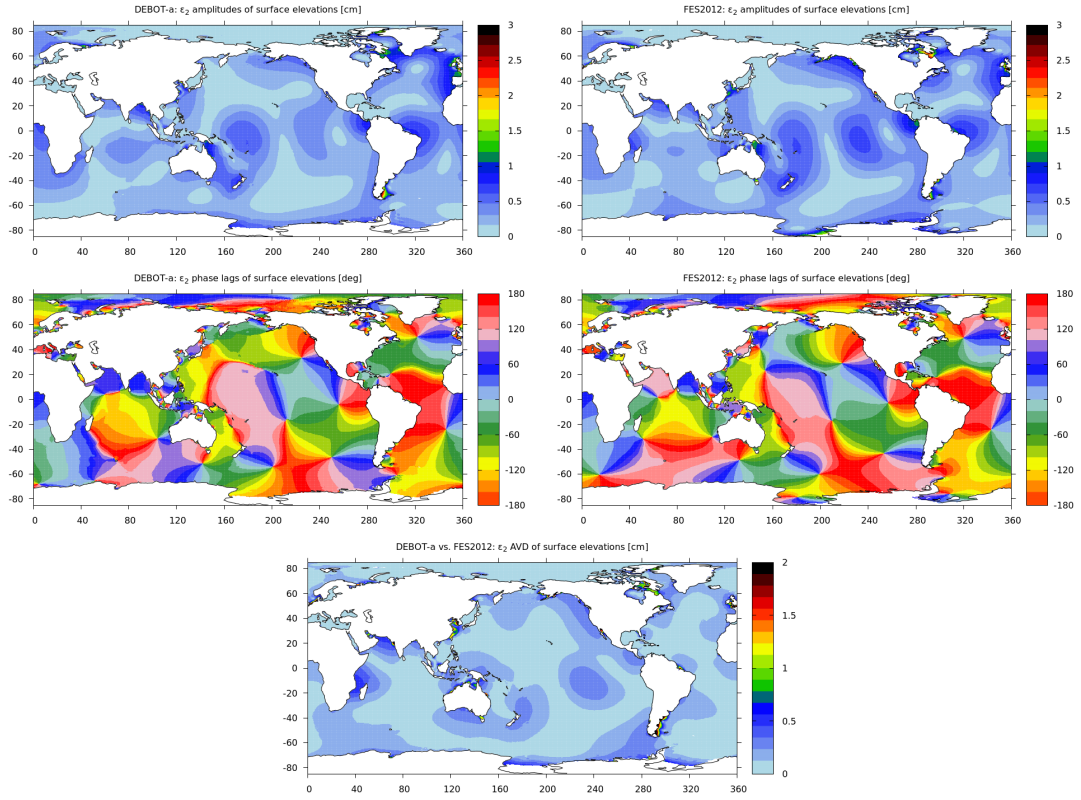

Figure B.22: ϵ_2 surface elevation amplitudes (top) and Greenwich phase lags (middle) by DEBOT-a (left) and FES2012 (right) and absolute value differences between the two models (bottom).

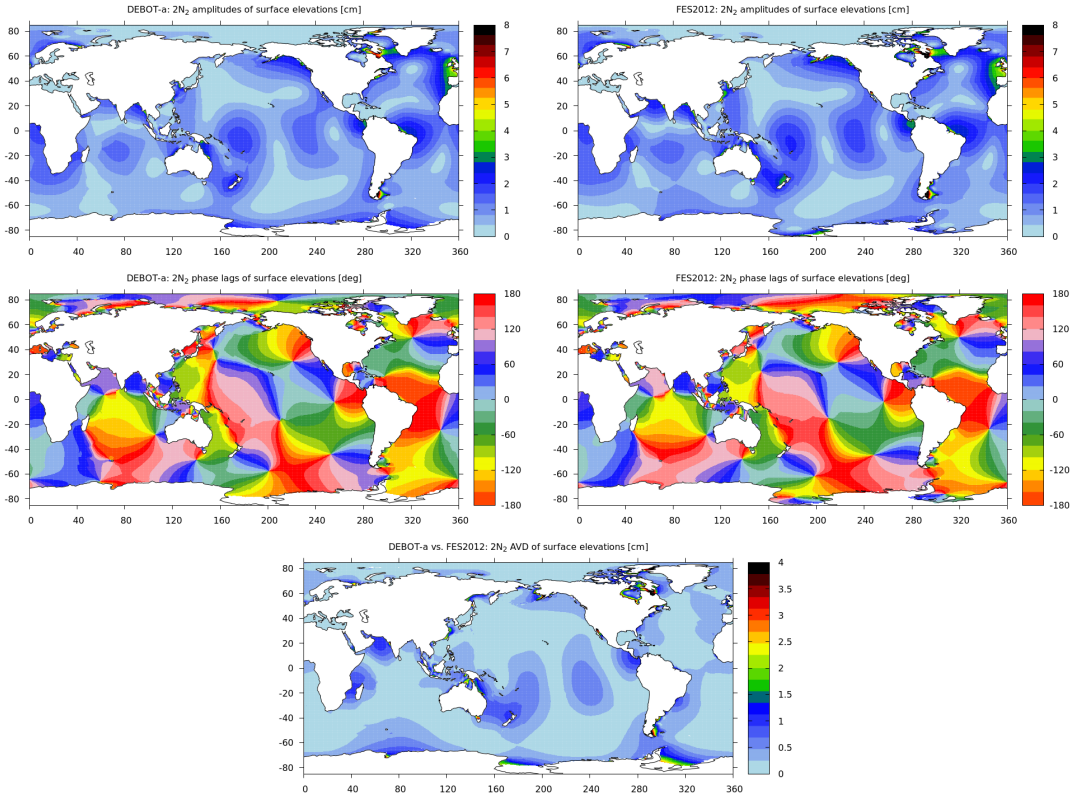

Figure B.23: $2N_2$ surface elevation amplitudes (top) and Greenwich phase lags (middle) by DEBOT-a (left) and FES2012 (right) and absolute value differences between the two models (bottom).

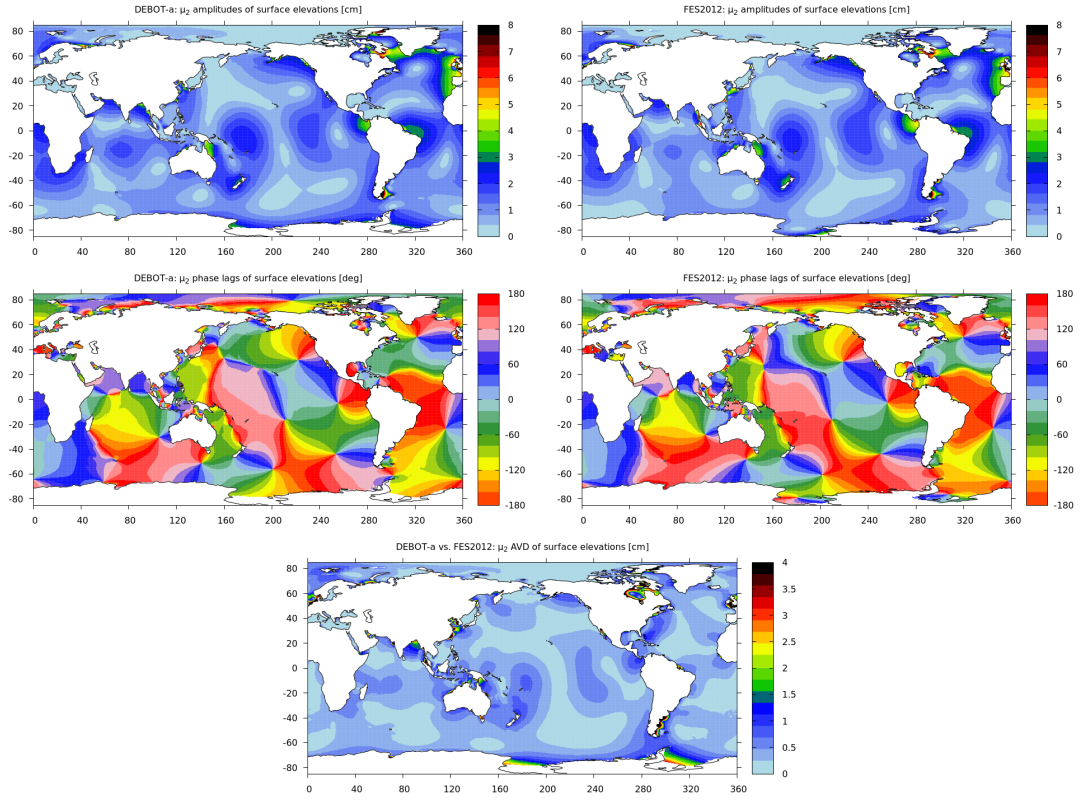

Figure B.24: μ_2 surface elevation amplitudes (top) and Greenwich phase lags (middle) by DEBOT-a (left) and FES2012 (right) and absolute value differences between the two models (bottom).

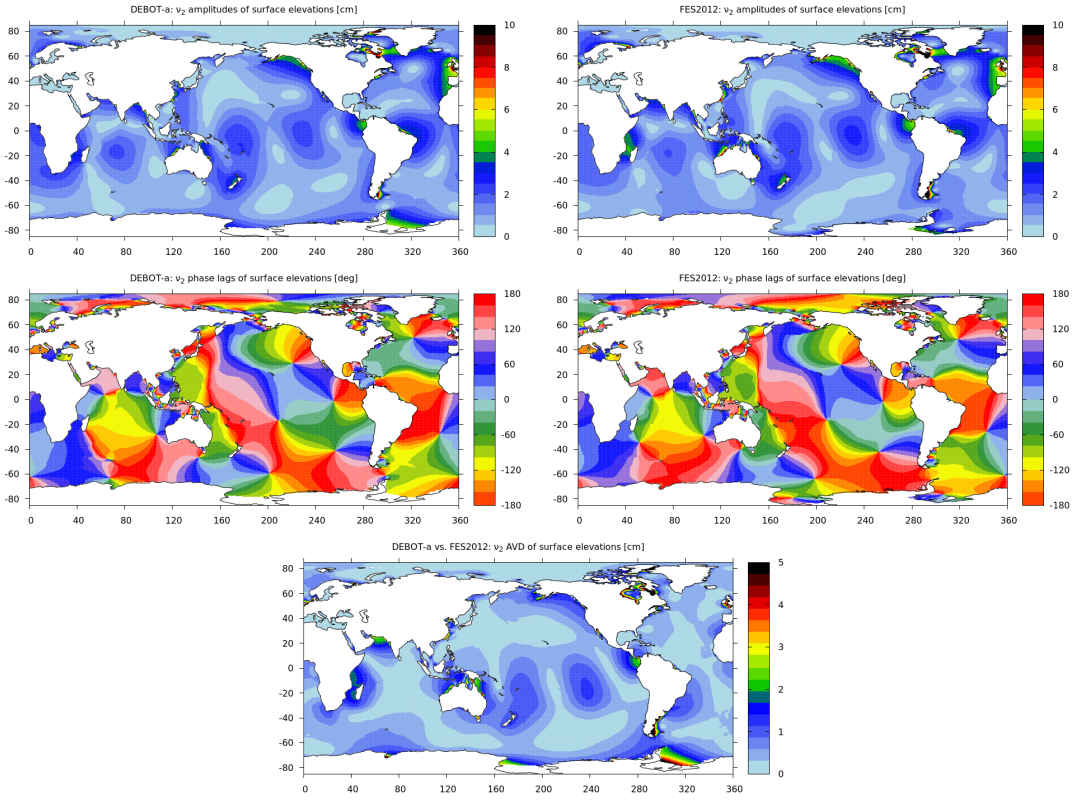

Figure B.25: ν_2 surface elevation amplitudes (top) and Greenwich phase lags (middle) by DEBOT-a (left) and FES2012 (right) and absolute value differences between the two models (bottom).

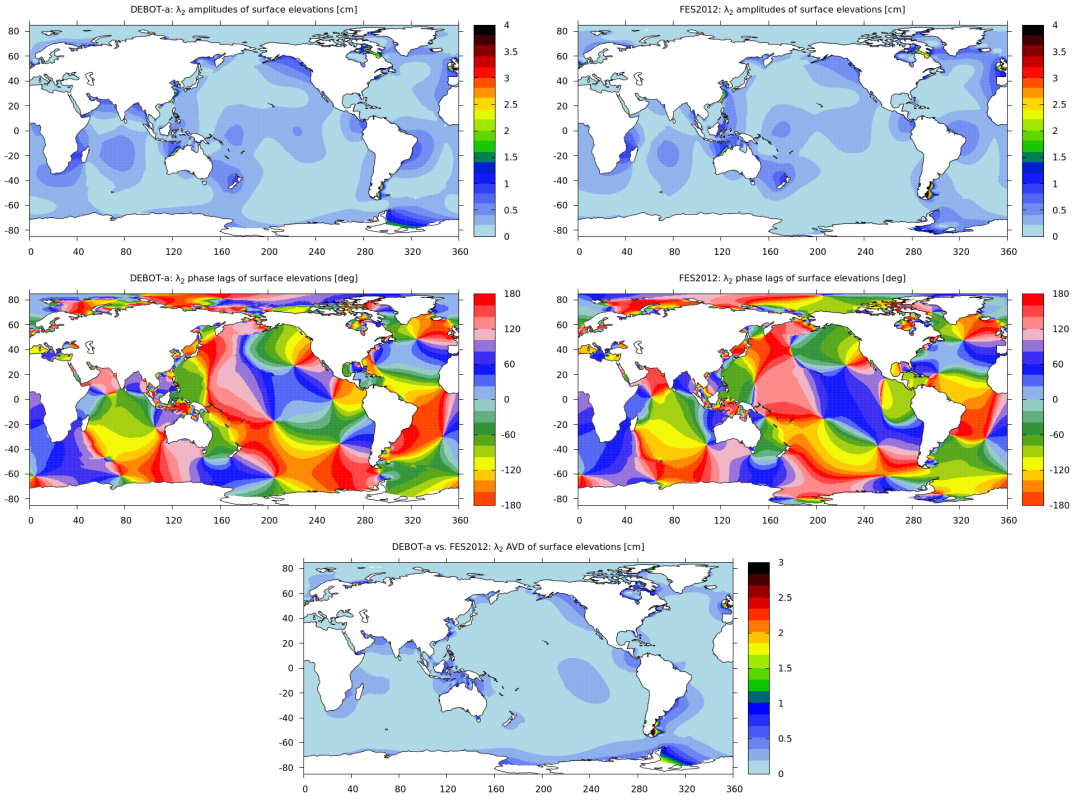

Figure B.26: λ_2 surface elevation amplitudes (top) and Greenwich phase lags (middle) by DEBOT-a (left) and FES2012 (right) and absolute value differences between the two models (bottom).

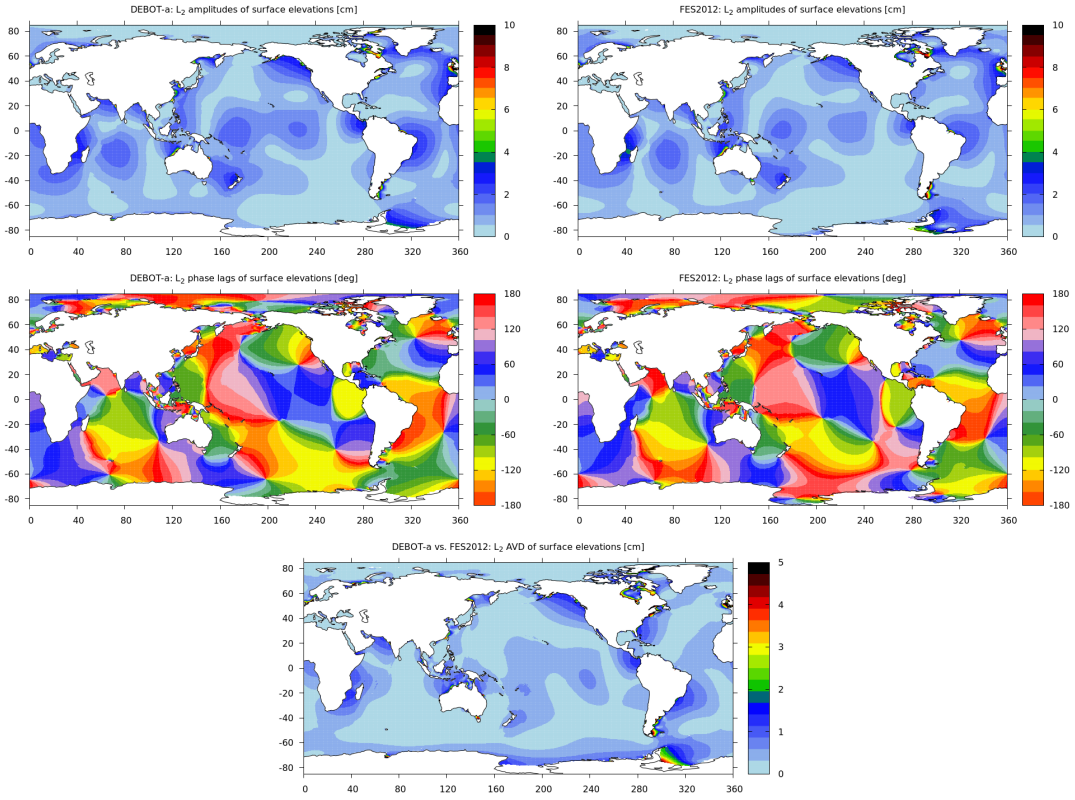

Figure B.27: L_2 surface elevation amplitudes (top) and Greenwich phase lags (middle) by DEBOT-a (left) and FES2012 (right) and absolute value differences between the two models (bottom).

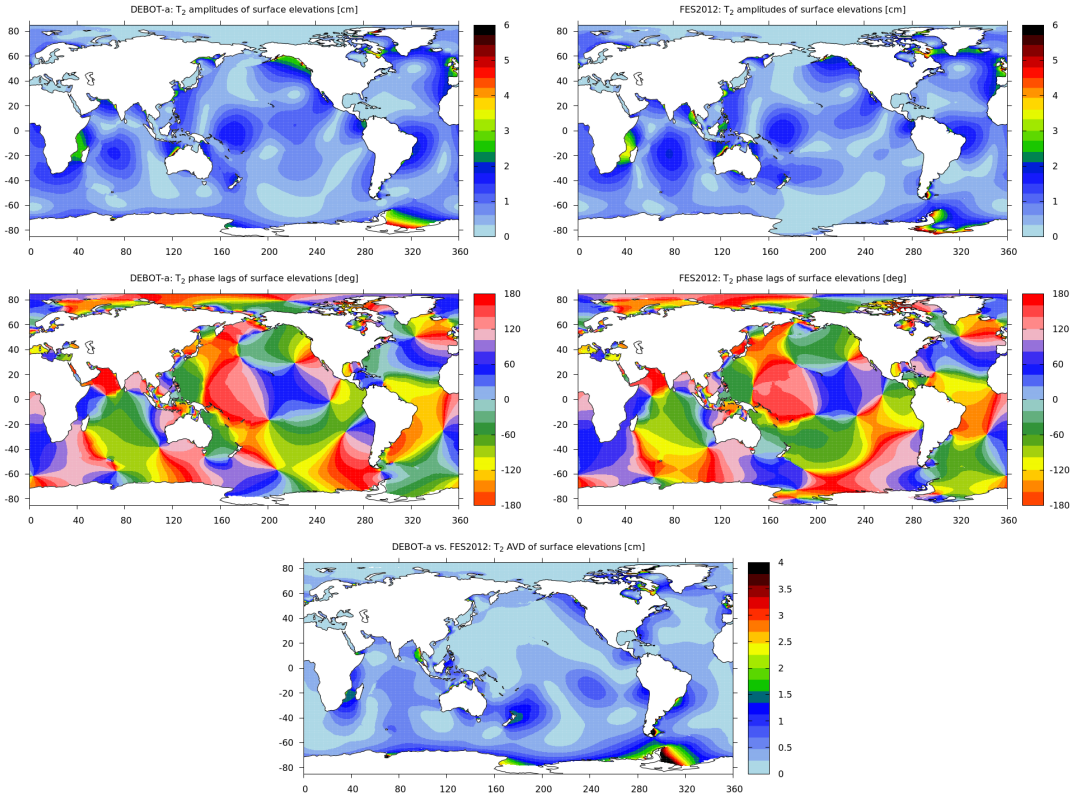

Figure B.28: T_2 surface elevation amplitudes (top) and Greenwich phase lags (middle) by DEBOT-a (left) and FES2012 (right) and absolute value differences between the two models (bottom).

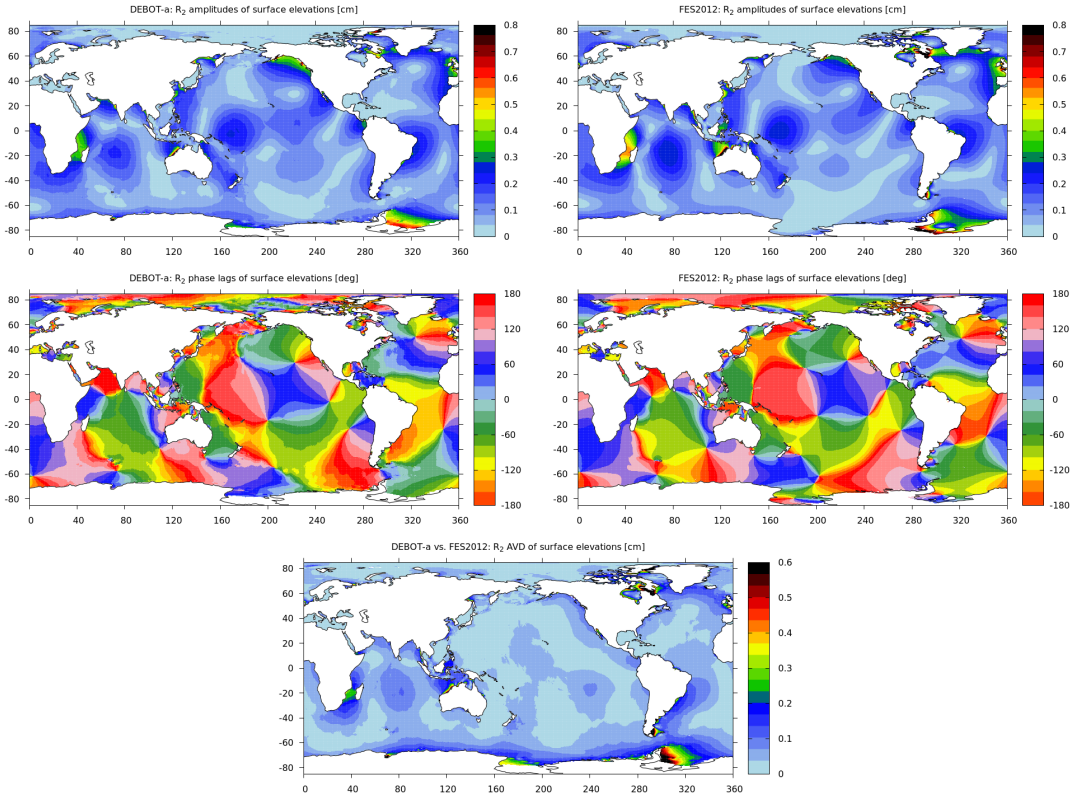

Figure B.29: R_2 surface elevation amplitudes (top) and Greenwich phase lags (middle) by DEBOT-a (left) and FES2012 (right) and absolute value differences between the two models (bottom).

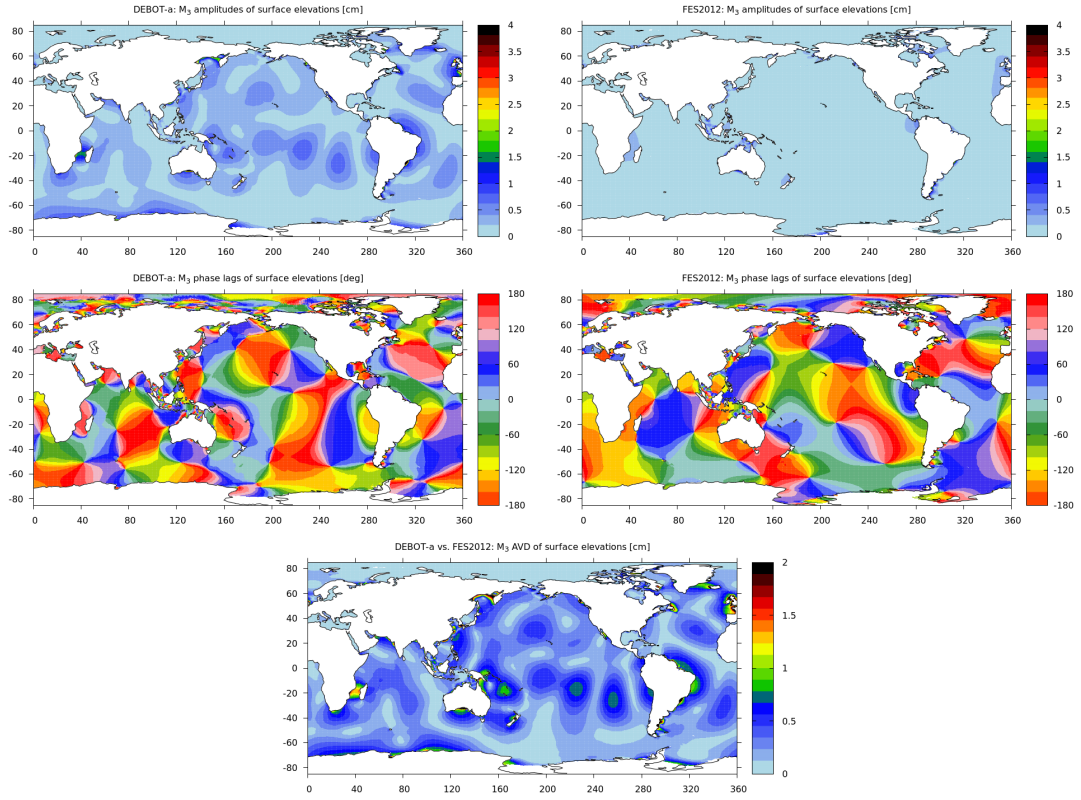

Figure B.30: M_3 surface elevation amplitudes (top) and Greenwich phase lags (middle) by DEBOT-a (left) and FES2012 (right) and absolute value differences between the two models (bottom).

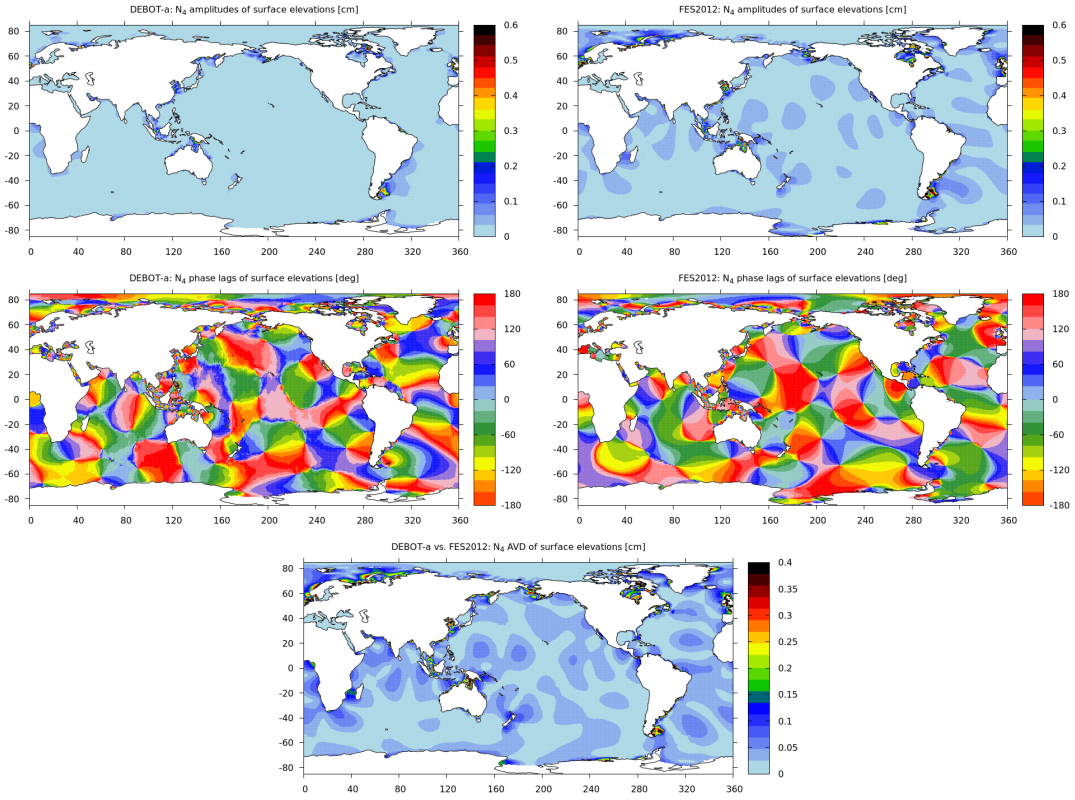

Figure B.31: N_4 surface elevation amplitudes (top) and Greenwich phase lags (middle) by DEBOT-a (left) and FES2012 (right) and absolute value differences between the two models (bottom).

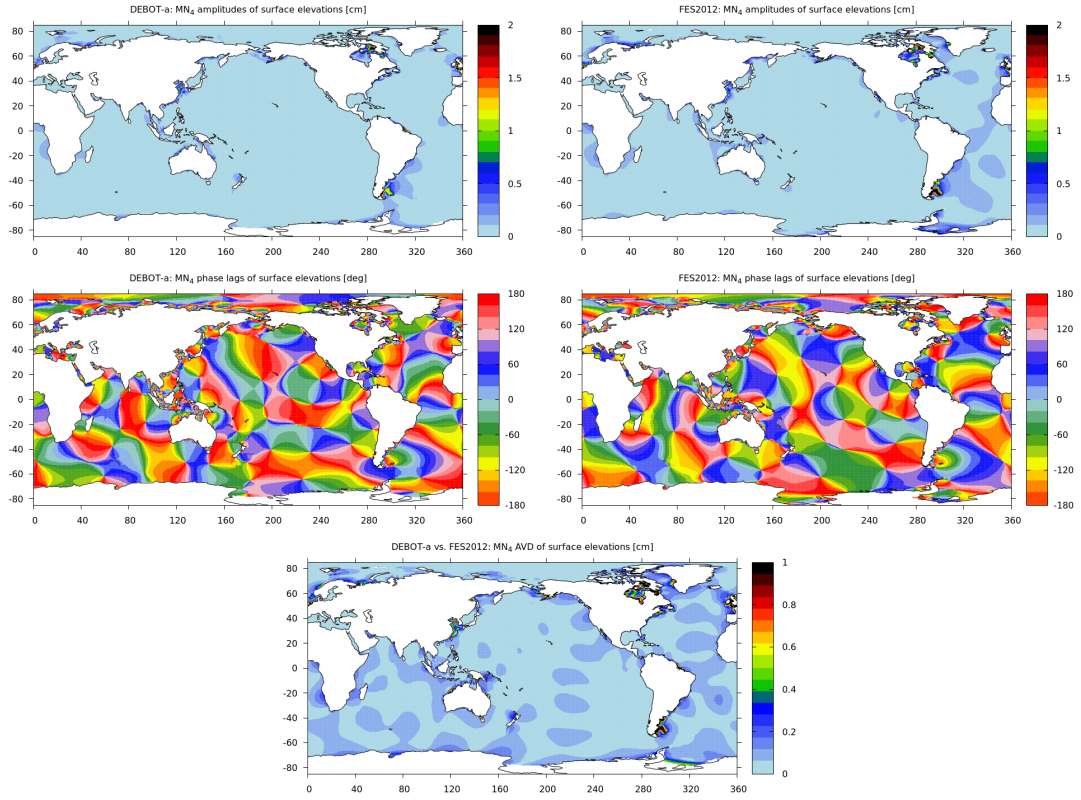

Figure B.32: MN_4 surface elevation amplitudes (top) and Greenwich phase lags (middle) by DEBOT-a (left) and FES2012 (right) and absolute value differences between the two models (bottom).

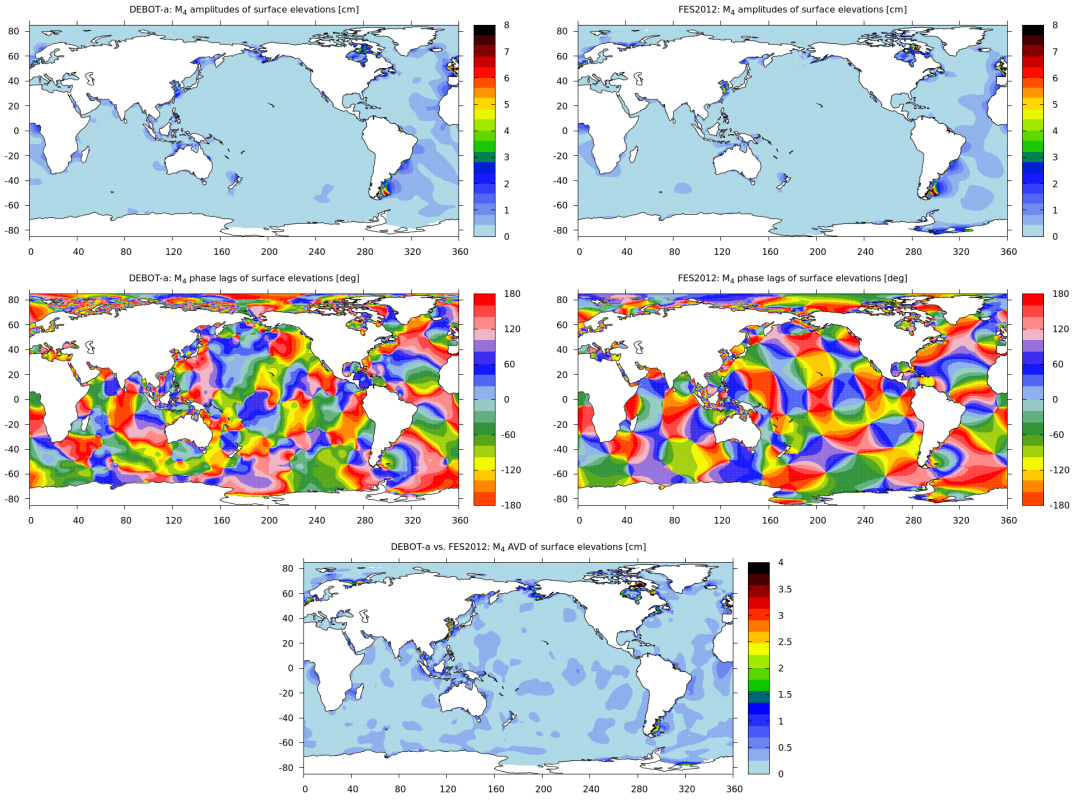

Figure B.33: M_4 surface elevation amplitudes (top) and Greenwich phase lags (middle) by DEBOT-a (left) and FES2012 (right) and absolute value differences between the two models (bottom).

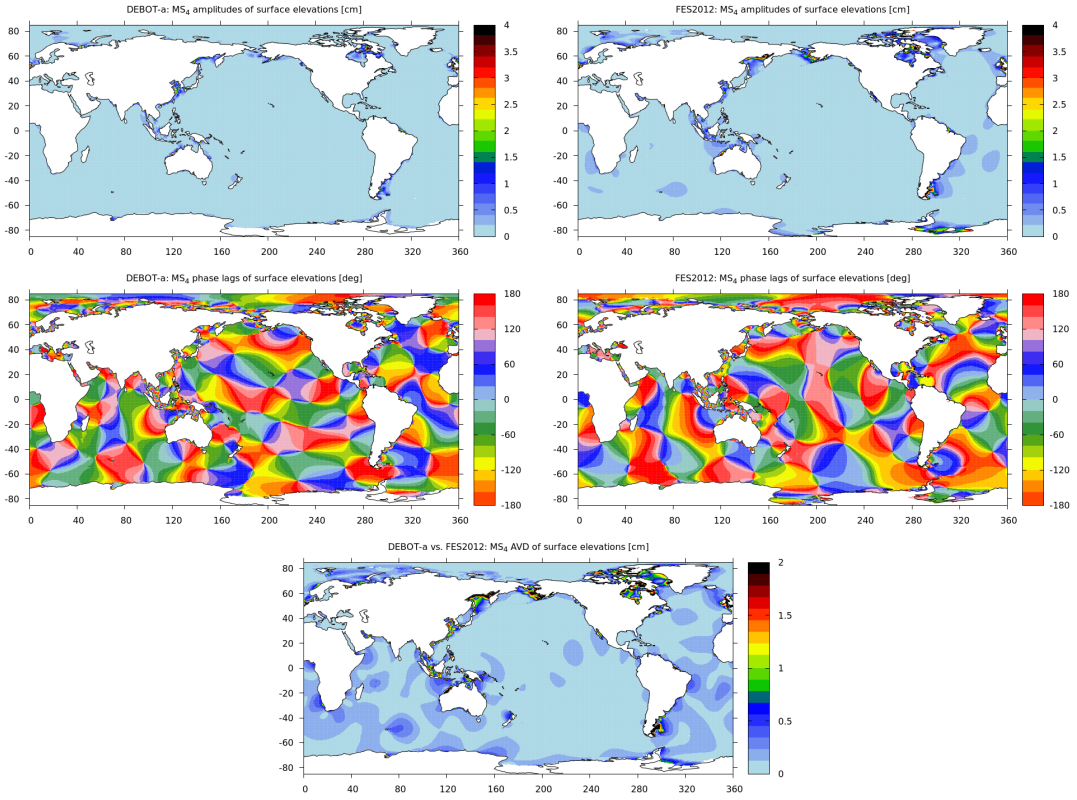

Figure B.34: MS_4 surface elevation amplitudes (top) and Greenwich phase lags (middle) by DEBOT-a (left) and FES2012 (right) and absolute value differences between the two models (bottom).

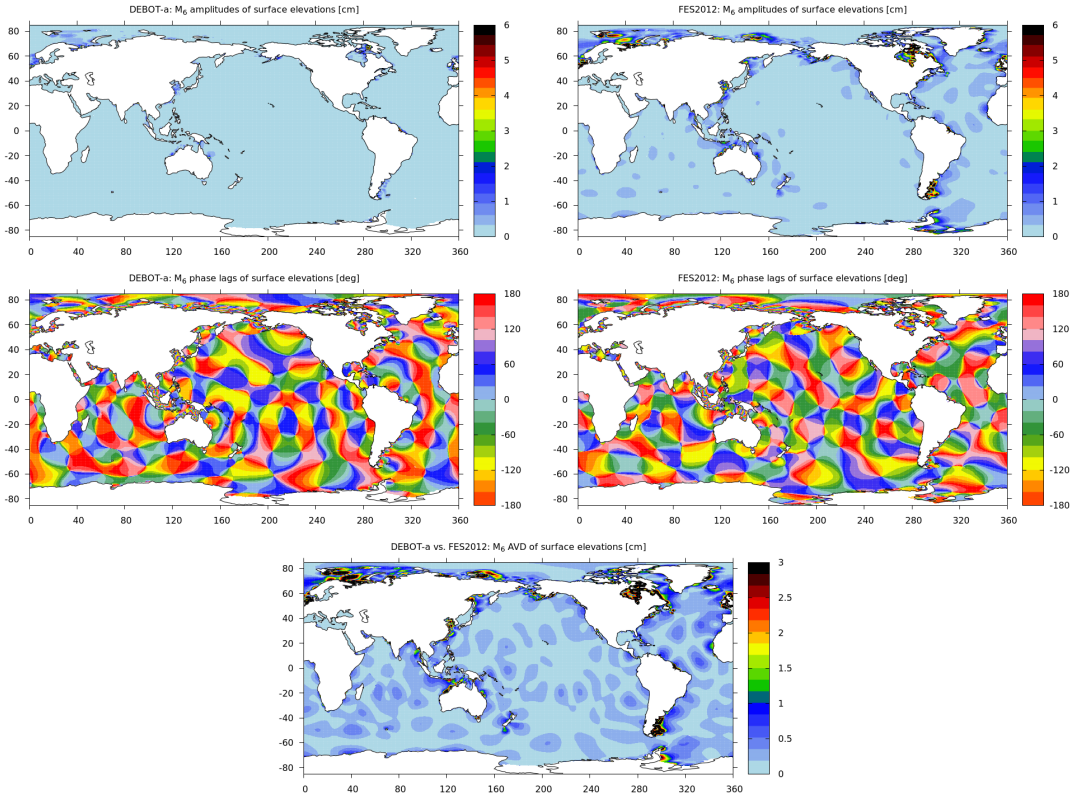

Figure B.35: M_6 surface elevation amplitudes (top) and Greenwich phase lags (middle) by DEBOT-a (left) and FES2012 (right) and absolute value differences between the two models (bottom).

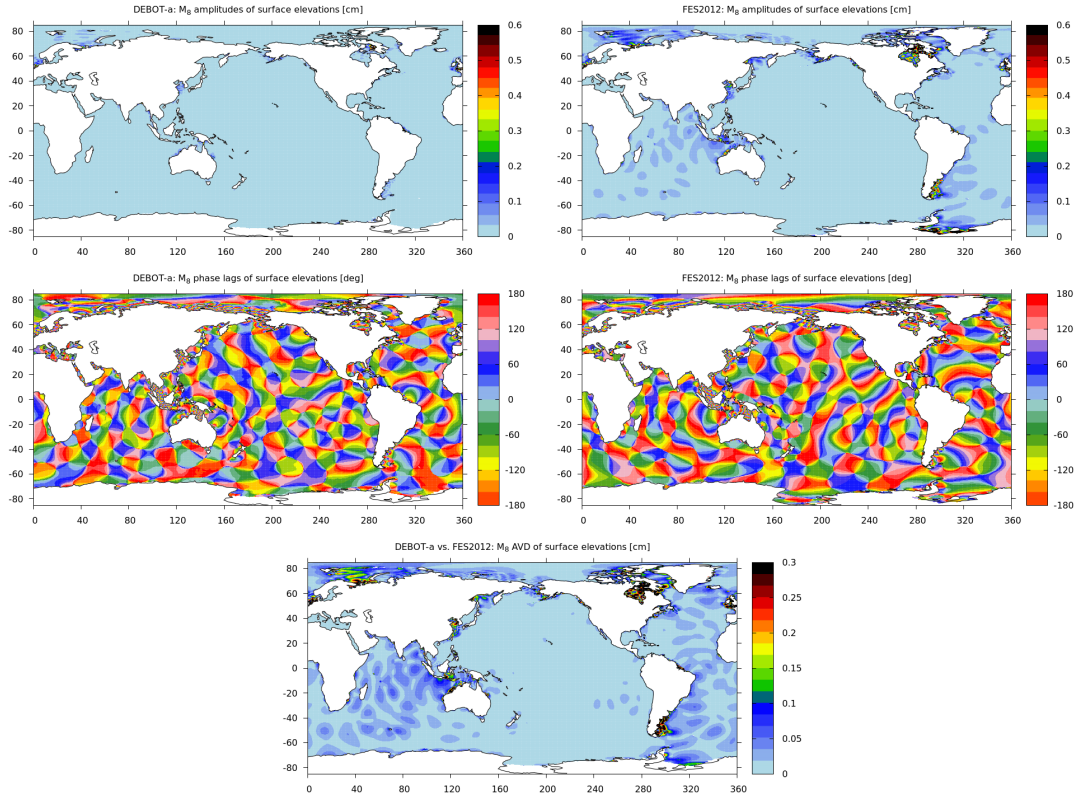

Figure B.36: M_8 surface elevation amplitudes (top) and Greenwich phase lags (middle) by DEBOT-a (left) and FES2012 (right) and absolute value differences between the two models (bottom).

LIST OF FIGURES

LIST OF TABLES

LIST OF ABBREVIATIONS

2D . . . . . two dimensions
3D . . . . . three dimensions
AB3 . . . . . third-order Adams–Bashworth step
AB3-AM4 FB . generalized forward-backward with a combined third-order Adams–Bashforth and fourth-order Adams–Moulton step
AM4 . . . . . fourth-order Adams–Moulton step
AVD . . . . . absolute vector differences
BPR . . . . . bottom pressure recorder
CNES . . . . . Centre national d'études spatiales
CTE . . . . . Cartwright and Tayler (1971); Cartwright and Edden (1973)
DEBOT . . . . David Einšpigel Barotropic Ocean Tides
FB . . . . . forward-backward
ITD . . . . . internal tide drag
MAD . . . . . median absolute differences
MPI . . . . . Message Passing Interface
NASA . . . . . National Aeronautics and Space Administration
OpenMP . . . Open Multi-Processing
OSTM . . . . . Ocean Surface Topography Mission
RMS . . . . . root mean squares
RSS . . . . . root sum squares
SAL . . . . . self-attraction and loading of the water
T/P . . . . . Topex/Poseidon
XDO . . . . . extensive Doodson number